Ultra-low vibration closed-cycle cryogenic surface-electrode ion trap apparatus

Von der Fakultät für Mathematik und Physik
der Gottfried Wilhelm Leibniz Universität Hannover

zur Erlangung des Grades
Doktor der Naturwissenschaften
- Dr. rer. nat. -

genehmigte Dissertation von

Dipl.-Phys. Timko Dubielzig

2021

Referent:	Prof. Dr. Christian Ospelkaus Institut für Quantenoptik Leibniz Univerität Hannover
Koreferent:	Prof. Dr. Piet O. Schmidt Institut für Quantenoptik Leibniz Univerität Hannover
Koreferent:	Prof. Dr. Christof Wunderlich Department Physik - Quantenoptik Universität Siegen
Tag der Promotion:	17. Dezember 2020

Abstract

Trapped ions are one of the leading platforms for building scalable quantum information processors. Current ion traps run on less than 100 qubits. A useful quantum computer needs to operate thousands or even millions of qubits. If systems reach gate fidelities that allow for quantum error correction, gate errors below the physical fidelity can be reached, which is important for scaling. The most promising platform for scaling up ion-based quantum computers are surface electrode traps in connection with the so-called QCCD (Quantum Charge Coupled Device) architecture. In an evolution of the standard (laser-based) approach to quantum logic gates, gates can be performed by applying an oscillating magnetic near-field gradient to the ions. Current fidelities are about one order of magnitude away from reaching the fault tolerant threshold with no fundamental limitations in sight. Scaling QCCDs is impeded by heating rates of the ions as well as vacuum quality. Ions have to be stored for at least as long as it takes for an algorithm to run and subsequent readout. Collisions with background gas and heating can expel ions from the trap. The microwave near-field approach of driving gates benefits from ions that are trapped close to the trap surface. Unfortunately, heating becomes more prominent near the surface. A cryogenic environment reduces the background pressure by several orders of magnitude and the kinetic energy of gas molecules by two orders of magnitude. Heating rates in a cryogenic trap are about two orders of magnitude lower than in a room temperature trap with otherwise equal physical properties. To operate a QCCD processor, it is required to employ phase-stable Raman laser beams. The cryogenic design of the apparatus needs to take into account the resulting requirements for ultra-low vibration amplitudes. This is particularly relevant for closed-cycle cooling systems, which are desirable from an economic point of view compared to liquid cryostats that boil off helium, but which also feature moving mechanical parts that can introduce a serious amount of vibrations.

Here, we present a vibration isolated closed cycle Gifford-McMahon cryocooler with record low vibration amplitudes of 29 nm (RMS=7.8 nm) in the vertical and 51 nm (RMS=13.5 nm) in the horizontal direction. It contains a self-sustained inner vacuum chamber that houses the trap. It features 100 DC connections, 10 of which are able to carry up to 1 A of current and 8 high frequency lines. At 5 K, we can apply continuous 3.4 W of microwave power continuously at 1 GHz to the trap electrodes without heating the system. This is about 5.8 times more than state of the art near-field gates require. We also present the laser systems required to for single-shot ablation loading and Doppler cooling of $^{9}Be^{+}$ ions: a 70 mW 313 nm Dopper cooling laser, a 1064 nm ns-pulse laser for ablation of neutral beryllium atoms and a 235 nm laser for ionizing them. The detection system features an in vacuum imaging system on a cryogenic 3D translation stage that is able to scan and image the complete surface of an ion trap. The light can be detected on a photomultiplier tube or spatially resolved on an EMCCD camera. Our trap features a meander structure for driving gates and can trap up to 5 ions of which we, so far, did not lose any due to background gas collisions. This hints at a vacuum pressure of 10^{-12} mbar or lower.The demonstrated system could hold a cryogenic QCCD chip with a few 10 qubits.

Keywords: trapped ions, quantum computing, cyostats, cryogenic ion trap

Contents

Chapter 1

Introduction

1.1 Quantum computing and quantum simulation with trapped ions

In 1981, Richard Feynman developed the idea of building a computer that 'will do exactly the same as nature' [1], a machine that does not utilize numerical approximations like a classical computer does to simulate quantum physics but quantum mechanics itself. He showed that there are physical problems of interest that cannot be simulated adequately on a classical computer. Four years later David Deutsch proposed what is now known as a universal quantum computer [2]. A number of useful quantum algorithms have been published. Two of the most prominent ones are Shor's algorithm for factorizing large numbers into their primes [3] and Grover's algorithm for inverting functions [4].
A quantum computer stores information in a quantum bit, a so-called qubit, which is superposition between the states of a two-level system. Coherently manipulating either a single qubit or multiple qubits at once is called driving a quantum gate. An entangling operation between two qubits is called a two-qubit gate. It has been shown that a combination of arbitrary single-qubit and one type of maximally entangling two-qubit gates is a universal set of gates to build a quantum computer [5, 6]. Therefore a lot of research effort has been invested in performing and perfecting these two types of gates.
Currently, many technological platforms are under investigation to build a universal quantum computer. These include but are not limited to realizing a qubit as a polarization state of a photon, as a nuclear spin-state in molecules, as quantum dots in semiconductors, as quantized superconducting currents and as trapped atoms or ions [7]. All of these approaches have their distinctive advantages and disadvantages.
It is not clear, which platform, if any, will ultimately outperform the others. Therefore research effort into all of these systems is warranted.
David DiVincenzo has defined criteria that have to be fulfilled by a machine in order to be considered a universal quantum computer [8]. Besides the mentioned universal set of gates, the system needs to be 'scalable with well characterized qubits' and these qubits have to be initialized and every qubit has to be measurable. Additionally, the coherence times of the qubits have to be much longer than the gate operation time.
The scalable system requirement assumes the ability to store many qubits in a so-called quantum processor and the coherence time requirement assumes the ability to keep the quantum information within the processor intact until the quantum algorithm that is

run on the computer is finished.
Ions in Paul traps [9] are a promising platform because they feature long coherence times on the order of seconds, while gate times on the order of microseconds can be realized. Reliable initialization and readout is possible via laser cooling and fluorescence detection. There are also promising proposals to scale the system [10]. The qubits are encoded in electronic energy levels of identical atoms. The ions are confined in a 3 dimensional harmonic electric potential in which the ions exhibit harmonic oscillatory motion. Ions with the same charge that are trapped in the same potential repel each other. The Coulomb interaction couples the motion of the ions and if they are sufficiently cold they can be treated like coupled quantum mechanical harmonic oscillators and they exhibit collective modes of motion as well as modes of motion that only affect certain combinations of ions [11]. Simultaneous manipulation of these modes of motion and selected individual qubit states can mediate the controlled exchange of quantum information between two or more qubits and is the base of quantum computing with trapped ions [12].
It has been demonstrated that trapped ions can realize a programmable quantum computer [13] and run the aforementioned Shor algorithm [14] and Grover's algorithm [15].

1.2 Improving the scalability of ion trap based quantum computers

Although it has recently been demonstrated that for calculating a very specific quantum mechanical problem, a 53 qubit quantum circuit can outperform a classical computer [16], thousands or even millions of qubits are required to perform error corrected computations of problems that are relevant beyond purely academic interests.
A sophisticated algorithm that runs on a multi qubit machine may rely on successive gate operations on several qubits. Yet errors in these operations are unavoidable due to imperfect control in any architecture. Quantum error correction schemes that rely on auxiliary control qubits can correct gate errors reasonably well, if the probability of being erroneous is lower than about 10^{-4} per gate [17, 18].
Running a comparatively short algorithm on a low number of qubits might not require error correction schemes because just repeating the experiment and accumulating statistics of the results might be more resource efficient. For more sophisticated algorithms that demand many gate operations, quantum error corrections becomes a necessity. Therefore, in order to scale the system up, it becomes vital to reach gate fidelities below the 10^{-4} threshold.
With an infidelity of 10^{-6}, single-qubit gates have already reached below the fault-tolerant threshold [19]. Laser-based two-qubit gates were able to reach a gate infidelity in the order of a few 10^{-4} [20, 21], which comes close to the threshold. Microwave near-field radiation based two-qubit gates like the ones we use in our group have reached infidelities in the 10^{-3} range [22, 23].

Another vital part besides gate fidelities is to increase the number of qubits that can take part in the computation. The first reasonable approach would be to just increase the number of ions in a Paul trap and use the motional mode structure to address the specific ion combinations. The numbers of normal modes associated with a chain of n ions is $3n$. The frequency spacing between neighboring modes in the mode spectrum becomes smaller with more ions in the chain [24]. At a certain point it will become difficult to address a specific mode without simultaneously also off-resonantly addressing spectator modes. It has been estimated that addressing normal modes in ion chains of more than approximately $n = 100$ becomes unpractical [25].
A particularly promising technology to tackle this problem is the so-called quantum charge-coupled device (QCCD), which was proposed in 1998 [11] and later discussed in more detail [10]. A QCCD is a Paul trap architecture that is composed of several specialized zones. There are zones for loading ions, storing them, detecting them and zones for driving gates, the so-called interaction zones. Several ion guides and junctions interconnect these zones. If a standardized design for each zone type is developed, connecting several of these modules can in theory lead to an ever increasing trap size and ion number [26]. The challenge of spectrally unresolvable normal modes is mitigated in a QCCD because the number of ions that interact can be controlled by transporting only as many as needed into an interaction zone.
The most promising approach to realize a QCCD is a so-called surface-electrode ion trap [27, 28]. These are structures in which all electrodes that produce the confining potential of the Paul trap are located in one plane. These traps can be produced by means of highly controllable and repeatable microfrabriaction techniques. A chip surface can potentially accommodate many copies of the specialized zones of a QCCD. To interconnect the zones, transport of ions through 'Y' or 'X' junctions has to be perfected [29, 30]. If the structure reaches a critical size, laser access to all relevant sites might become difficult as lasers have to be focused on only the relevant ions without hitting the others because that might disturb their qubit state. Cooling and detection lasers for one ion species are operated at virtually the same frequency and directing a laser on one ion will scatter photons in all directions. These photons might hit other ions. Therefore it is desirable to have a specialized detection zone that is positioned away from storage and manipulation areas and realize sympathetic cooling via a second ion species that requires a different laser wavelength [31, 32].
When scaling even further, the surface-electrode trap might require multiple interaction and multiple detection zones. This makes laser access even more complicated. There are technological approaches to include laser wave-guides, optics and detectors into the chip surface [33, 34, 35].
There are also approaches that rely on microwave radiation for driving quantum logic gates in trapped ions. These techniques require only cooling and detection lasers, thereby reducing the overall laser-overhead.
One way to drive gates on ions with microwave radiation is to place the ions in a magnetic field gradient and apply an oscillating magnetic field at the appropriate microwave frequency [36].

A second method is to apply an oscillating magnetic gradient at the appropriate frequency to the ions [37].

Even if the scaling through one or a combination of the mentioned techniques is realized, there are more challenges associated with surface-electrode traps in particular and with many-ion traps in general.
While a quantum algorithm is running, no ion must be ejected from the trap or change its relevant quantum state. Although almost all ion traps are operated under ultra-high vacuum (UHV) conditions, background gas collisions cannot be eliminated. These collisions can disturb the quantum state of an ion or even eject it out of the trap. The lower pressure in the vacuum chamber is, the less collisions will occur.
All ions traps suffer from heating of the motional state of the ions through electric-field noise. These so-called heating rates $\dot{n}$ depend on the ion-to-surface distance d with $\dot{n} \propto d^{-4}$ [38, 39]. Compared to larger 3D traps, surface-electrode traps usually have a lower distance d and suffer more from heating effects.
Cooling down the complete apparatus to a few Kelvins will reduce the average kinetic energy of the background gas by a factor of at least 70, thereby making the trapped ions more resilient to background gas collisions.
In a cryogenic environment, much lower pressures can be achieved, making background gas collisions rarer [40].
A trap that is cooled to about 5 K also experiences heating rates suppressed by about two orders of magnitude compared to a 300 K trap [41].
A cryogenic environment is thus highly desirable for a large scale QCCD chip.

Our group at the Leibniz University of Hannover (LUH) and the Physikalisch-Technische Bundesanstalt (PTB) is focused on developing surface-electrode Paul traps for quantum information processing applications. We have established a simulation and production line for these types of traps and run an experiment at PTB in which these traps are used to drive two-qubit gates [42, 43, 44, 23, 45, 46]. While the gate fidelities that our group can achieve improved over time [47, 48] and the manufacturing capabilities are developed to a point that allows for production of larger scale traps, they still lack operation in a cryogenic environment.

1.3 Thesis outline

This thesis describes the cryostat that was built to house a surface-electrode ion trap that could accommodate a QCCD architecture with integrated microwave guides to apply near-field oscillating magnetic gradients to drive quantum gates between ions [49].

In **chapter 2**, the basic principle of surface-electrode trap design is presented. It also summarizes the electronic level structure of $^9Be^+$, why it is our ion of choice, what levels need to be addressed to use it as a qubit and how they are addressed. **Chapter 3** details the advantages of a cryogenic ion trap compared with a room temperature

trap. It also explains the design of the cryostat, which includes the choice of cooler and how to decouple the intrinsic vibrations of the cooler from the experiment. The design and performance of the vacuum system is also discussed and detailed calculations of the heat-load are presented. One focus is on the demanding task of guiding a few Watts of microwave currents into a 5 K environment without heating it up too much. **Chapter 4** contains a description of the electronic hardware that is required to operate the system. In **chapter 5**, we will present the laser systems that are required to load the trap and to cool and detect the ions. **Chapter 6** describes the imaging system that is employed to detect the ions. It includes a fully achromatic objective that is operated and adjusted at cryogenic temperatures. **Chapter 7** summarizes the relevant results and provides an outlook into the next generation of traps that can be installed in the cryostat.

Chapter 2

Trap design and atomic transitions in $^9Be^+$

The production of surface-electrode ion traps require precise control over advanced micro fabrication techniques as well as a deep understanding of high-frequency current behavior and the methods of simulating them.
The task of designing and fabricating these traps was first assigned to Martina Wahnschaffe who established during her PhD work the first production process and developed the first microwave near field simulations for our project [50]. Together with Amado Bautista-Salvador, she improved on the microfabrication process and we were able to show, that the production tolerances were small enough such that the resulting fields and potentials matched simulations [43].
While Amado Bautista-Salvador improved the production process even further [44], Giorgio Zarantonello took over trap design as part of his PhD work [48]. He developed and carried out experiments with several traps at room temperature [44, 45, 46, 51, 23]. He also developed three generation of traps, that were used during this work, one of which was able to trap ions.
In this chapter, I will introduce the main concepts for designing these traps. For an exhaustive discussion please see references, especially[50, 43, 42]. I will also describe the traps used over the course of this work and discuss why only the third generation was able to trap ions.

2.1 Surface-electrode Paul traps

According the the Earnshaw theorem [52], a charged particle can't be trapped purely by static electric fields $\vec{E}$ since $\vec{\nabla} \cdot \vec{E} = (\partial_x, \partial_y, \partial_z)\vec{E} = 0$ only holds if at least one component has a different sign than the other two and therefore at least one dimension is not confining but repelling the particle.
While Hans Dehmelt invented a device known as a Penning-trap [53] that uses a combination of static electric and magnetic fields to confine ions, Wolfgang Paul devised the so-called Paul-trap [9], a combination of static and oscillating electric fields to achieve a confining potential.
The first generations of Paul-traps had 3D electrode geometries. One popular geometry is the four-rod Paul-trap. An oscillating voltage $V_{rf} = V\cos(\Omega_{rf}t)$ with amplitude V

and rf drive frequency Ω_{rf} is applied to two opposing electrodes, while static voltages (or DC voltages) are applied to the others. The oscillating voltage is usually in the radio-frequency range and therefore called rf voltage. A configuration of a four-rod Paul-trap is shown in figure 2.1 a).

The potential shown in figure 2.1 b) is a quadrupole potential around the y-axis (green

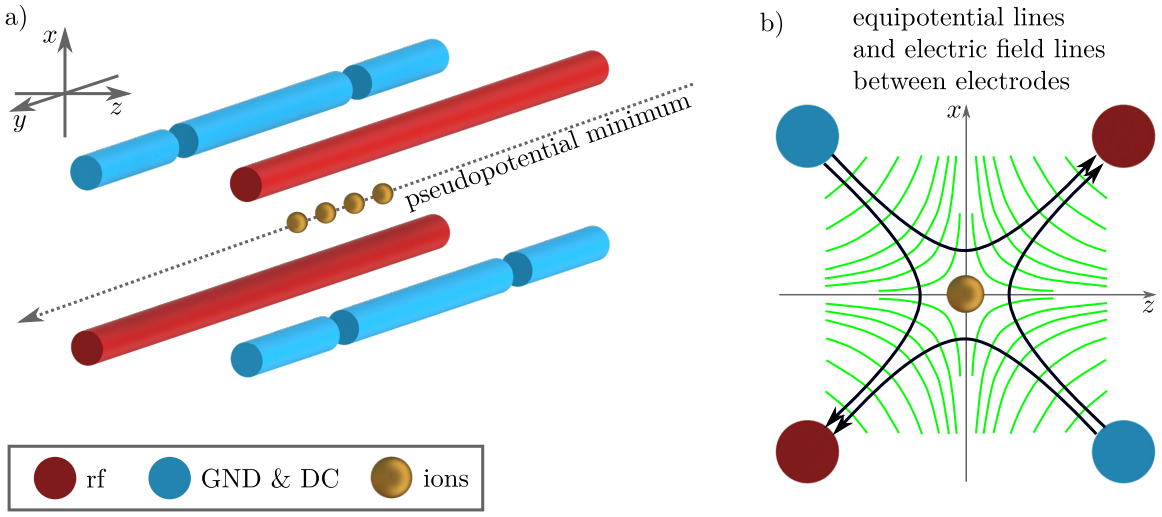

Figure 2.1: a) Electrode configuration of a four-rod Paul-trap. An rf voltage applied to the red electrodes generates a confining potential in the x-z-plane. The blue electrodes generate the axial confinement along the y-axis. b) Equipotential lines of the rf potential (green) and corresponding electric field lines (black) at a point in time, when the oscillating field reached maximum amplitude. Half an oscillation period later, the arrows would point in the opposite direction.

lines). An ion's motion in such a potential can be described with normalized Mathieu equations. A complete treatment can be found in [54]. The electric field produced by the rf electrodes cancels out in the center and the potential vanishes. The shown field configuration would push the ion towards the rf electrodes. If it were static, the ion in the middle would escape along the axis between the rf electrodes. Since the rf voltage switches its sign twice per oscillation period $\tau = {}^{2\pi}/_{\Omega_{rf}}$, the confining and repulsive directions change at the same rate. If these changes happen fast enough, the ion will not escape and the mean ion position does not change by much in during τ. This leads to the more intuitive so-called pseudopotential approximation: Let $\vec{x}_\mu$ be the ion's position in the x-direction that results from the small amount of motion during τ. The motion that is associated with this small position change is called the micromotion. An electric rf field in x-direction can be written as:

$$\vec{E}(\vec{x},t) = \vec{E}(\vec{x})\cos(\Omega_{rf}t) \tag{2.1}$$

With q as the charge and m as the mass of the ion, Coulomb's law states:

$$q \cdot \vec{E} = \vec{F} = m \cdot \vec{a} = m\frac{\partial^2 \vec{x}_\mu}{\partial t^2} \tag{2.2}$$

With equation 2.1 this yields:

$$m\frac{\partial^2 \vec{x_\mu}}{\partial t^2} = q \cdot \vec{E}(\vec{x}) \cos(\Omega_{rf} t) \tag{2.3}$$

Integrating yields the resulting velocity of an ion that undergoes micromotion:

$$\vec{v_\mu} = \frac{q\vec{E}(\vec{x})}{m\Omega_{rf}} \sin(\Omega_{rf} t) \tag{2.4}$$

The so-called pseudopotential V_{pp} is the averaged kinetic energy associated with the micromotion:

$$V_{pp} = \frac{1}{2} m \langle v_\mu^2 \rangle = \frac{q^2 E^2(\vec{x})}{4m\Omega_{rf}^2} \tag{2.5}$$

A Taylor expansion around the center $\vec{x} = 0$ of the potential, where the field vanishes, yields: $\vec{E}(\vec{x}) = \vec{E}(0) + \vec{E}'\vec{x} = \vec{E}'\vec{x}$. Inserting this in equation 2.5 yields:

$$V_{pp} = \frac{q^2 E'^2 x^2}{4m\Omega_{rf}^2} = \frac{1}{2} m\omega_x^2 x^2 \text{ with } \omega_x = \frac{qE'}{\sqrt{2}m\Omega_{rf}} \tag{2.6}$$

This represents a confining harmonic potential in the x-direction. The corresponding harmonic oscillator has a resonance frequency ω_x. This can also be equivalently derived for the z-direction, resulting in ω_z. According to [54], this agrees with the solution of the Mathieu equations as long as the relevant approximations hold. In the y-direction, voltages applied to the outer lying blue electrodes in figure 2.1 yield an additional harmonic potential along the pseudopotential minimum with corresponding oscillation frequency

$$\omega_y = \sqrt{\frac{2\kappa V_0}{m}}, \tag{2.7}$$

where V_0 is the static potential that is generated by the DC electrodes and κ is a geometric factor that is specific to the used trap [11]. It should be mentioned that this harmonic approximation holds only for small oscillation amplitudes of the trapped ions [11]. Cooling the ions with a Doppler cooling laser (see section 5.3) reduces their kinetic energy sufficiently.

In case of surface-electrode ion traps, the confining potential is generated by applying different voltages to differently shaped electrodes which are all located in the same plane and are separated by small gaps [27]. A method of mapping the potential generated by the above 3D electrode configuration onto a 2D electrode configuration by using a Möbius transformation can be found in [55]. An analytical way to calculate the electric field of a 2D electrode is presented in [56]:

Suppose that a voltage V is applied to a planar electrode that is located in the y-z-plane, with contour C and is surrounded by a large ground plane and that the gap between the electrode and ground plane is small. In such a case, the gapless plane approximation holds and the Biot-Savart-like law for electrostatics can be applied to analytically determine the electric field $\vec{E}$ at any point $\vec{r} = (x, y, z)$ above the surface that is generated by the electrode [56].

$$\vec{E}(\vec{r}) = \frac{V}{2\pi} \oint_C \frac{(\vec{r} - \vec{r'}) \times \mathrm{d}r'}{|\vec{r} - \vec{r'}|^3} \tag{2.8}$$

In case of multiple electrodes, adding up the individually generated fields give the resulting overall field.

This analytical expression and the resulting pseudopotential help the designer to achieve a quick overview of the design. For the final trap design a full finite elements simulation that does not rely on the approximations is required. For this purpose Ansys HFSS was used in our group.

2.2 Integrated microwave control of the ion's motion

From the first proposed trapped-ion quantum logic gate [12] to the Mølmer-Sørensen gate [57] that our group employs successfully in our room temperature trap at PTB [45, 23], all schemes for quantum logic with trapped ions require control over the ion's motional states. To be more precise, a coupling between internal atomic states and the external motional state is required. Most experiments with trapped ions rely on the use of Raman-laser beams to implement control over internal and external states. There are two alternative approaches to control an ion with long wave radiation in the microwave regime. The first proposal was published in 2001 [36] and uses a combination of a static magnetic field gradient and an oscillating microwave field. Since it relies on magnetic gradient-induced coupling the name MAGIC was coined for this scheme. It was first demonstrated in 2009 [58] and several research groups are using it or are planing to use it.
The approach that our group uses is based on an oscillating magnetic gradient and was first proposed in 2008 [37]. The first demonstration was successful in 2011 [49].
It was shown that both schemes actually realize the same Hamiltonian but in a different base [59].
Since the required microwave gradients are supposed to be generated by trap electrodes, a trap designer has to be aware of the underlying physical processes that in the end drive the relevant transitions. The next section will give a brief overview over the required physics and the section that follows will describe the concepts of how to design a trap that fulfills these physics requirements. For reasons detailed below, the atomic species of our choice is $^9Be^+$.

2.2.1 Electronic structure of $^9Be^+$

A useful property for a qubit choice is to exhibit a first-order magnetic-field independent transition [60, 21, 61]. A field-independent qubit features a stable transition frequency, even in the presence of slight magnetic field fluctuations. The inset on the left of figure 2.2 shows the evolution of two states of $^9Be^+$ with respect to the magnetic field. At 22.3 mT, the derivative of both states with respect to the magnetic field is the same, leading to a transition frequency which is independent of first order magnetic field changes. Among other factors, magnetic field independence leads to relatively long coherence times and less dephasing of the qubit states during gate operations. As an example, the typical decoherence time of a field-independent qubit in $^{43}Ca^+$ is about one thousand times longer that that of a qubit in $^{40}Ca^+$ [62]. There are many species like Yb, Ca, Mg, Be to chose from, if it came down to only this atomic property.
The surface-electrode traps that are being produced by our group consist of gold electrodes grown on a dielectric substrate. During trap loading, a small amount of neutral atoms is ejected from a source and some of these neutral atoms are ionized and trapped (see section 5.4). Most of the neutral atoms will not be trapped but deposited on surfaces around the source. In thermal equilibrium, there is an electrostatic potential between different conductors that is proportional to the work-function difference. If the neutral atoms are deposited near the gold electrodes, the resulting potential can disturb the trap potential. Over time, more atoms may accumulate and the effect may increase. In surface-electrode traps, the distance from the ions to the surface is relatively small compared to other trap types. Therefore in surface-electrode traps, these unwanted potentials can have more influence on the trapping potential and have to be avoided. We try to minimize this by carefully producing very few neutral atoms and by shielding most of the trap surface from them (see section 5.4). By choosing an atomic species that has a work function (W) difference to gold that is as low as possible, we can further reduce these effects: $W(\mathrm{Au}) - W(\mathrm{Yb}) = 2.77\,\mathrm{eV}$, $W(\mathrm{Au}) - W(\mathrm{Ca}) = 2.59\,\mathrm{eV}$, $W(\mathrm{Au}) - W(\mathrm{Mg}) = 1.71\,\mathrm{eV}$, $W(\mathrm{Au}) - W(\mathrm{Be}) = 0.39\,\mathrm{eV}$ [63, 64]. In this category, beryllium seems to be the best candidate.
Beryllium also has a comparatively simple electronic structure without meta-stable optical states, which would require additional repumping lasers, like for example calcium does. Compared to magnesium, the lasers for cooling and detecting beryllium are technologically more mature. Magnesium requires a wavelength of 280 nm [65], which is overall not as comfortably produced and a handled as the 313 nm required for beryllium. The Doppler cooling limit depends on the natural linewidth Γ of the cooling transition:

$$T_{Doppler} = \frac{\hbar\Gamma}{2k_B}, \tag{2.9}$$

where k_B is the Boltzmann constant. An ion in a harmonic potential occupies a motional state $|n\rangle$, where n is the number of stored phonons with energy $\hbar\omega_{trap}$, where ω_{trap} is the trap frequency (see section 2.2.2). The temperature of a particle is proportional to the kinetic energy, which in turn is proportional to the number of phonons and the energy per phonon. The trap frequency depends on the inverse mass in case of radial

motion (see equation 2.6) or the square root of it in case of axial motion (see equation 2.7). Combining all these proportionalities yields:

$$T \propto E,\ \ E \propto n\hbar\omega_{trap},\ \ T \propto \Gamma,\ \ \omega_{trap,radial} \propto 1/m,\ \ \omega_{trap,axial} \propto 1/\sqrt{m} \tag{2.10}$$

$$\Rightarrow n_{radial} \propto \Gamma m,\ \ n_{axial} \propto \Gamma\sqrt{m} \tag{2.11}$$

For quantum logic applications it is advantageous to reach a phonon number as small as possible (see section 2.3). The motional state that can be reached through Doppler cooling is therefore dependent on the ratio of the ion mass or its square root and the natural linewidth. Magnesium has a natural linewidth of $\Gamma_{\mathrm{Mg}} = 42\,\mathrm{MHz}$ [66] and a mass of $m_{\mathrm{Mg}} \approx 25\,\mathrm{u}$ and $\Gamma_{\mathrm{Mg}} m_{\mathrm{Mg}} \approx 1050$ and $\Gamma_{\mathrm{Mg}}\sqrt{m_{\mathrm{Mg}}} \approx 210$. Beryllium has a natural linewidth of $\Gamma_{\mathrm{Be}} = 19.6\,\mathrm{MHz}$ [67] and a mass of $m_{\mathrm{Be}} \approx 9\,\mathrm{u}$ and $\Gamma_{\mathrm{Be}} m_{\mathrm{Be}} \approx 176$ and $\Gamma_{\mathrm{Be}}\sqrt{m_{\mathrm{Be}}} \approx 58.8$. Therefore beryllium can reach a lower motional state through Doppler cooling and is in this regard better suited for quantum logic applications.
A final argument for beryllium is that our group also runs an experiment which aims at sympathetically cooling a proton with an atomic ion in a Penning trap [68]. For efficient energy transfer, the mass to charge ratio of the atomic ion has to be as close to that of the proton as possible. Beryllium is the best candidate for that as Li^+ and He^+ do not have suitable atomic transitions [69]. Since $^9Be^+$ is already a good candidate for the physics that we want to research and we can share technology between projects, we chose beryllium as the ion to work with. The electronic structure of $^9Be^+$ at a magnetic field of 22.3 mT is shown in figure 2.2. The states in the hyperfine manifold of $^2S_{1/2}$ are in the Zeeman-regime and labeled $|F, m_F\rangle$. The transition between $|2,+1\rangle \equiv |\downarrow\rangle$ and $|1,+1\rangle \equiv |\uparrow\rangle$ is first order field-independent and we use it as the qubit transition. This magnetic 'Q' transition has a frequency of $\omega_0 = 1083\,\mathrm{MHz}$ and can therefore be resonantly driven with oscillating magnetic microwave fields. Placing a conductor in the vicinity of the ion and applying an AC current with frequency ω_0 to it, produces a field around the conductor that drives Q. Such a conductor is required to perform single-qubit operations and can probably be integrated in many ion traps in a rather straightforward way.

To initialize the ion in a qubit state, we would apply the cooling laser which optically pumps the ion into the $|2,+2\rangle$ state and then apply a microwave pulse on transition A. This places the ion in one of the qubit states; the other is accessible via the transition Q. We would then run single-qubit operations on transition Q, the result of which is an arbitrary state

$$\psi = {}^1/\sqrt{|a|^2+|b|^2}\,(a\,|\uparrow\rangle + b\,|\downarrow\rangle) \tag{2.12}$$

with a and b as complex numbers.

To detect the qubit state, we would drive transitions B, C and D to transfer population from $|2,+1\rangle$ to $|1,-1\rangle$ as well as transition A to transfer population from $|1,+1\rangle$ to $|2,+2\rangle$. If we then appply the detection beam and observe resonance fluorescence from that transition, this is equivalent to a measurement that has found the ion in the $|1,+1\rangle$ state prior to the detection sequence. If, on the other hand, no fluorescence is observed, this is equivalent to a measuremen that has found the the ion in the $|2,+1\rangle$

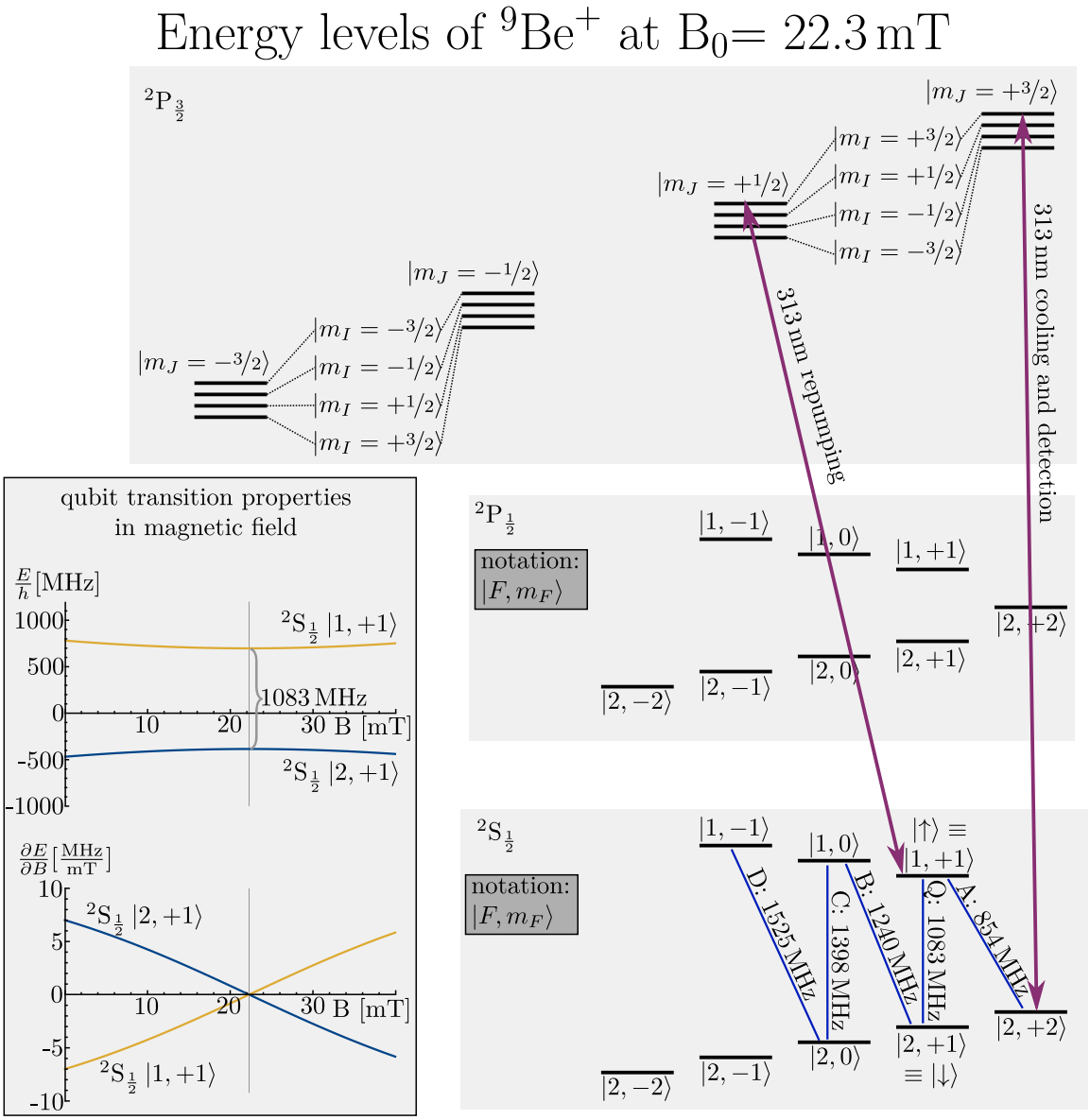

Figure 2.2: Electronic level structure of $^9Be^+$ at a magnetic field of $B_0 = 22.3\,\text{mT}$. Energy differences not to scale. While the $^2S_{1/2}$ and $^2P_{1/2}$ states are in the Zeeman-regime, the $^2P_{3/2}$ state is in the Paschen-Back-regime, therefore different state labeling conventions are used. Transitions that are relevant in the context of this work are labeled. Transition Q is first order magnetic-field-independent at 22.3 mT. The inset on the left shows Q as a function of magnetic field and the first derivative with respect to the magnetic field.

state. The so-called shelving pulse sequence B, C, D is used because $|1,-1\rangle$ is maximally off-resonant for the detection beam and the probability of accidental excitation is minimal.

For multi-qubit (multi-ion) operations, some sort of logical interaction between the

qubit states of all ions has to be generated. Applying a microwave current as described above would drive the transition in all ions but without mediating any interaction between them. For entangling interactions like the Mølmer-Sørensen gate, control over shared motional state of the ions is required.

2.2.2 Energy level structure of one beryllium ion in a Paul-trap

As shown in section 2.1 and equation 2.6, the potential in a surface-electrode Paul-trap is harmonic in all directions. The energy levels in a quantum mechanical harmonic potential are equally spaced and the energy between them is $\hbar\omega_i$ with $i = \{x, y, z\}$. In traps like ours, these trap frequencies ω_i are usually in the 1-10 MHz range. A cold ion in the trapping potential will not only have a defined internal state that can be accessed in the way described in the previous section, but also a defined external state in the trapping potential. This is called the motional state and is denoted with $|n\rangle$, where $n = \{0, 1, 2, 3, ...\}$ with $|0\rangle$ as the ground state of the harmonic potential. The wavefunction of equation 2.12 can now be written as

$$\psi = {}^{1}/\sqrt{|a|^2+|b|^2}\,(a\,|\uparrow, n\rangle + b\,|\downarrow, n\rangle) \tag{2.13}$$

Figure 2.3 shows the resulting level structure. To control the qubit, one can apply a current with frequency ω to a conductor near the ion and produce a magnetic field $B = (\vec{e}_x B_x + \vec{e}_y B_y + \vec{e}_z B_z)\cos(\omega t + \varphi)$. Tuning the frequency to ω_0 results in driving a so-called carrier (car) transition. The corresponding Hamiltonian for the x-direction of the ion's motion, if the center of the harmonic potential is at $x = 0$ is [37]

$$H_{car} = \frac{\hbar}{2}\Omega_0(\sigma_+ e^{-i((\omega-\omega_0)t+\varphi)} + \sigma_- e^{i((\omega-\omega_0)t+\varphi)}) \tag{2.14}$$

$$\overset{(\omega=\omega_0)}{=} \frac{\hbar}{2}\left(-\frac{\mu}{\hbar}B(x=0)\right)(\sigma_+ e^{-i\varphi} + \sigma_- e^{i\varphi}), \tag{2.15}$$

where Ω_0 is the resulting Rabi frequency, σ_+ the spin-raising operator, σ_- the spin-lowering operator, φ the phase of the magnetic field and μ the projection of the ion's magnetic moment on the x-axis. The Rabi frequency for carrier transitions depends on the magnetic field B.
It might be reasonable to suggest that to gain control over the motion of an ion, say for example to reduce the motional state by one quantum of motion, one can apply ω_i. In practice, applying just ω_i will increase the motional state as the ion just absorbs the energy and it heats up until it leaves the trap. To extract one quantum of motion from the system, so-called sideband transitions can be used. The red sideband is red detuned by the motional frequency from the carrier transition ($\omega_{rsb} = \omega_0 - \omega_i$). The blue sideband is blue detuned ($\omega_{bsb} = \omega_0 + \omega_i$).
Applying a sideband to the ion changes the internal state and also changes the motional state by $|n\rangle \rightarrow |n \pm 1\rangle$. Applying it again reverses the operation. The Hamiltonian in

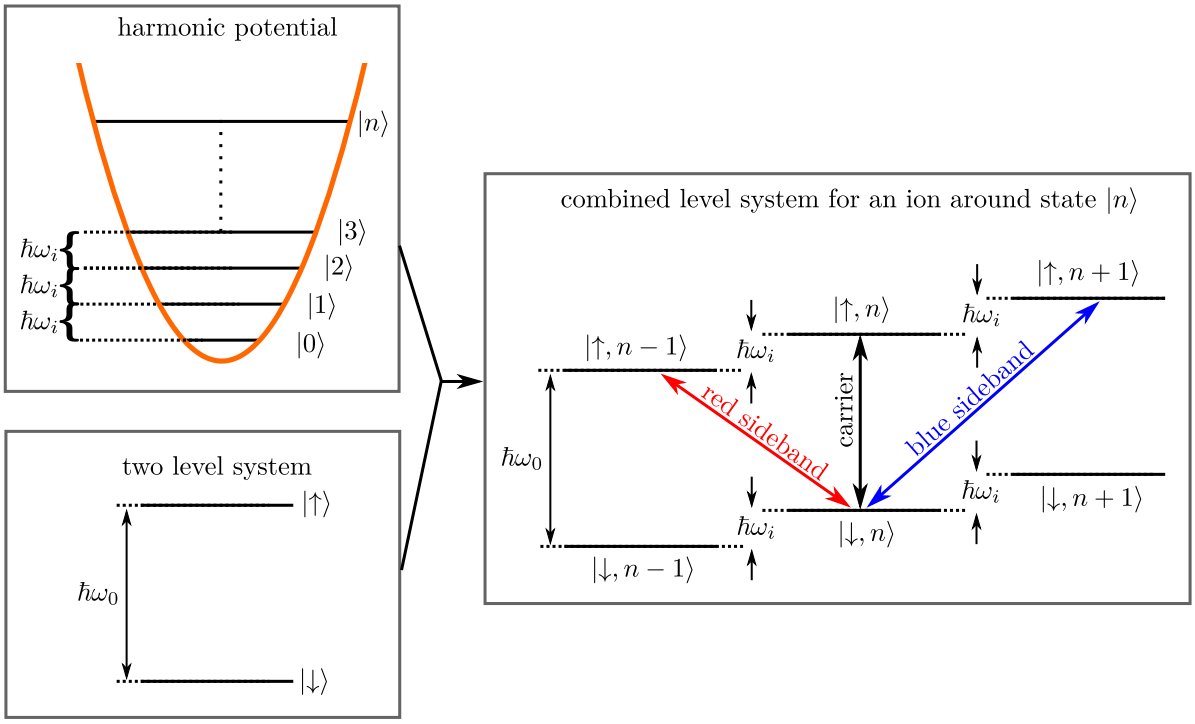

Figure 2.3: Combining a harmonic trap potential with a two level system gives rise to the two level system on the right-hand side. While the carrier transition can be driven with an oscillating magnetic field, the red and blue sideband transitions can only be addressed with an oscillating magnetic gradient.

the x-direction of the ion's motion, if the center of the harmonic potential is at $x = 0$ and if a red sideband (rsb) is applied is [37]

$$H_{rsb} = \frac{\hbar}{2}\Omega_1(\sigma_+ e^{-i((\omega-(\omega_0-\omega_x))t+\varphi)}a_x + \sigma_- e^{i((\omega-(\omega_0-\omega_x))t+\varphi)}a_x^\dagger) \tag{2.16}$$

$$\overset{(\omega\,=\,\omega_0\,-\,\omega_x)}{=} \frac{\hbar}{2}\left(\underbrace{\sqrt{\frac{\hbar}{2m\omega_x}}}_{q_0} - \frac{\mu}{\hbar}\left.\frac{\partial B(x)}{\partial x}\right|_{x=0}\right)(\sigma_+ e^{-i\varphi}a_x + \sigma_- e^{i\varphi}a_x^\dagger), \tag{2.17}$$

where $\sqrt{n}\Omega_1$ is the Rabi frequency that depends of the initial motional state $|n\rangle$, a_x and $a_x^\dagger$ are the annihilation and creation operators for the harmonic oscillator states and q_0 is the ground state wave package size. The Rabi frequency depends on the magnetic

gradient. For a blue sideband (*bsb*), the Hamiltonian is

$$H_{bsb} = \frac{\hbar}{2}\Omega_1(\sigma_+ e^{-i((\omega-(\omega_0+\omega_x))t+\varphi)}a_x^\dagger + \sigma_- e^{i((\omega-(\omega_0+\omega_x))t+\varphi)}a_x) \tag{2.18}$$

$$\overset{(\omega=\omega_0+\omega_x)}{=} \frac{\hbar}{2}\left(-\frac{\mu}{\hbar}\underbrace{\sqrt{\frac{\hbar}{2m\omega_x}}}_{q_0}\frac{\partial B(x)}{\partial x}\bigg|_{x=0}\right)(\sigma_+ e^{-i\varphi}a_x^\dagger + \sigma_- e^{i\varphi}a_x), \tag{2.19}$$

where $\sqrt{n+1}\Omega_1$ is the Rabi frequency for the blue sideband, which depends on the magnetic gradient.
A more intuitive explanation for requiring a gradient is that the sidebands act on the motion in a different way, depending on the ion's spin state. This would require a spin-dependent force, which requires a gradient since it has to point in different directions depending on the spin state.
Depending on the internal state, a sideband either reduces the motion or increases it. These conditional dynamics, where the internal two level system dynamics have a deterministic influence on the dynamics of the external level system provides the basis of quantum logic operations [11].
It has been shown that a magnetic field gradient is necessary to couple to the ion's motion [36, 37]. Just applying an oscillating field at the sideband frequency will not drive that sideband as it does not couple to the motion. Microwave fields of 1083 MHz have a vacuum wavelength of 27.7 cm. The magnetic field gradient over the extent of the ion's wave packet (in the nm regime) of that radiation is negligible and the motion will not be addressed if the trapping potential itself does not depend on the spin state, as assumed above. As mentioned above at the beginning of this section, there are two approaches to circumvent this problem: Supplementing an oscillating magnetic field with a static magnetic gradient to make the trapping potential state dependent or using an oscillating magnetic gradient. Our group follows the latter approach.
Figure 2.4 illustrates the thoughts, presented below: A current-carrying wire will produce

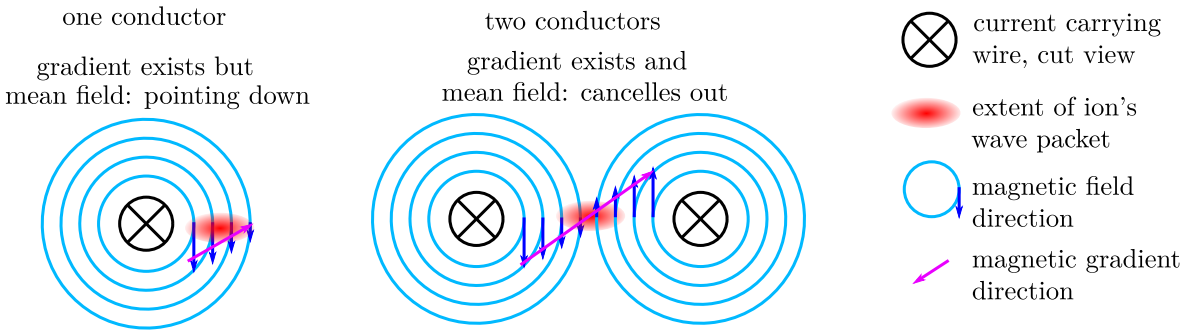

Figure 2.4: Illustration of the near field gradient idea. For more detail, see text.

a magnetic field around it. The magnetic field becomes weaker with increasing distance

from the wire. Putting an ion in that field would expose it to a gradient. However, because the relative variation of the field over the motional wave packet is still small, mostly off-resonant carrier transitions will be driven according to equation 2.14. Reducing the wire-ion distance will increase the gradient but a strong field will remain. Placing an ion in the middle between two wires with the same currents flowing through them cancels the residual field out and a gradient remains. Under this condition driving sideband can be possible. In case of a surface-electrode ion trap, this geometry would mean that the ion is placed inside the surface. A third microwave conductor in the same plane as the other two but carrying a current in the opposite direction adds an additional degree of freedom and can move the point of zero field above the surface.

2.2.3 Designing a trap with integrated microwave lines that can drive sidebands

The first realization of this aforementioned three wire scheme was presented in [49]. One of the complex challenges that were encountered was to precisely control relative phase and amplitude between the three wires. The approach that we presented in [42] shifted the challenge from electronics to design and simulation. We introduced a meander structure through which one microwave current flows and changes direction twice. The resulting field has a minimum at a fixed position relative to the meander and is given by the meander geometry. The meander is integrated in the trap-chip and the geometries of rf and DC electrodes have to be designed in a way that the resulting pseudopotential minimum is at the same position as the microwave field minimum. Since all these potentials are set by the electrode geometry, careful simulation and precise production was required. We have shown in [43] that the simulation and production tool chains are sufficiently well developed in our group to handle these requirements. Figure 2.5 a) shows a surface-electrode trap geometry. Figure 2.5 b) shows the corresponding simulation of the magnetic field that is produced by the meander electrode, suitable for driving sidebands and the surface currents in all electrodes. These currents are produced by the oscillating magnetic field that is generated by a current flowing through the meander electrode. These currents generate new magnetic fields which in turn produce new currents. The coupling between the electrodes has to be simulated to arrive at a full picture of the resulting magnetic field. The trap also features a non-meander microwave electrode for carrier operations as well as six DC electrodes for axial confinement and a split up rf electrode for radial confinement. Martina Wahnschaffe designed and simulated that trap with the finite elements simulation software Ansys HFSS. Production was carried out by Martina Wahnschaffe and Amado Bautista-Salvador in the PTB cleanroom. This trap was operated in a room temperature setup at PTB. The cryogenic traps that were operated over the course of this thesis are described in more detail in section 2.3.

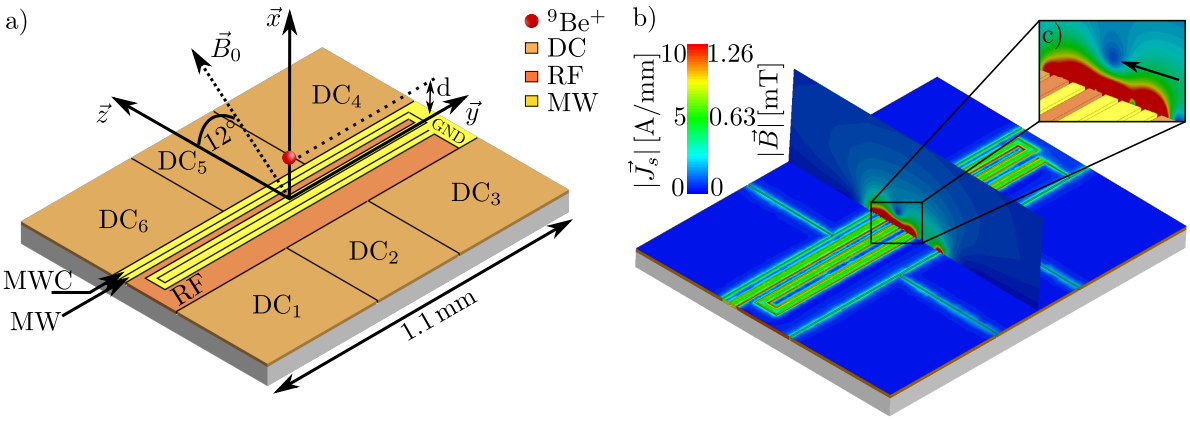

Figure 2.5: a) Surface-electrode trap geometry. DC and rf voltages are applied to orange electrodes to generate the trapping potential. The yellow MWC conductor drives carrier transitions. The yellow MW conductor has a meander geometry and can be used to drive sidebands. b) In the surface plane, the current distribution, resulting from a microwave current flowing through the MW electrode are shown. A cross section through the magnetic field that results from this current is shown perpendicular to the trap surface. c) The arrow indicates the minimum of the microwave near-field. Original pictures by Martina Wahnschaffe [50]. The pictures were slightly modified for this thesis.

2.2.4 Entangling operations between two qubits

A combination of arbitrary single-qubit rotations and an entangling two-qubit gate constitutes a universal set of gates [5, 6]. This means that any quantum logic operation between multiple qubits can be reduced to a series of single-qubit operations and entangling gates between pairs of participating qubits. As described above, single-qubit operations, including sidebands, on ^{9}Be$^+$ can be accomplished by sending a microwave current through a trap electrode. Entangling two qubits requires acting on their shared mode of motion.

Two ^{9}Be$^+$ ions in the same harmonic potential will repel each other due to the Coulomb force. They also experience a confining force from the trap potential. For small motional amplitudes, this behavior can be modeled as coupled harmonic oscillators, which share normal modes of motion [24]. Trapping two ions at the position of the microwave field minimum produced by current flowing through the meander (see figure 2.5 b) and c)), allows driving of sidebands on both ions simultaneously. They share a common motion and the spin-dependent force that acts on the common motion depending on the internal states of each individual ion mediates an effective interaction between the internal states of both ions.

It has been shown in the setup of our group at PTB that a microwave electrode with meander geometry can drive Mølmer-Sørensen gates between two beryllium ions with infidelities in the 10^{-3} range [23].

2.3 Trap design and production for use in a cryogenic environment

There were three generations of traps designed for use in a cryogenic environment by Giorgio Zarantonello and produced by Amado Bautista-Salvador. Well established design and production processes for room temperature traps needed to be modified and/or optimized.

The traps are produced in the PTB cleanroom and consist of gold electrodes grown on a wafer material and, depending on the wafer material, one or more additional layers in between. During the trap design stage, important parameters to consider are: thickness of the wafer, additional layers and gold electrodes; dielectric constants, electric resistivity and high frequency loss tangent (electric and magnetic) of the different materials. A combination of suitable materials and trap electrode geometries has to be found in a complicated iterative process between simulation and production. This has been successfully established for room temperature traps.
The mentioned parameters change with temperature and for cryogenic applications, the geometry has to be slightly changed. Also thermal contraction and conduction of participating materials has to be taken into account.

First generation trap

The first trap that was designed and produced for the cryogenic setup was based on a silicon wafer with a 2 µm thin silicon-nitride layer on which the gold electrodes were grown. The production process was well established for these materials and simulations showed promising low temperature behavior. It was designed to generate a pseudopotential with an rf frequency of 100 MHz. We mounted the trap inside the inner vacuum chamber in the PTB clean room, transported it to the Hannover lab and connected the rf-resonator for alignment and calibration measurements as described in sections 4.4, 4.4.1 and 4.4.2. While the resonator was working well, when not connected to the trap, we could not detect a well characterized resonance when the trap was connected. The loss tangent for the rf signal of the wafer at room temperature was too high. From the PTB crew's experience and rough estimations, we were optimistic, that we could align the resonator with a dummy-load attached and expected good enough results at cryogenic temperatures. We were indeed able to see a sufficient rf resonance but that did not matter because we measured strange capacitances and resistances for electrode to ground and electrode to electrode connections for all DC lines. We were not sure, if we could even apply correct voltages anymore. We could only explain this behavior by changing electrical contacts between electrodes which would have entailed some mechanical malfunction of either wire bonds, trap electrodes or filter board.
We could not move our objective around over the trap surface because, at that point in time, we did not have the 3D translation stage on the imaging objective (see section 6.2.2) but only the limited capabilities of the first generation objective mount (see section 6.2.1). We decided to warm up again and debug. It turned out that during cooldown,

mechanical stress lead to cracking of the 2 µm thin SiN film and all DC electrodes as well as some others peeled off the wafer. A picture of the damages trap is shown in figure 2.6. The trap was not usable and a different wafer material was needed. We

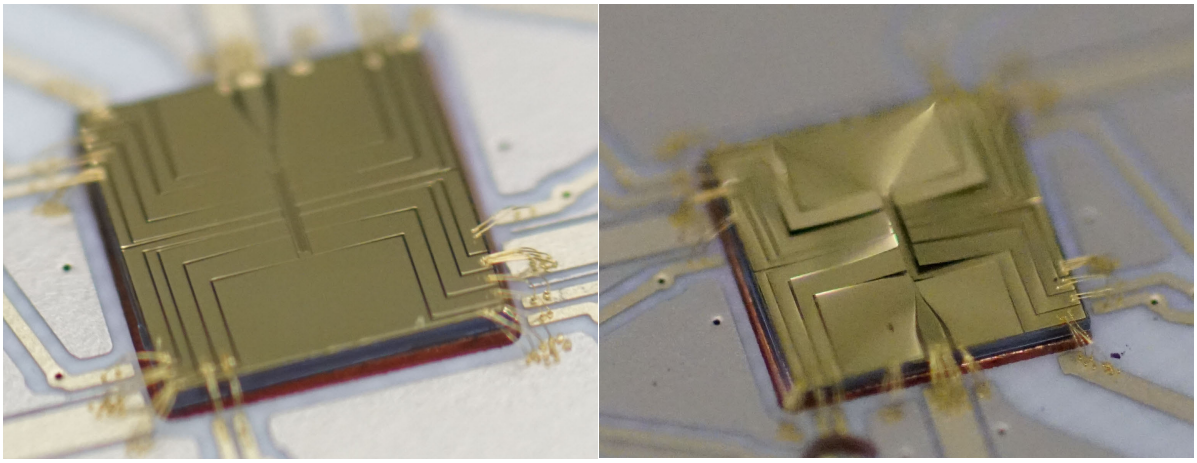

Figure 2.6: Left: Before cooldown. The electrodes are properly attached to the wafer. Right: Damaged trap. During cooldown, the electrodes in the center peeled off.

decided to use a sapphire wafer as this also facilitates optimization of the RF resonator at room temperature. Amado Bautista-Salvador developed a production process for the new material combination and Giorgio Zarantonello simulated a new trap design. This resulted in the second generation trap.

Second generation trap

The second trap generation was built on a sapphire wafer and the rf calibration process was successful. Trapping was impossible because we accidentally deposited some amount of graphite particles on the trap surface, which produced a lot of stray light from cooling laser beams and because of their conductive properties potentially distorted the trapping potential. For a detailed description of that accident, see chapter 6.
The trap surface to ion distance was designed to be at 35 µm. This goal was regarded as ambitious because the first working room temperature trap had an ion to surface distance of 45 µm and suffered from significant (as of now not fully understood) issues that ultimately led to issues in motional state control. For the room temperature setup, a new trap with an ion to surface distance of 70 µm improved these issues such that motional control and high-fidelity gates could be implemented. Heating rates $\dot{n}$ depend on the ion to surface distance d with roughly $\dot{n} \propto d^{-4}$ [38, 39]; therefore a higher distance is of advantage. The magnetic gradient used to drive sidebands is stronger the closer the ions are to the conductors that produce it. It seemed that for our room temperature traps this compromise between heating rates and gradient was better at $d = 70\,\mu\text{m}$. Heating rates also depend on the trap temperature and at 5 K they can be approximately two orders of magnitude smaller that at 300 K [41]. In terms of heating rates it was predicted

that by reducing the distance to 35 µm compared to the 70 of the room temperature chip, heating rates would increase by a factor of $2^{3.8} \approx 14$ but that cooling it down to 5 K would reduce them by a factor of 100, leading to overall favorable parameters compared to the room temperature trap. Since trapping was not possible and we could not completely rule out that $d = 35\,\mu m$ was too small of a distance for stable trapping, we opted for a third generation trap with a $d = 70\,\mu m$.

Third and current generation trap

The third generation trap is built on a sapphire wafer and a low temperature compatible version of the 70 µm ion to surface distance trap that was used in the room temperature setup [45, 23]. The electrode configuration and a picture of the trap are shown in figure 2.7. The trap chip has a surface area of $4.75 \times 4.75\,mm^2$. We trap ions in the center

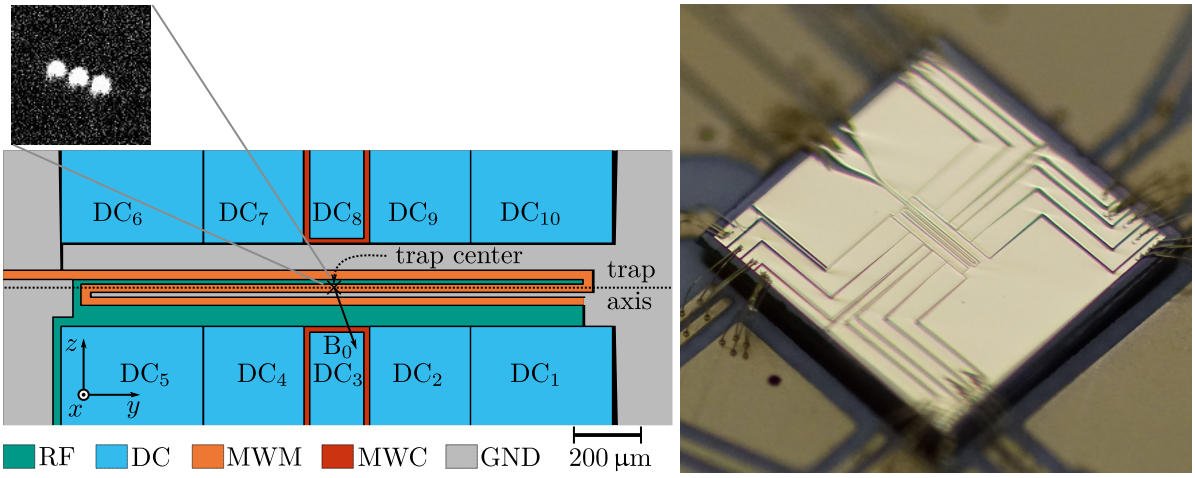

Figure 2.7: Left: Electrode geometry around the trap center. The meander electrode MWM is used to generate a magnetic field similar to that in figure 2.5 b). Each of the MW electrodes can be used to drive microwave carrier transitions. The RF electrode provides the psedopotential along the trap axis and the DC electrodes provide axial confinement along y. The quantization field B_0 has an angle of 70° to the trap axis. Right: Photo of the trap chip.

region, which is approximately 100 µm long. The trap has 10 DC electrodes to allow for rotation of trap axes and for moving ions around. The calculated trap depth is 39 meV. The radial modes are rotated by applying appropriate DC voltages so that no mode is parallel to the x-axis because the Doppler cooling beam is perpendicular to that axis and would not be able to cool a mode parallel to it. The angle of the nearest radial mode to the x-axis is 17°. In order to trap ions, we apply previously calculated DC and RF voltages and ramp up the quantization field. We shoot with an ablation beam at a beryllium target and produce an ablation plume. Some of these neutral atoms fly trough the trap center and are ionized and Doppler cooled. Section 5.4 describes in detail how we load the trap. Section 5.2 describes the ionization laser. Section 5.3 describes the

cooling and detection laser. Chapter 4 describes the electronics needed to apply required voltages and currents.
To operate the trap after loading, we shine in the cooling laser to optically pump the ion into $|2, +2\rangle$ (see figure 2.2). We calibrate the quantization field strength by driving a π-pulse on the A transition with a microwave current flowing through one of carrier (MWC) electrodes and detect the population in $|2, +2\rangle$ by shining in the detection beam. Ideally there would be no counts on the PMT. Since the system is not calibrated yet, we detect photons. We scan the microwave frequency around the calculated value for perfect magnetic field of 854 MHz, and compare the position of the resonance with theory. We change the magnetic field until the resonance on that transition is at the calculated value. We than scan the microwave pulse length to determine the π-time of that transition. When we are sure that we have determined the proper parameters to drive that transition at the calculated frequency of 854 MHz, we transfer all population to $|1, +1\rangle$ and calibrate the π-time of the qubit transition the same way but with transferring the population back to $|2, +2\rangle$ for detection. We also calibrate transition frequencies and π-times for B, C and D. For a final characterization of the qubit, in addition to the Doppler laser, we also apply the repumper for state preparation to empty the $|1, +1\rangle$ state and pump the population into $|2, +2\rangle$. We drive a π-pulse on transition A. We drive transition Q and scan over the microwave pulse time. For detection, we shelve the population of $|2, +1\rangle$ to $|1, -1\rangle$ and transfer the population in $|1, +1\rangle$ back $|2, +2\rangle$. We then detect the population in $|2, 2\rangle$ by shining in the detection laser and collecting photons on a photo-multiplier tube (see section 6.2). The measured Rabi oscillations are shown in figure 2.8. Steps to better

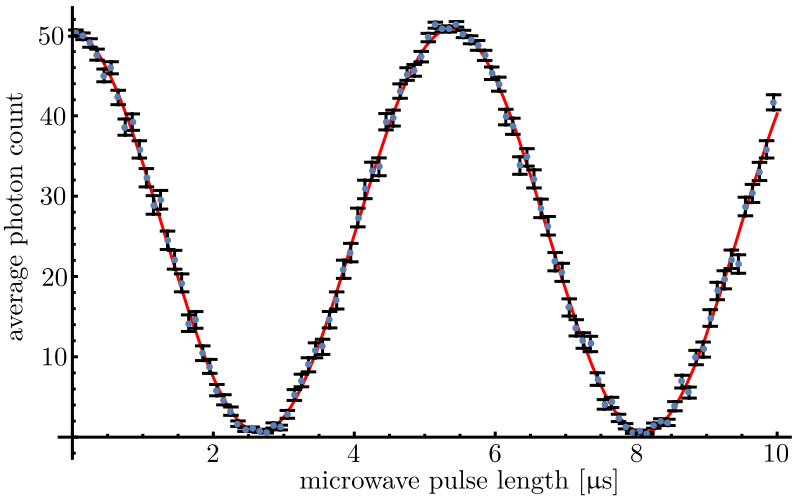

Figure 2.8: Rabi oscillations on the qubit transition. Every point is the average over 500 experiments with the same pulse length. The error bars are standard deviation averaged for 500 experiments. A sine was fitted to the data points. The contrast is 97.8%.

characterize this trap, to improve state detection and preparation are underway and in part completed and will be published in the PhD thesis of Sebastian Halama. These steps are: Better alignment of cooling and detection lasers with respect to the magnetic

field. Polarization optimization of the cooling and detection beam as well as stray light suppression. These measures will improve preparation and detection. Micromotion compensation also has to take place. Jannik Hertzberg is currently working on a more stable quantization field with permanent magnets and compensation coils. The results will be published in his bachelor thesis. If these steps have been taken, driving the first sidebands is the next logical step.

Chapter 3

Cryostat design

A cryostat is an apparatus that is able to cool a sample down to a desired temperature. For low complexity applications, it might just be a dewar vessel with a cold liquid inside in which one can dip a sample. Operating an ion trap at temperatures in the single digit Kelvins requires substantially more effort. This chapter will discuss why it is useful to cool an ion trap below 10 K, what devices can be used to accomplish that task, which device we chose, how we designed it and how it performs. Figure 3.1 shows the main components of a cryostat in which an ion trap can be operated. Operating an ion trap

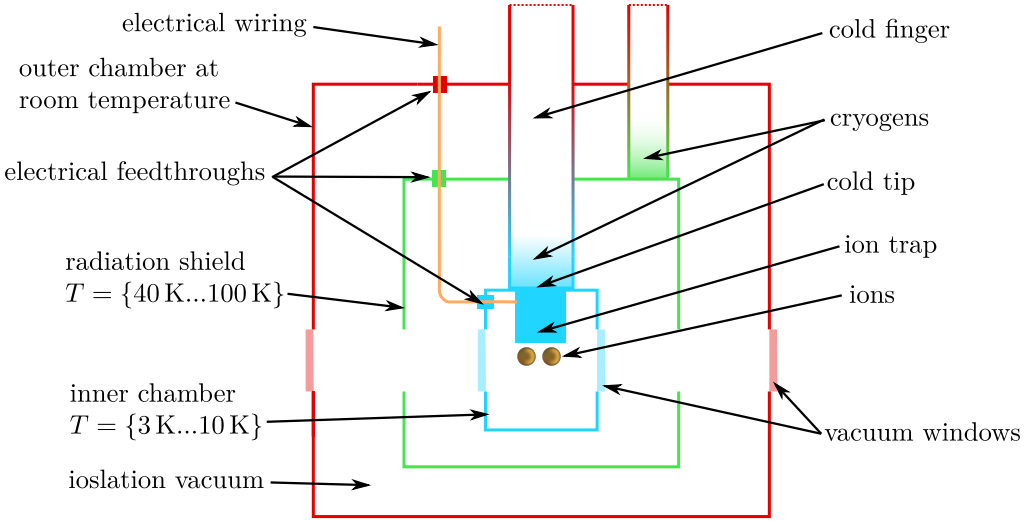

Figure 3.1: Cross section through a conceptual cryostat design. Red: room temperature components; outer vacuum chamber. Green: radiation shield components at moderately low temperature. Blue: inner vacuum chamber at low temperature. Orange: electric wiring that guides signals from room temperature into the inner chamber.

---

under cryogenic conditions requires a larger and more complex technological overhead than operating it at room temperature. In both cases the trap sits in a vacuum chamber. Therefore UHV compatible materials have to be used. In addition, the chamber that houses a cryogenic trap has to be built out of materials that perform at low temperatures and this inner chamber itself is enclosed by another vacuum chamber which provides isolation from warm air. Between this outer chamber and the inner chamber resides a

so-called radiation shield that hinders room temperature thermal radiation from hitting the inner chamber. Both, radiation shield and inner chamber have to be cooled down by some sort of cryogen, either a liquid helium dewar or a low maintenance and more economical closed cycle system. In case of a closed cycle cryocooler, a considerable design effort has to be put into isolating the intrinsic vibrations from coupling to the trap - a consideration not present in room temperature designs.
Electronic signals have to be sent through wiring that changes electric resistance when cooled down and also transports heat to the inner chamber. UHV compatible wiring material combinations have to be found that transport the least amount of heat while carrying the required voltages and currents. If the trap is at the same temperature as the environment, normal low-resistance copper wires can be used, which is only partially the case for cryogenic experiments. Viewports in a room temperature setup are usually bought off the shelve. Cryogenic windows need to sustain cooldown while not changing their optical properties, like birefringence, too much. A room temperature chamber can have arbitrarily large and many windows to allow for optical access from all desired angles. In a cryogenic environment, the windows have to be as small as possible to prevent thermal radiation from heating up the cold parts. Because it is typically enclosed by two chambers and a shield, a cryogenic trap is usually further away from the air side than a room temperature trap. Combining these restrictions of small windows and long distance to air, exclusively air side imaging optics are much harder to realize than in warm setups and in most cases some sort of low temperature optics are put into the inner chamber. Adjusting these optics while they are cold is an additional challenge. Keeping the number of windows as small as possible also reduces observation opportunities which can lead to more challenging alignment routines just because it might be impossible to directly observe the effect of the procedures.
The only procedure that requires more care in a room temperature setup is the bakeout of the vacuum chamber which in certain cases can be completely avoided in a cryostat. A rendering of our cryostat system can be found in figure 3.2.
There are three main reasons why, despite all these challenges, it is desirable to work with a cryogenic surface-electrode ion trap.

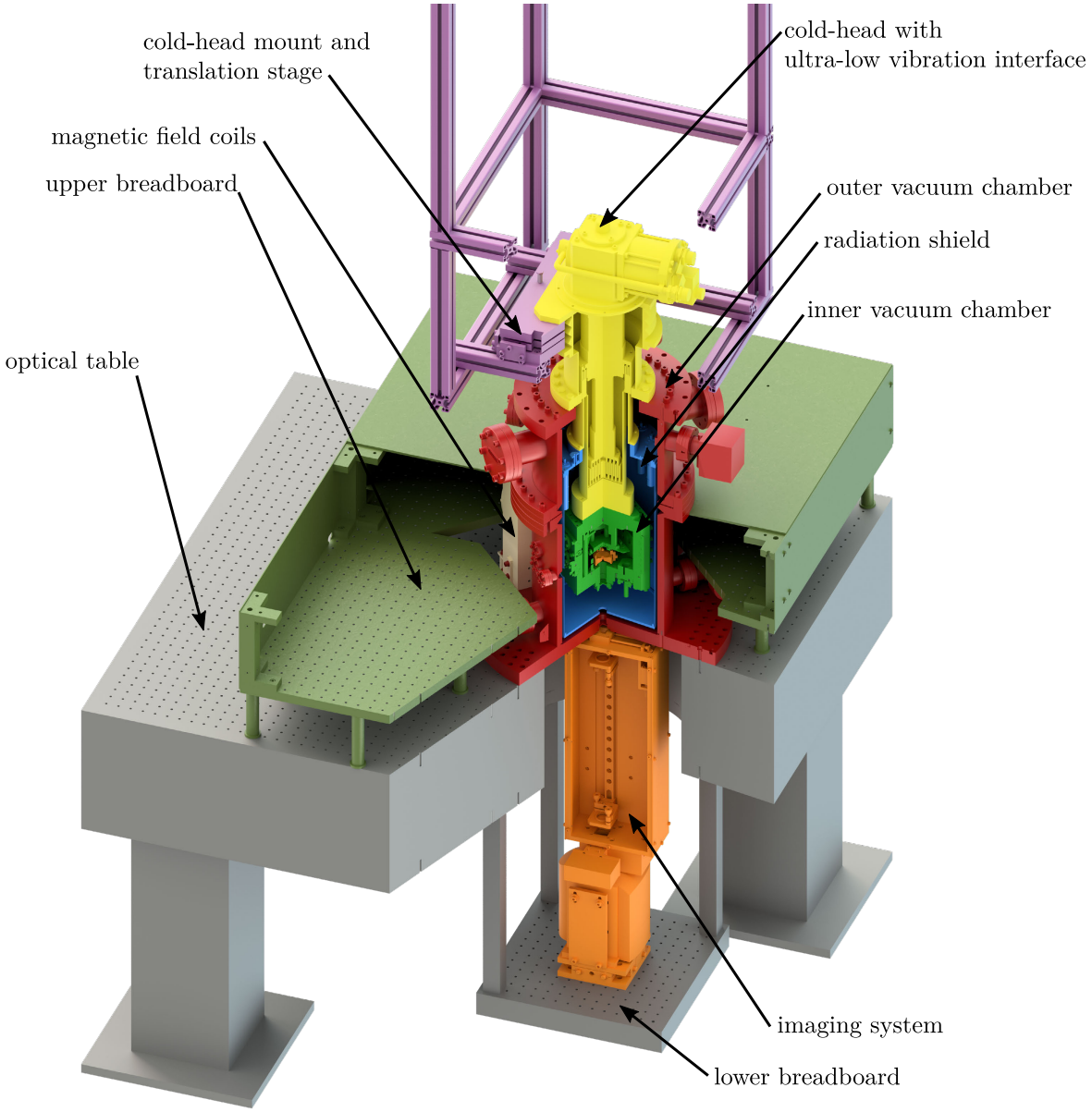

Figure 3.2: Overview of the functional components of the system.

3.1 Advantages of cryogenic ion traps over room temperature traps

A trapped-ion quantum logic gate, like the Mølmer-Sørensen gate, is based on the entangling of atomic states of two ions, mediated by acting on the common motion. If the motional state changes due to external factors during the gate process, the gate may not perform as expected and the overall gate fidelity drops. The heating rate is the number of phonons per unit time, that an ion in the trap gains due to external, non

controlled excitations [38]. These excitations could be caused by electric field noise that is caused by thermal random motion of electrons in conductors near the ions, so-called Johnson noise. It was shown that in particular for small traps, the expected heating effect from Johnson noise can be much smaller than the measured noise, about two orders of magnitude in the example of [70]. The term 'anomalous heating' was coined in 1995 to point out that the origin of the heating was unknown [71]. The source of the observed heating rates has still not been fully identified but is believed to originate in surface imperfections and/or contaminations [39]. An extensive review of heating behavior in ion traps and descriptions of several physical models to explain it can be found in [72]. It has been shown that heating rates in a given trap can be reduced by about two orders of magnitude, if the trap is cooled down from room temperature to 4 K [41].
One possible explanation for this effect is that charges that have accumulated on dielectric surfaces (see section 5.4.2 for one example) as well as surface contaminations on trap electrodes that might distort the electric field are subject to random Brownian motion which in turn randomly affects the electric field and acts as electric field noise. If noise components near the trap frequency are present, the ion can absorb the energy and heat up. Under cryogenic conditions, the Brownian motion is frozen out because the surface binding energy is greater than the thermal energy. Therefore contaminations only produce a static potential which can distort the trapping potential but will not heat the ions.
The microwave near-field approach that was described in chapter 2 profits from high magnetic gradients. The closer the ions are to the microwave guides, the higher the achievable gradient. Therefore it is advantageous to design a trap with a small ion to surface distance. The heating rates $\dot{n}$ in surface electrode traps has been observed to scale with the distance d as $\dot{n} \propto d^{-4}$ [38, 39]. If ions heat up during gate operations, the gate is disturbed and the fidelity drops. Therefore, with a given gate time, a cryogenic trap can afford to bring the ions closer to the surface than a room temperature trap, which in turn leads to a higher magnetic gradient, which in turn leads to faster gates, which can tolerate a higher heating rate, which can eventually lead to a trap with even further reduced surface to ion distance.
Collisions with background gas can also lead to heating of the ions or even expulsion from the trap. In a cryogenic environment, the vacuum is orders of magnitude better than at room temperature because most substances are solid or at least liquid at low temperatures and therefore will not disturb the vacuum. It has been shown that pressures in the 10^{-17} mbar [73] or even 10^{-18} mbar [40] range can be achieved at 4 K. This reduces the likelihood of ion-gas collisions. According to kinetic gas theory and assuming a Boltzmann distribution of kinetic energy within a gas, the average kinetic energy $E_{kin}(T)$ of a gas molecule of temperature T is

$$E_{kin}(T) = \frac{3}{2}kT, \tag{3.1}$$

where k is the Boltzmann constant. For T =4 K and for $T = 297\,\mathrm{K}$ this yields:

$$E_{kin}(297\,\mathrm{K}) = 6.15079 \cdot 10^{-21}\,\mathrm{J} = 38\,\mathrm{meV} \tag{3.2}$$

$$E_{kin}(4\,\mathrm{K}) = 8.28389 \cdot 10^{-23}\,\mathrm{J} = 0.5\,\mathrm{meV} \tag{3.3}$$

If a collision takes place in one of our traps with a trap depth of 39 meV, at room temperature, the ion will most likely be ejected, while there is no danger of loosing the ion in the cryogenic regime. This leads to increased ion life-times in cryogenic traps, which is of importance when it comes to running quantum logic algorithms that require multiple gates and take a longer time. It is also important to be able to store ions for a longer time in a so-called quantum processor.

In conclusion a cryogenic surface electrode trap can offer faster gates, lower heating rates and longer storage times than its room temperature counterpart.

3.2 Choosing the type of cryocooler

3.2.1 Bath cryostat

The simplest method of cooling an experiment down to below 10 K is a so-called bath cryostat: A helium filled dewar vessel is enclosed by an isolation vacuum, which itself is enclosed by a second dewar, filled with liquid nitrogen. That nitrogen dewar is also in an isolation vacuum. Small diameter mechanical connections with a low thermal conductivity connect the respective parts for mechanical stability. A radiation shield is attached to the liquid nitrogen vessel at 77 K and surrounds the experiment that is attached to the 4.2 K helium vessel. A device like this is called a bath cryostat. An early example of an ion trap cooled down in such a way can be found in [74]. This type of cryostat has a high regular maintenance overhead since the cryogens need to be replenished regularly because the cooling effect comes from boiling off helium. Helium prices fluctuate and long term financial planing becomes more complicated. Helium has a latent heat of vaporization of $2.589\,\mathrm{J/m\ell}$ [75]. A cooling power of 1 W, which can easily be required for operating the microwave conductors in the surface traps that are described in section 2.3, would boil off 1.4 ℓ of helium per hour. Eight hours of operation a day at that capacity and 16 h in the idle state with approximately 170 mW power drain yield a helium consumption of 14.9 ℓ per day. Considering the vacuum vessel and the liquid nitrogen dewar around it, we could have engineered our lab to provide enough space to accommodate a 50 ℓ dewar. This would have meant replenishing helium up to once every three days. To operate such a system in a more economic way, a helium recovery system is of advantage. Such a system is considered to be a substantial investment in lab infrastructure and was not present in our lab building. The handling of liquid cryogens in our building was also considered a complicated process from a work safety perspective and new, appropriate storage space would have been needed. Although it does not suffer from acoustic noise that introduces vibrations to the system (like a

closed cycle cold head; see section 3.3), we chose not to pursue the acquisition of a bath cryostat.

3.2.2 Flow cryostat

A flow cryostat operates very similarly to a bath cryostat as the cooling power comes from boiling off helium. The part of the system around the inner chamber can be engineered to be smaller in camparison because a large helium storage vessel is not required. Liquid helium is constantly pumped through pipes near the inner chamber, coming from a larger reservoir. In many cases, the reservoir is connected to a helium liquefier, which recycles the boiled off helium. An example of an ion trap that is cooled by a flow cryostat can be found in [76]. A flow cryostat, if not connected to a helium liquefier, shares many of the disadvantages with the bath cryostat regarding helium economy. It does not suffer from acoustic noise if the liquefier is either not present at all or placed far away from the ion trap. A helium liquefier contains a closed cycle cryocooler that cools down the used helium below boiling point and replenishes the reservoir. Summarized, a flow cryostat either offers the unfortunate helium economics of a bath cryostat or features the additional costs of a closed cycle cooler. In the context of our application, a flow cryostat would be a means of isolating the vibrations of a closed cycle cryocooler from the ion trap. At the time of decision making, a buffer gas vibration isolation promised the same amount of vibration isolation at a more affordable price with less severe space requirements. Therefore we decided against a flow cryostat.

3.2.3 Dilution refrigirator

For most trapped ion experiments, the long ion lifetime and low heating rates that a 4 K environment offers are sufficient. A design for a combined ion-superconducting qubit system that relies on a dilution refirgirator to keep it at 100 mK was proposed in 2016 [77]. Since a dilution fridge is more complex and expensive and offers little improvement for our application of microwave near-field driven quantum logic, we did not entertain the idea of procuring one.

3.2.4 Closed cycle Gifford-McMahon cooler

The so-called Gifford-McMahon (GM) cryocooler was invented in 1960 [78] and has been in wide-spread use since. Although it has been improved continuously by choosing more suitable materials or reducing abrasion of moving components, the general working principle has stayed the same:
A compressor is used to compress gaseous helium and the generated heat is removed by cooling it against an external coolant, most often water. This helium of usually more than 10 bar and about 20°C is guided through an intake valve into the top of a two-stage cylinder with low thermal conductivity. This is a cylinder that changes diameter somewhere near the middle of it's length. In each of the cylinder's stages, there are a displacer piston and a regenerator. The regenerator is made out of a porous

material with a high thermal capacity and high surface to volume ratio. Some of the more prominent regenerator materials in use today are Pb, Er-alloys or Er-Pr alloys for the first stage and Er_3Ni, Nd or $HoCu_2$ for the second stage [79]. Research into the use of other alloys like $Er_xHo_{1-x}N$ is under way [80]. The exact compositions are not published by the manufacturers. The displacers are steel pistons that are wound in a rubber band helix over their full length that keeps the gas from flowing between the piston and the cylinder wall.
At the beginning of the cooling cycle, the displacer is near the bottom of the cylinder (the cold side) and the intake valve at the top is open. The piston is moved to the top, while the intake valve is still open. The high pressure helium passes through the regenerator, which stores some of it's heat. Since the displacer is at the top, the maximum amount of high pressure gas has flown through and is now below the regenerator. The intake valve is closed and the low pressure output valve is opened. The gas at the bottom expands isochorically and thereby cools the bottom of the cylinder. The expanding gas flows through the regenerator, thereby extracting the heat from it, and further on out of the cylinder to the compressor. The out-flowing helium has a higher temperature than the in-flowing. While the output valve is still open, the piston is moved to the bottom. The output valve closes, the input valve opens and the cycle repeats. This happens simultaneously for each part of the cylinder. The upper part, called first cooling stage, pre-cools the helium and delivers it to the bottom part, the second cooling stage.
The piston is usually moved by a motor, located at the top of the cylinder. The acoustic noise of the motor and the valve operations as well as the movement of the pistons generate vibrations at the bottom of the second cooling stage on the order of 100 µm [75]. The combination of motor, valves, cylinders and pistons is called the cold head. The two cylinders are called the cold finger. The bottom of the second cooling stage, where the experiment or sample can be attached is called the cold tip.
GM coolers can reach temperatures of 3 K. Their cooling power is usually specified at 4.2 K to compare them to liquid helium. The cooling power at 4.2 K can reach up to 2 W. If the experiment can tolerate higher temperatures, more cooling power is available.
Despite the intrinsic vibrations, we chose to operate a GM cooler for reasons described below in section 3.2.6.

3.2.5 Closed cycle pulse tube cooler

A pulse tube can be seen as an advancement of a GM cooler. The moving pistons were removed and helium flows back and fourth from a compressor through a regenerator, which is placed in a tube. At the compressor side helium gets pushed in or taken out, depending on the state of the cooling cycle. At the other end of the tube, helium can flow through an adjustable flow resistance into a reservoir tank, called the helium buffer volume. The movement of hot high pressure helium through the regenerator in one direction and low pressure cold helium in the other direction follows the same thermodynamic principle as the GM cooler. The difference is that the flow through the regenerator is not caused by the moving piston. An extensive review of pulse tube operations can be found in [81].

A pulse tube has lower intrinsic vibrations than a GM cooler and usually on the order of 1 µm [75]. Although these are significantly lower vibrations than those of a GM cooler, it is still too much for our application (see section 3.2.6). For both closed cycle systems, a vibration isolation stage is necessary.

3.2.6 Vibration isolation systems

Although driving Raman transitions with lasers is not the primary goal of our experiment, being able to employ a Raman system can be useful for debugging, comparison and, as shown by our room temperature setup [45], ground state cooling. It may also be useful to implement sympathetic ground state cooling via a second ion species.
In order to be able to drive Raman transitions, two laser beams have to be phase stable at the position of the ions. If the inner chamber is attached to a vibrating cooler, the trap will vibrate and therefore the ion's position will not be stable with respect to the laser beams. If the vibration amplitude is not well below the laser wavelength, phase stability will not be ensured. It was shown that it is possible to drive 674 nm wavelength laser based gates [82] in a cryostat with a vibration level of 106 nm [83]. Based on the same ratio of 6.4 between laser wavelength and vibration amplitude, we chose to aim at below 50 nm vibrations for our 313 nm laser setup.
There are some commercially available options for vibration isolation of closed cycle cryocoolers. The company Cryomech offers a pulse tube cooler that has copper braids attached to it's cold tip which connect to the inner vacuum chamber with the ion trap. The vibration amplitude of that system is below 1 µm [84]. Cryomech also offers a pulse tube that liquefies a small helium reservoir. An apparatus like that has been used for ion trapping [85, 86] and offers vibration amplitudes on the order of 100 nm. Although the second option might work, especially when considering longer wavelength transitions in sympathetic cooling ions, both Cryomech solutions offer only about 0.6 W cooling power at 4.2 K, not enough to sustain sending high power microwave pulses to the ion trap.
Montana Instruments offers GM based cryostats with vibration levels below 20 nm but with a cooling power below 140 mW at 4.2 K, which would not be enough even for our static heat load (see section 3.7).
Janis Research Labs (recently acquired by Lakeshore) offers a buffer gas vibration isolation system that uses a Sumitomo GM cold head with a buffer gas tube attached. The vibration amplitudes are on the order of several 100 nm and can be reduced to around 100 nm [87].
Coldedge also offers a buffer gas vibration isolation for a Sumitomo GM cold head. The vibration amplitude is specified to be below 20 nm. Both the Janis and the Coldedge version offer near 1.5 W cooling power at 4.2 K. Currently, Coldedge offers more vibration isolation systems with better performance, either in cooling power or in vibration isolation, but at the time of procuring our system, only the buffer gas isolated GM cooler fulfilled our requirements. It later became clear, that the promised 20 nm vibration amplitude was not directly measured by the company but as the results of this thesis show, it was nevertheless a good decision to buy the system.
It should be noted that a custom designed vibration isolation system for a pulse tube,

based on a heavy pendulum, connected via annealed cooper braids to the pulse tube and alto to the experiment, exists at PTB [88] that features remarkable vibration levels of below 100 nm but offers only around 1 W of cooling power.

Buffer gas vibration isolation

The vibrations from either a GM cooler or a pulse tube are significant enough to prevent phase stable Raman transitions. A vibration isolation system was required in order to use either of these systems. At the time, ColdEdge promised the lowest commercially available vibration levels and they only offered buffer gas solutions. As a result a buffer gas vibration isolation was chosen.
In order to decouple mechanical vibrations resulting from the pumping of helium through the cold finger of a closed cycle cryocooler from the ion trap and the laser beams, no substantial mechanical connection between cold finger and optical table should be established. The first step is to mount the cold head to either the lab floor or the ceiling and hang it over the ion trap. A cylinder with low thermal conductivity walls (stainless steel for example) and a bottom plate of high thermal conductivity (OFE copper for example) is fitted around the cold finger. At the bottom plate, the inner vacuum chamber that houses the ion trap will be attached. The fist cooling stage of the cold finger has a larger diameter than the second cooling stage. The cylinder also has two diameters and can accommodate the cold finger in a way that only a small gap remains between them. The principle of buffer gas isolation is to fill the cylinder with helium gas and start the cryocooler. It will cool the helium and all vibrations will be absorbed by the gas. The cold gas accumulates at the bottom of the cylinder, cools the base plate and therefore also cools the ion trap. A way to keep the gas from escaping the cylinder without establishing a mechanical connection between cold head and cylinder is to attach rubber bellows between the two components. These bellows, if sufficiently flexible, will absorb most vibrations. Since helium gets denser while cooling it down, a helium gas supply needs to be connected to the top of the cylinder to keep the helium pressure inside at a constant level. Otherwise air would flow in and freeze on the surfaces which in turn would establish a mechanical connection and transfer vibrations. The helium pressure is kept a few mbar above ambient pressure to avoid air flowing into the cylinder. One disadvantage of a buffer gas solution is that it only works well, if the helium is gaseous. If the temperature falls below 4.2 K, the helium liquefies and the vibrations couple through the liquid. For ion trapping, temperatures around 5 K are fine (see section 3.1) but in situations where helium background gas plays a role, a buffer gas vibration isolation has to be chosen with care. It is true, that even though liquid helium transfers vibrations to the ion trap, these vibrations are still damped compared to the raw vibrations of the cold head. Many manufacturers make use of this fact to advertise extremely low vibration levels and state that their system reaches below 4 K. Both facts are technically true but cannot be achieved simultaneously although advertising suggests it without explicitly putting it in writing.
A rendering of parts of the buffer gas cylinder that we use are shown in figure 3.3. In section 3.3, a more detailed description of our vibration isolation system can be

found.

3.2.7 Choosing between a GM cooler and a pulse tube

Since both types of closed cycle cryocoolers can be equipped with a buffer gas vibration isolation, a decision, which system to buy had to be made.
A GM cooler can be operated in any direction relative to gravity, whereas a pulse tube has to be mounted in such a way that the cold finger points down. Since a buffer gas vibration isolation also has a preferred orientation (cold helium at the bottom), this distinction was not relevant for us.
A pulse tube has lower intrinsic vibrations than a GM cooler. According to manufacturers, a buffer gas vibration isolation damps both to the same level. Therefore the intrinsic vibrations were no important parameter for us.
A GM cooler sells at about half the price of a pulse tube with similar cooling power. Since a GM cooler has more moving parts, it has to go into maintenance once every 10000 h compared to 20000 h of a pulse tube. Costs per maintenance event are comparable and we calculated that after about 11 years of continuous operations, a GM cooler would cost more than a pulse tube. For a GM cooler, maintenance can be done on site. For a GM cold head in a buffer gas isolation system it takes about 1 h plus as much time as it takes for the system to warm up and cool down again. A pulse tube has to be send back to the factory for maintenance. Mainly because of the lower initial costs and the less time consuming maintenance, we decided to buy a Sumitomo RDK-415D GM cold head equipped with a ColdEdge ultra low vibration buffer gas isolation system.

3.3 Ultra low vibration interface

A rendering of the ultra low vibration interface is shown in figure 3.3. About 5 mm thick and a few cm long concentric copper cylinders are mounted to the first cooling stage and also the cold tip of the GM cooler. The gaps between them are about 6 to 7 mm wide. Another set of 5 mm thick concentric copper cylinders is mounted to the inside of the buffer gas tube. Fitting the lower rings in the gaps of the upper rings leaves less than 1 mm space between them. If the rings do not touch, the helium gas between them transfers the temperature but not the vibrations. In order to keep the vibrations from coupling into the experiment via a different path, the cold head has to be mounted to either the lab floor or the ceiling.
The cold head position has to be adjusted so that the the relative position of the concentric cylinders is near perfect. The lower part of the cylinders is mounted via the outer vacuum chamber to the optical table and fixed in position. The upper part that is connected to the cold head has to be positioned in such a way that the upper and lower cylinders fit into their respective gaps without touching. In the vertical direction the margin for alignment is quite large. If the cold head is moved upwards by 1 cm the cooling power might drop insignificantly but vibrations won't couple through. Positioning in the

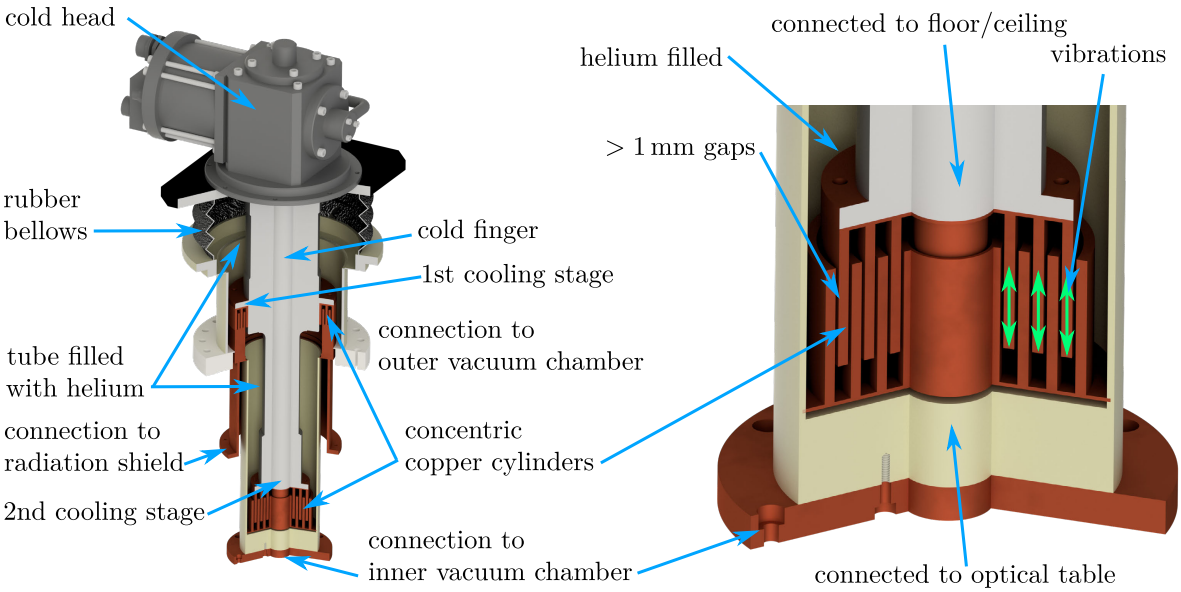

Figure 3.3: Left: Redering of the ultra low vibration interface. Right: Magnification of the low vibration interface's second cooling stage. If the concentric cylinders touch, the vibrations are transferred from the cold head to the ion trap. If there is a gap, the helium in between will absorb the vibrations.

horizontal plane, parallel to the optical table, is more prone to misalignment. Movement of less than 1 mm in each direction will lead to vibration transfer. The relative angle between the cold head's base plate and the optical table is the most sensitive alignment parameter. Depending on how much space is left between the lowest point of the upper cylinders and the bottom of the exchange gas tube, an angular misalignment between 2° and 3° can lead to vibration transfer.

3.3.1 First version of the cold head mount

The ColdEdge ultra low vibration interface came with a stand that was tailored to the geometry of our setup. A rendering of it is shown in figure 3.4. The stand has a cutout in its bottom plate to accommodate our imaging setup (see chapter 6). It resides on four feet. The distance of each foot to the bottom plate can be adjusted with a 1/2"-13 UNC screw. The feet are tightly connected to the screws and rotate when the screws are turned. These are used for height and angular alignment. A fork that has a cutout to house the cold head is mounted to a long rod. It is fixed to the rod by one clamp. This clamp does not provide fixation of the rotational degree of freedom. There is no translation mechanism to move the cold head in the plane parallel to the optical table. The manual of the low vibration interface stated that measuring of electrical connection between outer chamber and cold head would be a good indicator of correct alignment. If the copper cylinders touch, a connection would be established. If they do not touch,

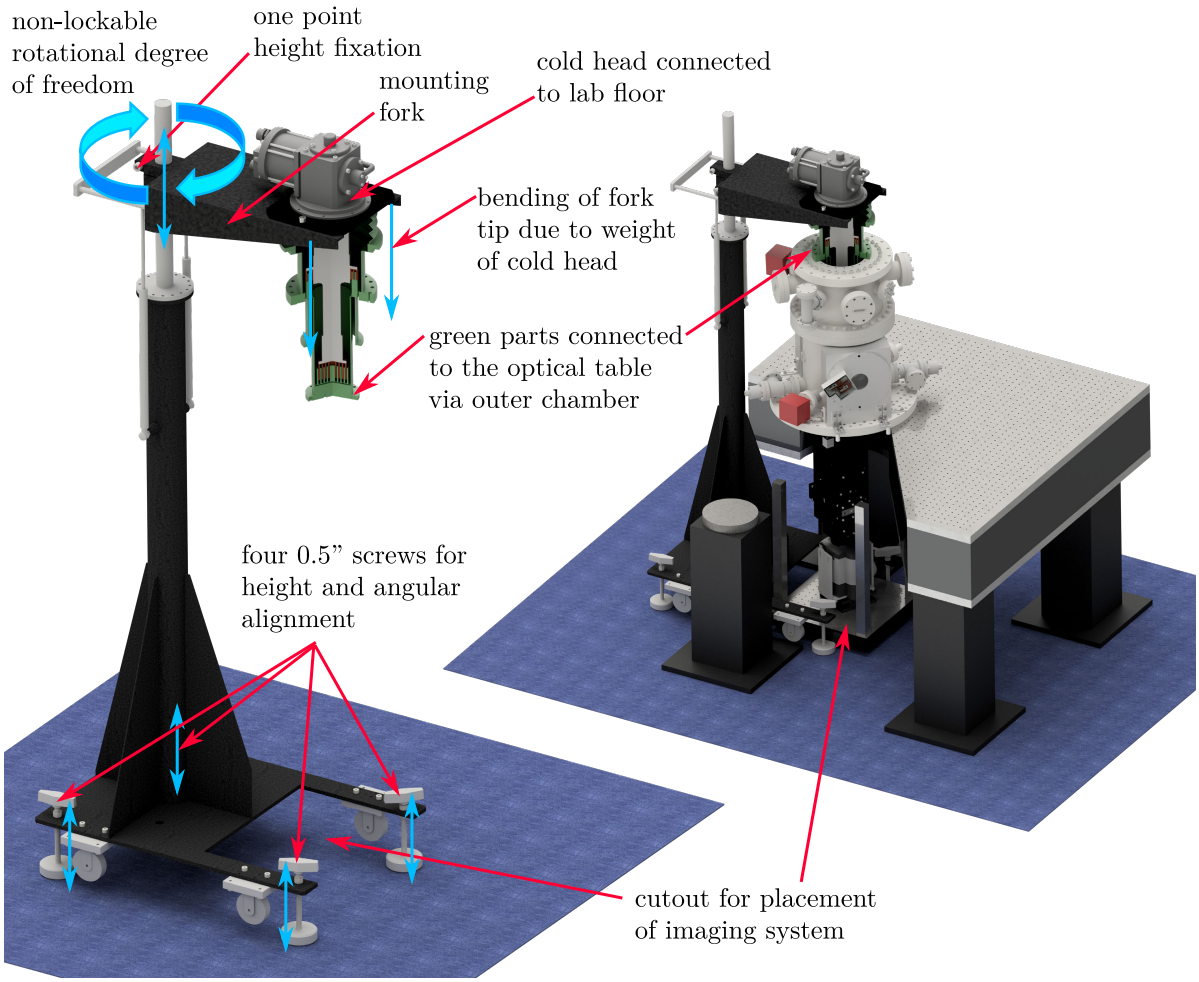

Figure 3.4: Left: Redering of the ultra low vibration interface mounted to the stand that was delivered by ColdEdge. Right: Position of the stand relative to the rest of the experiment.

no connection could be measured. The helium lines as well as the electrical connection between cold head and compressor provide electrical groudning to the cold head. The optical table and therefore the outer chamber are also grounded. We had to remove the helium lines and cables to be able to discern between the two alignment states.
The alignment procedure began by fixating transport rods that provide a stable connection between cold head and exchange gas tube. This way, the cold head was positioned perfectly relative to the optical table but was also mechanically connected to it. We moved the stand to a position so that the fork would fit under the cold head, bolted both parts together and fixated all possible alignment screws on the stand. We removed the transport rods. As a first consequence, the fork tip bend downwards and we measured an electrical contact. We adjusted the screws on the bottom of the stand to compensate for the tilting. Since the feet were co-rotating with the screws, tiny irregularities on the lab

floor would lead to a slight translation of the stand in addition to the height change of the feet. There are four feet. A plane is defined by three points and a four feet mount is vulnerable to wobbling. Combining this with the fact that the screw thread is very coarse and the lever is very long, effective alignment of the cold head position took between 1.5 h and more than a day. The torque required to reconnect the helium lines to the cold head after alignment frequently misaligned it again. The optical table floats on pressurized air. Moving the table also meant moving the cold head since the concentric cylinders inside the low vibration interface would touch and transfer movement. Since the rotation of the mounting fork around the rod could not be locked, even a small table movement in the few mm regime required a re-aligning procedure. With the method of measuring electrical connections, the cold head had to be disconnected from the compressor during re-alignment. Since aligning took a long time and this non-lockable degree of freedom made it mandatory to do this several times a day, and it also was impossible to do while the cold head was running, multiple solutions needed to be found.

3.3.2 Second and current version of the cold head mount

The problem that was fixed the easiest way was to measure inductance, instead of electrical connection, between cold head and outer vacuum chamber during alignment. This essentially was a measurement of the properties of a current loop. No matter if the helium lines were attached or not, the current loop properties change if the copper cylinders change between touching and not touching. We were able to align with attached helium lines by observing jumps in inductance of two orders of magnitude, from 10^{-7} H when misaligned to 10^{-5} H when aligned.
The next problem to fix was the stand. Since multiple properties of this stand made long term stable alignment pretty much impossible, we designed a new mount from scratch. We decided to attach it to the ceiling to save space around the optical table. A rendering of the new mount is shown in figure 3.5 Three fine thread screws with a stainless steel ball tips allow for tilting and height alignment. They are placed in a half-sphere stainless steel receptacle. Eight M6x1 screws with plastic ball tips are used for translation in the x-y-plane. The aluminum plate that they move glides on PTFE cushions. The plastic tip and PTFE cushions prevent electrical contact between cold head and outer vacuum chamber and therefore also prevent ground loops.
For aligning the cold head, we retract the three fine thread screws and put in the transport rods to achieve perfect relative positioning between cold head and optical table. We loosen all translation screws and move the aluminum plate that contains the receptacles such that they are below the fine thread screws. We lower the screws into the receptacles. This fixates the movable aluminum plate. We tighten the side-screws and remove the transport rods. If done right, we did not observe any change in inductance between cold head and outer chamber during this process, meaning the alignment is complete.
When the optical table moved, we still suffered from permanent misalignment. This was

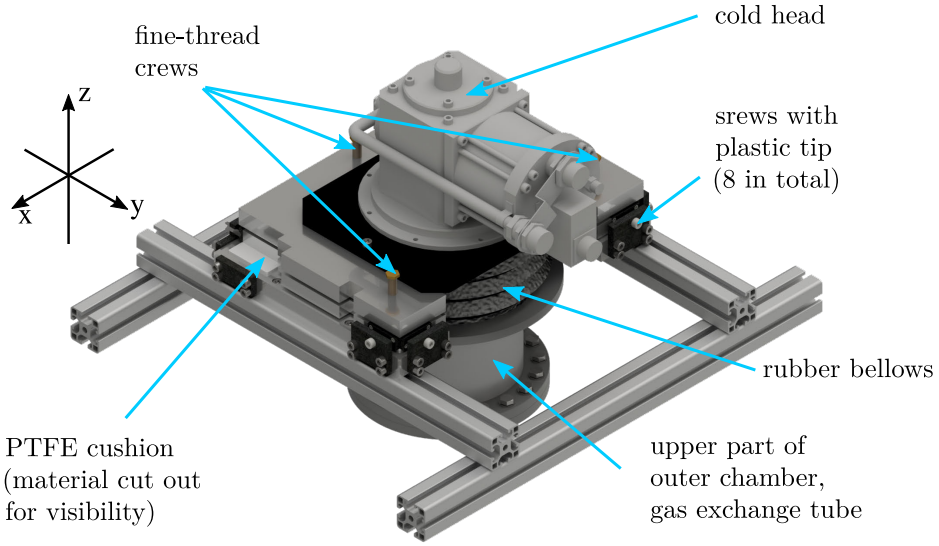

Figure 3.5: Rendering of the new cold head mount. The Structure is attached to the ceiling. The aluminum profiles used to do that are not shown for clarity. They can be seen in figure 3.2. The three fine thread screws are used for tilting and height alignment. The eight screws that are attached to the side are used for shifting.

due to low repositioning precision of the table. We exchanged the positioning control valves of the table from the standard versions with a repositioning accuracy of 2.5 mm to a precision version with an accuracy of 0.3 mm.

With all these changes, the alignment procedure takes less than 5 minutes and is long term stable. Even movement of the table only leads to temporary misalignment. Under normal working conditions the mount has to be re-aligned about once in two weeks.

In case of pressurized air supply failure, the optical table settles down by about 3 cm. The rubber bellows between the cold head and the outer chamber are then stretched by that amount. We made sure that they are long enough to endure this. Also, the concentric copper cylinders are pulled away from each other vertically. It may be that for non-ideal vertical alignment, which is hard to detect because it will only marginally reduce cooling power, the 3 cm movement is enough so that the cylinders are completely separated in the vertical direction. When the pressure comes back, the table moves upwards with a superimposed sheering movement; as a result, the cylinders might chock and the cold head could be lifted out of its mount. To prevent this, an interlock monitors the air pressure and prevents the return of pressurized air after pressure loss so that the system can be brought back in position while under observation.

3.3.3 Vibration measurements

A Michelson-type interferometer has been built to characterize the residual vibrations of the inner vacuum chamber relative to the optical table. The optical pathway is shown in figure 5.2. The interferometer uses 626 nm light from the sum frequency generation setup (see section 5.3). The 1050 nm and 1550 nm lasers have a specified short-term linewidth of less than 10 kHz and less than 1 kHz, respectively which leads to a linewidth of the interferometer light of about 11 kHz. The probe mirror is mounted to the inner chamber, while the reference mirror is on the optical table, supported by a piezo actuator. The arm-lengths were equal to within 5 cm. For the measurement of movement parallel to the optical table, we placed the interferometer on a breadboard surrounding the outer chamber (see figure 3.2). For a second measurement, along the direction of gravity, we placed it on a smaller breadboard below the optical table, usually reserved for ion imaging optics and camera (see 'lower breadboard' in figure 3.2).
We detected the signal on one port of a differential photodetector (2007 Nirvana, Newport). The second port was illuminated with laser light that was split off from the laser source before entering the interferometer. We adjusted the respective power levels to obtain a signal centered around 0 V. We locked the signal to the zero-crossing with a PID controller (PID 110, Toptica) by acting on the piezo actuator, therefore forcing the corresponding mirror to exhibit the same movement as the probe mirror. The bandwidth of the control loop is approximately 10 kHz. We recorded the piezo voltage on an oscilloscope (HMO 3524, Hameg) with a sampling rate of 1 kSa/s and calculated the corresponding travel distance. The voltage to distance relation of the piezo was calibrated by replacing the probe mirror with a mirror on the optical table and scanning over four fringes. We measured vibrations at different temperatures around the boiling point of helium. At temperatures where the exchange gas is in fact liquid, vibration amplitudes of about 50 nm in the vertical direction and about 1.5 µm in the horizontal direction were observed. When the helium was gaseous, we measured vibration amplitudes of 51 nm (13.5 nm RMS) in the horizontal and 29 nm (7.8 nm RMS) in the vertical direction. Figure 3.6 shows time series, power density spectra (PSD) and vibration amplitude rms spectra. Figure 3.6 a) and f) contain recorded time series for vertical and horizontal displacement, respectively. The measurements were conducted at temperatures where the helium was gaseous and vibrations were maximally damped. The time series signal contains N discrete displacement values d_j taken at times t_0 to t_{N-1}. The root mean square RMS is the square root of the arithmetic mean of the squares of each displacement:

$$\mathrm{RMS} = \sqrt{\frac{1}{N}\sum_{j=0}^{N-1} d_j^2} \tag{3.4}$$

It is a measure for the mean displacement amplitude over the time series. While a) does not show distinguishable features, f) shows recurring displacements. We attribute the presence of the signals, recurring at about 1 s intervals, not to a failure or misalignment of the ultra-low vibration interface but to acoustic excitation of the upper breadboard by the sounds emitted by the cold head operating at a rate of about 1 Hz. When the cold

head motor moves the piston, a short clacking sound is emitted. This served as a short excitation pulse to the breadboard which starts vibrating at it's eigenfrequency and is quickly damped. A similar result can be observed when the cooler is off and one just claps hands to emit a short sound. The interferometer was placed on that upper breadboard for this measurement and the resonance frequency of the breadboard is the only signal present in the data (see h) and j)). A more rigid breadboard can be desirable in the future. Early measurements have shown one order of magnitude larger displacements which were reduced to the present level by adding more mechanical connections or posts between the upper breadboard and the optical table.
Figure 3.6 b) and g) show the power spectral densities of the displacement time series for several temperatures. The power spectral density (PSD) gives the strength of the variations of a signal within a frequency interval. It can be calculated as follows: The sampling rate is 1 kSa/s which leads to a time interval between successive t_j of $\Delta t = t_j - t_{j+1} = 0.001\,\mathrm{s}$. The signal recording time is the product of the number of data points taken and the interval in between them: $t_{tot} = N\Delta t$. According to Nyquist's theorem [89] the maximum frequency component which can be extracted it at half the sampling rate: $f_{\max} = 500\,\mathrm{Hz}$. A discrete Fourier transform gives access to the spectrum that corresponds to the d_j [90]:

$$D_k = \sum_{j=0}^{N-1} d_j e^{2\pi i j k/N} \quad , k = 0, ..., N-1 \tag{3.5}$$

This spectrum has discrete frequency intervals between each data point of $\Delta f = \frac{1}{t_{tot}} = 0.16675\,\mathrm{Hz}$. This is called the resolution bandwidth (RBW). This leads to the first data point being at frequency $f_0 = \Delta f \cdot 0 = 0\,\mathrm{Hz}$ and the last data point at $f_{N-1} = \Delta f \cdot (N-1) = 999.833\,\mathrm{Hz}$. Due to the Nyquist theorem, all data belonging to frequencies of more than $f_{N-1}/2 \approx 500\,Hz$ can be disregarded. The power spectral density with respect to frequencies f_k is given by:

$$\mathrm{PSD}(f_k) = 2\Delta t |D_k|^2, \tag{3.6}$$

where $2\Delta t$ is a normalizing factor for which, depending on the application different versions can be chosen [90]. This particular choice will become clear when evaluating equation 3.7 below. From figure 3.6 b) and g) it becomes clear that the vibrations are prominent, if the helium temperature is below its boiling point. Liquid helium will accumulate between the concentric copper cylinders of the vibration isolation system (see figure 3.3) and transfer vibrations. There are three noteworthy features in the spectrum. The peak at around 40 Hz is the eigenfrequency of the upper breadboard (see figure 3.2) surrounding the vacuum chamber. The peak at around 100 Hz is the eigenfrequency of the lower breadboard (see figure 3.2). We attribute prominent features in b) between 100 Hz and 200 Hz to vibrations either of the exchange gas tube or vibrations inside the exchange gas tube. Changing equilibrium vapor pressures for different helium temperatures lead to different amounts of liquid helium present in the tube. These different helium levels are sloshing around in the tube at different frequencies. The buffer gas tube can be considered a pendulum that swings mostly in the horizontal plane, making these features

more significant in the vertical spectrum. The 100 Hz feature is very prominent in b) and the 40 Hz feature as well as its harmonics at around 80 Hz and 120 Hz are more prominent in g). The reason is that for measuring the vertical displacement, the interferometer was placed on the breadboard with 100 Hz eigenfrequency and for the horizontal measurement on the breadboard with 40 Hz eigenfrequency. The inlet c) shows the vertical PSD only for gaseous helium and compares this with the data collected while the cooler was shut off. The 'cooler off' measurement was done approximately 1 min after shutting the cooler off at a temperature of 5 K. Comparing with b), there is about one order of magnitude in PSD between helium below and above boiling point and another order of magnitude between helium above boiling point and cryocooler off. The inlet h) shows vertical displacement PSD with the helium gaseous. There are about two orders of magnitude difference in PSD between helium above and below boiling point.
Figure 3.6 d) and i) show the displacement amplitude RMS spectrum. This is a useful representation to determine the mean displacement within a given frequency interval. It can be calculated from the PSD:

$$\mathrm{RMS}(f_k) = \sqrt{\mathrm{PSD}(f_k) \cdot \Delta f} \tag{3.7}$$

Integrating over the complete RMS spectrum from 0 to the Nyquist frequency yields the RMS as calculated in equation 3.4. Calculating the same RMS via these two different methods is a sanity check for choosing the normalization factor in equation 3.6.

Comparison with state of the art vibration isolation systems in ion trap experiments

For comparison, consider the system described in [87] based on a cryogenic ion trap mounted to a GM cooler, mechanically decoupled via an exchange gas, comparable to our system. Relative to the time series of vertical vibrations in figure 3.6 a) to figure 7c) of reference 87, our vibration amplitudes are roughly a factor of two smaller. Comparing the horizontal rms spectra of figure 3.6 j), obtained with a resolution bandwidth (RBW) of 0.167 Hz with the 7.7 K measurement of figure 7a) of reference 87, obtained with a RBW of 0.1 Hz, our dominant rms values are about a factor of 7 lower.
Now consider the custom vibration isolation for a pulse tube cooler described in reference 88. Comparing the vertical rms spectra of figure 3.6 e) to figure 13 f) of reference 88, obtained with a RWB of 0.1 Hz, our system shows more than one order of magnitude lower vibration amplitudes. Comparing the horizontal rms spectra of figure 3.6 j) to figure 13d), our results show the same order of magnitude, with reference 88 performing slightly better at some frequencies.
Reference 76 describes an alternative approach based on a flow cryostat. Comparing horizontal time series and rms spectra of figure 3.6 f) and j) with corresponding graphs in figure 5 of reference 76, our system has only twice the time-series amplitude and comparable amplitudes in the rms spectrum relative to this system that does not have any moving parts at all close to the trap. Reference 76 does not show data for vertical vibrations.

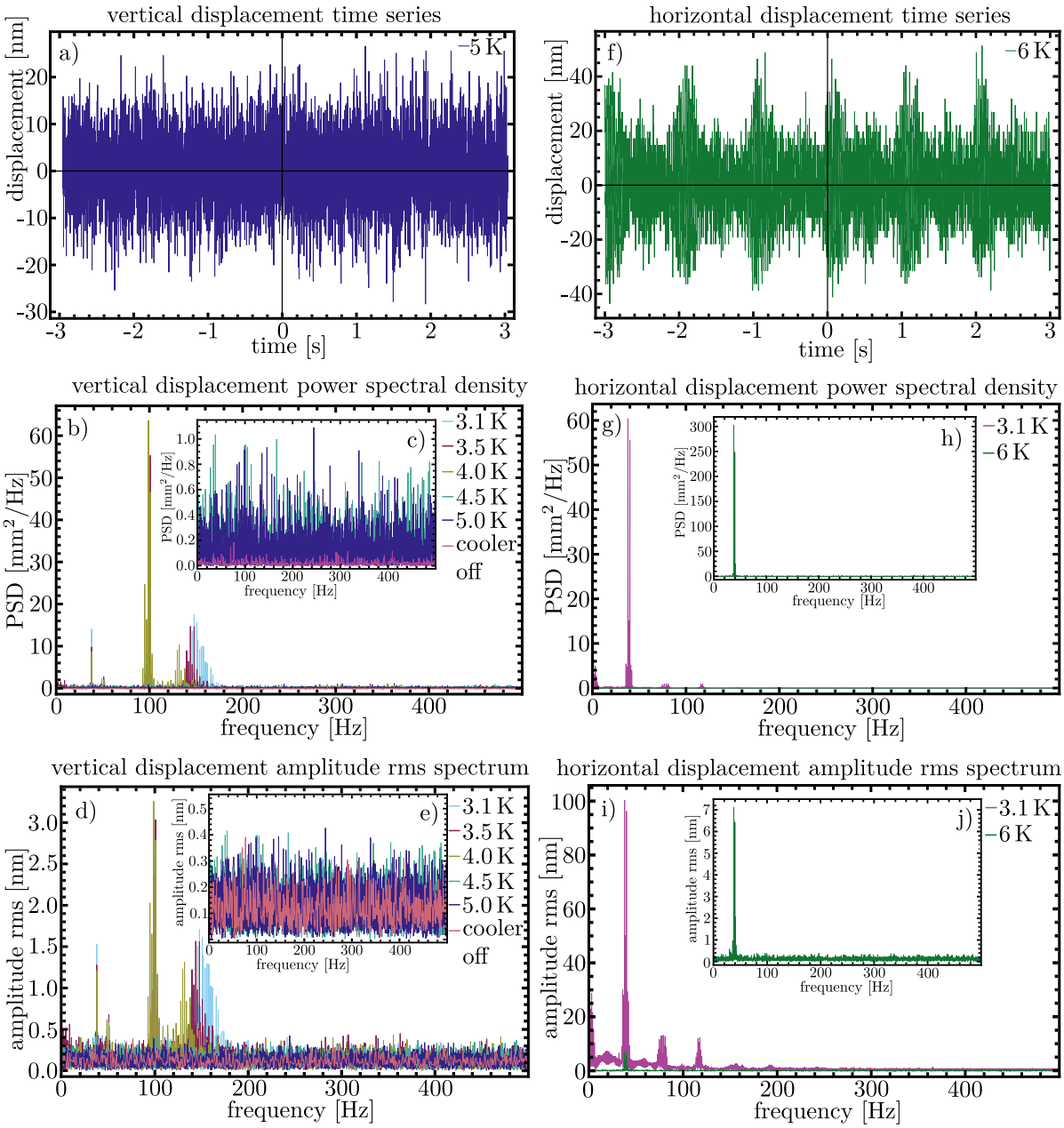

Figure 3.6: Vertical and horizontal vibration time series, resulting power density spectra (PSD) and vibration amplitude spectra. a) Time series for vertical vibrations at 5 K. b) Comparison of PSD spectra for different second stage temperatures and the case of shut-off cold-head. c) Same as b) but showing only data for 4.5 K and above, where no liquid helium is present. d) Comparison of vibration amplitude rms spectra for different second stage temperatures and the case of shut-off cold-head. Data from b) converted to rms with a resolution bandwidth of 0.167 Hz. e) Same as d) but showing only data for 4.5 K and above, where no liquid helium is present. f) Time series of horizontal vibrations at 6 K. g) Horizontal PSD spectra for 3.1 K and 6 K. h) Same as g) but only at 6 K. i) Horizontal vibration amplitude rms spectra for 3.1 K and 6 K. Data from g) converted to rms with a resolution bandwidth of 0.167 Hz. j) Same as i) but only at 6 K.

3.4 Inner vacuum chamber

The ion trap is housed in the inner vacuum chamber. The chamber has three main purposes for us. Fist, it provides cryogenic vacuum conditions suitable to prolong the ion lifetime in the trap compared to room temperature chambers (see section 3.1). Second, it shields the ion from external electromagnetic noise. Third, it acts as a thermal buffer to compensate for short temperature spikes that might occur while high-power microwave pulses are applied to the trap (see sections 2.3 and 4.2).

Technological requirements

The inner chamber has to house the ion trap, which has to be thermally anchored at the second cooling stage of the low vibration interface. Around the trap, there has to be enough space to accommodate a printed circuit board, the so-called filter board that contains an RC filter and electrical feed lines which are connected via bonding wires to the trap (see section 4.6 and figure 4.6). Although the current trap design requires only 4 high frequency lines (1 RF and 3 MW) as well as 10 DC connections, we decided to aim for a system that can support up to 8 HF and 100 DC lines. The walls have to contain feedthroughs to guide high frequency and DC signals from the outside to the filter board (see chapter 4). The inner chamber also has to provide room for in vacuum imaging optics (see section 6.2.2). Windows are required to provide optical access for laser beams (see chapter 5) and for imaging (see chapter 6). The inner chamber has to be a self contained vacuum chamber. Therefore, a port for a pinch-off tube has te be considered.

3.4.1 Materials and outer dimensions

Most of the inner chamber is made out of oxygen free electrolyte (OFE) copper. This is high purity copper that has excellent conductive properties for heat as well as for electric currents. The thermal conductivity of OFE copper at 4.2 K is approximately $850\,\mathrm{W/m \cdot K}$ [75], whereas that of stainless steel at 4.2 K only is $0.3\,\mathrm{W/m \cdot K}$ [64]. This becomes most important, when microwave currents heat up the trap and the heat has to be quickly extracted. The trap is glued to a copper block, that itself is connected via copper structures to the cold tip (see section 4.6).
According to the law of induction, changes of an external magnetic field induce current loops in the copper that themselves produce a magnetic field that in part counteracts the changes. The current loops will slowly disappear since the copper has some electrical resistivity. It has been reported that a copper chamber can effectively shield an ion from short term magnetic field fluctuations. The reported decay of the shielding effect was measured to follow an exponential law with a time constant of 3.8(2) s [91]. The chamber used in that experiment is comparable in its dimensions to our chamber.
The inner vacuum chamber is surrounded by a radiation shield and an outer vacuum chamber. The outer chamber was designed to be fully UHV compatible and the simplest way to achieve that was to use a round structure (see section 3.6). To maximize the

available space for the inner vacuum chamber, the radiation shield was also designed to be round. A round inner chamber would be a logical follow up and indeed many experiments chose to work with a round inner vacuum chamber[91, 86]. We chose to build a chamber with a quadratic footprint. The reasoning behind it was as follows: To block as much room temperature thermal radiation from reaching the radiation shield as possible, the inner chamber or the ions, the windows had to be as small as possible. Small window diameters lead to the placement of small optics in front of them. To achieve a desired focus waist at the ion position, the optics have to become larger, the further they are away. Hence a compact system is desirable. The minimum distance between the radiation shield and the inner chamber is restricted by cables that are attached to the outside by some sort of plug and the bending radius of the attached wire. Having a round footprint of an inner vacuum chamber would lead to the radiation shield being as close as possible to the biggest plug/wire combination and relatively far away from the rest of the chamber walls. Placing the electrical connections in the center region of a quadratic footprint leads to almost the same radiation shield diameter but with more space inside the chamber since there are parts of the wall closer to the shield. Another feature is that we can accommodate larger flanges since there are larger flat surfaces available. In a round setup, parts of the wall need to be flattened in order to connect flanges. In an early design, we envisioned a filter board with nearly 100 DC connections (see figure 4.8). We chose the dimensions of the inner vacuum chamber to house that filter board and to guide all electrical signals to it. We decided to have 15 mm thick walls. Multiple renderings of the outside of the inner vacuum chamber with annotated dimensions are shown in figure 3.7.

3.4.2 Flanges

The inner vacuum chamber has an OFE copper support structure. Most commercially available UHV feedthoughs and flanges for our application are made out of non-magnetic stainless steel, either 316LN or 1.4429. The vacuum seal between two parts has to be softer than each of the parts. Otherwise the parts might suffer damage. A common material for sealing copper and steel is indium. With a melting point of about 156.6°C, baking the vacuum chamber becomes difficult, if indium is used. With a melting point of 1064°C, gold can be used if baking becomes necessary. For cryogenic applications, baking is often not required therefore we used the cheaper indium.
Instead of having one separate flange for each feedthrough and window, sealed individually to the inner chamber, we chose a design with four large stainless steel flanges that contain most of the required hardware. We use two additional flanges for mounting the imaging window and the pinch-off tube (see top left of figure 3.7). Both types of custom flanges are shown in figure 3.8. Each of the larger flanges contains two welded-in floating SMA feedthroughs and one D-Sub 25 pin feedthrough, both from Kurt J. Lesker Company. Three of the four have one DN16CF port and the fourth has three of these ports (see figure 3.7). The two smaller custom flanges adapt a DN16CF flange to the copper chamber.
The indium seal between stainless steel and copper is made from a 1 mm diameter indium

wire. A piece of wire, about 1 cm longer than required is placed at the final position on the copper surface. The in the middle of the overlapping cm, a diagonal cut is made through both wires. This results in two plane faces with the same surface area at both ends of the wire. A drop of hydrochloric acid (10% solution in water) is placed on the two ends. The acid dissolves the oxide layer that is present on the indium surface. If both sides of bare indium come into contact, they will combine into one indium piece. This takes a few seconds. The surplus acid can be soaked up by a tissue and cleaned with drops of water and tissue.
Once the indium seal is complete, the flange is put into place and the screws are tightened. For the large flanges and their M5 screws, the torque is increased in steps of 0.2 Nm until reaching 1 Nm. For the smaller flange and it's M3 screws, the final torque is 0.7 Nm. If a leak is detected at some point in time, the screws can be tightened further..
After sealing all flanges and putting all viewports on them (see next section), we connect the pinch-off tube (seef igure 3.8) to a vacuum pump and evacuate the inner chamber. We do leak testing by spraying isopropanol on the flanges and observe the potentially rising pressure. In case we detect a leak, we tighten the screws of the affected flange. If that does not result in better vacuum, we make a new seal. If we cannot detect any leak with isopropanol, we pump the inner chamber below 10^{-8} mbar (this is possible because it is empty at this point, during normal operations we do not reach such low pressure). We apply helium gas to the flanges and detect its presence in the chamber with a residual gas analyzer that is also connected to the pump. We have managed to make the seals helium tight to the 10^{-11} mbar level.

This process took a long time since we had to repeat it several times and each run takes up several hours since pumping down took a long time. In the future, a dedicated leak tester might be of advantage.

3.4.3 Viewports

Laser access has to be provided in two perpendicular directions. One direction would be sufficient for the Doppler cooling, ionization and ablation beams but a perpendicular direction is useful for implementing Raman beams. For beam diagnostics and alignment observation it is useful to let every beam that enters the inner chamber leave it as well. This leads to a minimum number of four windows for laser access. Another window is required for imaging.
In an early design, we had planned a different way to load our trap which has quickly proved to be too ambitious to implement. For the way we currently load the trap see section 5.4. The early suggestion relied on an ablation target being further away from the trap and the ablation beam passing through a separate viewport, which is now used for the probe mirror of the vibration observing interferometer. It turned out that the distance would have been too large and not enough atoms would travel through the trap center. Before switching to the beam configuration that we use today (see section 5.4), we thought that the windows would be used primarily for two Raman beams coming in under a right angle. Therefore we planned with windows that are anti-reflection coated

for 313 nm. The efficiency of cooling and detection beams are relying on σ^+ polarization to drive only the cycling transition (see figure 2.2). During cooldown, there is a chance that the viewport glass experiences mechanical stress that is caused by different thermal contraction coefficients of the glass and the rest of the flange. Although that stress will not directly lead to a broken window, it may induce an unpredictable amount of birefringence in the glass, which may disturb the polarization. So called re-entrant viewports can in part reduce that effect. These viewports have a tube sticking into the vacuum side. On the end of the tube, a window is mounted. If the tube has a thermal contraction coefficient that is closer to that of the glass then to that of the flange, most of deformations due to mechanical stress will occur in the tube. Off the shelve re-entrant viewports are usually not rated for cryogenic applications. We were able to acquire a batch of custom re-entrant viewports from MPF Products that were rated for use at 4 K. At the time we thought that we would need five of these, two for each laser direction and one for the imaging port. We ordered eight viewports. After about five years, within a time span of about four months, all but one developed leaks. Even those that remained on shelf in their original package were inoperable. We were not able to figure out, what caused this wide-spread malfunction. As a result, only one re-entrant viewport remains in operation. We use it for the entry port of the cooling and detection beam. The output port of that beam as well as the imaging viewport are common anti reflection coated for UV DNCF16 viewports.
Since the originally envisioned way of trap loading did not work because of a too far away beryllium target, we decided to place the target about 13 mm away from the trap center. We would have to translate the ionization laser, which is passing through the viewport center and also the trap center, by 6 mm to hit the beryllium wire. That is the path the ablation beam has to take: 6 mm parallel to the ionization beam. Hence a window must be used that lets both beams pass.
The optically active area of a DN16CF viewport is a circle with less than 16 mm diameter. Under perfect conditions, the ionization beam passes through the center and the ablation beam 6 mm off center, which still leaves 2 mm between ablation beam and flange wall. Since production and assembly tolerances as well as shrinking of the apparatus during cooldown and the finite diameter of the laser beam have to be taken into account, we decided that a larger window would be desirable. We had two options: design a new custom flange that can house a larger CF flange or modify the current flange. Since feedthroughs were already successfully welded in and leak tight, we decided to modify the existing flanges. There was a DN16CF knife edge with corresponding screw threads already in the custom flange. We milled out the knife edge and produced a flat surface that is suitable for indium sealing a glass plate to it. Figure 3.9 contains the rendering of the design. A window is pressed with an aluminum ring into an indium ring which gets flattened and fills out every space between flange and window. That constitutes the vacuum seal. The indium is quite soft and the previous design was for pressing a knife edge into a comparatively hard copper gasket. The M5 screws were perfectly capable of bolting the CF flange but turned out to be ill suited for applying minimum pressure evenly to the indium seal. Even a low amount of torque results in a comparatively long travel range of the M5 screw. Since there are only six evenly spaced screws around the

seal, we were not able to evenly distribute the pressure to the indium ring. Even after more than fifteen sealing attempts, helium leak testing was still negative. In a regular indium seal design, one would use more screws with a smaller size. Instead of redesigning the whole flange, we produced a PTFE ring that is placed between the window and the aluminum ring to distribute the forces more evenly. We needed four attempts to seal the two windows leak tight to the flange.

3.4.4 Inner chamber interior

The interior of the inner chamber consists mainly of the trap mount with the filter board on it and the imaging optics. A detailed description of the filter borad can be found in section 4.6. A detailed description of the imaging optics can be found in section 6.2.2. There are various cables that connect the feedthroughs on the flanges to the filter board. They are described in chapter 4.
There are three small copper cages of $1 \times 2 \times 1\,\mathrm{cm}^3$ dimensions that contain activated charcoal pellets. These pellets have a high surface to volume ratio and act as a cryopump once they have been cooled down. The cryopumping effect stems from the fact that at low temperatures almost any chemical compound is either solid or liquid, which reduced the probability of atoms or molecules being in the gas phase. Due to a low vapor pressure, a few molecules might either evaporate or sublimate. If these hit a cold surface, they will usually stick to it. The surface binding energy between the activated charcoal and that molecule is usually higher than the thermal energy of the molecule. This makes for an effective pump as the residual gas freezes on the surfaces.
At room temperature and under low pressure, molecules caught by these pellets might get thermally excited to a point that they gas out. This limits the pressure in the inner vacuum chamber at room temperture to $10^{-6}\,\mathrm{mbar}$ levels (see next section). Before assembly, we clean the chamber with water and isopropanol. Afterwards we soak paper tissue in a water/citric acid solution and stick it to all copper surfaces. After about 15 min, we remove the tissue and cleanse with isopropanol. While in air, the copper parts oxidize over time, which reduces their reflectivity. A high reflectivity is required for optimally reflecting thermal radiation (see section 3.7.2). The thermal considerations that involve the inner chamber including the wiring and the thermal radiation are discussed in section 3.7.

3.4.5 Vacuum quality in the inner chamber

After sealing all flanges and installing the trap and the imaging optics (see sections 6.2.2 and 4.6), the inner chamber is already mounted to the cold finger (see figure 6.7). We connect the pinch-off tube of the inner chamber to a pumping station consisting of an Edwards nXDS 10i scroll pump that is backing a Pfeiffer TMU 521 turbo molecular pump. Between the turbo pump and the inner chamber, a valve can be used to disconnect the pump from the inner chamber. It is useful to close the valve before pinching the tube to protect the turbo pump from a sudden increase in pressure in case the pinch-off fails and air is being sucked into the system. We use an SAES NEXTorr D 100-5 ion

combination pump to assist with the pumping and to monitor the pressure. After about 1.5 days, the pressure reaches below 6×10^{-6} mbar and will not fall significantly further due to outgassing of the charcoal pellets that were discussed in the previous section. We close the valve, deactivate the NEXTorr and pinch the tube. After closing the outer chamber, cooling down and trapping an ion we are able to characterize the achieved crygenic pressure.

As explained in section 3.1, a background gas molecule has an average kinetic energy of 0.5 meV and will not be able to kick an ion out of the trap with a trap depth of 38 meV. Kinetic collisions with background gas will most likely not be a source of ion loss and therefore cannot be used to reach conclusions about the background gas density. A useful method to characterize vacuum quality under these conditions was presented in [92]: The main loss channel for Doppler cooled $^9Be^+$ ions in a cryogenic trap is a chemical reaction with hydrogen. The reaction of a hydrogen molecule with an ion is endothermic and will not happen without supplying an activation energy. During Doppler cooling, for a portion of the time the ion is in the ^{2}P state. That excited state has enough energy to make the reaction with hydrogen exothermic: $Be^+(^2P) + H_2 \rightarrow BeH^+ + H$. The reaction rate can be described with a Langevin model and was found to be $k_L = 1.6 \times 10^{-9}\,\mathrm{cm^3\,s^{-1}}$ [93]. The H_2 pressure P_{H_2} can be deduced from the loss rate τ^{-1} of Be^+ in the following way: With k_B as the Boltzmann constant, T as the temperature and ρ_{H_2} as the H_2 number density, the ideal gas law for background gas hydrogen reads

$$P_{H_2} = k_B \rho_{H_2} T. \tag{3.8}$$

Assuming that this is the only relevant loss channel [92], the effective ion lifetime τ' is inversely proportional to the number density of hydrogen. The proportionality factor is the inverse reaction rate k_L^{-1}:

$$\rho_{H_2} = \frac{1}{k_L \tau'} \tag{3.9}$$

This model assumes that the ions are permanently in the excited state, which is not true. The observed ion lifetime τ is the effective lifetime scaled with the probability of the ions being in the excited state $p(^2P)$:

$$\tau' = \frac{\tau}{p(^2P)} \tag{3.10}$$

For the early trapping trials, we used a cooling beam with about 5 times the saturation power. During those trials we can assume $p(^2P) \approx 0.5$. The background pressure could be determined by measuring the ion lifetime and combining equations 3.8 to 3.10:

$$P_{H_2} = \frac{k_B T}{2 k_L \tau} \tag{3.11}$$

We have not observed any ion loss which we did not trigger, either deliberately or accidentally. Therefore we cannot give an ion loss rate. We use a statistical model that follows [40] to give lower bounds on ion lifetimes.

We model the probability that an H_2 molecule collides with an ion as a Poisson process:

$$f(n:\lambda) = \frac{\lambda^n e^{-\lambda}}{n!}, \tag{3.12}$$

where n is the number of collision events and λ is the expected value of the probability. Let t_{exp} be the accumulated time that ions were trapped while $p(^2P) \approx 0.5$ was fulfilled.

$$t_{exp} = \sum_i t_i \cdot m_i, \tag{3.13}$$

where i is a period when trapping occurred, t_i is the time of that occurrence and m_i is the number of ions trapped during that time. λ is given by the exposure time and the lower limit on the ion lifetime τ_{lower} [40].

$$\lambda = \frac{t_{exp}}{\tau_{lower}} \tag{3.14}$$

We can chose a confidence level CL for which we can determine a lower limit on the ion lifetime. A confidence level of CL=1 makes no sense since we did not measure any ion decay. It has to deviate from 1 by a factor ϵ: $CL = 1 - \epsilon$. An infinitesimally short time after trapping, no ion loss event will have occurred and $n_0 = 0$ holds. The confidence level is given by [40]:

$$\mathrm{CL} = 1 - \epsilon = \sum_{n=n_0+1}^{\infty} f\left(n; \frac{t_{exp}}{\tau'_{lower}}\right) \tag{3.15}$$

It follows that

$$\epsilon = \sum_{n=0}^{n_0} f\left(n; \frac{t_{exp}}{\tau'_{lower}}\right) = \frac{(\frac{t_{exp}}{\tau'_{lower}})^0 e^{-\frac{t_{exp}}{\tau'_{lower}}}}{0!} = e^{-\frac{t_{exp}}{\tau'_{lower}}} \tag{3.16}$$

$$\rightarrow \mathrm{CL} = 1 - e^{-\frac{t_{exp}}{\tau'_{lower}}} \tag{3.17}$$

We have accumulated about 15 days of ion lifetime under the described conditions: $t_{exp} = 15\,\mathrm{d}$. Solving equation 3.17 for τ'_{lower} and converting days to seconds yields

$$\tau'_{lower} = -\frac{1296000\,\mathrm{s}}{\ln(1 - \mathrm{CL})} \tag{3.18}$$

Inserting this in equation 3.11 yields

$$P_{\mathrm{H_2}} = \frac{-\ln(1 - \mathrm{CL})}{1296000\,\mathrm{s}} \frac{k_B T}{2k_L} \tag{3.19}$$

At 5 K and a confidence level of 68%, this yields a maximum H_2 background pressure of $P_{\mathrm{H_2}} = 1.2 \times 10^{-12}\,\mathrm{mbar}$. At a confidence level of 90%, this yields a maximum H_2 pressure of $P_{\mathrm{H_2}} = 2.5 \times 10^{-12}\,\mathrm{mbar}$.

To determine the pressure more accurately, we would have to monitor the time that ions are trapped, the number of ions and the laser power in units of saturation power. We also have to monitor ion loss and if it is caused by external effects like cooling laser malfunction or deliberate trap voltage changes. This is quite an experimental overhead to realize. Since we have not observed unexplained ion loss in all of 2020, we are confident that the pressure is low enough to support future traps that might hold more ions.

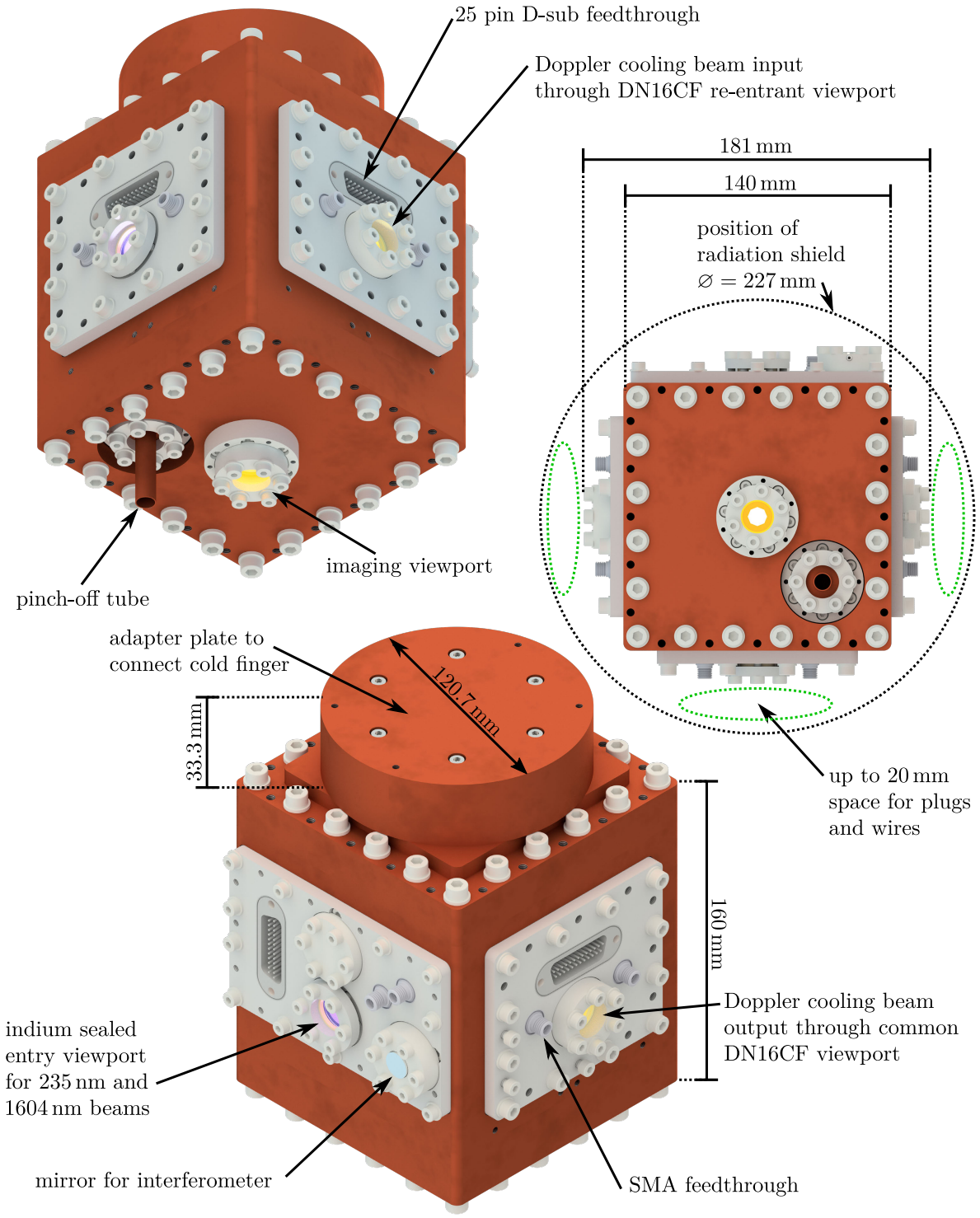

Figure 3.7: Different renderings of the outside of the inner vacuum chamber. For description see text.

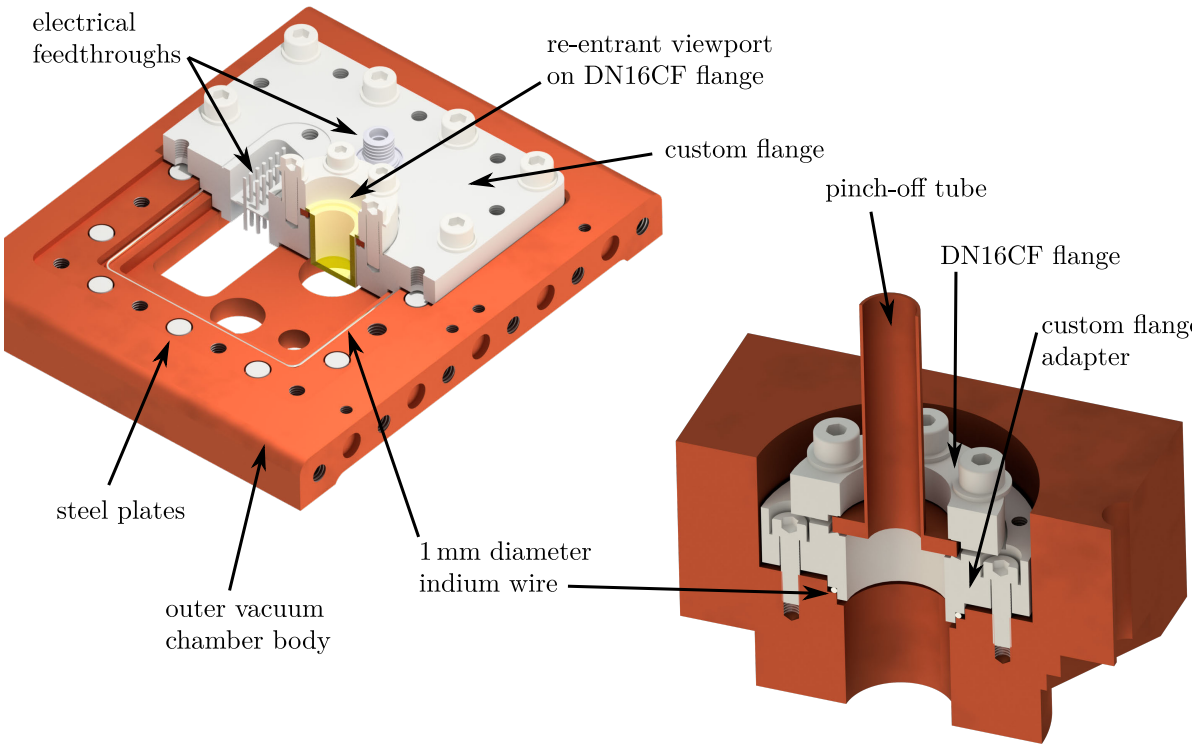

Figure 3.8: Two sorts of custom flanges connected to the inner chamber. Top left: Flange with welded-in electrical feedthroughs and a DN16CF knife edge to accommodate a re-entrant viewport. Bottom right: Adapter flange between the inner vacuum chamber and a DN16CF flange, in this case the port for the pinch-off tube.

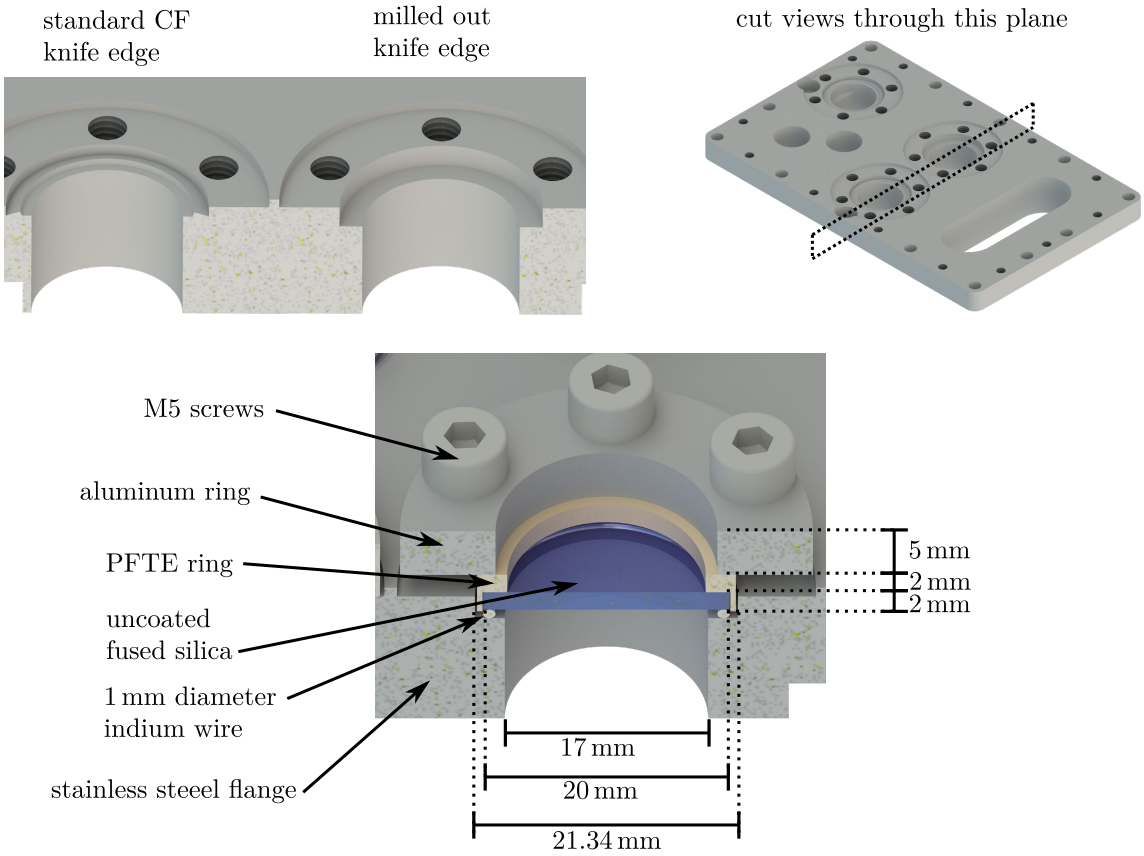

Figure 3.9: Top right: Custom flange. Top left: cut view through the plane depicted in the top right. The left port has the original CF knife edge. The right side has the newly milled out knife edge. Bottom: Cut view through the indicated plane with attached window. The PTFE ring transfers pressure from the screws to the window which is pressed into the indium ring.

3.5 Radiation shield

The radiation shield is connected to the first cooling stage at around 40 K. It surrounds the inner chamber and blocks room temperatue thermal radiation from hitting the second cooling stage, which has limited cooling power. It has an outer diameter 231 mm and a height of 393 mm. It is made out of OFE copper and features a few holes for laser access and imaging as well as for electrical wiring. The total area of holes has to be minimized in order to block the most thermal radiation. It has a top plate, which is mounted to the first cooling stage, a bottom plate that has a hole in the middle to let the imaging light through and a cylindrical body between the two plates that has 6 holes for optical access. An adapter plate allows for removal of the cylinder without detaching the top plate from the cooler. The top plate has anchor spots for electrical wiring where it can thermalize to 40 K before connecting to the inner chamber. Figure 3.2 shows the position of the radiation shield relative to the rest of the system. Figure 3.10 shows an overview of the

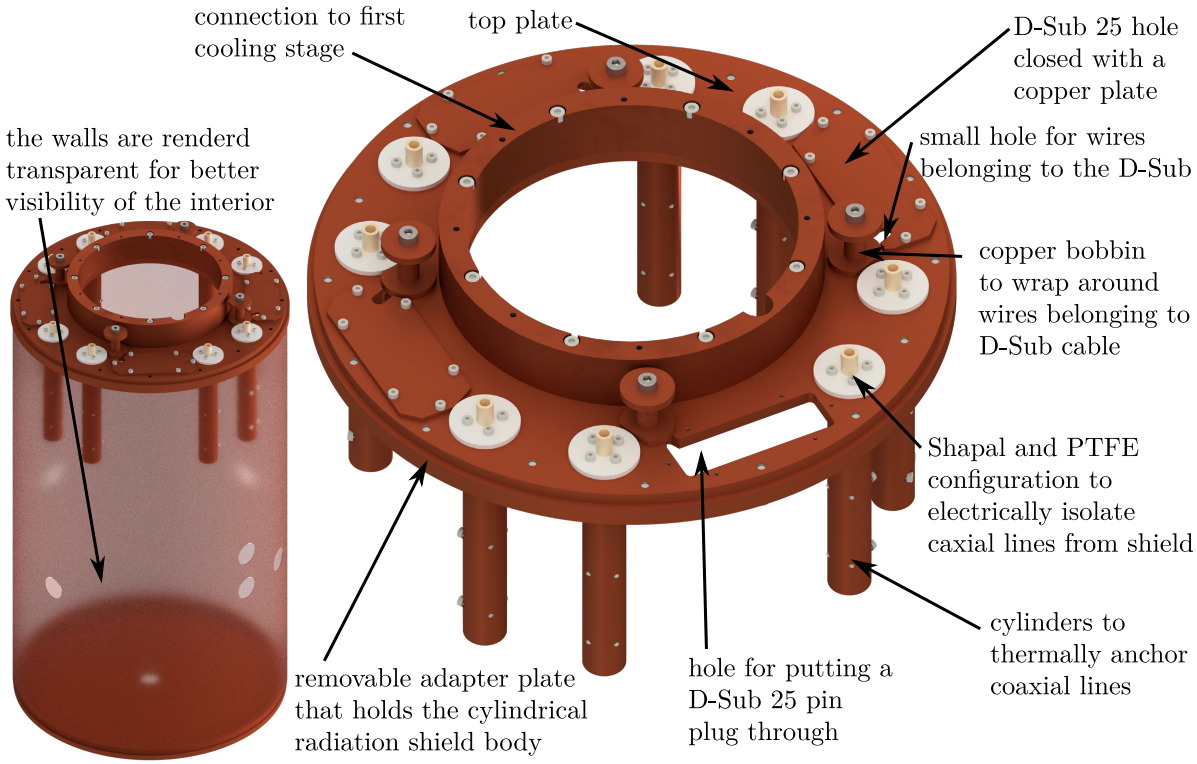

Figure 3.10: Left: Overview of the radiation shield. The walls are made out of OFE copper. There are six holes for optical access. Five on the side and one at the bottom. Not shown is the inner vacuum chamber that is situated in the middle of the shield. Right: Overview of the top plate. The adapter plate and with it the cylindrical wall can be removed from the top plate. During maintenance of the inner chamber, the top plate and all cables can stay in place.

radiation shield and the features of the top plate. Once all wires are thermally anchored

to the top plate, it becomes tedious to remove them again. For maintenance of the inner chamber, the cylindrical wall can be removed without unmounting the top plate. The cylindrical walls are mounted to the adapter plate, which can be removed by unscrewing it from the bottom. Unscrewing it from the top would be impossible without lifting all of it out of the outer chamber (see figure 3.12) which is impractical since that would require unbolting a lot of feedthrough flanges. Before assembly, we clean the shield with water and isopropanol. Afterwards we soak paper tissue in a water/citric acid solution and stick it to all copper surfaces. After about 15 min, we remove the tissue and cleanse with isopropanol. While in air, the copper parts oxidize over time, which reduced their reflectivity. A high reflectivity is required for optimally reflecting thermal radiation (see section 3.7.2). The thermal considerations that involves the radiation shield including the wiring and the thermal radiation are discussed in section 3.7.

3.6 Outer vacuum chamber

The outer chamber is made out of non-magnetic steel, either 316LN or 1.4429. A rendering is shown in figure 3.11. It has an overall cylindrical form with an inner diameter of 243 mm, an outer diameter of 273 mm and a height of 567 mm. It rests on a 500 mm diameter and 30 mm thick plate that has a DN16CF knife edge in the middle to house the window for imaging the ions. It also has a 243.3 mm diameter knife edge for connecting it to the main cylinder. There is a grid of M6 through-holes that matches the optical table's grid to be able to bolt the chamber to the table and to connect auxiliary hardware to the table. It is divided into a lower and an upper part. The parts are connected via a 14" CF flange that is welded to the bottom part. The top part of the flange is rotatable to allow for relative positioning of. The lower part has four DN40CF half nipples welded to it. These currently house a valve to connect a pump and a NEXTorr D 100-5 ion combination pump. A third port is used for a so called fall-off flange. This is a blank CF flange with a rubber seal that is tightened only to a point that allows for evacuation of the chamber. If the pressure has fallen in the chamber to operating levels, the screws on that flange are loosened. If for some reason the pressure inside the chamber rises to a significant level over ambient pressure, this flange is supposed to let the gas out, thereby protecting the windows in the viewpotrs from breaking. A malfunction like that can occur if during cryogenic operations a small leak appears and stays undetected. This would, over time, let air freeze or condense on the inner chamber and the radiation shield. During warm up, this air will evaporate and a fast rise in pressure will occur. The fourth DN40CF port is currently not in use.
The lower part also houses six viewports. Four for laser access to the ions, one for laser access for the interferometer that monitors vibrations and an auxiliary port that is currently not in use.

The upper part is connected to the low vibration interface (see section 3.3) and also supports the cold head, if the chamber is opened and the transports rods are in place. It has four DN63CF half nipples welded into it that house overall 100 DC pins distributed

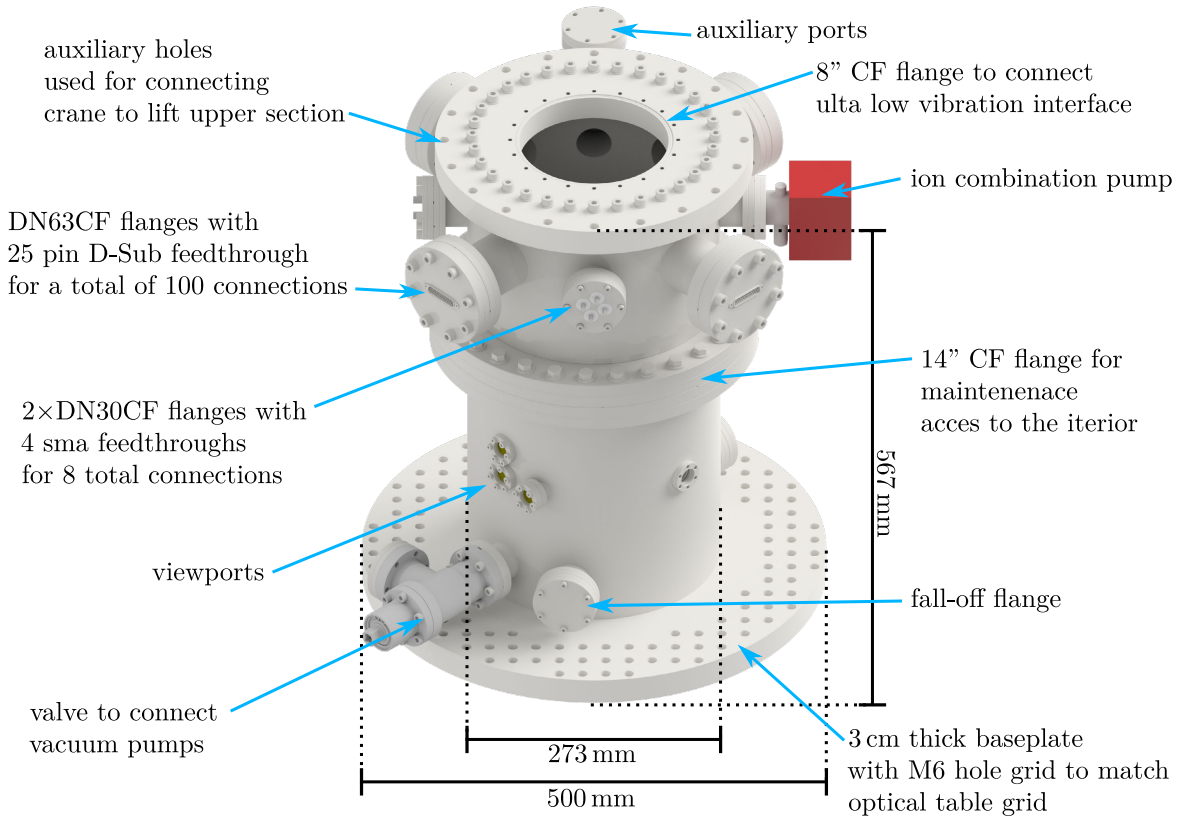

Figure 3.11: Rendering of the outer chamber. Not shown because they are on the back side are an ion combination pump on the lower part of the chamber and a vacuum gauge on the top part.

over four 25 pin D-Sub feedthroughs. A total of four DN40CF half nipples are also welded in that support two flanges with four SMA feedthroughs each and one flange with a NEXTorr D 100-5 ion combination pump. The fourth flange houses a 40CF Tee with a blank flange and a Pfeiffer PKR 251 full range vacuum gauge connected to it. The cylinder of the upper part has a 243.3 mm diameter knife edge on it's top. A corresponding knife edge can be found on the top flange. This top flange also connects to the low vibration interface and has a circle of M6 through-holes to mount auxiliary hardware to the chamber. Is is mostly used for connecting a crane that can lift the system out of the lower part, which is bolted to the table and surrounded by optics (see figure 3.2) and can therefore not be moved without considerable dismantling of the complete setup. The outer chamber is completely UHV compatible. It currently only provides isolation vacuum, which has to be lower than 10^{-3} mbar. For this reason we do not bake the chamber although theoretically possible. Before installing the wiring but with the inner chamber inserted and cooled down, the chamber has been pumped down to high 10^{-10} mbar levels. During normal operation with all cables installed, we use mostly rubber seals on the outer chamber. In this configuration and with deactivated

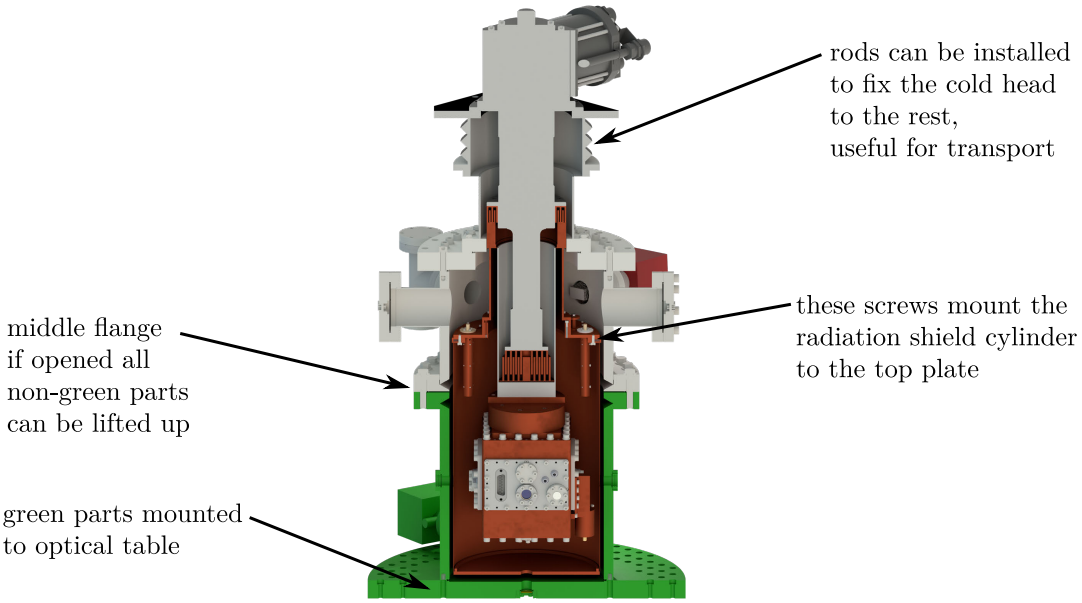

Figure 3.12: Cut view of the outer chamber, inner chamber, radiation shield and low vibration interface. Disconnecting the middle flange opens up the possibility of lifting out every non-green part. The bottom plate of the radiation shield can afterwards be removed and, by reaching the marked screws from below with a 55 cm long Allen wrench, the radiation shield cylinder can be removed to provide access to the inner chamber. While all in vacuum wiring stays untouched and intact.

ion combination pumps, we reach 3×10^{-8} mbar.
In future iterations of the experiment it might be necessary to remove viewports of the inner chamber due to stress induced birefringence or even the complete inner chamber due to space restrictions. In that case we are ready to provide UVH vacuum levels. In either case it might be important to have a cryogenic copper cage around the ion trap to provide shielding from radiation and magnetic field fluctuations as well as cryopumping and, if the holes in it are small enough, differential pumping.

3.7 Thermal design

The cooling power at the second cooling stage of our system is specified at approximately 1.5 W at 4.2 K. A great deal of care has to be taken to avoid too much heat load on it. There are three passive paths that contribute to the heat load and one active. Contact of the inner chamber to hot air would not only lead to condensed or frozen air on the viewports which would disturb laser access but first and foremost it would just heat up the chamber. Therefore we need the outer chamber to provide an isolation vacuum. Radiative heat transfer also has to be considered as having the thermal radiation of the room temperature chamber hit the cold inner chamber would heat it up. Therefore a radiation shield at with ample cooling power at around 40 K was built to block that radiation.

Having a solid contact between the inner and outer chambers would lead to heat transfer between them. Electrical feed lines provide this solid contact and materials have to be chosen to minimize thermal conduction. Electrical lines that carry a current are also prone to Joule heating, which depends on the resistivity of the wire. For electrical lines a combination of materials has to be found that conducts as much current as necessary while simultaneously having an electrical resistivity as low as possible.

3.7.1 Heat conduction through residual air in vacuum

Warm air heats up the inner chamber by fast molecules hitting it. The more air, the more heat transfer. The rule of thumb that was given by the manufacturer of the cryocooler was to keep the isolation vacuum pressure below 1×10^{-3} mbar in case a radiation shield is installed. This rule can be checked:
First consider heat conduction from the outer chamber to the radiation shield. A hot air molecule that was heated up at the outer chamber wall can either collide with the radiation shield or another air molecule. In both cases energy can be transferred. If the pressure in the outer chamber drops, the air density also drops and molecule to molecule collisions become less likely and the mean free path l of the molecules increases. If the distance d between the outer chamber walls and the inner chamber or radiation shield walls becomes significantly smaller than the mean free path ($d \ll l$), a molecule that was warmed up by the wall of the outer chamber will most likely not collide with another molecule before hitting the wall of the radiation shield. Therefore direct transfer of heat between both walls can take place. At 20°C, the mean free path of air is $l_{air}(P) = \frac{6.7\times10^{-5}}{P}$ m, where P is the pressure in mbar [94]. This yields $l_{air}(10^{-3}) = 6.7\,\text{cm}$. The distance between the walls of the radiation shield and the outer chamber is 6 mm, one order of magnitude below, therefore the $d \ll l$ approximation holds with pressures below 10^{-3} mbar.
The heat conduction through air between two surfaces in the $d \ll l$ regime does not depend on the distance between the surfaces since a molecule would not loose energy to any other object while flying between the surfaces. How much energy one molecule can transfer depends on how much energy gets transferred to it when it collides with the warm surface and how much energy it transfers to the cold surface upon hitting it. This can be described with the so-called thermal accommodation coefficient $\alpha = {E_{in}-E_{re}}/{E_{in}-E_w}$, where E_{in} is the energy flux on incident, E_{re} is the energy flux on reflection and E_w is the energy flux that would be achieved if the reflected molecules were emitted in thermal equilibrium with the surface [95].
We can approximate the walls of radiation shield and outer chamber as cylindrical. The heat conduction $\dot{q}_{air}$ in watts trough air of pressure P, measured at room temperature, between two cylinders with temperature difference ΔT is given by [75]:

$$\dot{q}_{air}(P) = 1.2 \cdot a_0 P A_i \Delta T, \tag{3.20}$$

where 1.2 is a factor that was determined for air [96], a_0 is related to the accommodation coefficients of the surfaces through $a_0 = {\alpha_i\alpha_o}/{[\alpha_o+(A_i/A_o)(1-\alpha_o)\alpha_i]}$, where α_i and α_o are the

thermal accommodation coefficients of the inner and outer wall and where A_i and A_o are the surface areas of the inner and outer surface.
It has been pointed out that for a rough estimation, which will not underestimate the heat conduction, $a_0 = 0.5/[1 + (A_i/A_o)0.5]$ can be used [75]. Inserting the geometries of our system and a temperature difference of 253 K yields an upper estimate of

$$\dot{q}_{air}(P) = 4053 \cdot P \tag{3.21}$$

At a pressure of 10^{-3} mbar, about 4 W heat load will be on the radiation shield. A few holes in the radiation shield will lead to transfer of a portion of that load to the inner chamber. If the isolation vacuum were at 10^{-3} mbar, we would have to calculate the heat load on the second stage carefully but since we designed the vacuum system to reach well below that pressure, this effort has not been undertaken. At a pressure of 10^{-6} mbar, only 4 mW of heat load will be on the radiation shield. Even if the complete heat load were present at the second cooling stage, it would be negligible. We can reach two orders of magnitude lower pressure therefore heat conduction through residual air can be neglected.

3.7.2 Radiative heat load

Thermal radiation can lead to a significant heat load on the second cooling stage. A radiation shield at the first cooling stage is required.
If the radiation shield were a perfect mirror, all radiation would be reflected back and the best shielding could be achieved. The emissivity of a surface ϵ is related to the reflectivity R via $\epsilon = 1 - R$. According to the Stefan-Boltzmann law, the power radiated from a surface $\dot{q}_{rad}$ at temperature T is related to the emissivity via $\dot{q} = \sigma\epsilon AT^4$, where σ is the Stefan-Boltzmann constant and A the surface area.
The heat exchange between two surfaces of temperatures T_{hot} and T_{cold} is the difference of the heat radiated from one and the heat radiated from the other and is given by [75]:

$$\dot{q}_{rad} = \sigma E A_i (T_{hot}^4 - T_{cold}^4) \tag{3.22}$$

A_i is the surface area of the inner(smaller) surface. E is a factor that depends on the emissivity of the involved materials and the involved geometry. For polished surfaces that feature mostly specular reflection, like stainless steel and copper with the surface quality that we used, E for the cylindrical geometry that is involved is given by [75]:

$$E = \frac{\epsilon_{cold}\epsilon_{hot}}{\epsilon_{hot} + \epsilon_{cold} + \epsilon_{hot}\epsilon_{cold}} \tag{3.23}$$

The emissvity of different materials can be found in the literature but not always for the required temperature. For stainless steel at room temperature it is $\epsilon_{steel}(293\text{K}) = 0.07$ [75]. For highly polished materials with a low electrical resistivity ρ, the emissivity can be calculated via [75]:

$$\epsilon = 265\sqrt{\frac{\rho}{\lambda_r}}, \tag{3.24}$$

where λ_r is the radiation wavelength in µm. It can be calculated with Wien's displacement law: $\lambda_r(T) = 2898\mu\text{m} \cdot \text{K}/T$. For the involved temperatures in our system, this yields: $\lambda_r(40\text{K}) = 72\,\mu\text{m}$ and $\lambda_r(4\text{K}) = 724\,\mu\text{m}$.
Since we are mostly interested in upper bounds of heat load and the resistivity of OFE copper at 77 K was found in [75] to be $0.21^{-8}\,\Omega\text{m}$ we took that number for our estimations. This would also allow the estimation to be conservative if the radiation shield heats up from the envisioned 40 K. This yields $\epsilon_{Cu}(40\,\text{K}) \approx 0.00197$. The radiation shield has a surface area of $0.39\,\text{m}^2$. Inserting all these numbers into equations 3.23 and 3.22 gives a radiative heat load from room temperature to the first cooling stage of

$$\dot{q}_{rad}(293\text{K} \rightarrow 40\text{K}) = 0.321602\,\text{W}. \tag{3.25}$$

This is well within the cooling power of the first stage.

In a next step we calculated the heat load on the second stage at 4 K that is induced by radiation from the radiation shield. The inner chamber is more or less a cube and, for the purpose of these calculations, can be approximated by a sphere [75], which means that equations 3.22 and 3.23 hold.
Many surfaces of the inner chamber that face the radiation shield are made out of stainless steel. Others are made of OFE copper. As a worst case approximation, we decided to calculate the heat load as if the whole chamber was made out of steel. The copper might not be perfectly polished and, over time, may show some oxidation, which leads to a rise in emissivity and therefore more radiation absorption.
The surface area of the inner chamber is $\approx 0.26\,\text{m}^2$. The resistivity of stainless steel at 4 K is $59 \times 10^{-8}\,\Omega\text{m}$ [97]. Plugging these numbers and the numbers for 40 K copper into equations 3.22 to 3.24 yields the radiative heat transfer from radiation shield to the inner chamber:

$$\dot{q}_{rad}(40\text{K} \rightarrow 4\text{K}) = 0.00006245\,\text{W}. \tag{3.26}$$

The radiation shield has holes in it through which room temperature radiation can hit the inner chamber. For estimating a worst case heat load, we assumed that a stainless steel object with a surface area of all holes combined is mounted to the second cooling stage and that the radiation shield does not exist. The same result would be reached if stainless steel tubes were mounted on the inner chamber in a way that they would extend outwards to fit perfectly in the holes of the radiation shield. This means that all radiation that reached through the holes actually hit the inner chamber. The surface area of all holes combined is $0.0075\,\text{m}^2$. Plugging these numbers and the numbers for 293 K steel into equations 3.22 to 3.24 yields the radiative heat transfer from radiation shield to the inner chamber:

$$\dot{q}_{rad}(293\text{K} \rightarrow 4\text{K}) = 0.0296249\,\text{W}. \tag{3.27}$$

A generous upper bound for the complete radiative heat load on the second cooling stage with a cooling power of 1.5 W is

$$\dot{q}_{rad}(\rightarrow 4\mathrm{K}) \approx 30\,\mathrm{mW}. \tag{3.28}$$

3.7.3 Heat conduction through electrical wires

Electrical signals are produced outside of the vacuum. Routing them into the chamber requires a physical connection from room temperature to the second cooling stage. There are two sources of heat that are related to wiring: Thermal conduction through the wire and resistive heating, also called Joule heating, of a wire, caused by a current that flows through it.
There are four different kinds of signals that need to be connected to the inner vacuum chamber (see chapter 4). To provide the trapping potential, DC voltages between -10 V and 10 V and RF voltages at around 100 MHz are needed. For addressing the hyperfine levels of beryllium ions, we use microwave currents of several Watts at around 1 GHz. The nanopositioning stages of the imaging system (see section 6.2.2) require peak currents of 1 A DC.

Joule heating occurs if some of the power of an electrical current is absorbed in a conductor. The heat $\dot{q}_J$ generated in a wire with resistance R by a current I is described by [75]

$$\dot{q}_J = I^2 R \tag{3.29}$$

Pouillet's law of resistivity states

$$R = \rho \frac{l}{A}, \tag{3.30}$$

where ρ is the specific resistance or resistivity of a wire, l its length and A it's cross section. Combining both equations yields:

$$\dot{q}_J = I^2 \rho \frac{l}{A} \tag{3.31}$$

To achieve minimum Joule heating it is advantageous to use short wires with a low resistivity and large cross section.

The amount of heat transported by thermal conduction $\dot{q}_{cond}$ through a wire between two surfaces of temperatures T_{hot} and T_{cold} is dependent on the thermal conductivity $\lambda(T)$ of the material, which is temperature dependent. In most electrical conductors, free electrons account for much of the heat transport and they roughly follow the empirical Wiedmann-Franz law [98]. It states that the ratio between thermal conductivity and electrical conductivity σ is proportional to the temperature. The proportionality constant is called the Lorenz number L and is approximately the same for most metals.

$$\frac{\lambda}{\sigma} = LT \Leftrightarrow \lambda = \sigma LT \tag{3.32}$$

The amount of conducted heat is given by [75]

$$\dot{q}_{cond} = \frac{A}{l} \int_{T_{cold}}^{T_{hot}} \lambda(T) dT \tag{3.33}$$

The electrical conductivity is the inverse of the electrical resistivity: $\sigma = 1/\rho$. Using this relation and inserting the Wiedmann-Franz law of equation 3.32 yields:

$$\dot{q}_{cond} = \frac{A}{l} \int_{T_{cold}}^{T_{hot}} \frac{1}{\rho} L T dT \tag{3.34}$$

To achieve minimum heat conduction it is advantageous to use a long wire with a high resistivity and a small cross section.
These requirements are opposed to the results found by examining Joule heating. For each individual type of electrical signal, an optimum combination of wire materials and geometries to minimize overall heat load has to be found.

DC lines

The trap that we use has 10 DC electrodes, which need 10 DC lines. The connector we use at room temperature and at the second cooling stage is a 25 pin D-Sub connector. Even though we only need 10 wires, we connected all of them to be able to use them later on with more complicated traps.
The DC lines do not have to carry any current as they have an open termination to ground and are low pass filtered (see section 4.5). The only current that might flow is parasitic AC current, which will be very small due to the strong filtering. Therefore Joule heating can be neglected and only thermal conduction has to be taken into account. A conducting material with a low thermal conductivity that is regularly used in cryogenic applications is constantan [75].
We have decided to use two wires for grounding. These are connected to the ground plane of the filter board around the trap (see section 4.6). Proper grounding might require, depending on future applications, some current to flow back out of the chamber via these cables. We therefore chose thin copper cables that have significantly less resistance than the constantan wires.
We assembled a 25 pin cable consisting of 23 constantan wires and 2 copper wires. The constantan wires are varnish isolated GVLZ087 wires from GVL Cryoengineering and have a diameter of 0.224 mm with and 0.193 mm without varnish. The copper wires are varnish isolated GVLZ175 wires from GVL Cryoengineering and have diameter of 0.28 mm with and 0.25 mm without varnish. The wires need to be thermally anchored to the first cooling stage before continuing on to the second stage. For calculating the heat conduction to the second stage, we assume perfect anchoring. The wire length from room temperature to the first stage is 0.16 m. The distance from the first to the second stage is 0.26 m.
For temperatures above 4 K, equation 3.33 can be written as

$$\dot{q}_{cond} = \frac{A}{l} \int_{T_{cold}}^{T_{hot}} \lambda(T) dT = \frac{A}{l} \left(\int_{4\,\mathrm{K}}^{T_{hot}} \lambda(T) dT - \int_{4\,\mathrm{K}}^{T_{cold}} \lambda(T) dT \right) \tag{3.35}$$

For the constantan cables, we used the thermal conductivity integrals starting at 4 K that are provided by [75]: $\int_{4\,\mathrm{K}}^{T_{40\,\mathrm{K}}} \lambda(T)dT = 0.312\,\mathrm{kW/m}$ and $\int_{4\,\mathrm{K}}^{T_{300\,\mathrm{K}}} \lambda(T)dT = 5.16\,\mathrm{kW/m}$. Inserting these values and the wire geometry into equation 3.35 yields:

$$\dot{q}_{cond}(\mathrm{con}, 300\,\mathrm{K} \rightarrow 40\,\mathrm{K}) \approx 0.89\,\mathrm{mW} \tag{3.36}$$

$$\dot{q}_{cond}(\mathrm{con}, 40\,\mathrm{K} \rightarrow 4\,\mathrm{K}) \approx 0.03\,\mathrm{mW} \tag{3.37}$$

For the copper cables, we used the data from the NIST cryogenic materials database [99], which provides the data for the wire's copper purity of RRR=100. The analytical function for the thermal conductivity is given by

$$\lambda_{RRR100} = 10^{\frac{2.2154 - 0.88068\tilde{T}^{0.5} + 0.29505\tilde{T} - 0.04831\tilde{T}^{1.5} + 0.003207\tilde{T}^{2}}{1 - 0.47461\tilde{T}^{0.5} + 0.13871\tilde{T} - 0.04831\tilde{T}^{1.5} + 0.0012810\tilde{T}^{2}}} \frac{\mathrm{W}}{\mathrm{m \cdot K}} \tag{3.38}$$

Inserting this function as well as the wire geometry in equation 3.33 and integrating from 40 K to 300 K and 4 K to 40 K yields:

$$\dot{q}_{cond}(\mathrm{Cu}, 300\,\mathrm{K} \rightarrow 40\,\mathrm{K}) \approx 49.1\,\mathrm{mW} \tag{3.39}$$

$$\dot{q}_{cond}(\mathrm{Cu}, 40\,\mathrm{K} \rightarrow 4\,\mathrm{K}) \approx 13\,\mathrm{mW} \tag{3.40}$$

The copper cables are not only used as grounding but also for supplying the up to 1 A of current to the nanopositioners that move the imaging objective around. There are three positioners with two cables each, making the total number of required current carrying DC lines seven. For future expansion, we designed the system to have three more installed, leading to a total number of 10 copper lines. We have 100 DC connections available through four 25 pin D-Sub connectors (see section 3.6). A total number of 90 constantan wires and 10 copper wires lead to a static heat load of

$$90 \cdot \dot{q}_{cond}(\mathrm{con}, 300\,\mathrm{K} \rightarrow 40\,\mathrm{K}) + 10 \cdot \dot{q}_{cond}(\mathrm{Cu}, 300\,\mathrm{K} \rightarrow 40\,\mathrm{K}) \approx (79.8 + 491)\,\mathrm{mW} \tag{3.41}$$

$$\Rightarrow \dot{q}_{cond,DC}(300\,\mathrm{K} \rightarrow 40\,\mathrm{K}) = 570.8\,\mathrm{mW} \tag{3.42}$$

$$90 \cdot \dot{q}_{cond}(\mathrm{con}, 40\,\mathrm{K} \rightarrow 4\,\mathrm{K}) + 10 \cdot \dot{q}_{cond}(\mathrm{Cu}, 40\,\mathrm{K} \rightarrow 4\,\mathrm{K}) \approx (3.1 + 130)\,\mathrm{mW} \tag{3.43}$$

$$\Rightarrow \dot{q}_{cond,DC}(40\,\mathrm{K} \rightarrow 4\,\mathrm{K}) = 133.1\,\mathrm{mW} \tag{3.44}$$

We assembled the wires in the following way: After cutting the wires to length, we removed the varnish by means of an ISOLEX Typ 02 from Fritz Diel GmbH. This is a motorized rotating blade wire stripper, with three quickly rotating blades with adjustable distance between them. We assembled a 25-pin D-Sub UHV compatible cable to provide two copper and 23 constantan wires. We used materials supplied by Allectra GmbH. One female PEEK connector (212-PINF-25-S) was mounted on each end. We folded the tip of each wire once by 180°, so that the effective cross section doubled and crimped it into a small crimp pin (212-PINM-25-S) that was fitted in the PEEK connector. The wires were then wound 10 times around and glued onto a copper bobbin which was anchored to the 40 K stage (see picture 3.10). We used a thermally conductive two-component epoxy with low outgassing properties: the epoxy resin LOCTITE STYCAST 2850FT

together with the catalyst LOCTITE CAT 24LV. The 160 mm long end was connected to a Sub-D feedthrough on a DN63CF flange at the outer chamber and the 260 mm long end was connected to a Sub-D feedthrough welded into a custom made flange at the inner chamber (see figure 3.7). The wiring between bobbin and inner chamber took place inside the radiation shield. A hole in the radiation shield, big enough for a 25 pin connector to pass though was later mostly covered with a copper sheet, leaving a hole only large enough for the wires, so room temperature thermal radiation would not pass through (see figure 3.10).

High frequency lines

To shield them from external noise, high frequency signals are usually routed through a coaxial line. A coaxial cable consists of an inner conductor that carries the signal and an outer conductor that shields the signal from external noise. Between both conductors is a dielectric that provides isolation. Most commercial coaxial cables also have an isolating outer layer. Some have additional layers of shielding. The geometric relations between the inner and outer conductor as well as the choice of materials define the impedance of the coaxial line. All signals that are supplied by our experimental control setup are routed through 50 Ω SMA cables to the outer chamber. To avoid impedance jumps and the inevitable signal reflections that they would cause, we chose to keep 50 Ω lines all the way to the ion trap (see chapter 4).
There are only a finite number of UHV compatible coaxial cables on the market. These feature different geometries and material combinations. We calculated the conductive as well as the resistive heat load for many available cables. The manufacturers usually provide a datasheet that includes remarks on the signal damping at different frequencies, including 1 GHz. Therefore we did not have to calculate this from first principles and could focus on calculating the conductive heat load. The damping comes into effect when we consider microwave pulses that are applied at a frequency around 1 GHz and with a certain pulse length, duty cycle and power. At the end, we decided to buy so-called semi-rigid coaxial cables from Microstock (UT141B-SS) with a beryllium copper inner and a stainless steel outer conductor. The label 'semi-rigid' seems to be more of a marketing term since bending these cables requires a lot of force and quickly leads to breaking of the outer conductor. For connecting cables to the various flanges inside the vacuum chamber, a bit of flexibility is needed. We decided to use small more flexible cables to connect the semi-rigid variant to the SMA feedthroughs and used the semi-rigid cable only as the main part between first and second cooling stage. We use a 25 cm long KAP50 cable from Allectra with SMA connectors on both ends to connect the room temperature feedthrough to the semi-rigid cable. The semi-rigid cable is then thermally anchored to the first cooling stage as shown in figure 3.13 and guides the signal to the inner chamber. A 3 cm long KAP50S cable from Allecta connects the semi-rigid cable to the inner chambers feedthrough. Both Allectra cables use copper as inner and outer conductor. The cooling power on the first stage is large enough to handle the heat load but the second stage does not have enough cooling power to allow for continuing copper lines. The semi-rigid cables were connectorized with Hubert+Suhner

11_SMA-50-3-15/111_N connectors. These connectors have a non UHV compatible rubber gasket inside, which we removed before mounting. We soldered them to both ends of the semi-rigid cable, using 315-LF-SOLDER-1M from Allectra as solder and Castolin 157 as flux. For better thermal contact, we applied Apiezon N grease to the cable and mounted it between two copper half-cylinders of 10 cm length. These were then mounted to the radiation shield with a 2 mm thick disk and a 22 mm long tube in between wire and shield. Both spacers are made out of Shapal because it is electrically isolating while still featuring a substantial thermal conductivity and it is also machinable with standard milling tools. We used a PTFE disk to electrically isolate screws from the radiation shield. This way the outer conductor of the cable was electrically isolated from the radiation shield to prevent ground loops.

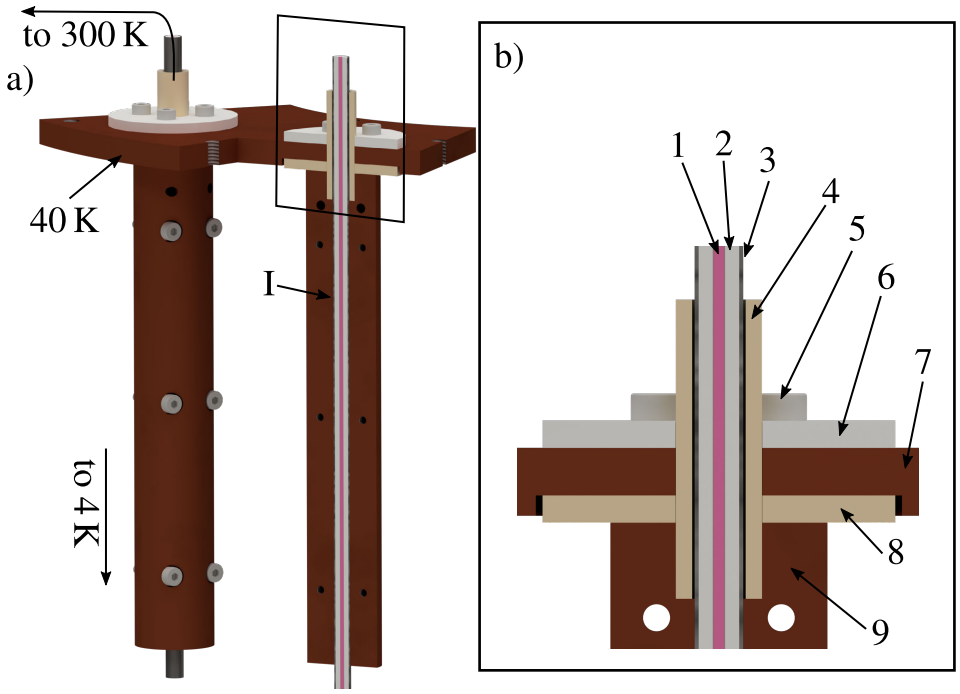

Figure 3.13: Thermal anchoring and electrical insulation of coaxial lines. The outer conductor has to be electrically isolated from the radiation shield to avoid ground loops. a) Overview of a pair of thermal anchors for high frequency wiring. Left: outer view, right: cross section. I: Coax-line, greased with Apiezon N and pressed between two copper half-cylinders. b) magnified cross section; 1: D=0.812 mm Ag coated BeCu center conductor, 2: D=2.985 mm PTFE dielectric, 3: D=3.581 mm 304 Stainless Steel outer conductor, 4: Shapal tube, 5: Mounting bolts, 6: PFTE spacer, 7: radiation shield on first cooling stage, 8: Shapal spacer, 9: OFE Cu half-tube
The Shapal spacers were chosen because they are electrically isolating, machinable and feature a moderate thermal conductivity.

To choose one of many possible cables, we calculated the heat load on the second cooling stage introduced by the presence of different cables, each with a length of 16 cm, with

Type	inner diameter	middle diameter	outer diameter	inner material	outer material	$\dot{q}_{cond,coax}$ ($\rightarrow 4\,\mathrm{K}$)
UT-085-SS-SS	0.511 mm	1.676 mm	2.197 mm	steel	steel	0.00098 W
UT-085-SS	0.511 mm	1.676 mm	2.197 mm	copper	steel	0.089 W
UT-085-AL	0.511 mm	1.676 mm	2.197 mm	copper	aluminum	0.19 W
UT-141-SS-SS	0.91 mm	2.985 mm	3.581 mm	steel	steel	0.002 W
UT-141 C	0.91 mm	2.985 mm	3.581 mm	copper	copper	1.6 W
UT-141B-SS	0.91 mm	2.985 mm	3.581 mm	BeCu	steel	0.0034 W

Table 3.1: Static heat load on the second cooling stage for several types of cables.

equation 3.33. The data for thermal conductivity for different materials was taken from the NIST cryogenic materials database [99]. Table 3.1 shows the results for different cables that can be bought from Microstock. The inner diameter is the diameter of the inner conductor. The middle diameter is the maximum diameter of the dielectric, which is PTFE in all cases. The outer diameter is the maximum diameter of the outer conductor. None of these cables feature outer dielectrics. We need at least four cables, three to connect the microwave electrodes and one for the RF voltage. We decided to design a system that can handle eight coaxial lines. The results show that cables with copper parts lead to the highest heat loads. Even one cable of the UT-141 C type would overpower the second stage with it's cooling power of 1.5 W at 4 K. The least impactful copper cable is the UT-085-SS. Eight of these would still provide a static heat load of 0.71 W, which can work if there is not much resistive heating.

In a next step, we combined the static conductive heat load $\dot{q}_{cond,DC}(\rightarrow 4\,\mathrm{K}) = 133.1\,\mathrm{mW}$ of the DC cables (see equation 3.44) with the radiative heat load of equation 3.28 $\dot{q}_{rad}(\rightarrow 4\mathrm{K}) \approx 30\,\mathrm{mW}$ and added for each cable type the static conductive heat load originating from eight coaxial lines $8 \times \dot{q}_{cond,coax}(\rightarrow 4\,\mathrm{K})$ from table 3.1. Subtracting this sum from the cooling power of 1.5 W at 4 K leaves us with the amount of resistive heating $\dot{q}_{tol}(\rightarrow 4\,\mathrm{K})$ that can be tolerated for each cable type.

$$\dot{q}_{tol}(\rightarrow 4\,\mathrm{K}) = 1.5\,\mathrm{W} - \dot{q}_{cond,DC}(\rightarrow 4\,\mathrm{K}) - \dot{q}_{rad}(\rightarrow 4\mathrm{K}) - 8 \cdot \dot{q}_{cond,coax}(\rightarrow 4\,\mathrm{K}) \qquad (3.45)$$

Table 3.2 shows the results. Some of the number are negative since the combined static heat load is more than 1.5 W. For the cables that show a positive tolerable heat load, we have looked at the damping that is given in the respective data sheet. As a measure of performance we determined the quotient of tolerable heat load and damping. The UT141B-SS cables with beryllium copper as a center conductor and a stainless steel outer conductor show the best performance and we proceeded our design with this type.

It is worth noting, that Microstock as well as other companies sell many more types of cables. We have looked at many more data sheets than these six cables. These six variants were chosen to be shown in this thesis because they represent cables that contain copper (Cu) and steel (St). These materials have been identified among the usually commercially available ones as the those with the lowest(St)/highest(Cu) ther-

Type	$\dot{q}_{tol}$ ($\rightarrow 4\,\mathrm{K}$)	damping at 1 GHz	quotient in W·m/dB
UT-085-SS-SS	1.33 W	4.13 dB/m	0.32
UT-085-SS	0.62 W	0.44 dB/m	1.4
UT-085-AL	-0.16 W		
UT-141-SS-SS	1.32 W	3.77 dB/m	0.35
UT-141 C	-11.52 W		
UT-141B-SS	1.31 W	0.83 dB/m	1.6

Table 3.2: Tolerable heat load originating from resistive heating af the cables and damping at 1 GHz as stated in the respective data sheets for the cables that feature a positive $\dot{q}_{tol}$. The quotient of both numbers serves as a measure of performance.

mal conductivity and the lowest(Cu)/highest(St) Joule heating. There are cables that contain exclusively one of these two materials and one cable with a combinations of both conductors.

Performance of the coaxial lines

We measured the input return loss along the entire transmission line, including the filter board's coplanar waveguide (see section 4.6), bonding wires and the trap chip (see figure 2.7) to be -2.2 ± 0.1 dB at 1.083 GHz. This measurement has been carried out with a Rhode & Schwarz ZNB8 vector network analyzer while the system was cooled down to 5 K. We have measured the insertion loss of all combined cables, leading to the filter board, at room temperature and at 1.083 GHz to be -1.16 dB. At lower temperatures this number should be smaller. Additionally including the coplanar waveguide, bonding wires and trap will increase it again. Since the current has to flow in and out of the trap, this number has to be roughly doubled, assuming mostly the same return path. This leads to the measured -2.2 dB or 39.5% power dissipation. This is the only variable source of heating in our system. Table 3.2 shows that we can work with an acceptable power dissipation of 1.31 W (UT-141B-SS), which leads, in the worst case scenario of all power being dissipated on the 4 K stage, to an acceptable average microwave input power of ≈3.4 W. To verify this number, we set the temperature controller that is connected to the second stage to 5 K, and measured the amount of heating that it puts out versus the microwave power we applied to the sideband electrode at 1.084 GHz. We ramped up the output power of our microwave source until the temperature controller did not need to heat the system to keep it at 5 K. We then measured the microwave power with the a Rhode & Schwarz FPC1000/FPC-B2 spectrum analyzer and a 40 dB attenuator (Mini-Circuits BW-N40W50+) to be 4.0 ± 1.0 W. This is in good agreement with the calculated value. For the implementation of multi-qubit gates, power would not be applied continuously, but only during gate operartion. Assuming the parameters of [23] (1122 µs pulse duration and ≈20 ms wait time between square-envelope gate pulses), it would be possible to apply peak powers of ≈64 W, to be compared to the 11 W used in [23], before reaching cooling power limits.

3.7.4 Cooling performance

The cooling power of our system at 4.2 K was specified to be 1.3 W when we bought the cryocooler. The cold head has a cooling power of 1.5 W. The 0.2 W difference was due to the low vibration interface construction. In the meantime we received an upgrade from the manufacturer which should give us more cooling power, closer to the 1.5 W at 4.2 K. The specs for the second cooling stage of the low vibration interface were not defined in the manuals that we received. The Sumitomo RDK-415D cold head data sheet states values around 20 W at 40 K, 40 W at 50 K and 60 W at 75 K. We do not expect this cooling power to transfer completely to the first stage of the low vibration interface since the upgrade did not include this section of the cold head or low vibration interface. We measured the time it takes to cool down the complete system with all cables attached to be approximately 15 h and 40 min. Figure 3.14 shows the temperature of both cooling stages over time during cooldown. The start temperature is at an unusual value of 308 K.

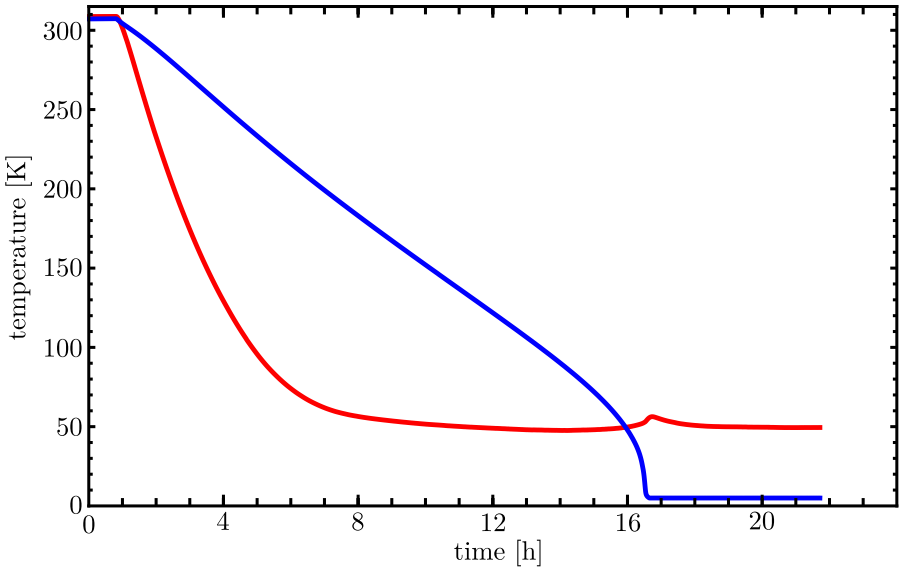

Figure 3.14: Cooldown of the complete system with all cables attached.

This measurement was taken after cooling water and subsequent air conditioning failure in the lab on a hot summer day. Our lab is usually at a temperature of 295 K stabilized to an accuracy of less than 1 K. The final temperature of the first cooling stage is 49 K. The final temperature of the second cooling stage is set to 5 K. A heating element that is attached to the second stage is controlled by a Cryocon 32 controller. A DT-607B0CU silicon diode sensor is attached to each cooling stage and to the controller. We set the temperature to 5 K because the low vibration interface does not perform well with liquid helium inside (see section 3.3). The bump that appears in the first stage temperature at the point in time when the second stage reaches the set-point of 5 K results from the heat that is deposited in the system by the temperature controller. An equilibrium is reached after about 4 h.

If we disable the temperature controller, we can reach 3.3 K at the second stage. There is liquid helium inside the exchange gas tube that transfers vibrations (see section 3.3), which makes this mode of operation less useful. If for some reason there is an application that demands 4.2 K without vibrations, one could shut of the cold head for a certain amount of time and let the liquid helium cool the inner chamber. Figure 3.15 shows the temperature over time during warm-up starting at 3.3 K. It shows that there is enough helium present to keep the inner chamber at a constant temperature of 4.2 K for about 23.5 min. Helium has a latent heat of vaporization of 2.589 $^{J}/_{m\ell}$ [75]. Assuming a static

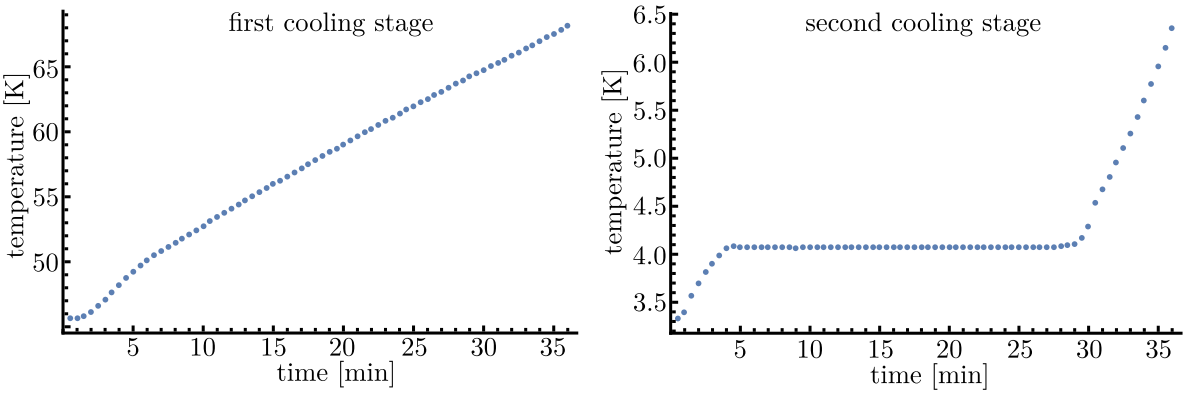

Figure 3.15: After cooling the system down to minimal reachable temperature, we switched off the cold head. Right: Temperature rise of the first cooling stage over time. Left: Temperature rise of the second cooling stage over time.

heat load of 190 mW, which can be inferred from equation 3.44 for the UT-141B-SS coaxial cables we use, leads to a vaporization of 0.0734 mℓ of helium per second. This means that 103 mℓ of helium were evaporated within 23.5 min.

Chapter 4

Electronics

This chapter contains descriptions of all electronics used during this thesis. That includes the experiment control setup, AOM driver electronics, microwave and radio frequency sources as well as magnetic field coils.

4.1 Experiment control setup

Everything in the experiment that has to be controlled by software is somehow connected to our experiment control system. We use it to switch all laser beams on and off (see section5.4), set AOM frequencies for the 313 nm beam line (see section 5.3), set voltages on DC trap electrodes, generate microwave pulses and detect signals from a photo-multiplier tube (PMT).
Hardware and software were developed at the NIST ion storage group. During his PhD work, Christopher Langer developed a field programmable gate array (FPGA) based experiment control system [100]. Other people who have contributed to the system at NIST include Manny Knill, Janus Wesenberg, Jason Amini, Ryan Bowler, Joe Britton and many others. The software was ported to work on Windows 7 by Sebastian Halama during his undergraduate work in our group [101].
The FPGA is a Nallatech Virtex-4 Xtreme DSP Kit. It is controlled by NIST's HFGUI software, expects a 32 bit Windows operating system and does not run stably on Windows 10 at the time of this writing. It handles all communication between PC and the rest of the control hardware. The original hardware featured 16 TTL outputs, 2 PMT pulse counting inputs, and up to 32 direct digital synthesizer (DDS) channels. It was upgraded by Ryan Bowler during his PhD work at NIST to contain arbitrary waveform generators [102, 103]. The FPGA requires a reference frequency of 62.5 MHz and the DDS boards require 1 GHz. Both frequencies are provided by a phase-locked loop (PLL) synthesizer, fed by a 10 MHz signal. The 10 MHz reference is currently provided by the reference output of a Rigol DG1022Z arbitrary waveform generator. For future improvements it is planed to receive a more stable 10 MHz reference from an oven controlled crystal oscillator, already bought by another experiment in the institute but not yet connected to ours.
The TTL outputs can switch between 0 V and 3.3 V in 16 ns. The PMT input channels can handle the same update rate. TTL's are used to switch all laser beams on and off and to chose between pre-set laser intensity levels.
The DDS modules are Nyquist-limited and can therefore generate sinusoidal signals up

to 500 MHz. They are used for providing AOM input frequencies and microwave signals. The arbitrary waveform generators can change their output voltage in steps of 0.3 mV and have an update rate of 50 MSamples/s. The output range is between -10 V and 10 V. These modules are used to apply voltages to DC trap electrodes.
For a more detailed description see references.

4.2 Microwave drive electronics

For driving hyperfine transitions in the $^9Be^+$ ground state, we use microwave fields in the frequency range from 850 MHz to 1530 MHz (see figure 2.2). We need to be able to pick or change a frequency, generate it and switch it on/off. The DDS modules of our experiment control setup fulfill the requirements of fast frequency setting and the TTL modules allow for fast switching. However the DDS modules can only generate up to 500 MHz signals (see section 4.1).
We therefore built three identical frequency quadrupling stages with TTL controlled switches, one for each microwave trap electrode. Figure 4.1 shows the signal routing through one of these stages. All parts, except for DDS and TTL modules, are available

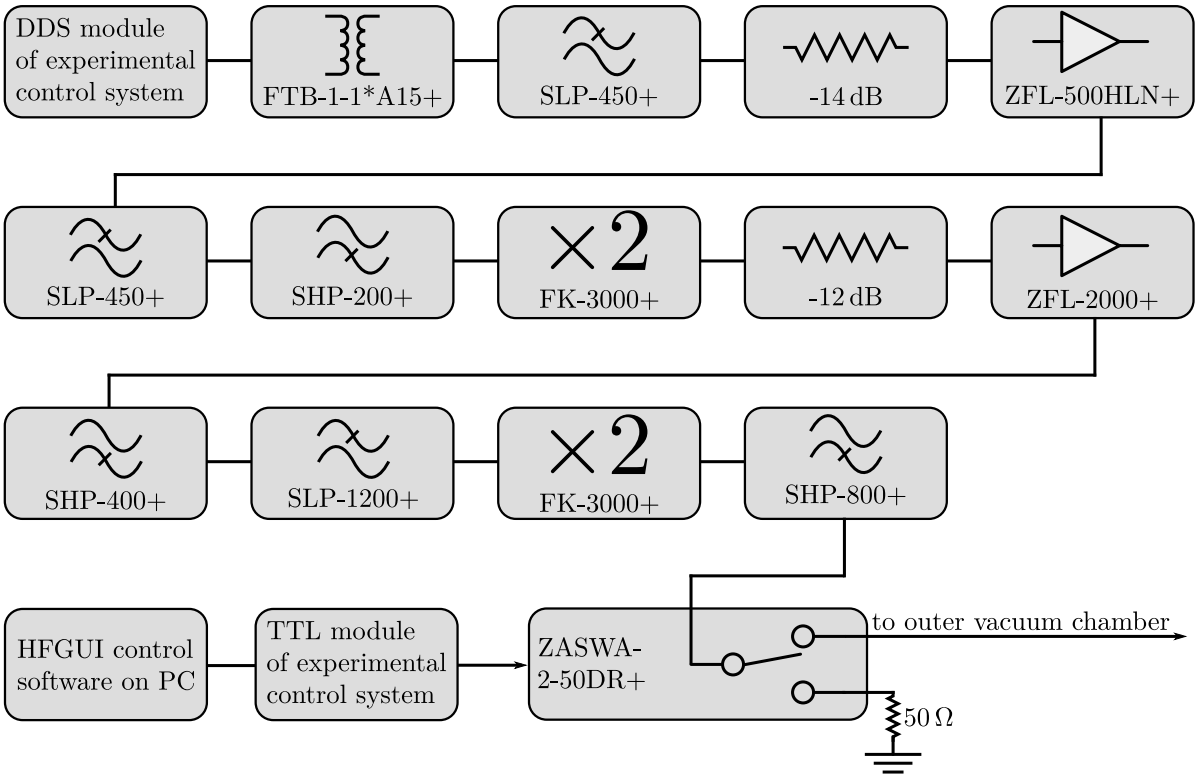

Figure 4.1: Signal routing within the microwave quadrupling stages. Mini-Circuits part numbers are shown, when applicable. In reality, one of the attenuators consists of a chain of multiple attenuating units.

from Mini-Circuits and their respective part numbers are shown. A FTB-1-1*A15+ transformer breaks potentially existing ground loops. There are two FK-300+ frequency doublers in series. The combinations of attenuators and amplifiers adjust the power levels according to the FK-3000+ specs. Combinations of high- and low-passes filter unwanted frequency components such as the Nyquist frequency, the DDS clock and others. A TTL controlled high-isolation ZASWA-2-50DR+ switch with rise/fall times of less than 20ṅs can be used to either send the microwave signals to the trap or dump them in a 50 Ω terminator.

For information about how the microwave signals are routed inside the vacuum chamber see section 3.7.3. For information about the design of the PCB filter board that guides all electrical signals to the trap, see section 4.6.

For sideband operations, it may be desirable to implement pulse shaping of the microwave pulses. This can lead to more robust quantum logic gates and to the suppression of undesired mirowave pseudopotential kicks on the ions. During his master thesis, Sebastian Halama developed a pulse shaping circuit that can be applied to shape the pulse envelope of the microwave signals [104]. Combined with the arbitrary waveform generator of our experiment control [102], this can be used to apply arbitrary pulse-forms to the microwave drive, as was successfully demonstrated at our sister-experiment at PTB and described in Henning Hahn's PhD thesis [47]. In this context, the pulse shaping setup was also outfitted with a feedback loop for more accurate amplitude control. In the future, this technique will also be employed in our experiment.

4.3 AOM diver electronics

We use six acousto-optic modulators (AOMs). Figure 5.2 shows, where in the setup they are placed.
Three of them, the two within the iodine spectroscopy setup and the one for the 313 nm power stabilization run on a set of fixed frequencies. We use Trinity Power TPI-1001 USB controlled frequency generators to supply these AOMs.
The other three AOMs are used for Doppler cooling and repumping. And although we only need to quickly change the frequency of the near-detuned Doppler cooling beam to transform it into the detection beam, the ability to scan frequencies of the other two beams as part of a experiment control sequence has proven valuable during the testing and calibration phase of the experiment. Therefore we chose to supply these AOMs with signals from the DDS modules of our experiment control setup.
Figure 4.2 shows the signal routing through the three different AOM supply chains, powered by TPI-1001 signal generators. The output power and frequency of each TPI-1001 signal generator is controlled via USB by the Synth Machine software from Trinity Power. Potentially existing ground-loops are broken by inner-outer DC blocks and the signal is amplified by a Mini-Circuits ZHL-1-2-WS+ amplifier. In case of the 40 MHz frequency modulation AOM of the iodine spectroscopy setup (see section 5.3.4), we connect the

lock-in amplifier to the modulation input of the TPI-1001-B. In case of the 313 nm power stabilization setup, we place a Mini-Circuits ZX73-2500M-S+ voltage controlled attenuator between the DC block and the amplifier. It's control voltage is the output of an FPGA based PID controller [105, 106] that monitors the laser power (see also section 5.3). Figure 4.3 shows the signal routing through the three different AOM supply chains,

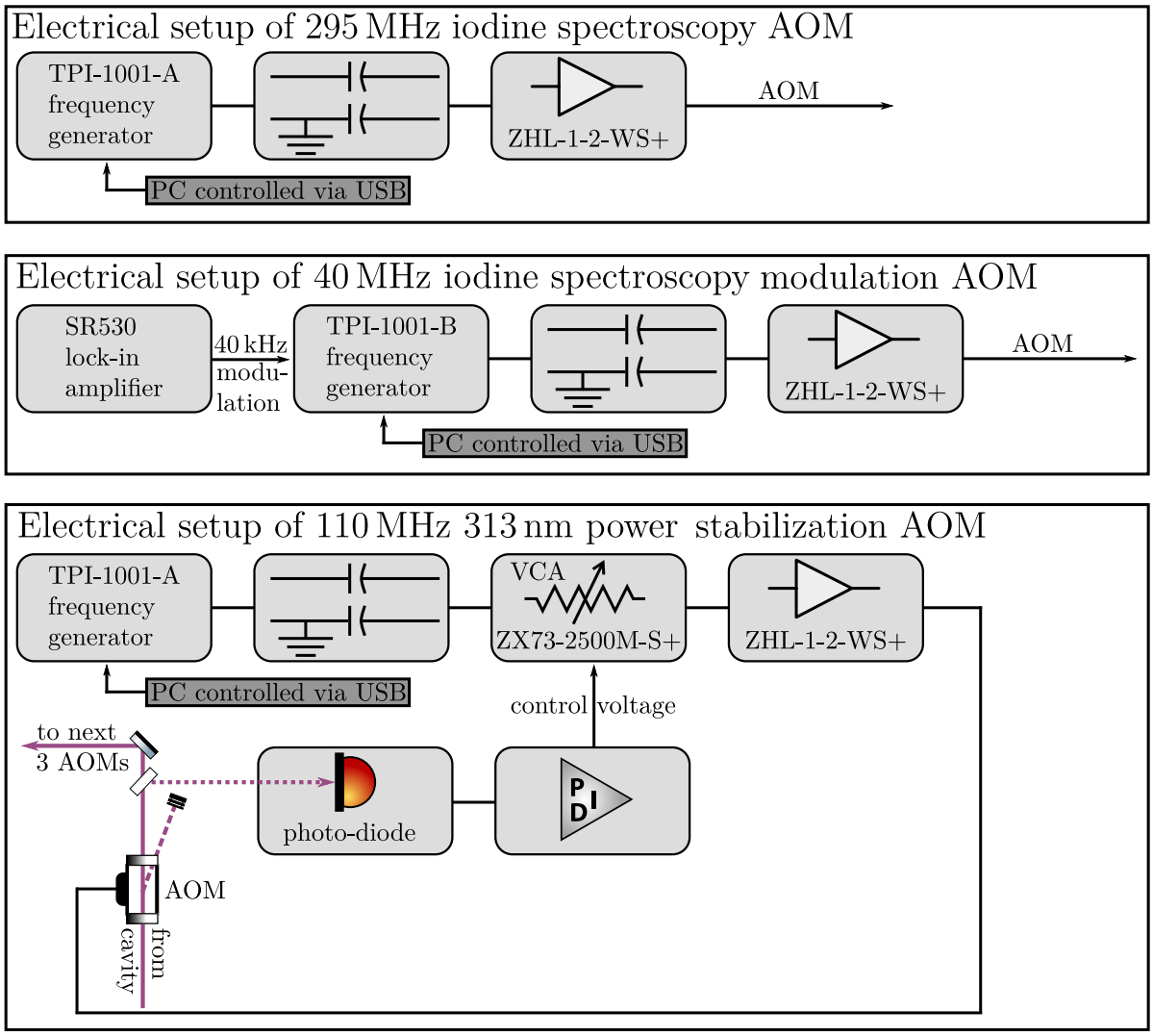

Figure 4.2: Signal routing for AOMs, powerd by Triniy Power TPI-1001 frequency generators. Mini-Circuits part numbers are mentioned, where applicable. Laser beam, photo-diode and PID controller taken from figure 5.2.

powered by DDS modules. When aligned to maximum power, the laser intensity is way above saturation intensity. As an example, we can reach more than 1 mW of near detuned Doppler cooling light at the ions, but the saturation intensity is reached at 5.4 µW, about three orders of magnitude lower. Therefore we need a method of decreasing laser power. We use a USB controlled attenuator, a Vaunix Lab Brick LDA-102, to lower AOM rf

input power to artificially decrease diffraction efficiency and therefore laser power at the ions to a desired level. Each rf chain features fixed attenuators and amplifiers to adjust power levels. The combinations are chosen such that each AOM does receive its maximum rated power level if the corresponding Lab Brick is at it's minimum attenuation. In case of the far detuned Doppler laser, we can switch the laser power between two preset values. The Lab Bricks have a fall/rise time that is too slow. So instead of changing the attenuation in a Lab Brick, we use a fast Mini-Circuits ZASWA-2-50DR+ high-isolation switch with a falls/rise time of less than 20 ns to switch between attenuation presets. All AOM setups feature inner-outer DC blocks for breaking potentially existing ground loops. Each AOM is mounted on a Thorlabs KM100PM/M platform mount to allow for tilting during alignment. Two aluminum adapter plates connect AOM and mount. Non electrically but thermally conductive pads (Kerafol 86/600) are placed between the two aluminum adapters, thereby eliminating ground-loops. We use plastic screws for connecting the adapters. While thermal conductivity from the AOM through these adapters, the mount and post to the optical table is sufficient to dissipate heat from most AOMS, the Gooch & Housego I-M110, used for the far detuned Doppler beam, is in danger of overheating. The mount-side aluminum plate of this AOM is connected with copper braids, crimped to 6 mm diameter cable lugs, to the optical table to allow for more heat flow into the table to prevent the AOM from overheating. The braids are flexible enough to allow for AOM tilting.

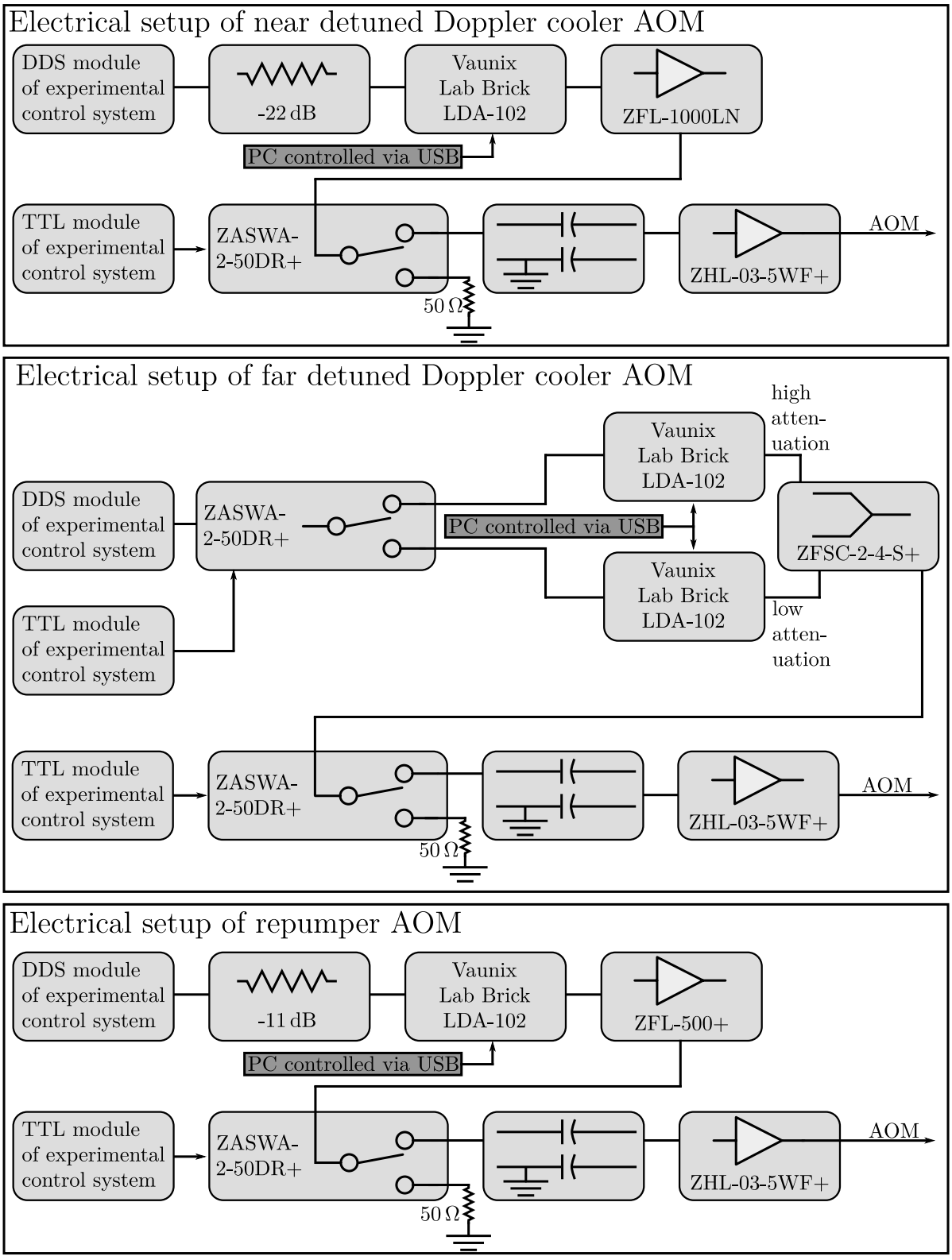

Figure 4.3: Signal routing for AOMs, powerd by DDS modules. Mini-Circuits part numbers are mentioned where applicable. See text for description.

4.4 Radio-frequency setup

Our trap requires a radio-frequency drive between 90 and 110 MHz. A HP 8640B frequency generator delivers the drive frequency and is connected to a -16 dB attenuator and a Mini Circuis ZHL-2-12+ amplifier. This hardware lacks the output voltage to directly drive the trap. We have built a helical resonator, mounted to the outside of the 5 K cold inner vacuum chamber for voltage step-up. The cryogenic UHV feed-lines that lead to the resonator are described in section 3.7.3.
A male SMA tip is soldered to the resonator's output wire and connected to the center pin of an Allectra 242-SMAD50 SMA feedthrough, guiding the signal to the inner vacuum chamber. Between resonator and feedthrough, we have constructed a copper shielding that is at least 4 mm away from the wire to reduce capacitance. Another wire with male SMA tip on one end and an MCX connector on the other end guides the signal to the filter board. A bare wire is used instead of the usual coaxial lines to reduce capacitive load on the resonator as it would pull the resonance frequency too much. We expect the copper body of the inner vacuum chamber to act as a shielding from outside noise, so a coaxial line is not strictly required inside. On the filter board, a 0.8 mm wide gap is used between rf guide and ground plane to minimize line-capacitance. For more information about the filter board layout, see section 4.6.
We have designed the resonator, following design guides for helical resonators [107, 108, 109]. With a cylinder height of 42.1 mm, an inner diameter of 28 mm and an outer diameter of 31 mm, we chose a very compact design. Apart from its size, it has no distinctive advantages over larger helical resonators. The small size is due to limited space at the second cooling stage. During early design stages, it was deemed feasible to build an amplification circuit on the outside of the vacuum chamber [104] and the possibility of a cryogenic resonator was only a backup solution. As it turned out, the proposed technology was not mature enough and we opted for the resonator as presented here. Figure 4.4 shows a rendering of the assembled resonator. A cylindrical shield houses a helix that is electrically connected to the center of the flat top of the cylinder. The helix is made out of a 1 mm thick oxygen free (OFE) copper wire, wound around a PTFE support cylinder. The PTFE cylinder has an inner diameter of 5 mm and an outer diameter of 8.2 mm. It features a 0.5 mm deep, 1 mm wide helix-bevel on the outside to house the wire. The helix has a diameter of 16 mm, a height of 23 mm and a pitch of 5.75 mm, leading to 4 windings. At the end of the helix, the wire is guided through a hole in the lid that is closing the cylindrical shield. A small PFTE ring prevents electrical contact of wire and shield.
The signal, produced by the HP 8640B, is connected to the outer vacuum chamber via an SMA feedthrough with subsequent cryogenic wiring to the resonator (see section 3.7.3). The SMA wire shielding is connected to the resonator shielding and a wire with a male SMA pin soldered to it, picks up the signal on the inside. This incoupling wire is a varnish isolated 0.5 mm diameter copper wire. We used an ISOL-EX Typ 02 rotating blade wire stripper to remove varnish at one end of the wire. We connected the male SMA pin with Allectra's 315-LF-SOLDER-1M vacuum compatible solder. The varnished wire is wound once around the helix, with the varnish touching the inner wall of the shielding.

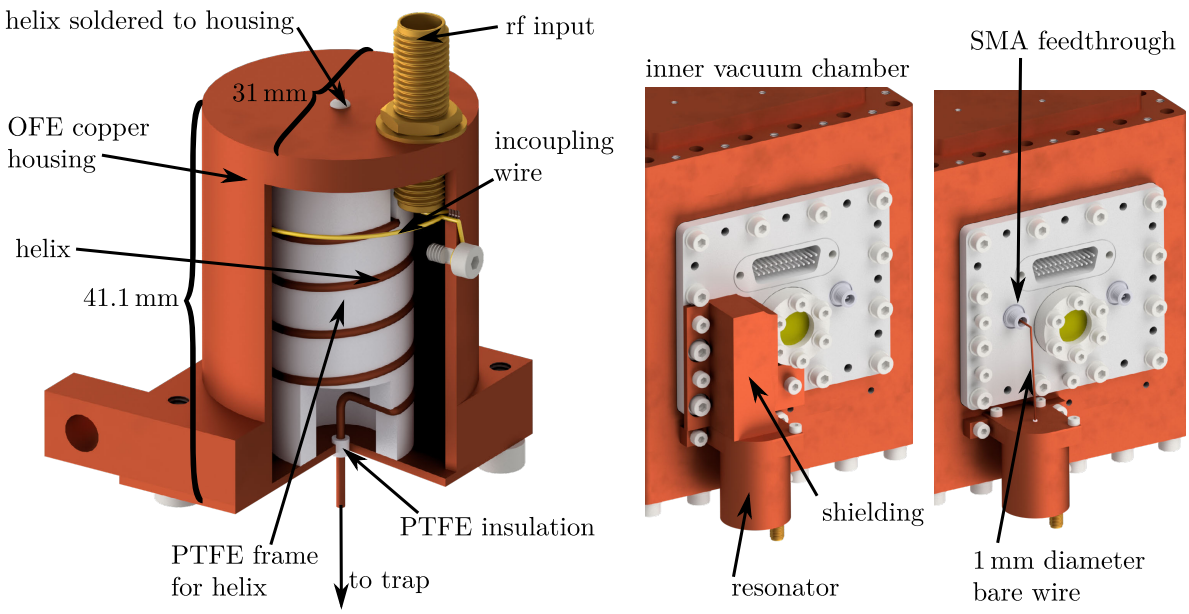

Figure 4.4: Left: Cut-view rendering of the rf resonator. Middle: Resonator mounted on the inner vacuum chamber. Right: Copper shielding removed to make wire visible. A male SMA tip is soldered to the wire and plugged into the SAM feedthrough.

It is guided to the outside of the cylinder through one of two M2 threaded holes. A screw in the other hole is used to fix the wire to the outside wall. To adjust incoupling into the resonator, we loosen the screw and carefully push or pull the wire. This can't be done at 5 K, since we have no means of reaching the incoupling wire while under vacuum. We adjust it at room temperature while everything, including outer and inner vacuum chamber as well as trap are electrically connected. We connect a Rohde&Schwarz ZNB8 Vector Network Analyzer to the outer chamber's SMA feedthrough that leads to the resonator. We measure the reflected power or S_{11} parameter over frequency. On resonance, a dip can be observed and the incoupling, measured in dB, is shown. We can maximize the incoupling at room temperature by adjusting the wire. During cooldown, the incoupling changes. If it was at it's maximum at 300K, it won't be at it's maximum at 5 K. It happened a few times, that the incouplig was so bad at cryogenic temperature, that we had to warm up again and redo the incoupling. Fabian Ude did extensive trails during his master thesis work to find a sweet spot to which we can adjust the incoupling at room temperature [110]. This has proven to be very helpful but far from reliably repeatable. We have converged on the technique of adjusting the incoupling to a value that is not too far from the maximum and cooling it down. We can monitor the resonance during cooldown. If incoupling decreases, right from the start, we know, that it will drift in the same direction until the final temperature is reached. We than abort cooldown and readjust. If the incoupling starts to improve during cooldown, we do not stop early. The incoupling will eventually reach its maximum, most likely before the final temperature is reached, and decrease again as the temperature falls further. Prepared this way, most of

the time the resonator is not perfect but usable.

We have measured loaded quality-factors, while the resonator was at 5 K, between $Q_{load} \approx 20$ for sub-optimal incoupling and $Q_{load} \approx 300$ for good incoupling. We currently run the resonator at $Q_{load} = 88.3$ with an incoupling of -8.05 dB. For detailed information about q-factor measurements, see section 4.4.1.

During normal operations, we monitor input and reflected output power levels with a self-built device near the outer vacuum chamber feedthrough at air-side. It contains a Mini-Circuits ZFBDC20-62HP-S+ bidirectional coupler and two ZX47-20LN-S+ power detectors. The bidirectional coupler features a directivity of 25 dB and a coupling factor of 20 dB. It picks up incoming rf-voltage and directs a small portion of it to one of the power detectors. It does the same with the return signal, coming from the resonator and directs it to the second power detector. The power detectors put out a voltage, that is depending on the input power. Those two voltages are detected by an Arduino Nano with an LC display attached. In case of small frequency drifts, we can adjust the HP 8640B's output to minimize return power.

Comparing our resonator with larger ones, like the one our group uses at PTB, it becomes clear, that it's small size makes it more difficult do adjust the incoupling. The set of acceptable incoupling wire positions is very small and it is hard to achieve an optimum. During cooldown, slight geometrical changes due to shrinking and slight electrical changes due to lower resistivity at cryogenic temperatures make it hard to predict a useful incoupling wire geometry. In a future design, a larger resonator would significantly decrease the adjustment work-load.

4.4.1 Determining the resonator's q-factor

The quality- or q-factor Q is the ratio of peak energy stored in the resonator and average dissipated energy per cycle, if driven at resonance frequency. As shown below in section 4.4.2, it can be used to determine required rf input power levels to reach desired trap electrode rf voltages.
For a series RLC circuit, it is:

$$Q = \frac{1}{R}\sqrt{\frac{L}{C}} \tag{4.1}$$

More generally, it is the ratio of the resonance frequency of an oscillating system and the full width at half maximum (FWHM) of it's resonance curve:

$$Q = \frac{\omega_0}{\mathrm{FWHM}} \tag{4.2}$$

The Rohde&Schwarz ZNB8 network analyzer, can measure the reflected power and plots it over frequency with respect to the input power. This is called the S_{11} parameter and is usually measured in dB. The network analyzer can show the q-factor, corresponding to a resonance curve. The software determines the two -3 dB points of a resonance curve

and takes the frequency difference to be the FWHM. Then it determines the minimum and the corresponding frequency ω_0. Then it calculates Q acording to equation 4.13.
This simple approach of determining Q relies on an approximation, the two assumptions of which are: 1) The baseline is at 0 dB, meaning that there is negligible Ohmic loss R_0 and a negligible frequency dependent loss coefficient Ω on the transmission lines: $R_0 \approx 0$ and $\Omega \approx 0$. 2) The incoupling is near perfect, so that $-3\,\mathrm{dB} \approx 0.5$ is actually the middle between baseline $0\,\mathrm{dB} = 1$ and the minimum near $-\infty\,\mathrm{dB} \approx 0$.
In our setup, both assumptions are not fulfilled as the feed lines within the vacuum chamber show significant Ohmic losses R_0 as well as frequency dependent losses Ω, due to unconventional but necessary material selection, detailed in section 3.7.3

A helical resonator combined with an ion trap can be modeled as a series RLC circuit [109].
The impedance Z of an RLC circuit with Ohmic resistance R, inductance L and capacitance C is dependent on the frequency ω and is given by:

$$Z(\omega) = i\omega L + \frac{1}{i\omega C} + R \tag{4.3}$$

Let Z_0 be the impedance of the transmission line. The voltage reflection coefficient of a transmission line is given by [111]:

$$V_{refl} = \frac{Z - Z_0}{Z + Z_0} \tag{4.4}$$

Since the network analyzer measures power and not voltage, squaring V_{refl} gives the power reflection coefficient:

$$P_{refl} = \left|\frac{Z - Z_0}{Z + Z_0}\right|^2 \tag{4.5}$$

If both impedances are matched, $Z = Z_0$, all power is transmitted from the transmission line into the resonator and perfect incoupling would be achieved.
By defining the resonance frequency $\omega_0 = \frac{1}{\sqrt{LC}}$ as well as factors $\gamma = \frac{R}{L}$ and $\gamma_s = \frac{Z_0}{L}$ and after many steps of rearranging equations, while assuming $\omega, R, Z_0, C, L > 0$ we can write:

$$P_{refl} = \frac{(\gamma - \gamma_s)^2\omega^2 + (\omega^2 - \omega_0^2)^2}{(\gamma + \gamma_s)^2\omega^2 + (\omega^2 - \omega_0^2)^2} \tag{4.6}$$

On resonance, $\omega = \omega_0$, the reflected power is

$$P_{refl}(\omega = \omega_0) = \frac{(\gamma - \gamma_s)^2}{(\gamma + \gamma_s)^2} \tag{4.7}$$

On resonance, an RLC circuit's impedance is real, $Z(\omega_0) = R$. If impedances are matched, $R = Z_0 \Leftrightarrow \gamma = \gamma_s$ holds and no power is reflected.
Equation 4.6 describes a Lorentzian line shape with FWHM of $(\gamma + \gamma_s)$. Taking into account that the measured S_{11} is usually given in dB, it follows that

$$S_{11} = 10\log_{10}\left(\frac{(\gamma - \gamma_s)^2\omega^2 + (\omega^2 - \omega_0^2)^2}{(\gamma + \gamma_s)^2\omega^2 + (\omega^2 - \omega_0^2)^2}\right) \tag{4.8}$$

Taking Ohmic losses R_0 as well as frequency dependent losses Ω into account, S_{11} reads:

$$S_{11} = 10 \log_{10} \left(\frac{(\gamma - \gamma_s)^2 \omega^2 + (\omega^2 - \omega_0^2)^2}{(\gamma + \gamma_s)^2 \omega^2 + (\omega^2 - \omega_0^2)^2} \right) - \Omega\omega - R_0 \tag{4.9}$$

We can use this model to determine Q. The combination of trap electrodes, SMA feedthrough and wiring act as a capacitive load on the resonator. Since the trap was connected to the resonator during this measurement and the we have modeled the combination of trap, wiring and resonator as a series RLC circuit, the model actually determines the loaded q-factor Q_{load}

Figure 4.5 a) shows a measurement of the S_{11} parameter, done at 5 K with all cables and trap connected. Least-squares fitting of equation 4.9 to the data yields:

$$\begin{aligned}
\omega_0 &= 2\pi \cdot 99.37\,\text{MHz} \\
\gamma &= 2\pi \cdot 0.79\,\text{MHz} \\
\gamma_s &= 2\pi \cdot 0.34\,\text{MHz} \\
\Omega &= 9.15 \times 10^{-9}\,\frac{\text{dB}}{\text{Hz}} \\
R_0 &= 0.474254\,\text{dB} \\
S_{11}(\omega_0) &= -8.05\,\text{dB} \\
Q_{load} &= \frac{\omega_0}{\text{FWHM}} = \frac{\omega_0}{\gamma + \gamma_s} = 88.3
\end{aligned}$$

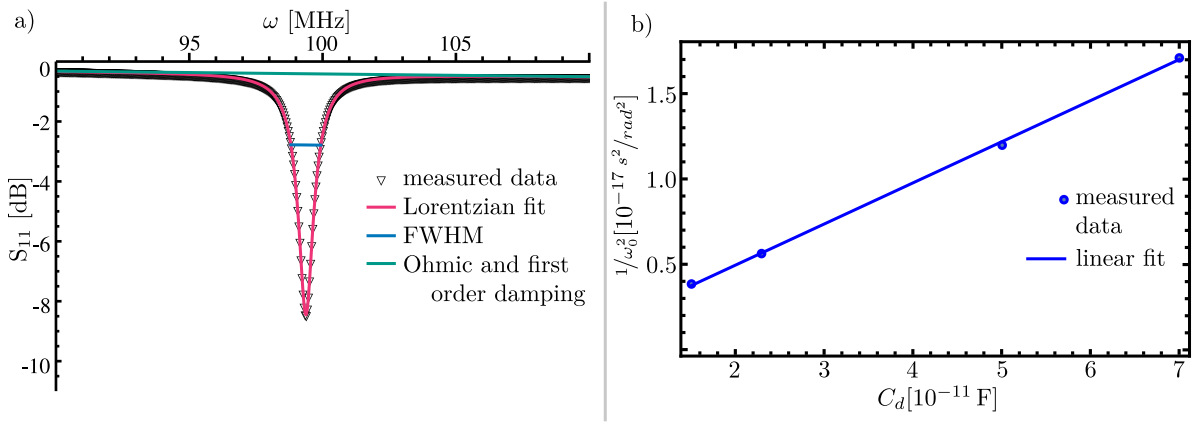

Figure 4.5: a) S_{11} parameter of the loaded resonator. Notice, that the base line (green) is not at 0 dB and that the FWHM is not at the -3 dB level which makes the network analyzer unable to determine Q correctly. The baseline is also tilted because of frequency dependent damping effects in the feed lines.
b) Auxiliary plot to determine trap capacitance: The resonator was loaded with several dummy capacitances C_d and the resulting resonance frequency was measured.

Now we determine the other two involved q-factors, the q-factor of the unloaded resonator

Q and the q-factor of the source Q_s that includes generator and transmission lines. Modeling all involved parts as series RLC circuits, on resonance the combined q-factors of unloaded resonator and source give Q_{load}:

$$\frac{1}{Q_{load}} = \frac{1}{Q} + \frac{1}{Q_s} \tag{4.10}$$

The coupling factor β describes how well the resonator is matched to the transmission line. This is true for the impedances as well as for the q-factors. The coupling factor would be

$$\beta = \frac{Q}{Q_s} = \frac{Z_0}{R} = \frac{\gamma_s}{\gamma} \tag{4.11}$$

In case of perfect matching, $\beta = 1$ holds. Combining equations 4.10 and 4.11 it follows for perfect coupling on resonance:

$$Q = 2Q_{load} \tag{4.12}$$

As our incoupling is only -8.05 dB, we cannot claim perfect matching and have to determine Q in a different way: Using the above values for γ and γ_s and inserting them in equation 4.11 yields:

$$\frac{Q}{Q_s} = \frac{\gamma_s}{\gamma} = 0.4327 \Rightarrow Q_s = 2.310945Q, \tag{4.13}$$

which means that we run an undercoupled resonator. Inserting this in equation 4.10 yields:

$$Q = 1.43272Q_{load} = 127.083 \tag{4.14}$$

4.4.2 Determining the required rf input power

In the previous section, we modeled the combination of resonator and trap as a series RLC circuit to determine the loaded q-factor Q_{load}. In this section, we exclude specifically the trap from the model, effectively splitting the capacitance C of section 4.4.1 into a resonator(plus wiring) and a trap-capacitance. To avoid confusion with previous nomenclature, let R_r, L_r and C_r be resistance, inductance and capacitance of the resonator and C_t be the trap capacitance. Then ω_0 reads:

$$\omega_0 = \frac{1}{\sqrt{L_r(C_r + C_t)}} \tag{4.15}$$

From the measurement of Q_{load}, we know ω_0 but cannot extract C_r and L_r as they are not directly accessible from fitting parameters.
At room temperature, we have connected several capacitors to the resonator, effectively acting as dummy trap capacitances C_d, and measured the corresponding resonance frequencies. Assuming no change in L_r and plotting $\frac{1}{\omega_0^2} = L_rC_r + L_rC_d$ over capacitance C_d yields the linear relation shown in figure 4.5 b). The slope of the linear fit

is equivalent to $L_r = 241 \pm 4\,\mathrm{nH}$ and the intersection with the y-axis is $L_r C_r$, yielding $C_r = 0.577 \pm 0.75\,\mathrm{pF}$.
Inserting these results and the measured resonance frequency of $\omega_0 = 99.37\,\mathrm{MHz}$ into equation 4.15, yields $C_t = 10.06\,\mathrm{pF}$.

Keeping in mind, that equation 4.1 is concerned with the unloaded q-factor, using the relation $C = C_r + C_t$ and assuming that the resistance of the trap is small compared to R_r, the resistance of the resonator is:

$$R_r = Q\sqrt{\frac{L_r}{C_r + C_t}} \tag{4.16}$$

Inserting all so far determined values yields $R_r = 19.124\,\mathrm{k\Omega}$.
Our calculated trapping potential requires an rf voltage amplitude of $U = 100\,\mathrm{V}$. To calculate the average rf power we need to couple into the resonator to achieve this voltage at the trap, we convert it to an effective or rms voltage of $U_{rms} = {}^{100\,\mathrm{V}}/_{\sqrt{2}} \approx 70.7\,\mathrm{V}$. Converting this voltage into power yields:

$$P_W = \frac{U_{rms}^2}{R_r} = 261\,\mathrm{mW} \tag{4.17}$$

The HP 8640B frequency generator can only set dBm as output power. Converting mW to dBm:

$$P_{dBm} = 10\log_{10} P_W = 24.1739\,\mathrm{dBm} \tag{4.18}$$

We can set our input power to P_{dBm} and are able to trap. If in future traps more rf voltage is needed, and power dissipation becomes a concern, we can either improve the resonator by fine-tuning of the incoupling wire to achieve a better q-factor or build a new one from scratch. An alternative might be to build a lumped-component rf-resonator, close to the trap, like the one shown to be working at the University of Innsbruck [112]. Another possibility is to use tunable varicap diodes at cryogenic temperature to achieve better impedance matching after cooldown, as was also proposed in the mentioned paper [112].

4.5 DC voltage setup

The trap has 10 DC electrodes (see figure 2.7 and section 2.3). Although a finite set of voltages is sufficient to trap ions, the ability to apply flexible voltage configurations in a fast and controllable way is required for experiments involving ion transport or the rotation of trap axes. The experiment control system features arbitrary waveform generators, that can supply voltages between -10 V and +10 V (see section 4.1).
We need to make sure that noise on these electrodes is suppressed so it does not affect the ions. Especially at the trap frequencies, high noise suppression is necessary. The arbitrary waveform generators have an SMA output. We connect them to a box that contains a Mini-Circuits LPF-B0R3+ filter on every lane. We call this the filter box. For

its location on the outer vacuum chamber, see figure 4.9. These low-pass filters have an insertion loss of at least 45 dB for the axial trap frequency at least 84 dB for the radial trap frequencies. The outputs of all filters are connected to the same 25 pin D-sub connector, bolted to the box's wall. It is plugged into a D-sub feedthrough on a flange on the outer vacuum chamber. Constantan wires guide the signal to the inner vacuum chamber and to the filter board (see section 4.6). A final 1 kΩ, 820 pF RC filter stage can be found on the filter board directly before the bonding wires guide the signal to the trap electrodes. This filter has a cut off frequency of 2.1 MHz and an attenuation of ≈-1.1 dB at the axial and of ≈-7.7 dB at the radial trap frequencies. Its main purposes is to short out any rf pickup on the DC electrodes to ground; for that purpose, the capacitors must be located as close to the trap electrodes as possible. The 1 kΩ resistor is included to provide a well-defined filter behavior.
During trap operations, it can be helpful, to expose the ions to trap frequency signals, e.g. to determine trap frequencies. By 'tickling' a trapped ion at one of it's motional frequencies, it can be heated up. This heat-up can be observed as a drop in fluorescence on the detection beam, as the ions are Doppler-shifted out of resonance. We can apply an AC voltage to DC electrode DC_2:
A TTL output and a DDS module of the experiment control system are connected to a Mini-Circuits ZASWA-2-50DR+ TTL controlled switch. One switch output is connected to a separate tickle-input in the filter box. A Mini-Circuits ADT1-1+ transformer acts as a ground-loop breaker. On the secondary side, a capacitor, connected to the output of a LPF-B0R3+ filter couples the DDS signal onto the DC_2 line, acting as a bias tee. We can set the DDS frequency and also control the TTL switching pulse in software.

4.6 Crygenic filter board

The filter board surrounds the trap. It guides all electrical signals to bonding wires, that are attached to the trap electrodes on the chip. Pictures of the filter board, taken during the inner vacuum chamber assembly, are shown in figure 4.6. The filter board has to be UHV compatible, work under crygenic conditions and feature a low loss tangent for high frequency signals. We chose a 1.6 mm thick Rogers Corp RO4305B board as a substrate. Conductors on both sides (layers) of the board are 80 µm thick and gold coated. The board was designed by us and produced by CONTAG AG. The filter board layout is shown in figure 4.7. The trap-chip is glued to an OFE copper block. That block has dimensions $49 \times 49 \times 7.9\,\mathrm{mm}^3$, a compromise between available space, thermal properties and mechanical stability. In the middle of the block, a 1.63 mm high, $4.75 \times 4.75\,\mathrm{mm}^2$ square platform rises above the surface, the footprint of which matches that of the trap-chip. The 0.611 mm thick trap is glued onto that block, raising the trap surface 2.241 mm above the copper block. A $5.21 \times 5.21\,\mathrm{mm}^2$ hole in the filter board fits around the trap platform. The filter board is 1.58 mm thick, leaving the trap surface 0.661 mm above the filter board. This height has to be bridged with bonding wires, which was done in the PTB clean room facility by Amado Bautista-Salvador.

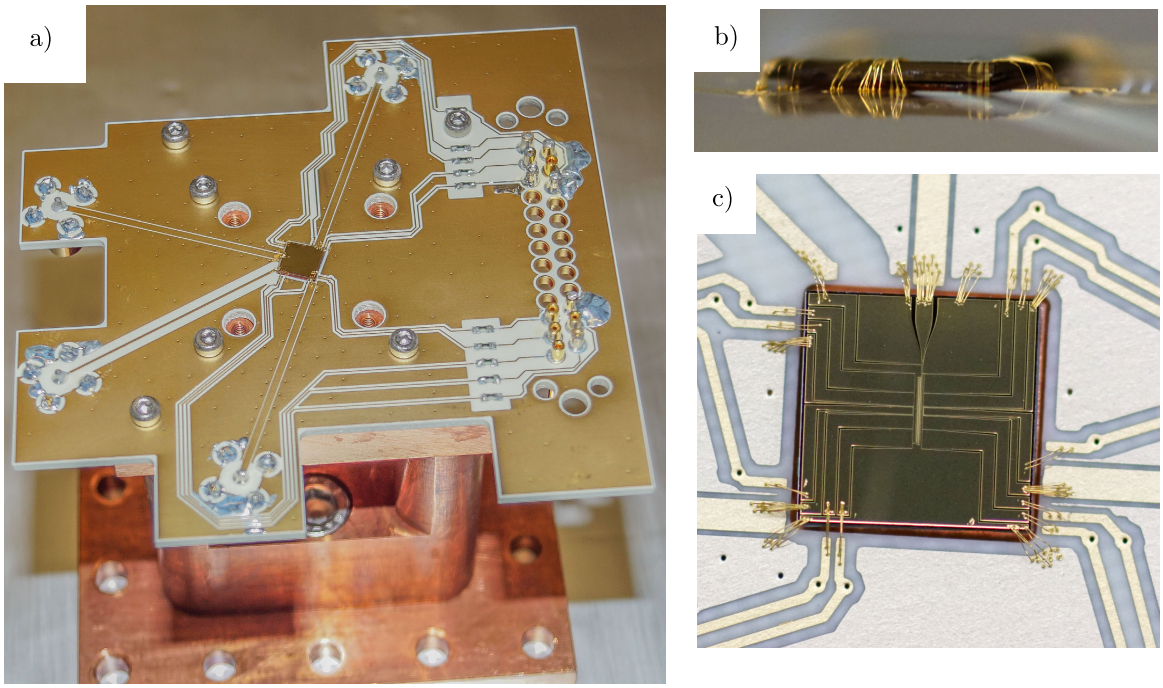

Figure 4.6: a) Picture of filter board and trap mounted. For electrical layout and a picture with Faraday cage on top, see figure 4.7. b) Side-view of trap bonded to the filter board. The trap is surface is $\approx 0.66\,\mathrm{mm}$ above the filter board, gold bonding wires are connecting both. c) Close-up top view of trap, bonding wires and filter board. The current carrying microwave electrodes feature more bonding wires than the only voltage carrying DC electrodes. The little black spots are through vias, electrically connecting top and bottom layer of the filter board. These vias can also be seen in a) and appear as little dots. Color differences in the pictures are only due to different lighting conditions (picture a) was shot with an in-camera flash and under a different angle than picture c)).

The filter board houses 1 RF line, 10 DC lines and 3 coplanar waveguides for microwave signals, the latter requiring large ground planes around and below them. There are 4 MCX connectors for MW and RF signals soldered to the board as well as a 25 pin D-sub connector, of which only the outermost 6 pins are connected, 5 DC and one ground pin on each side. This particular board design does not support all 25 pins because some of them would be in the way of a laser beam. Since a new trap requires a new filter board anyway, this is not a fundamental limit because it would be only slightly less convenient during assembly to move the D-sub connector. No signal is routed on the bottom layer as it touches the copper block for good thermal contact and electrical grounding. All connectors are facing away from the trap surface because they would interfer with the imaging optics in the other direction. The connectors are placed on the outside of the board so they do not intersect with the copper block.
Each DC signal passes through a $1\,\mathrm{k}\Omega$ resistor (Anaren R1A15081001J3A0) and is routed to the trap, in many cases around the MW connectors. As close to the trap as possible,

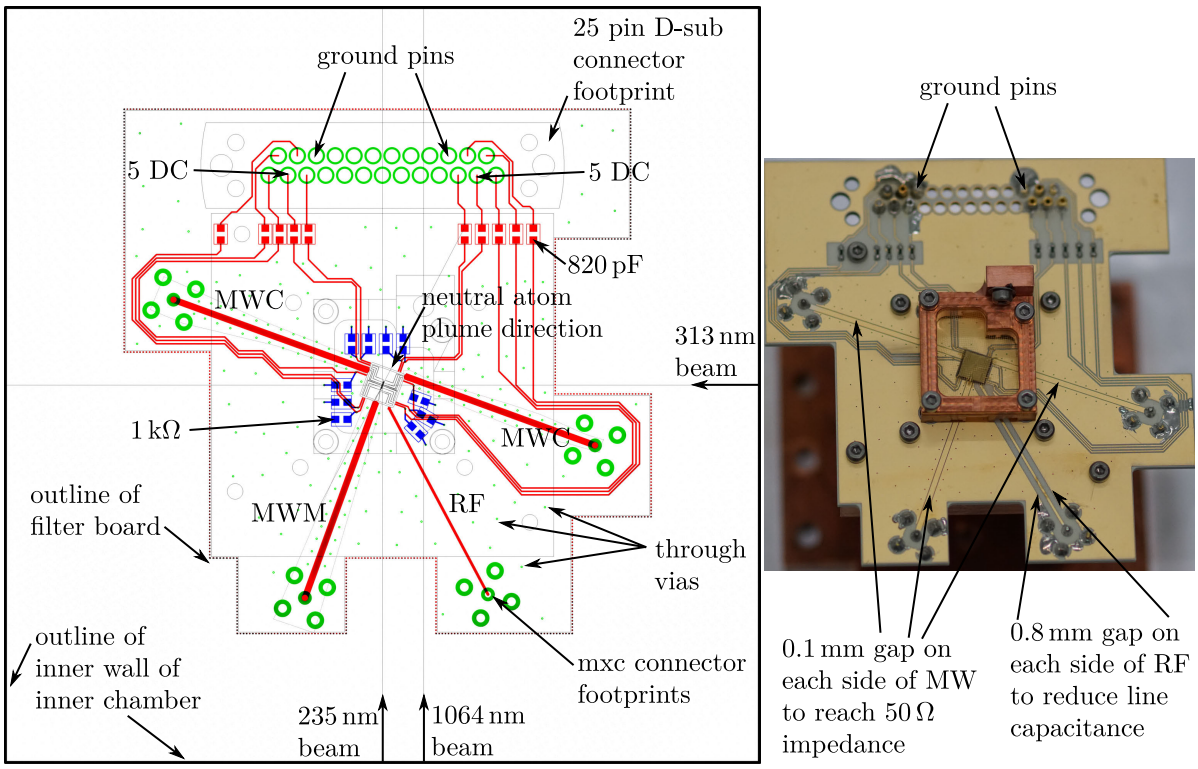

Figure 4.7: Left: Filter board layout. Red: Top layer electrodes. Blue: Bottom layer electrodes. Green: Through connecting vias and MCX connector footprints. Grey: Layout constrains such as trap (middle), Faraday cage (around trap), laser and ablation plume directions, screws.
Right: Picture showing the layout after assembly.

a via splits the signal over a parallel capacitance of 820 pF (Novacap 0603N821J101P) to ground. These capacitors are on the bottom layer of the filter board, so they are not in the way of laser beams. Contact to the copper block is avoided by having a pocket milled out of it in appropriate places. For RC filter specs see section 4.5.

Microwave waveguides

The MW signals are guided in a straight line to the trap to avoid impedance changes of the coplanar waveguide. In our case, the coplanar waveguide is a signal carrying track of width s with gaps of width w on either side, separating it from a ground plane. It sits on a dielectric material with thickness h and dielectric contstant ϵ_r. We calculated the impedance Z_0 of the waveguide according to equations given in the book 'Coplanar Waveguide Circuits, Components, and Systems' [113]:

$$Z_0 = \frac{60\pi}{\sqrt{\epsilon_{eff}}} \frac{1}{\frac{K(k)}{K(k')}\frac{K(k_1)}{K(k_1')}} \tag{4.19}$$

$$\epsilon_{eff} = \frac{1 + \epsilon_r \frac{K(k')}{K(k)} \frac{K(k_1)}{K(k_1')}}{1 + \frac{K(k')}{K(k)} \frac{K(k_1)}{K(k_1')}}, k = \frac{s}{s+2w}, \; k' = \sqrt{1-k^2}, k_1 = \frac{\tanh(\frac{\pi s}{4h})}{\tanh(\frac{\pi(s+2w)}{4h})}, k_1' = \sqrt{q - k_1^2},$$

where K is the elliptic integral of the first kind. A larger gap w increases Z_0, while a larger track width s decreases it. Relative changes of h have only a minor influence on Z_0 and therefore the substrate thickness is not suitable as a free design parameter. Although ϵ_r has a large enough influence to be regarded as a valuable design parameter, the choice of material has already been made for different reasons then for choosing Z_0. The minimal gap, that CONTAG was able to produce is $w = 0.1\,\text{mm}$. With $\epsilon_r = 3.66$ and $h = 1.6\,\text{mm}$ set by design, we chose $s = 0.95\,\text{mm}$ and $w = 0.1\,\text{mm}$, which leads to $Z_0 = 49.26\,\Omega$. Keeping in mind that this is the value for room temperature and applying a thermal contraction coefficient of 0.413 for gold from 295 K to 4 K [75] to s and w, we find $Z_0 = 50.3\,\Omega$. This makes sure, that we have as little reflections at the interface between $50\,\Omega$ connector and waveguide as possible. This leaves the impedance jump at the bonding wires as the only part, in the whole transmission line, beginning at a DDS (see section 4.2), where we can expect a potentially significant impedance mismatch.

Expanding the design

The inner vacuum chamber supports 8 SMA and 4 25-pin D-sub feedthroughs for a total of 100 DC connections. This filter board only accepts 25 DC pins and of those some could not be used due to laser beam path collisions. In early designs of the system, we investigated the possibility of using edge connectors to route DC signals to the filter board. During the PhD work of Martina Wahnschaffe, we have successfully applied those connectors to a room temperature setup [50]. Since we acquired edge connectors with beryllium-copper springs (Sullins Corp. MP-8100-06-DS-1Y), they should also work at cryogenic temperatures. With these, up to 100 DC connections should be possible. We also thought of making holes in the copper block to accommodate coaxial connectors. A rendering of a concept in an early design stage of the filter board is shown in figure 4.8.

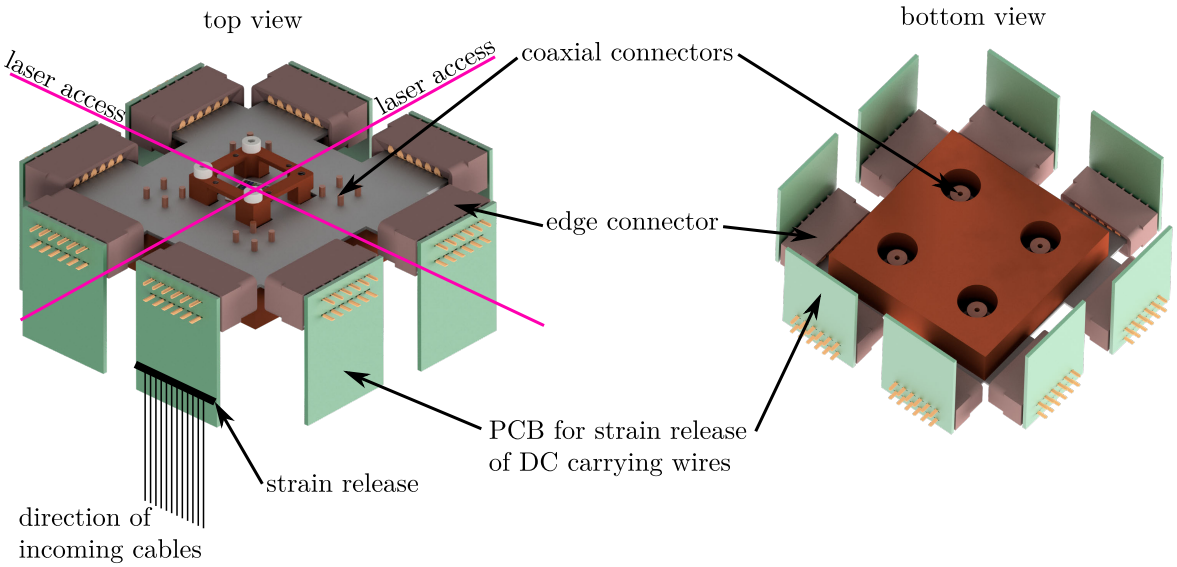

Figure 4.8: Early conceptual design of a filter board with 96 DC and 4 high frequency connections.

4.7 Magnetic field coils

At a magnetic field of $B_0 = 22.3\,\mathrm{mT}$, beryllium ions feature a first order field-independent hyperfine transition. At B_0, the transition frequency between ${}^2\mathrm{S}_{\frac{1}{2}}\,|2,+1\rangle$ and ${}^2\mathrm{S}_{\frac{1}{2}}\,|1,+1\rangle$ stays constant under slight changes of the magnetic field. Figure 2.2 shows the evolution of these two states at magnetic fields around B_0 as well as their derivatives with respect to the magnetic field. At 22.3 mT, the derivatives are equal and small changes in magnetic field strength act the same way on both states, thereby keeping the transition frequency constant

A magnetic field can be produced by permanent magnets, electromagnets or a combination of both. The latter is currently under development for our experiment. So far, we are using only coils to produce B_0. The design considerations of these coils are described below.

4.7.1 Geometric constrains

The cooling laser drives a σ^+ polarized cycling transition and has to propagate parallel to the quantization field to avoid driving parasitic π-polarized transitions. Therefore it has to pass through the middle of the magnetic field coils. The coils are wound around an aluminum structure with a 63 mm hole that lets laser beams pass and can fit the 1" input coupling lens of the 313 nm beam.

There is no space in the vacuum system to place coils. Therefore they have to be placed outside of the vacuum system. Figure 4.9 shows the position of the coils relative to the

outer vacuum chamber and contains most dimensions that are referred to below.
The outer chamber has an outer diameter of 273 mm. We have placed the coils 300 mm

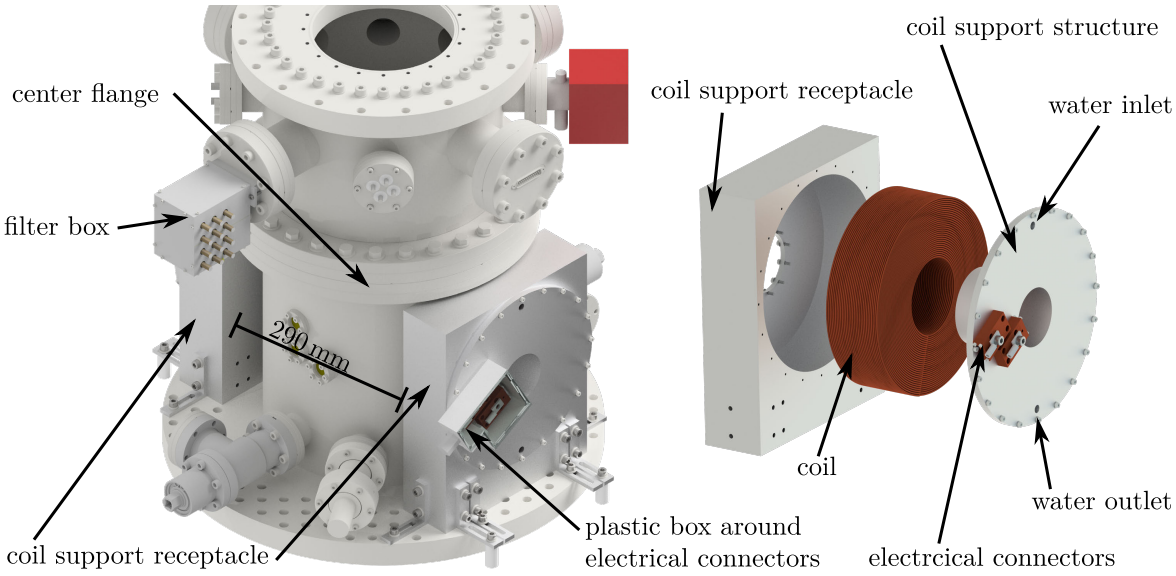

Figure 4.9: Magnetic field coils. Left: positioning relative to the outer vacuum chamber. Right: Explosion view of one coil assembly.

apart to leave some space for position adjustment and to leave room for the 5 mm thick walls of the coil's support structure. The coils have an inner diameter of 82 mm, an outer diameter of 204 mm and a thickness of 63 mm. There are 23 layers with space for 27 windings per layer, leading to 621 windings per coil. During production, we were not able to reach that exact number as we were not able to produce tight packed 27 windings in every layer. However the produced coils still are well in design specs as shown below. The wire is a 2 mm diameter copper wire with a 0.056 mm thick isolation varnish. The coils are electrically connected in series. We need to apply a current of about 36 A to reach desired magnetic field strength, leading to a power dissipation of about 8 kW.

The Biot-Savart law gives the magnetic field $B(z, r)$ produced by a circular current I with radius r along the symmetry axis of that current at a distance z from the plane in which the current flows, where μ_0 is the vacuum permeability:

$$B(z, r) = I \frac{\mu_0}{2} \frac{r^2}{(r^2 + z^2)^{3/2}} \tag{4.20}$$

We used this law to calculate operating parameters for different coil geometries. Assuming a coil-ion distance of 150 mm, the symmetry axis of the coil being collinear with the Doppler cooling beam and a maximum outer coil-radius of 102 mm, we calculated the dissipated power, required current and voltage as well as wire length for different wire diameters and inner coil radii. The maximum outer coil diameter is set by the placement

of the middle flange of the outer chamber (see figure 4.9). We cannot make the diameter bigger without moving the coil further apart, which would reduce overall efficiency. Figure 4.10 shows the results of these calculations. We tried to wind a small amount of windings

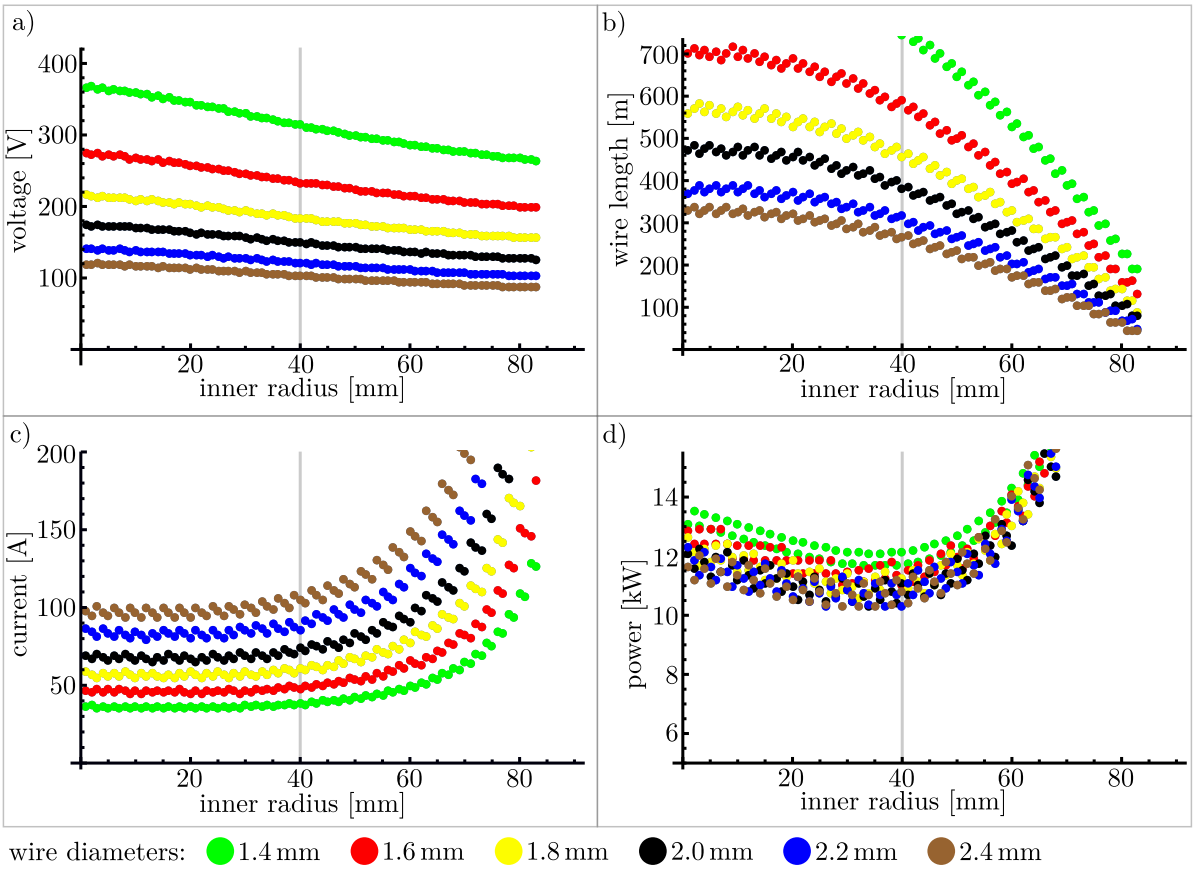

Figure 4.10: Design parameters a) voltage, b) wire length, c) current and d) resulting power dissipation for different inner coil radii and different wire diameters to achieve a magnetic field of 22.3 mT at the ion position. The vertical gray line in each graph is the inner radius that was chosen for the final design. A wire diameter of 2 mm was also chosen. Between some adjacent points in each graph there are small jumps visible. By changing the inner radius, the amount of space for the windings inside the coil support structure changes. If the change is by an amount smaller than the wire diameter, most times it only leads to small shifts in wire position but sometimes the change leads to the exclusion of a complete layer due to space restrictions.

on a test coil and estimated our production errors such as the spacing between layers and windings. The calculations leading to the results shown in figure 4.10 assumed 2 times the production errors. We were able to produce a coil with denser windings than in our simulation which reduced the power consumption to about 8 kW instead of the calculated more than 10 kW. Since we produced higher density coils than in in simulations, the required current is only 36 A. Two Delta Elektronica SM 70-45 D power supplies, each

capable of delivering 70 V and 45 A supply the coils. The generated heat is extracted by a cooling water circuit with 200 l capacity. A water inlet at the top and an outlet at the bottom of the coil support ensure cooling water circulation. The cooling water flows in a closed circuit that includes a sediment filter and a heat exchanger. About 13 $^{l}/_{min}$ of 21°C water are pumped through each coil. To prevent algae growth and corrosion and to provide even better cooling, Antiforgen is mixed with the water. Antifrogen is a mixture of monoethylene glycol and antifreeze.
In case of a cooling water failure, the varnish isolation around the wires would melt within seconds. To prevent that from happening, we have installed a thermometer and flow monitors. If any of these trigger an interlock, the power supplies shut down and, in case of leakage, magnetic valves close off water supply.

The coils were assembled by winding one layer and gluing a few pieces of approximately $15 \times 40 \times 0.8\,\mathrm{mm}^3$ polyethylene terephthalate (PET) foil onto the finished layer. These act as spacers and keep a gap between layers to allow cooling water to pass by. The glue was ethyl-2-cyanacrylat. The ends of the wire are guided to the outside of the coil support structure through small holes that were filled with UHU Endfest, a two component epoxy. The wire ends were stripped of the varnish and clamped between two copper bloks. One of them supports the connection of a cable lug for wiring to the power supplies. The copper blocks are electrically isolated from the coil support with the PET foil and enclosed in a plastic housing to prevent accidental human contact.

This design can be improved by a current stabilization circuit and magnetic field calibration through measurements on trapped ions. Currently there is an effort under way to replace these coils with a combination of permanent magnets and small, not water cooled, fine-tuning coils. Jannik Hertzberg is designing such a system during his bachelor thesis wok.

In an early design stage we discussed the use of superconducting coils around the inner vacuum chamber. Figure 4.11 shows this design. While it would have been possible to implement such coils, we did not deem it necessary as those would have been able to generate far greater fields than 22.3 mT and the overall goal of the project shifted more toward quantum simulation, which does not need more field. A possible improvement in future designs might be to rely on permanent magnets outside of vacuum to supply a bias field of near 22.3 mT and to use a structure like that in figure 4.11 to reach final field strength. That would have the advantage of minimizing possible magnetization effects in the vacuum system components. Coils like that do not need to be superconducting and also do not need to be mounted to the second cooling stage but possibly to the first, shifting heat load to the stage that has ample cooling power.

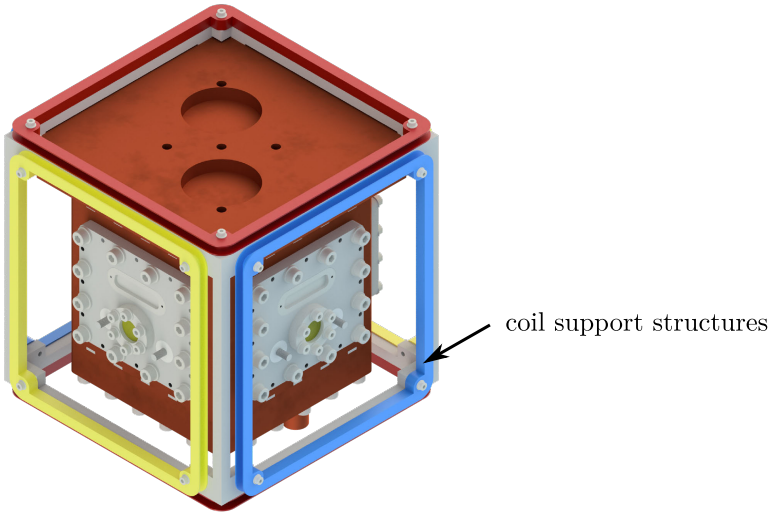

Figure 4.11: Idea from the early design stage. A cage of six coils, possibly superconducting, around the inner vacuum chamber could provide the quantization field.

Chapter 5

Laser systems

This chapter explains modes of operations for all three used laser systems. A 313 nm cooling laser, a 235 nm ionization laser and a 1064 nm pulsed ablation laser. Figure 5.1 explains the symbols used in figure 5.2, which shows a detailed layout of all laser systems.

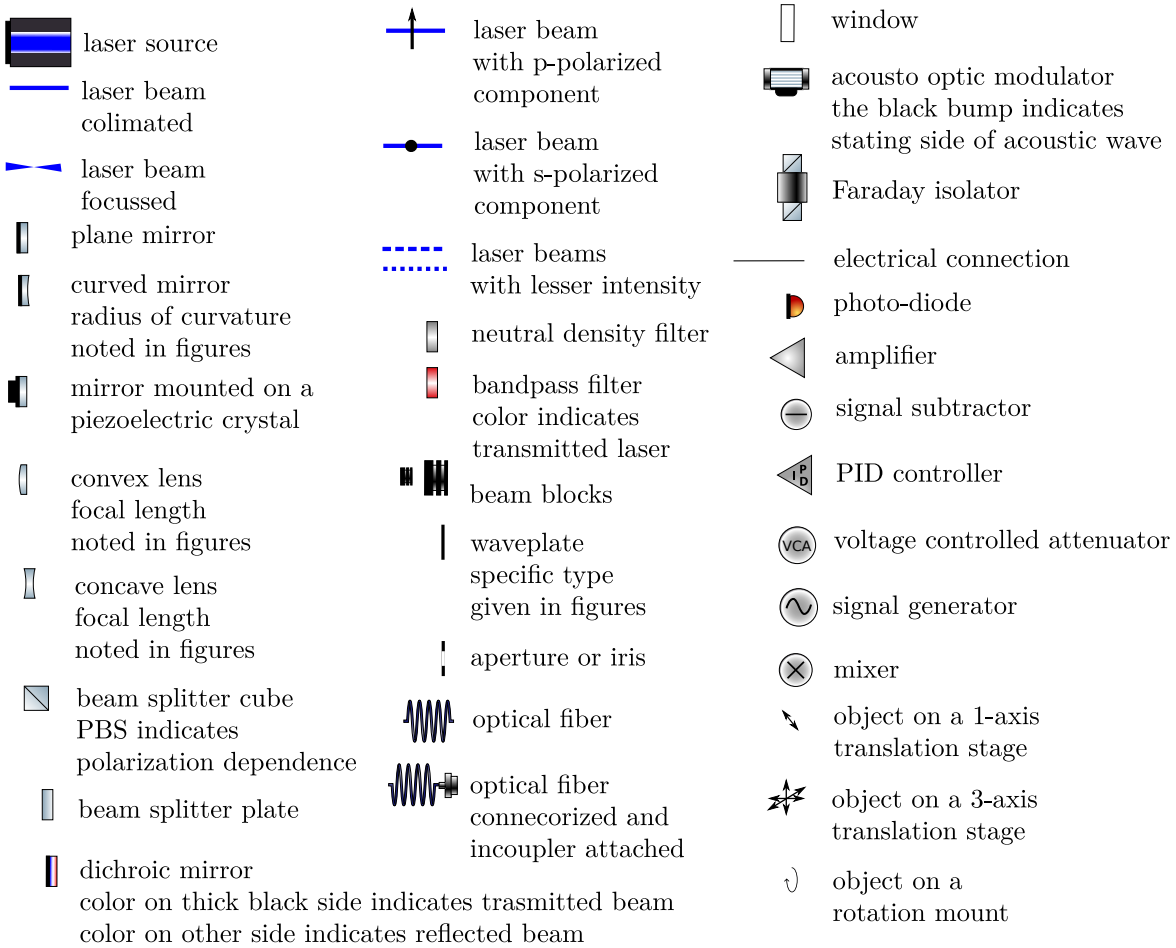

Figure 5.1: Explanation for most symbols, used in laser related figures throughout this thesis. Most symbols taken from the component library of Alexander Franzen [114].

5.1 Ablation Laser

On first impression, this laser system is probably the least sophisticated of the three. It is more or less a straight forward out of the box solution. The system is a Minilite 1 manufactured by Continuum[1]. As explained below, it comes with it's own unique set of challenges. It is a q-switched, Nd:YAG system with a center wavelength of 1064 nm, a pulse energy of 28 mJ and a tunable repetition rate from 1 Hz to 15 Hz. It consists of two major pieces of equipment, the laser head and the control unit. The laser head contains the pump source, a flash lamp, the active medium and the cavity. It also houses an either automatically controlled or externally triggered electro-optical q-switch to adjust the repetition rate, a combination of a $\lambda/2$ wave plate and polarizing beam splitter to adjust the output power as well as a manually controlled mechanical shutter at the output aperture. Some of these components need to be water cooled or supplied by a high voltage. The control unit contains a water tank and a small pump that provides the cooling water via flexible hoses to the laser head. It also houses a transformer that supplies the high voltage, some control electronics for tuning the repetition rate and an external trigger input. The printed circuit board, which supplies high voltage to the flash lamp is called the HV board and has been a source of technical difficulties not only in our laser but also in the Minilite 1 lasers of several experiments at PTB. A laser pulse is generated by firing a flash lamp pulse to pump the active medium and, after waiting a certain amount of time, triggering the q-switch. The Minilite 1 offers two power setting, full power and low power (4% of full power according to the data sheet, but we measured about 20%) as well as four modes of operation:
1) Internal triggering of both, flash lamp and q-switch. The timing between both triggers is set internally and always produces the same pulse energy in each pulse. This mode is most useful during alignment procedures, when a continuous pulse train is of benefit.
2) External triggering of the flash lamp with automatic successive internal q-switch triggering after a standardized delay time. A q-switch trigger synchronization output can be used to achieve repeatable timings and therefore repeatable pulse energies.
3) Internal triggering of the flash lamp and external triggering of the q-switch. The flash lamp will pump the medium in predefined intervals that match the set repetition rate. The q-switch will open at any user controlled time. This can lead to a timing jitter between flash pulse and q-switch which in turn leads to variable pulse energies.
4) External triggering of both. The respective timing can be chosen at will.
It has been diagnosed, that if the laser is ready to shoot in external flash lamp trigger mode and the lamp has not been fired over several minutes, a charge buildup can occur, that destroys the HV board irreparably. This means that the laser can be damaged if it is used in two of the four modes of operation specified in the manual, namely modes 2 and 4. This is due to European electrical safety regulations that require a capacitor at the flash lamp feed lines within the laser head. That capacitor is mandatory to prevent voltage spikes but it also can store more energy that can, under certain operating conditions,

[1]Manufacturer: Continuum Lasers, San Jose, CA, USA; distributor: Amplitude Technologies, Evry, France

damage the HV board. Non-EU versions of this laser do not suffer from this disadvantage. We were not aware of this problem at the time and have managed to produce a defect HV board. We have since implemented a fail safe: On the front panel of the laser, two buttons, 'Start' and 'Stop', can be used for manual control, if it is in full internal trigger mode. To make any shot at all, no matter the mode of operation, the 'Start' button has be activated. Pressing 'Start' would let the laser shoot pulses continuously with a chosen repetition rate. To make manual control from a distance as well as single shot mode possible, the laser was shipped with a BNC cable, connected to a button at the end. By connecting the cable to the laser's 'SINGLE SHOT' port the user can press the button once to interrupt the continuous shooting. In theory, every short press of the button would then shoot a pulse. In practice, a laser pulse is only generated, when the button is pressed within a small window of time. During this mode of operation, the flash lamp pulses at the set repetition rate. A button press triggers the q-switch. Since the laser operates in mode 1), both internally triggered, which relies on an internal timing to produce a laser pulse, the button has to be pressed at the exact moment, when the q-switch would be triggered internally. Thankfully, the user can press the button for an extended amount of time until a laser pulse was emitted. In our case, we have set the repetition rate to 2 Hz. Therefore, if the user presses the button for 0.5 s, a shot will be fired. A 2 s long press of that button would return to continuous shooting. This leads to a button press-time sensitive manual timing. The user has to press the button for a while but not too long.d For ion loading (see section 5.4), one could just switch on the 235 nm ionization laser (see section 5.2) and press the ablation laser shoot button for 0.5 s. The 235 nm light can charge up dielectric surfaces in the trap. These charges can disturb trapping potentials and are therefore to be minimized. In a room temperature setup these charges can migrate due to Brownian motion and when they eventually hit a conducting surface, they get neutralized, leading to a slow decay of 235 nm induced stray fields. In a cryogenic environment, most of the Brownian motion is frozen out. The charges will build up over time. Therefore it is beneficial to keep the ionization pulse as short as possible and to optimize the respective timings of ablation pulse and ionization beam. For reliable loading, it is preferable to work with pulse energies, that do not fluctuate shot to shot. Therefore mode 3) should not be used. Modes 2) and 4) could lead to the destruction of the HV board due to external triggering of the flash lamp. On the other hand, mode 1) does not allow the computer control desirable for implementing accurate laser pulse timings. We have solved this problem by assembling a new remote control cable. Instead of the button, we connected two pins of an Arduino Nano microcontroller to the cable. The Arduino is connected ground-loop free to one of the TTL ports of our experimental control, which can be controlled via software. The repetition rate is set to 2 Hz. If the control software puts out a TTL pulse, the Arduino shorts the cable for 0.5 s, ensuring emission of a laser pulse. Therefore the ionization laser is controlled by the same software and an appropriate timing of the two laser beams is possible. The 235 nm beam still must be on at least 0.5 s to guarantee a pulse-timing overlap between the two beams. There is a source of error: In the TTL control software, there are three modes of operation to chose from. 'Always on', 'always off' and 'software controlled'. If a user would accidentally click always on, the Aduino would 'press the

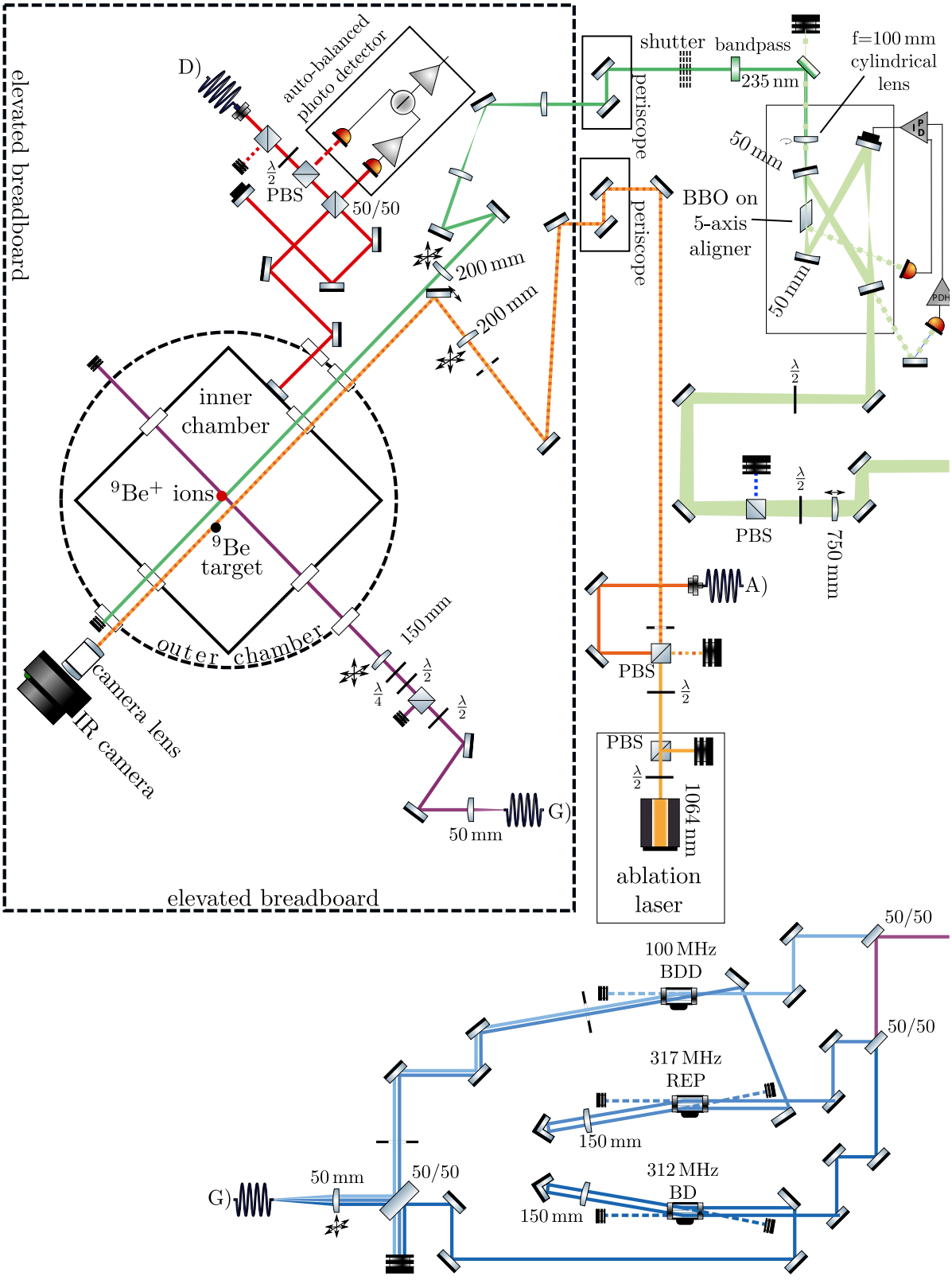

Figure 5.2: Laser system schematics. For explanation see text, for legend see figure 5.1.

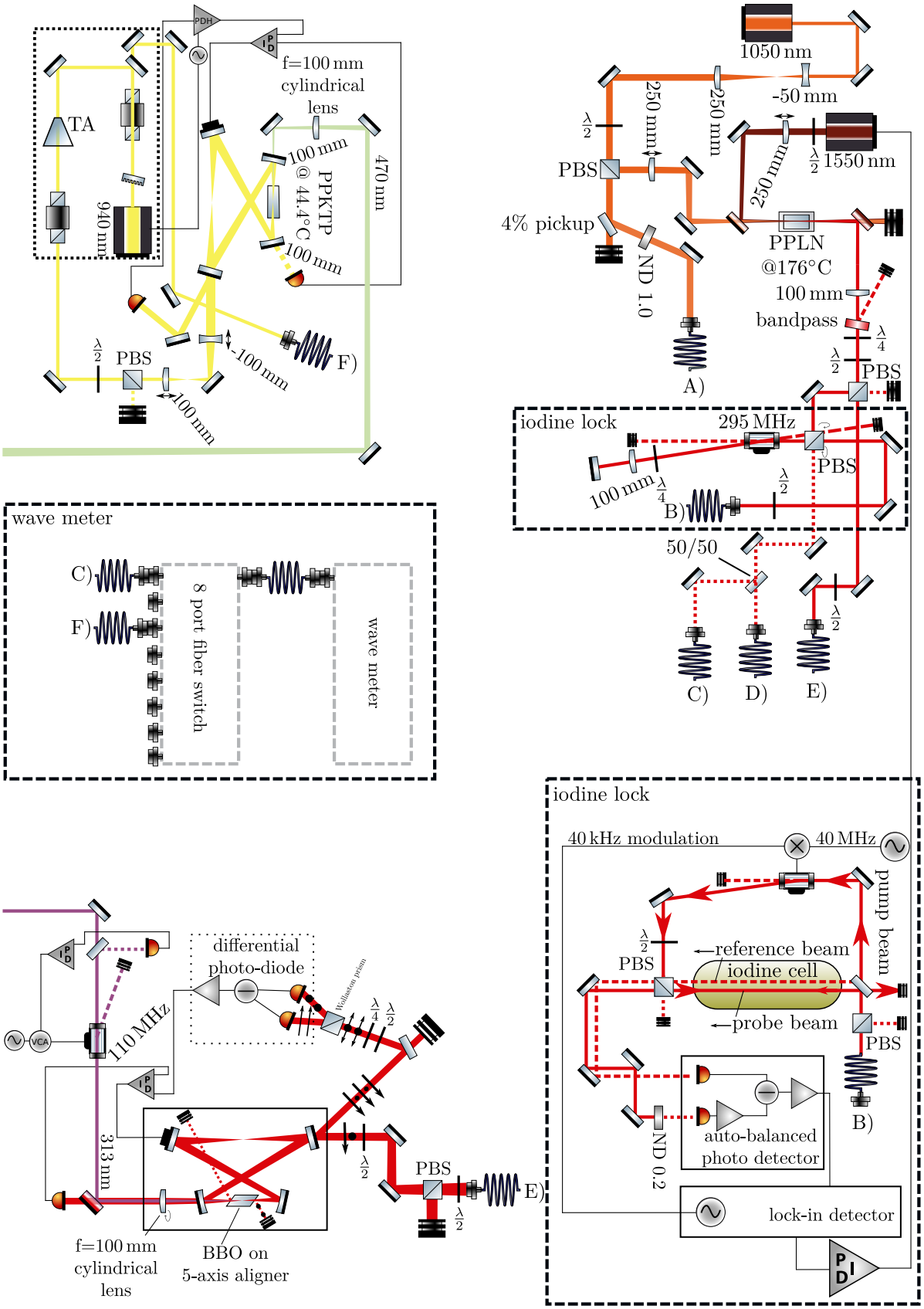

Figure 5.2 continuation: Component placement closely resembles reality.

button' for longer than 2 s, switching the laser into continuous shooting mode, producing a stream of neutral Be atoms, that, if left unchecked, could coat significant portions of the trap structure. Also the Be wire might get destroyed. To prevent this, the Arduino is programmed to ignore any command longer than 1 s.

5.2 Ionization laser

In a two photon process, 235 nm light can ionize neutral beryllium atoms. This light is generated by a frequency quadrupled 940 nm diode laser. This type of laser system was first described in literature by Lo et al. [115]. Our laser system was designed by Johannes Mielke during his master thesis work [116] and made more reliable by Fabian Ude during his master thesis [110]. Since then, we have performed only minor modifications on the system. A detailed description and design considerations can be found in the references above. In the following paragraphs, I will summarize only the important features and bugs of this laser. Figure 5.2 contains the complete layout and relevant parameters (e.g. focal lentghs).
Light with 940 nm wavelength is generated by a laser diode belonging in a Toptica TA Pro. Inside the laser head, there is a rotatable grating for wavelength selection and a beam pickup, that guides a fraction of the light to a monitor port, which we couple it into a multimode fiber and send it to a Highfinesse MC8 multimode switch, connected to a Highfinesse WS7 wave meter. The majority of the diode-light is guided into a tapered amplifier, also situated in the laser head. The laser head is sealed ex factory and there are only three components, which can be adjusted from the outside. The grating, for coarse tuning of the wavelength and two mirrors, that guide the light into the tapered amplifier.
The wavelength can be fine-tuned by changing temperature, diode-voltage and diode-current settings in the laser controller.
The laser emits about 1.3 W of continuous wave power. After leaving the laser head, the beam can be attenuated to desired power levels, in our case between 350 and 900 mW. With optimal alignment 350 mW is enough power to run the experiment. Over time the systems becomes slightly misaligned. Instead of re-aligning, which takes time and can, in case of slight imperfections, lead to a cascade of realignment work throughout the system, we gradually increase cavity input power to match desired output power levels. Above approximately 900 mW, thermal lensing effects become dominant enough to make locking the cavity difficult. We then reduce power and do a thorough re-alignment.
The laser output light is formed by a telescope, to match the main spatial cavity mode and coupled into a bow-tie cavity for power enhancement. The four cavity mirrors are, in order of light hitting them, a flat incoupling mirror, a flat mirror, mounted on a piezoelectric crystal and two curved mirrors. Between the curved mirrors, there is a non-linear, $1 \times 2 \times 20\,\mathrm{mm}^3$ large, periodically poled potassium titanyl phosphate (PPKTP) crystal from Raicol Systems. It has a poling period of 5.925 µm and is anti-reflection coated for 970 as well as 470 nm. The beam is focused into the cavity midway between

input coupler and piezo. The first curved mirror images this focus into the crystal. The second curved mirror images the light back onto the first focus, thereby closing the cavity. Inside the PPKTP crystal some of the 940 nm light gets converted into 470 nm light, leaving through the second curved mirror, as it is only highly reflective for the fundamental mode. The PPKTP crystal has to be orientated in a specific position relative to the laser light as well as to be kept at a temperature of 44.4°C, both to achieve quasi phase-matching conditions and maximum frequency conversion. The crystal is housed inside a custom built oven, mounted on a 5-axis aligner. The oven is connected to a Thorlabs TED 200C temperature controller.
The cavity length has to be controlled to keep the cavity resonant with the laser light. This is done via a Pound-Drever-Hall (PDH) locking scheme [117, 118]. A Toptica PDD110 PDH controller generates the modulation frequency and is connected to the laser controller. It modulates sidebands on the diode-current, which also produces frequency sidebands on the laser radiation. The light, reflected at the cavity's incoupling mirror, is detected on a photo-diode and demodulated on the PDD110. After manual phase-adjustment, the PDD110 output signal is fed into a Toptica PID110 controller. A photo-diode, detecting leaked light behind the first curved mirror, provides the PID controller with the so called 'INTENS' signal. A signal level can be chosen, below which the PID attempts re-locking procedures. This prevents accidental locking on a zero-crossing of the error signal, that does not belong to the main cavity mode. We are satisfied with power levels between 200 and 300 mW of 470 nm light.
The converted light is collimated and coupled into a second doubling cavity. That cavity has the same principal design but different dimensions. A beta barium borite (BBO) crystal is used for second harmonic generation. The phase-matching conditions are met via type-I critical phase matching, meaning that the relative position of crystal and laser beam has to be carefully aligned but the crystal's temperature is not a critical parameter. A resistive heating element, powered by a constant current of 0.41 A at 9 V, keeps the crystal-mount at about 47°C, which is 25°C above room temperature, to prevent water condensation on the crystal. There is also a constant stream of oxygen, flowing around the crystal to keep it clean and also prevent water adsorption, which would eventually lead to a drastic decrease in frequency conversion efficiency, as was observed during Johannes Mielkes work on the laser. Since adopting these two precautions, crystal degradation has not been observed.
The cavity is also locked via the Pound-Drever-Hall method. Light, exiting the first doubling stage, still contains sidebands from the diode-current modulation, which can be used to stabilize the second cavity's length. At the incoupling mirror reflected light is detected by a photo-diode. The signal is processed by the Toptica PDD110. In contrast to the fist doubling stage, we do not use a Toptica PID 110 to control the piezo but an FPGA based PI controller, developed by Julia-Aileen Coenders during her bachelor thesis [105]. That controller also features a re-lock mechanism and the 'INTENS' input is fed by a photo-diode, detecting the light, reflected by the Brewster-cut BBO crystal's entrance facet.
Behind the cavity, a dichroic mirror and a bandpass filter out the remaining 470 nm light, leaving only 235 nm light. We can achieve up to 12 mW of UV power but that optimum

is very sensitive to fluctuations of any kind and degrades over the course of a work-day to about 3 mW. Since ion loading is possible with less than 1 mW and very reliable at 1.5 mW, we do not maintain optimum conversion efficiency. A loading sequence with more power than necessary can also lead to additional unwanted charging effects on surfaces close to the ions, which can disturb trap potentials. Therefore we aim at powers levels around 1.5 mW, which are stable over at least a week.
At last, the 235 nm light gets guided to the trap. The process of which is detailed in the description of trap loading in section 5.4.2.

Features and problems, that were observed during use of the ionization laser

The first step of two-photon ionization of ^{9}Be, is to resonantly drive the $2s^1S_0 \rightarrow 2p^1P_1$ transition. Provided it arrives within the lifetime of the exited state, a second photon of the same energy can then ionize the atom from there. During her PhD work in our group, Martina Wahnschaffe has investigated the transition frequency by observing fluorescence behavior of Be clouds [50]. The transition frequency was determined to be at around 1276.079 THz. Since the movement of the neutral atom cloud relative to the direction of the ionization beam introduces a Doppler shift, we have scanned our laser frequency around that number and were able to trap within the frequency range of 1276.0780 to 1276.0786 THz. As described above, the frequency is coarsely set by a grating inside the laser head and fine tuning happens by setting diode-voltage, -current and -temperature. The laser controller features internal PID controllers for each of these parameters. We detect the 940 nm monitor output on a Highfinesse WS7 wave meter. Note, that we monitor at 940 nm and thus detect a quarter of the above mentioned UV ionization light's frequency.
It should in principle be be straightforward to set the laser frequency to a few MHz accuracy within the 319.01950 to 319.01965 Thz range, in practice this was fraught with difficulty and often unreliable and unstable. The laser diode experienced spontaneous mode jumps and a substantial amount of time during Fabian Ude's masters thesis [110] was spend on determining stable parameter combinations of current, voltage and temperature. But even with these parameters the laser still experienced random mode jumps and was never stable for more than a few hours.
We exchanged the laser head with a second version of the same model, that behaves more stable in terms of mode hopping but still requires regular frequency tuning during use. While the frequency behavior of this model is more stable, the incoupling into the tapered amplifier (TA) proved less stable than before.
Figure 5.4 contains an oscilloscope screen shot, showing the reflection signal at the fist cavity's incoupling mirror. The many vertical lines, that show up all over the signal degrade the PDH error signal so much, that the cavity does not lock anymore. The lines appear to result from a mode-mismatch between laser diode and TA. Most of the time, they can be reduced to zero by tuning diode-voltage or -current. While we have not definitively determined the cause of these effects, two possible explanations remain:
1) Changing of laser diode emission frequency, via current/voltage tuning, leads to a

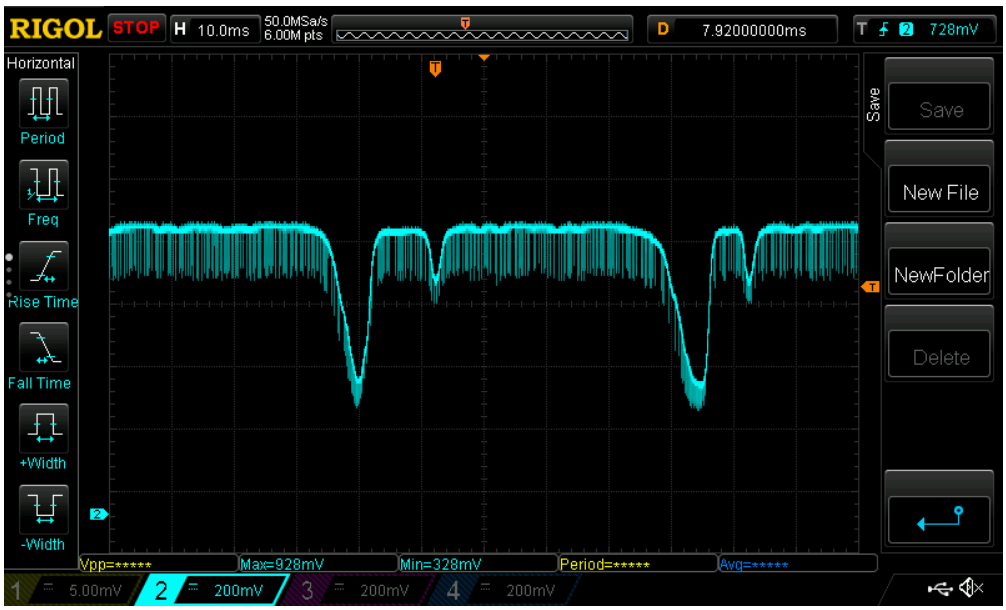

Figure 5.4: Signal of photo-diode, detecting light, reflected at the incoupling mirror of the 940 → 470 nm cavity. The vertical lines result from a mode mismatch between laser-diode and tapered amplifier and make locking the cavity impossible.

slight beam direction change and subsequent change in TA incoupling. This could be caused by a slightly different refraction at the grating.
2) The TA might show internal etaloning effects, sensitive to frequency and beam location changes, which might result in weak lasing of the TA.
If that voltage/current changed the laser frequency to a value, that does not allow for photo-ionization, re-aligning the two very sensitive TA incoupling mirrors is the next best choice.
Changing the spatial TA incoupling can lead to vastly different output powers, spatial mode profiles or beam divergence. In a worst case scenario, which we experienced two times within a year, the beam forming optics in front of the first cavity have to be replaced to accommodate new beam parameters. Other experiments did not report similar issues but we have only heard from people using a different model of laser controller. At this stage, it is pure speculation, if our controller is responsible for these stability issues.

The first doubling cavity is exceptionally long-term stable. It's optics as well as connected electronics only need to be touched for re-aligning when the input beam suffers from the aforementioned changes in spatial mode profile.
If we switch off the PID that controls the cavity length, the cavity should no longer be resonant to 940̇nm light. By chance, it features a self locking mechanism that keeps the cavity resonant even without active control: The PPKTP crystal is not perfectly transparent for 470 nm light. Some light is absorbed, which warms the crystal and changes its index of refraction and thereby the optical path length for all wavelengths.

Additionally, thermal lensing effects due to the changes of the index of refraction focus the beam tighter and lead to more local light absorption and even more change in the index of refraction.
For quasi phase-matching, the temperature has to be stable, so in case of high 470 nm power and accompanied by high absorption, the temperature controller delivers less power to the oven. After a few minutes an equilibrium is reached and both heat sources stay more or less constant.
If we deliberately switch off the PID110 that controls the piezo or if it malfunctions, after that thermal equilibrium was reached, the cavity might no longer be resonant to 970 nm, leading to a drop in 470 nm power, leading to less power absorption, leading to less heat from that source. The crystal therefore cools slightly, changing it's index of refraction and also the optical path length. That change leads to the cavity being again resonant to the laser light. This all happens on time scales too short for the temperature controller to react. We have deliberately switched off the cavity length stabilizing PID controller and observed 470 nm, coming out of the free running cavity for up to 5 minutes.

Over the course of a week, the second doubling cavity drifts to a point, where the output power is not high enough for reliable ionization anymore. Realigning usually takes up to 30 min and involves slight changes of cavity mirror and/or crystal positions, accompanied by a slight output beam walk. In that case we have to undergo the standardized alignment procedures, described in section 5.4.2, which also take up to 30 min.

5.3 Doppler cooling laser

In a magnetic field of 22.3 mT, Beryllium features a first order magnetic field independent ground state hyperfine transition, suitable as a qubit in quantum logic applications (see section 2.2.1). In the same magnetic field, a σ^+ polarized cycling transition exists between the $^2S_{1/2}|F = 2, m_{F=2}\rangle$ and $^2P_{3/2}|m_{I=3/2}, m_{J=3/2}\rangle$ states. The cooling wavelength is in the UV at 313 nm. We generate the light following techniques, first published by Wilson et al. [119]. The original design of our laser system was done by Kai Voges during his master thesis [120]. We have only performed small design changes to the system. A detailed description and design considerations can be found in the references above.
There is no commercially available active laser medium, that emits at 313 nm. At twice the wavelength, 626 nm, there are, to my best knowledge, only dye lasers commercially available, which are bulky and require a substantial maintenance overhead. At slightly higher wavelengths, diode laser are available. There have been successful attempts at cooling a 635 nm frequency-tunable external cavity laser-diode down to approximately $-31°C$ to achieve lasing at 626 nm. However, 313 nm light, generated via frequency-doubling, had a power level of only 5-7 mW [121].
It has been demonstrated, that a distributed Bragg reflector (DBR) ridge waveguide laser diode, cooled to moderate 5.6°C but still below the dew point, can generate 626 nm light [122]. The 626 nm output power of that system is not sufficient to generate enough

313 nm light for Doppler cooling while simultaneously allow for locking it to an atomic reference, which is a crucial requirement for keeping it at the desired cooling frequency. Although this is no fundamental limit, as amplification through a tapered amplifier at 626 nm can potentially alleviate this limitation [122].
While Doppler cooling is certainly possible with those two systems, the technologies seem not mature enough for our purpose and the convenience of having up to 120 mW of UV power available, as our laser system provides, can't be denied.
We rely on sum-frequency generation (SFG) of two infrared lasers at 1050 and 1550 nm to generate 626 nm light, which is then frequency doubled to 313 nm. We stabilize the frequency of the red light to a molecular transition of iodine. The frequency stabilization was first implemented by Mariia Stepanova during her bachelor thesis [123].

5.3.1 Sum-frequency generation of 626 nm light

We use two infrared fiber laser systems from NKT-Photonics, an ytterbium doped Koheras BoostiK Y10, emitting at 1050 nm and an erbium doped Koheras BoostiK E15, emitting at 1550 nm. They feature an output power of 5 W each. We use full power of 1550 nm and half the power of 1050 nm. We have bought an additional E15, wich will be combined with the remaining 2.5 W of the Y10 for future implementation of a Raman-laser beam line. This setup is currently being developed by Simon Roßmann during his master thesis. A schematic of this laser system can be seen in figure 5.2.
The lasers features a fiber output with an attached output coupler. We overlap the beams on a dichroic mirror and focus them into a non linear periodically poled lithium niobate (PPLN) crystal. Since the PPLN's index of refraction is different for the two wavelengths but we need to achieve similar focus sizes inside the crystal, each beam has a separate incoupling lens. While the 1550 nm beam has a useful beam diameter right out of the box, the 1050 nm beam is widened by a telescope before focusing into the crystal. The crystal is 0.5 mm thick, 10 mm wide and 40 mm long. It contains three optically active, 40 mm long lanes, each with an entrance aperture of $0.5 \times 0.5\,\mathrm{mm}^2$. The gratings of the lanes are slightly different at 11.12 µm, 11.17 µm and 11.22 µm. The crystal was supplied by Covesion Ltd. and came with a matching oven and temperature controller (Covesion OC1). To reach optimum quasi phase-matching conditions, not only size, position and polarization of each beam, relative to the crystal and the other beam have to adjusted but also the crystal's temperature has to be kept at a specific value. The crystal is kept at approximately 176°C while we use the middle, 11.17 µm grating lane for SFG.
While we observed a maximum power of 1.3 W 626 nm light, we operate the SFG stage at about 1 W output power as this has proven be be long time stable and sufficient.

5.3.2 Second harmonic generation of 313 nm light

The beam is split up into a 300 mW frequency stabilization beam which will be discussed below and a 700 mw beam for subsequent frequency doubling, which is coupled into a polarization maintaining fiber (Thorlabs P5-630PM-FC-2 with CFC8-B fiber collimator attached) and guided to a frequency-doubling cavity. We host the fiber collimator on a standard 1" mirror mount and have replaced the standard 1" fiber collimator mount from Thorlabs by a custom mount as the model at the time (AD10) did not provide easy fiber detachment. We have build a version that has half the thickness and allows us to actually reach the screw at the fiber connector.
About 500 mW of power is emitted at the other end of the fiber by a Thorlabs CFC8-B fiber-output coupler. It's tunable lens position lets us, within a certain range, choose a focus size. A doubling cavity, very similar to the second doubling stage of the ionization laser (see section 5.2), is used for field enhancement and second harmonic generation (SHG). The focus size is chosen to be 162 µm as this is required for mode matching with the main cavity mode and it's position is 59 cm behind the output coupler, which is placed this distance from the center between the cavity's incoupling and second mirror, so mode matching is complete. A curved mirror images that focus into a BBO crystal, which has a Brewster-cut entrance facet that introduces polarization sensitive losses into the cavity.
For polarization cleaning, a PBS in combination with a subsequent $\lambda/2$ wave-plate is used in front of the cavity. The light reflected at the incoupling mirror is directed through a combination of $\lambda/2$ and $\lambda/4$ plates and split by a Wollaston prism, the outputs of which are detected on a self-built differential photo-diode. This combination of polarization selective intra-cavity element and polarization dependent differential detection can be used to implement a Hänsch-Couillaud cavity length locking procedure [124]. The error signal, generated by the differential photo-diode is amplified and fed into a Toptica PID110 controller. Behind the cavity, a dichroic mirror reflects 313 nm light and a photo-diode behind it detects red light, coming out of the cavity. This signal is used to feed the PID110's 'INTENS' input (see section 5.2 for more details on the PID110). The PID110 output is connected to a piezoelectric crystal to which the second flat cavity mirror is attached. The cavity length can therefore be controlled to be resonant for 626 nm light. We can generate up to 120 mW of UV light but keep it at about 70 mW because it is more long term stable at this power level and we do not need more power.
As in the second cavity of the ionization laser, we use a constant stream of oxygen around the crystal, to prevent water adsorption. In contrast to the other cavity, we do not heat the BBO crystal as we have not observed any evidence for crystal degradation so far. 313 nm photons carry less energy than 235 nm photons are less prone to induce photo-chemical reactions in the crystal.

A more sophisticated quasi-monolithic, hermetically sealed and impressively stable version of the doubling cavity has been developed by Stephan Hannig and Johannes Mielke [106]. In future iterations of this experiment, a cavity like that is preferable as it

is more long term stable and features a higher conversion efficiency.

5.3.3 Generation of cooling, detection and repumping beams

Laser frequency considerations

The generated 313 nm light is guided through a Gooch & Housego I-M110 acousto-optic modulator (AOM), where the 1st order of diffraction is blocked, effectively acting as a controllable attenuator. Behind the AOM a pickup guides some light onto a photo-diode, connected to an FPGA based PID controller [105]. The PID's output is connected to a voltage-controlled attenuator, which sits between the frequency source (see section 4.3) and the AOM. The amount of light, diffracted in the AOM, is, until it reaches a saturation power level, proportional to the RF power, applied to the AOM. We can set a desired laser power level, 60 mW in our case, and the PID will stabilize it.
We need four 313 nm beams with different frequencies, two of which are only different by a few MHz and never on at the same time. We use one AOM as a frequency shifter to produce those two beams and two other frequency shifting AOMs to produce the other two. The transition driven by the different beams are shown in figure 2.2.
The frequency of the 626 nm light is stabilized to a transition in molecular iodine (see section 5.3.4). If the iodine line with transition frequency f_I had exactly half the frequency of the beryllium cycling transition frequency f_{cyc}, only slight frequency shifts would be necessary. The doubled iodine frequency is still off by 1863 MHz:

$$f_{cyc} = 2f_I + 1863\,\mathrm{MHz}$$

Partly this shift is realized in the iodine spectroscopy beam line, as shifting red light by a certain frequency shifts the UV light by twice the amount, thus requiring a less sophisticated AOM setup. We have calculated the frequency of a suitable iodine transition with the IodineSpec5 software package, developed by Horst Knöckel and based on the model discussed in a 2004 publication [125], to be $f_I = 478697768$ MHz. Two AOMs in the spectroscopy beam line shift the SFG generated 626 nm light (with frequency f_{626}), by effectively -610 MHz to be resonant with the iodine transition. It is more complicated and explained in section 5.3.4.

$$f_{626} = f_I + 610\,\mathrm{MHz}$$

The 313 nm light, produced by the doubling cavity has a frequency of $f_{313} = 2 \cdot f_{626}$. For trapping fast ions, produced during the trap loading sequence (see sections 5.4.1 and 5.4.2), we use a far detuned Doppler cooling beam, called BDD, which is shifted by -100 MHz with respect to f_{313}, which gives us a beam, that is 743 MHz red detuned from the $^2\mathrm{S}_{1/2}|\mathrm{F} = 2, \mathrm{m_{F=2}}\rangle$ to $^2\mathrm{P}_{3/2}|\mathrm{m_{I=3/2}}, \mathrm{m_{J=3/2}}\rangle$ cycling transition.

$$f_{BDD} = f_{313} - 100\,\mathrm{MHz} = 2f_I + 1120\,\mathrm{MHz} = f_{cyc} - 743\,\mathrm{MHz}$$

As the BDD can cool relatively hot ions, it cannot reach the lowest temperatures, because of it's large detuning. A near detuned Doppler cooling beam (called BD), that

generates the lowest Doppler cooling ion temperature is therefore needed. We shift f_{313} by +624 MHz, which gives us a beam, that is 19 MHz red detuned from the cycling transition. The 19 MHz is the half linewidth of the exited state.

$$f_{BD} = f_{313} + 624\,\mathrm{MHz} = 2f_I + 1844\,\mathrm{MHz} = f_{cyc} - 19\,\mathrm{MHz}$$

With the same setup, we also produce the detection beam (called DET), 9 MHz red detuned from the cycling transition. Since BD and DET are never on at the same time, we use the same AOM to generate them ans switch between frequencies.

$$f_{DET} = f_{313} + 634\,\mathrm{MHz} = 2f_I + 1854\,\mathrm{MHz} = f_{cyc} - 9\,\mathrm{MHz}$$

During operations on the qubit transition ($^2\mathrm{S}_{1/2}|\mathrm{F}=2,\mathrm{m}_{\mathrm{F}=1}\rangle$ to $^2\mathrm{S}_{1/2}|\mathrm{F}=1,\mathrm{m}_{\mathrm{F}=1}\rangle$), like sideband cooling, we would like to be able to depopulate the $|\mathrm{F}=1,\mathrm{m}_{\mathrm{F}=1}\rangle$ state. As neither f_{BD} nor f_{BDD} are resonant on a transition from that state to the $^2\mathrm{P}_{3/2}$ manifold, a third beam, called repumper or REP is needed. We shift f_{313} by -634 MHz to resonantly drive the $^2\mathrm{S}_{1/2}|\mathrm{F}=1,\mathrm{m}_{\mathrm{F}=1}\rangle$ to $^2\mathrm{P}_{3/2}|\mathrm{m}_{\mathrm{I}=3/2},\mathrm{m}_{\mathrm{J}=1/2}\rangle$ transition.

$$f_{REP} = f_{313} - 364\,\mathrm{MHz} = 2f_I + 586\,\mathrm{MHz} = f_{cyc} - 1277\,\mathrm{MHz}$$

AOM setup

There are three beam lines, produced by two successive 50/50 beam splitter plates. The output of the first splitter contains the most laser power and becomes the BDD beam. The two outputs of the second splitter are used for BD/DET and REP beams.
The BDD beam is guided through a 100 MHz Gooch & Housego I-M110 AOM in -1st order single pass configuration.
The BD/DET beam is guided through a 312ṀHz IntraAction ASM-320 AOM in double pass configuration. Beam separation is done geometrically as the AOM crystal is polarization sensitive and a polarization based beam separation like in the iodine spectroscopy line (see section 5.3.4) would not work, since the returning light would be mostly absorbed by the AOM crystal. The plane of diffraction is parallel to the optical table. The incoming beam is slightly tilted downwards and passes just 1 mm above the flat edge of a D-shaped mirror in front of the AOM. It is diffracted (+1st order) and a lens is hit slightly below it's center and makes the beam parallel to the table. A cat-eye reflector guides the light back into the lens but slightly above it's center, tilting it downwards. Again, the light passes through the AOM (+1st order) and, this time, hits the D-shape mirror, getting reflected out of the AOM setup.
The REP beam has exactly the same setup as BD/DET but runs with 317 MHz and is diffracted into -1st order.
The beams have to get overlapped again. This is not done by two additional 50/50 beam splitters but with only one and a neat trick. The BDD is only used for trap loading and the REP is only used for measurements of some sort, the two beams are never on at the same time. We also send the REP beam through the BDD AOM but under an angle, such that it does not experience diffraction (0th order). This lets us overlap the -1st oder

of diffraction of the BDD with the REP light (see figure 5.2). The combined BDD/REP beam is than overlapped on a 50/50 splitter with the BD/DET beam.
With a 50 mm lens, the combined beam is coupled into the bare end of a 40 cm long, single-mode hollow-core photonic crystal fiber, produced at the Max Planck Institute for the Science of Light [126]. We can transmit upo to 40% of the beam's power through the fiber. Since the beam profiles of all three beams are different in front of the fiber, we cannot reach 40% with all beams at the same time. We chose the incoupling lens position as a compromise so that enough power in every beam reaches the ions. The end of the fiber is mounted on an elevated breadboard, that surrounds the vacuum chamber. For a continuing description of the beam path see section 5.4.2.

During Simon Roßmann's master thesis work, currently under way, we have designed a quasi-monolithic RF duty-cycle compensated double pass AOM setup. This has proven to be long-term stable and does not suffer from beam pointing fluctuations due to thermal effects in the AOM crystals. Even though we are, at the time of writing, not limited by such effects, more sophisticated pulse schemes might be in the future. The new setup is also more compact.

5.3.4 Laser frequency stabilization

As mentioned at the beginning of section 5.3, approximately 300 mW of red light can be used in a frequency stabilization setup. As mentioned above, the iodine transition on which we lock the laser is 610 MHz below the frequency of the red light that goes into the doubling cavity $f_I = f_{626} - 610\,\mathrm{MHz}$. The iodine lock setup takes care of the task of keeping it that way.
After the spectroscopy light is separated behind the SFG setup, it is fed into a 295 MHz double pass Gooch & Housego 3360-125 AOM. It is aligned to -1st order and shifts the frequency by -590 MHz: $f = f_{626} - 590\,\mathrm{MHz}$. Beam separation is done with a $\lambda/4$ wave-plate behind the AOM and a polarizing beam splitter in front of it. The light is coupled into a fiber and transferred to the spectroscopy setup. We get up to 40 mW through the fiber but usually run the system at 20 mW because it is less maintenance demanding. A thick glass plate reflects two low intensity, parallel traveling, pickup beams, the probe and reference beams. Most of the light is transmitted and guided in -1st order through a 40MHz IntraAction AOM-402AF1 AOM. An internal mixer in a USB controlled Trinity Power TPI-1001-B frequency generator is used to modulate a 40 kHz signal, originating in a Stanford Research SR530 lock-in amplifier, onto the 40 MHz rf signal. Therefore 40 kHz sidebands are modulated on the laser frequency. The pump beam is overlapped with the probe beam. All beams propagate through a glass cell that contains iodine gas. Within the iodine gas cell, molecules are moving in different directions with different velocities. Relative to the laser beams, there are different Doppler shifts, depending on the projection of the molecule velocities onto the laser direction. By connecting a custom-built PID controller, to the piezo-input port of the 1550 nm laser and scanning the piezo voltage, we effectively scan the frequency of that laser and therefore the frequency of the 626 nm light. If it is on resonance with

an iodine transition, the weak probe beam is mostly absorbed within the glass cell. If the pump beam is resonant at the same time, it will excite some molecules, therefore making the iodine more transparent for the probe beam. Since the pump is shifted by -40 MHz with respect to the probe but both beams are traveling in opposite direction, they are both simultaneously resonant with the velocity class where the Dopper shift is 20 MHz compared to the probe beam. Resulting in an effective additional -20 MHz shift of the produced red light versus the iodine line. Together with the -590 MHz of the first AOM, this results in the required -610 MHz shift. On resonance, both beams reach an input of a Newport Nirvana 2007 auto-balanced photodetector. Both signals levels are matched and subtracted to cancel background noise. The result is amplified and send to the lock in detector, which demodulates the signal at 40 kHz and feeds the error signal into the PID controller. The PID has a feature that puts out a trigger pulse each time, the scanning ramp crosses the set point. We can control set point and scan range. On an oscilloscope, triggered to that reference, we can select the iodine line to lock to and move it to coincide with the trigger pulse, creating a situation where the controller is set to keep the error signal at a certain level, which corresponds to the selected iodine line. The lock is low on maintenance as it stays stable over the course of several days.

5.4 Trap loading

To load the trap, we apply proper voltages to all trap electrodes and proper current to the magnetic field coils. We shoot with the ablation laser onto a Be target, which creates a plume of neutral Be atoms. Some of these atoms fly through the trap center and are ionized by the ionization laser. The cooling laser reduces the ion's motional energy to a level that allows stable trapping. The beam geometry relative to the trap is shown in figure 5.6. Details of this process are laid out below.
All three involved laser beams have to be aligned within a narrow range of acceptable positions and set to be within a specific frequency interval.

5.4.1 Properties and aligning of the ablation laser

The ablation laser (see section 5.1) has to hit the Be target at the right position, so that the enough ejected neutral atoms fly through the trap center. Its exact frequency is not important and cannot be controlled.
Ablation is the process by which energy from a laser pulse is absorbed by a material, in our case Beryllium, in a way, that it locally evaporates the material. For ablation to work, the material needs to exhibit absorption at the laser wavelength. For the effect to be confined to a small volume, the energy used to evaporate, has to reach evaporation temperature on a timescale short enough so thermal conduction inside the material is negligible. Irradiating with a continuous wave laser might heat up a material so much that it evaporates but that evaporation will occur over a large portion of the material and not stop immediately after the laser shuts off. A pulse laser can deposit the necessary

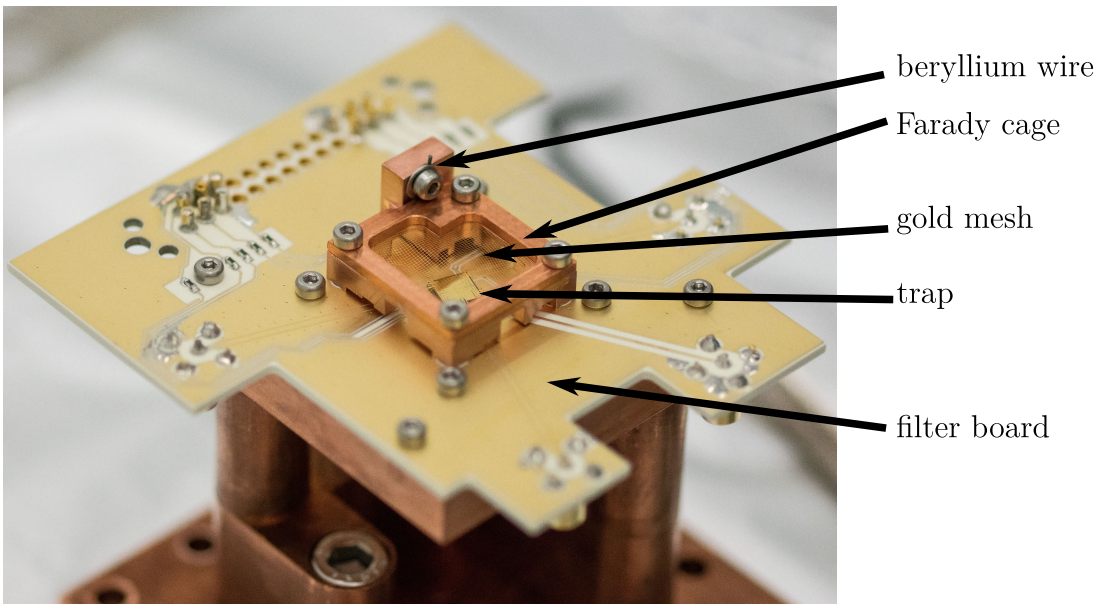

Figure 5.5: Photo of the assembled stack of trap, Faraday cage, filter board, beryllium wire and support structures.

energy within a short amount of time, so that thermal relaxation cannot occur.
The irradiance (pulse power density, measured in $^{W}/_{cm^2}$) must be low enough to not accidentally create non-linear absorption phenomena like plasma creation or cavitation bubbles, as those are unwanted effects (and can also occur, if the laser radiation is absorbed in a non-linear way). The plasma may contain ionization levels of Beryllium, higher than 1, that can be trapped and, although not resonant with the cooling beam, sympathetically cooled by co-trapped Be^+. This process might fill the trap with unwanted, dark and not controllable ions. Even if one implements elaborate ways to get rid of unwanted ions, cavitation bubbles will speed up the disintegration of the beryllium target as their dynamics may induce additional mechanical stress and can lead to fractures and expulsion of beryllium fragments. This way, significant beryllium deposits can accumulate between trap electrodes, thereby shortening them [127]. Since these unwanted effects are becoming more prominent with higher irradiance, one has to make sure not to exceed certain levels.
In a Gaussian beam with focus waist radius w_0, $1 - {}^1/_{e^2} \approx 86.5\%$ of the beam's energy passes through an area of πw_0^2. Assuming a Gaussian pulse envelope, and recognizing, that is is convention to state the full width at half maximum as pulse duration, approximately 76% of the pulse energy is contained within the stated duration. Provided the pulse energy stays constant, a shorter pulse duration and/or smaller waist radius lead to higher irradiance and therefore higher probability of non-linear absorption occurring.
To control irradiance, one way is to change the beam waist at the target. This is ill advised in our case because the distance between Be target and the air side of the vacuum system, where the focusing optics are placed, is fixed. We chose a lens with 200 mm focal

length. Making the waist smaller by placing a lens with shorter focal length is impossible, since it would need to be in vacuum. A larger waist at the target can be realized by either using a lens of longer focal length or keeping the 200 mm lens and not focusing on the target. Both options are not desirable because the area on the target, effected by ablation, is increased in this way. All other parameters kept equal, the area on the target, in which neutral atoms are produced gets bigger but the acceptance angle of the channel, that guides atoms to the trap center (see figure 5.7) stays the same, leading to a higher number of atoms being ablated but not flying to the trap.
A second way to control irradiance is to change pulse energy, which we do by adjusting laser power with a combination of two $\lambda/2$ wave-plates and polarization beam splitters, one inside the laser head and one directly behind the output aperture (see figure 5.2).
A third way to control irradiance is to change pulse lengths. This parameter is strongly dependent on the overall design of the laser cavity and q-switching mechanism, which cannot easily be changed, especially in moderately priced commercial units. Therefore pulse duration is the main parameter, apart from wavelength, that has to be considered before procuring the laser. Since non-linear effect are known to mostly occur in fs pulse lasers, we opted for a ns pulse laser. During his time as a master student, Kai Voges built a vacuum chamber with a Be target inside and a pressure gauge, that was later paired with a residual gas analyzer, attached to it. It was shown that Be atoms can be ablated with the Minilite I laser we bought.
The Be target is a 0.5 mm diameter wire, mounted perpendicular to the the filter board at a distance of $\approx$ 13 mm away from the trap center onto the Faraday cage structure (see figures 5.6 and 5.7). We found, that a 9.3 mJ pulse is sufficient to ablate enough Be atoms for single-shot trap loading. We measure the pulse energy by placing a Thorlabs S470C power sensor in the beam and setting the laser to it's maximum repetition rate of 15 Hz. The thermal power sensor's integration time is short enough so that at 2 Hz repetition rate, which we use for actual loading (see section 5.1), the power-meter displays fluctuating values. At 15 Hz it converges at the average power value. The ratio of average power and repetition rate gives the pulse energy.

Aligning the ablation beam can be divided into three main procedures. At first, we pre-align the beam, while the outer vacuum chamber is open and the inner chamber is not inside. We overlap a few mW of 1050 nm light, picked up and coupled into a fiber in front of one of the sum-frequency generation stages (see figure 5.2), with the 1064 nm beam, attenuated to barely detectable levels. We switch off the pulse laser and do pre-alignment with the CW beam. We have produced two circular disks with small apertures in them, that fit the holes in the outer chamber, which let light in an out. The holes are each 6 mm of center, the distance between parallel traveling 235 nm and 1064 nm beams. Placed on opposite sides of the chamber we guide the 1050 nm beam through both holes. Since it it overlapped with the pulse laser beam, that one also passes through. If both beams pass through, we remove the disks.
A second pre-alignment is carried out, while the inner chamber is inserted and cooled down. We place a camera[2] at the output port of the outer chamber (position see figure

[2]The Imaging Source DMK 22BUC03 camera with a Navitar Zoom 7000 lens

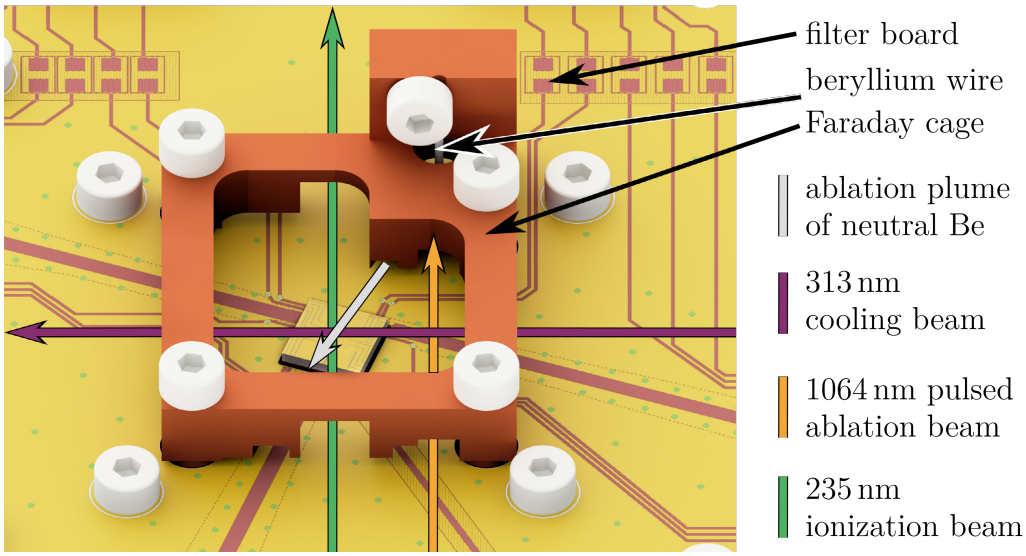

Figure 5.6: Faraday cage placed on filter board. The rendered filter board has a texture, imported from the PCB layout program. The red shapes are electrical feed lines, which in reality are made of gold (see figure 4.6 and section 4.6). Not shown here is a gold mesh on top of the cage, that can be seen in the photo of figure 5.5. The Faraday cage has openings for laser beams and over electrical lines to avoid shorts. The ablation beam (orange arrow) hits the beryllium wire and ablates atoms. The ablation plume gets mostly blocked by the Farady cage except for a small portion (grey arrow) that is directed at the trap center and passes through a channel in the cage (see also figure 5.7).

5.2), reduce pulsed laser power to a minimum and also place an ND4 filter in front of the camera to protect it further (see figure 5.8 to appreciate the damage done to the camera when we forgot the filter). With the camera, we observe the 'back' side of the beryllium wire and can detect, if the laser passes through the Faraday cage close to the wire. We cannot observe, if we focus on the wire. For that, we would need a viewport from a different angle, which does not exist. Our sister experiment at PTB has such a viewport, which makes aligning the beam much easier, than in our case. For maximum shielding of the apparatus from room temperature, we opted out of such a port. With the incoupling optics, two mirrors and a lens, we align the beam until we are certain, that it hits the wire. Camera pictures of this process are shown in figure 5.8.

The final alignment is carried out by observing the trap through the imaging optics below the optical table (see e) in figure 3.2). If we shoot one laser pulse onto the wire some light will experience diffuse scattering. Some of that light will pass through the channel that guides ablated atoms to the trap (see figure 5.7). A portion of that light will hit the trap surface and some fraction of it will be diffracted or diffusely scattered by the trap surface. Some of this light will be collected by the imaging system. Figure 5.9 reveals that it shows up as a large bight defuse spot on the EMCCD camera.

The fraction of light that is absorbed by the wire or reflected in a non-diffuse way, will not pass through the channel and therefore does not reach the imaging system.

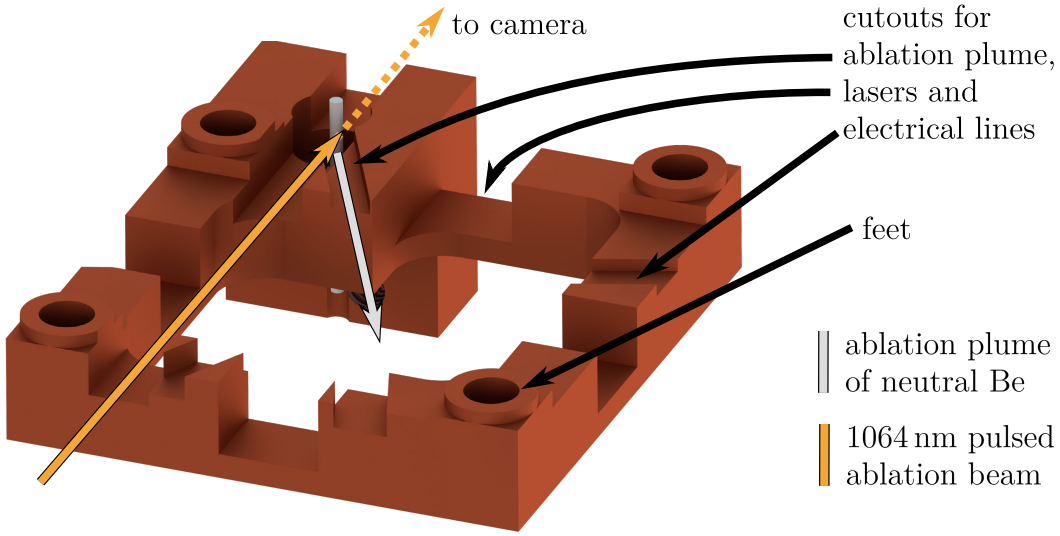

Figure 5.7: Bottom view of the Faraday cage. The round feet fit in holes in the filter board. The various cutouts are for laser access and to prevent shorting of electrical feed lines (see figure 5.6). If the ablation beam does not hit the wire, we can detect it with a camera outside the vacuum system (see figure 5.8).

Diffuse reflection follows Lambert's cosine law [128], which states, that the largest fraction of diffusely scattered light will be emitted at a 90° angle with respect to the scattering surface. If we move the laser beam's position on the beryllium wire to maximize the amount of light, seen by the camera, we make sure that we hit the point on the surface of the wire on which the tangent plane has a 90° angle to the direction of the channel. This is also the spot from which the ablation plume ejects most atoms in direction of the trap: In vacuum, an ablation plume, originating from a surface, has the shape of a semi-ellipsoid, with it's major axis pointing out perpendicular to the surface [129]. The maximum amount of atoms is ejected in direction of the major axis [129]. This is also the direction, in which most light is scattered. Therefore we maximize the number of atoms that reach the trap per ablation pulse by aligning the laser to a spot, where we maximize the light collected on the EMCCD camera.
The solid angle relative to the tangent plane at the ablation spot, in which atoms are ejected is 2π. The channel accepts only a solid angle of 0.006π, thereby shielding the trap and the rest of the system from the majority of ejected atoms, letting only those pass that have a chance of reaching the trap center. This is a major component of reducing beryllium accumulating between trap electrodes and minimizing the risk of shorting them. Another feature that prevents beryllium accumulation is the fact that we can load with a single pulse, which ejects only a small amount of atoms compared to more conventional methods like heating the Be source with an oven.

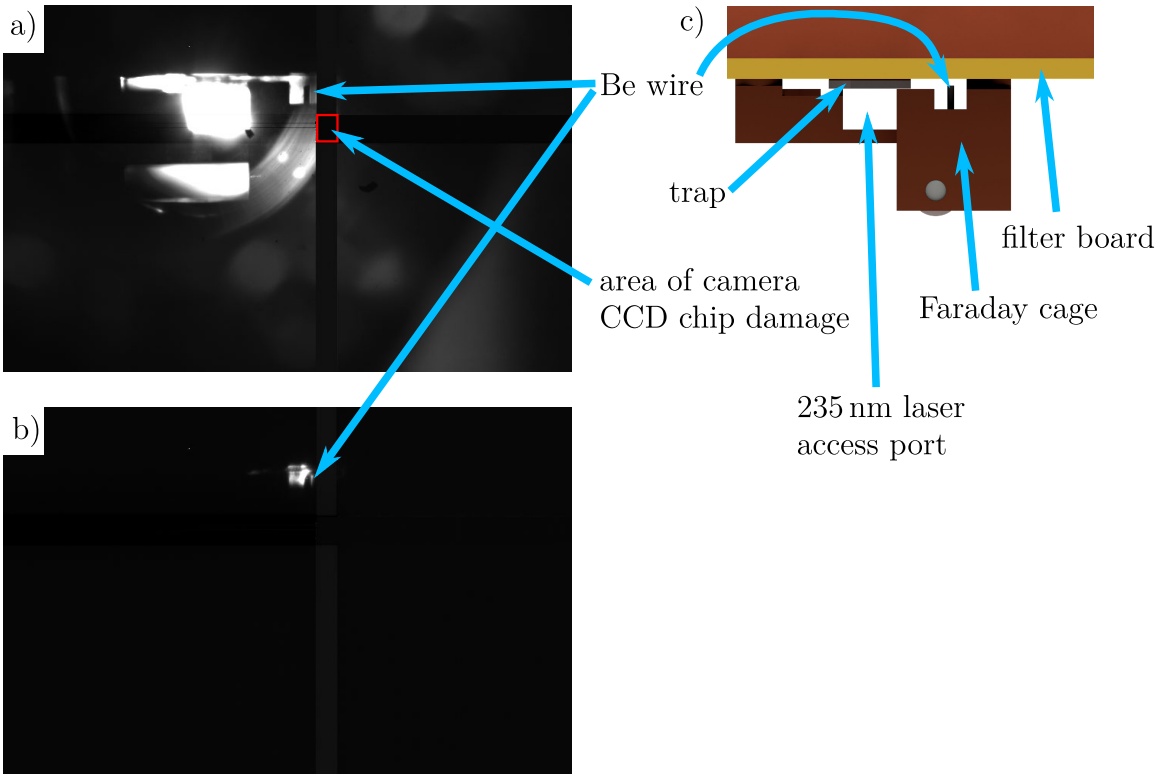

Figure 5.8: Fraday cage, mounted on filter board, cooled down to 5 K, with beryllium wire as seen by the camera.
a) Camera picture, illuminated with white light from a flash lamp. These types of picture are taken when aligning the inner vacuum chamber relative to the outer chamber during assembly. We have to make sure, that light passes the Be wire in order for laser alignment to succeed. If the wire cannot be seen, the relative angel of both chambers is off and the ablation laser won't be able to hit the wire. Notice dead black pixels, marked by a red border. By accident a high energy laser pulse hit the area. Note also a black vertical line originating there and a thick horizontal line reaching to the right as well as several thin horizontal black lines reaching out to the left. These areas are not sensitive to light anymore.
b) Camera picture of the ablation beam hitting the tip of the beryllium wire. If the camera shows such a picture, the ablation beam is sufficiently pre-aligned. The last alignment step can commence from here.
c) Rendered image to help identify different components in the camera pictures. The scale is chosen to match the other pictures.

5.4.2 Properties and aligning of ionization and cooling beams

The final alignment process of both, ionization and cooling beams, is the nearly identical. In the next section, I describe, how we guide the 235 nm beam into the chamber, followed

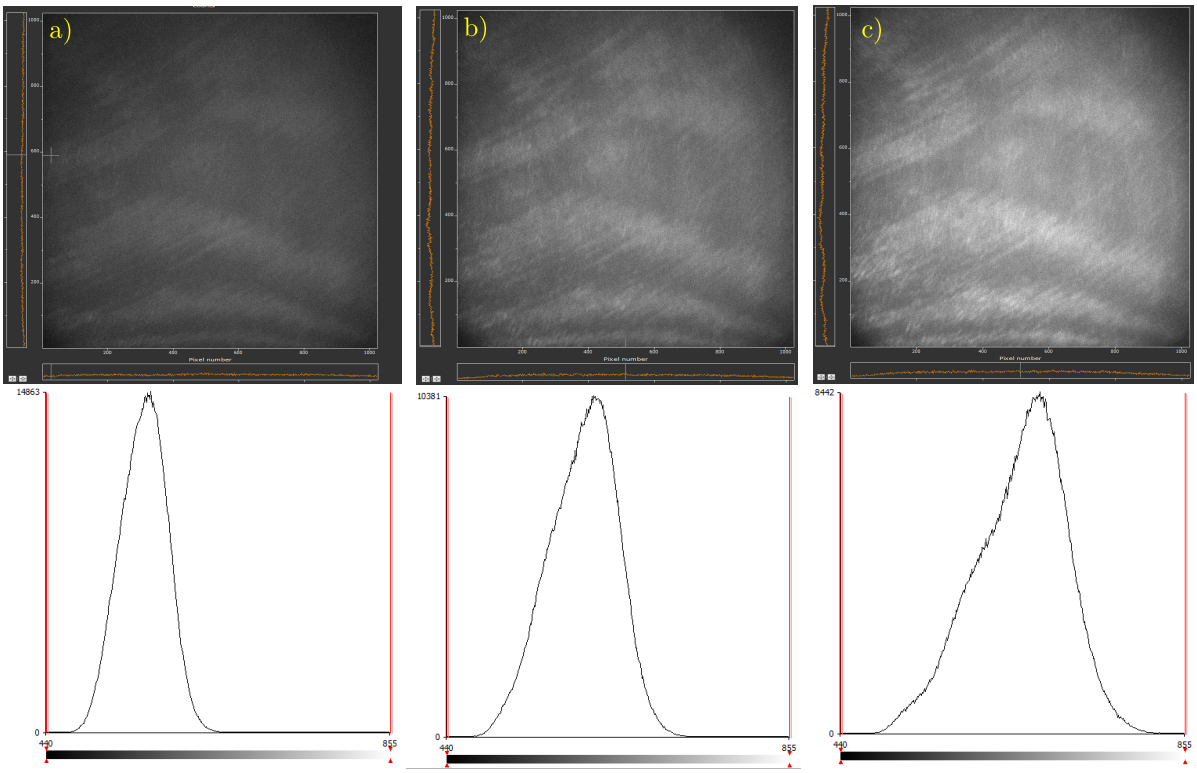

Figure 5.9: Determining optimum ablation laser position on the beryllium wire. Top: The pictures show the light pattern detected by the EMCCD camera. Bottom: The histograms corresponding to the pictures. Note that from left to right, the maximum of the histogram moves to brighter regions. a) Beam 250 µm off target. b) Beam 150 µm off target. c) Beam on target.

by a section about how to do the same for the 313 nm beam. Afterwards, there is a section about aligning both beams to hit the trap center.

Guiding the ionization beam into the vacuum chamber

Every time, the ionization laser is directed at the trap, some 235 nm photons can charge up dielectric surfaces of the trap, leading to unwanted stray fields. Therefore, we try to keep the exposure to a minimum.
For aligning, we use about 0.1 mW of 235 nm light. The beam is transfered to the elevated breadboard around the outer chamber via a periscope. All our highly reflective mirrors for 235 nm have a very small angle of incidence, making them transparent for a small percentage of light. This leaking UV light is a not ideal but usually not harmful. The periscope introduces a beam perpendicular to the optical table. Caution has be be taken to avoid leakage of that beam into the lab. The beam is widened by a telescope to allow for a smaller focus waist after being focused into the vacuum system by an additional 200 mm focal length lens; for the beam path see figure 5.2.

Guiding the cooling beam into the vacuum chamber

Although 313 nm light does not induce as many unwanted charging effects as 235 nm light, we still lower the power to about 100 µW. The cooling beam is delivered to the elevated breadboard via an optical fiber (see section 5.3). The fiber is not connectorized. A lens behind it collimates the beam. As with the ionization beam, two mirrors and a lens are used to guide the beam into the chamber. Since this laser is used to drive polarization sensitive transitions in the ion, an αBBO Glan-laser polarizer followed by a $\lambda/2$ and a $\lambda/4$ wave plate ensure polarization control. All three are mounted on a rotation mount. The waveplates are additionally mounted on a normal mirror mount to allow for tilting along two axis.

Aligning both beams to hit the trap center

The ideal alignment is achieved, when a beam is propagating parallel to the trap surface and passes directly through the trap center, which is 70 µm away from the surface.
First, we guide the beam onto the trap surface under an angle, so it is not parallel. It is reflected by the trap and, provided that the angle is sufficiently small, leaves the vacuum chamber at the other side, where it hits a piece of paper. The shape of the spot gives us informations about the angle. We change the angle by aligning the two mirrors, located in front of the input coulper lens. Since there is a vacuum chamber between these mirrors and the piece of paper, we cannot directly see it, while adjusting, but film it with a Sony A68 with a 100 mm 2.8 macro lens attached. The different shapes, we observe are shown in figure 5.10. If the beams are reflected completely, we will see a round spot. If we change the angle to be more parallel to the surface, while still hitting it, we can see two spots appearing. One produced by a portion of the beam that passes over the surface and another spot from a portion that is reflected. The wider these spots are apart, the larger the angle between surface and beam. We align the optics so that the two spots are touching and nearly vanishing. Now we have created a situation, where the beam is nearly parallel but still illuminates the trap structures.
We use the 3-D translation stage shown in figure 6.8, to scan the objective over the trap surface and image it onto the EMCCD camera below the optical table (see figure 3.2). At some position, we will find the laser beam on the surface. We alternate small movements of the beam with those of the objective to guide the beam to known structures like gaps between trap electrodes and follow those structures to the trap center. We make sure that the 235 nm beam illuminates corners of DC electrodes 5 and 10 (points γ and δ in figure 5.11) as this ensures that is passes through the trap center as it is located between the two points. For the 313 nm beam, we use corners of the microwave carrier electrodes (points α and β in figure 5.11). Figure 5.11 also shows pictures taken during this process. Although it is convenient to have these points of orientation to hit the trap center, notice that neither beam is orientated parallel or perpendicular to the trap axis, which runs parallel to the orange electrode.
In case of the 235 nm beam the angle is not critical as it would just introduce a slightly different Dopper shift with respect to the ablation plume, which can be compensated

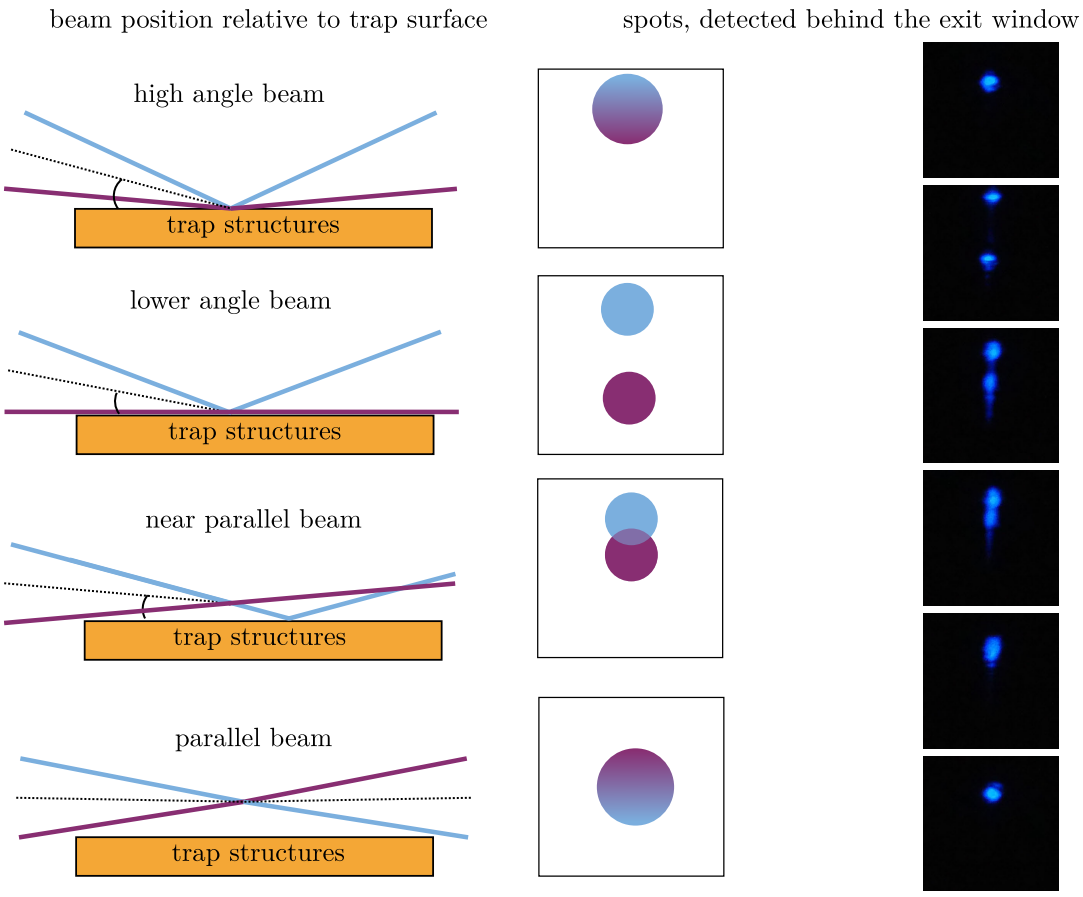

Figure 5.10: Spots seen on a paper screen during 235 nm and 313 nm beam alignment. Depending on the angle between laser and trap surface, one or two spots can be detected. If the spots are nearly joined, the laser is nearly parallel to the surface but still quite well visible as a lane of light by our imaging system (see also figure 5.11).

by adapting the laser frequency. In practice we set the frequency to the middle of the interval, in which we are able to trap and whatever Doppler shift change occurs does not matter.
In case of the 313 nm beam, we have to ensure that it is not perpendicular to any trap axis, as it has to have an overlap with each axis to allow for cooling. Later, during detection sequences it also has to be parallel to the magnetic field axis B_0. Passing it through points α and β does not make it perfectly parallel to B_0. Optimization of that angle can be done later by optimizing state preparation and detection on trapped ions.

Now that both beams are pointing along the right direction on the trap surface, we need to make them more parallel to the surface and move them away from it by 70 µm, since that is, where the minimum of the trapping potential is.
To make them more parallel, we maximize the overlap between the double-spots shown

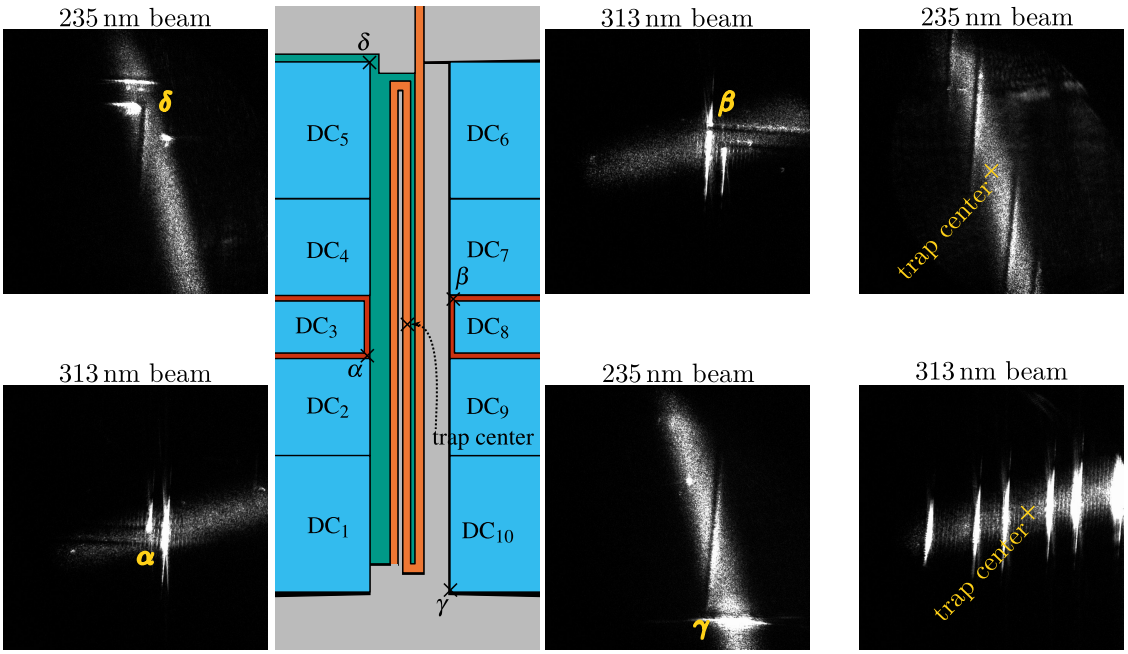

Figure 5.11: Alignment of 235 nm and 313 nm beam to the trap center. Making sure to hit point γ and δ with the ionization beam and points α and β with the cooling beam leads to both beams hitting the trap center. All pictures, that display the same wavelength have been taken with the respective beam at the same position. Only the objective was moved. Point γ is not hit perfectly but well within tolerance.

in figure 5.10 until only one spot appears. The beams are now sufficiently parallel to the surface.
If a beam passes through the incoupling lens, close to it's center, in paraxial approximation, small movements of the lens in the plane perpendicular to the optical axis, is directly transfered to movements of the focus, also in the plane perpendicular to the optical axis. If the lens is moved, e.g by x µm, the focus will also move by x µm in the same direction. Therefore we move the incoupling lens by 70 µm in the appropriate direction and the beam is in position, ready to trap.

5.4.3 Trap loading sequence

First we switch on the magnetic field coils (see section4.7) and apply all DC and RF voltages to the trap electrodes to provide the quantization field as well as the trapping potential (see chapter 4). To load the trap, the different beams have to be switched on and off according to a specific timing. We control all switches via our experimental control system's TTL outputs and implement the timings accordingly. The ablation beam is controlled via a self-built triggering device, described in section 5.1. We have implemented a Thorlabs SH05 mechanical shutter, connected to a Thorlabs SC10 controller that accepts TTL pulses, directly behind the second doubling cavity of the ionization laser. The

shutter is not directly bolted to the optical table but rests on a foam cushion that absorbs mechanical noise, which would otherwise disturb the cavity-lock. We have placed a TTL controlled switch between every signal generator and corresponding amplifier that feed the AOMs of the 313 nm beam line.
We switch on the near and far detuned cooling beams, with power levels around 10 µW and 250 µW, well above saturation power, which is in our case at ≈ 5.5 µW, and leave them on all the time until we trap an ion.
We open the shutter of the ionization beam for 1 s. Th shutter is mostly vibrationally decoupled from the cavity but sometimes the cavity lock is not perfect after switching and we allow the cavity 0.4 s to reach the required stability and output power.
Now we trigger the ablation laser for 0.5 s. Since we do not know, at which specific time within this 0.5 s interval a pulse is fired (see section 5.1), we leave the ionization laser on for an additional 0.6 s. Shortly after the ablation laser has been fired, neutral atoms from the ablation plume will fly through the trap center and ionized by the ionization beam, trapped by the potential and cooled by the 313 nm beam. We shut off the far detuned cooling beam and reduce the power of the near detuned to normal operating levels of 2 µW.

System parameters and loading efficency

Alignment of the ablation beam is critical to achieve a high enough atom flux. The procedure described in section5.1 is systematic and repeatable enough to allow single-shot loading, provided all other parameters are within an acceptable interval.
Alignment of the 313 nm laser is also sufficiently systematic and repeatable with the procedure described in section 5.4.2. It might not be at the perfect position but we have not observed a case, where it was too far off the trap center. If it is slightly misaligned, less light will scatter the ions but since we use more power than really required, that is of no concern.
The correct alignment of the ionization beam is of more importance. The position of the incoupling lens and therefore the position of the 235 nm focus, has to be correct within a small margin. We can only trap Be ions that were ionized within the trap center. Therefore a neutral atom has to fly through the center and undergo ionization. We can ionize atoms at the trap center even if the laser focus does not exactly overlap with the center. The beam has a slightly elliptical profile. The focus is also elliptical and has an intensity full width at half maximum (FWHM) of approximately 42 µm in horizontal and 25 *upmu*m in vertical direction.
The region that we can scan with the beam and still achieve sufficient power at the trap center is therefore also elliptical. With 1.5 mW of power and assuming the focus is perfectly at the trap center, we could move the incoupling lens around within an ellipse, perpendicular to the optical axis, having a major horizontal axis of 50 μm and a minor vertical axis of 30 µm to still be able to ionize atoms.
Assuming that at we can still ionize with half the maximum intensity and combining the ellipsis in which we can move the beam and still ionize with the focus ellipsis at FWHM, we can determine the area in which we can trap. It is an ellipsis with a major

horizontal axis of 92 µm and a minor vertical axis of 55 µm. This can change if the cooling laser position changes or if we use a different 235 nm laser power. Increasing 235 nm power would probably increase that area but can induce more stray charges on dielectric surfaces (see below).
The frequency has to be between 1276.0780 and 1276.0786 THz to reliably trap.
During first trapping trials, scanning the ionization laser frequency and position was the main key to achieve successful trapping.
Now, with all parameters sufficiently under control, we can reliably trap 3 ions with a single shot. Frequently we trap up to 5 ions with a single shot. If ionization beam position is slightly off, we usually only trap 1 ion per shot.
Since our ion-lifetimes are only dependent on a functioning cooling laser and are not limited by background gas collisions (see section 3.4), we can now take care of trapping once at the beginning of each workday and only have to re-trap if we run diagnostics that require the ejection of ions from the trap, such as taking a background noise image for detection calibration.

Proposed trap loading improvements

We run the inherent risk of charging dielectric surfaces by hitting them with 235 nm photons. These charges can potentially induce stray fields that disturb the trapping potential. Due to the low temperatures, these charges will not undergo the random walk of Brownian motion and therefore not reach a neutralizing trap electrode after some time. With every time the 235 nm laser is on, we probably accumulate more charges. At the time of this writing, we see so far unexplained trapping potential behavior, which could be connected to accumulated charges. Further investigation is needed.
A few optimization strategies are:
1) Reduce ionization laser power. We can reliably load three and more ions with one shot of 1.5 mW. Reducing that power leads to, on average, less ions per shot. We could determine the power levels at which we load one ion reliably. For comparison: Our sister experiment at PTB loads with 0.5 mW but has a stronger focus due to the incoupling lens being closer to the trap. However, that experiment is at room temperature and features a decay of stray charges due to Brownian motion.
2) Optimize loading sequence timings: 2.1) Because of mechanical feedback between laser shutter and cavity-lock, we currently open the 235 nm laser shutter and wait for 0.4 s before attempting to load with an ablation pulse. To reduce the wait time, we can either implement a more sophisticated vibration decoupling of shutter and optical table or use an AOM as an optical switch. 2.2) Since the ablation laser has to be used in complete internal trigger mode, we have implemented a crude workaround to be able to control it with our experimental control software (see section 5.1). There is a timing window of 0.5 sec, during which the ablation pulse is fired. We do not know, when exactly the pulse is emitted. During all that time, the ionization laser is on. The easiest option is to buy a new laser, that does not suffer from this trigger to shoot jitter problem, but this is probably quite expensive. A more complicated but cheap option is to shoot two pulses of the ablation beam with a known repetition rate but letting only the second one reach

the target. The first gets emitted at an unknown point during a 0.5 s window. This first pulse could be detected on a photo-diode. Since the repetition rate is known, a shutter, which was blocking the first pulse, could be opened to let the second one through. The ionization beam could be synchronized accordingly.
Implementing both timing optimizations, we can probably reduce the pulse length of 235 nm light from 1.0 s to about 0.1 s. Combining this with less 235 nm power, charging of dielectric surfaces could be reduced significantly.

Chapter 6

Imaging

The imaging system consists of three main parts, an in vacuum Schwarzschild-type objective, photo-detectors and a relay optics arrangement to transfer light from the former to the latter. While the objective was designed by Christian Ospelkaus and first commissioned at NIST's ion storage group in 2009, additional expertise on how to assemble and mount it, which detectors to use and how to design the relay optics was gained over the course of this work.

6.1 Schwarzschild objective

Known from telescope design for astronomy, a Schwarzschild objective consists of two spherical mirrors, concentric with each other, separated by twice the system's focal length [130]. Provided that the aperture stop is located at the common center of both mirrors, third-order spherical aberations, coma and astigmatism are corrected for [130]. The optical path through the objective used in this work is shown in figure 6.1 a). The image was extracted from ZEMAX OpticStudio, the software used to design and simulate the objective. The objective consists of 5 pieces (see figure 6.1 f)): a primary mirror with a $\approx 5\,\mathrm{mm}$ diameter hole in it and a radius of curvature of $r_1 \approx 22\,\mathrm{mm}$, two glass pillars with dimensions of $\approx 4 \times 4 \times 13\,\mathrm{mm}^3$, a glass beam with dimensions of $\approx 2 \times 2 \times 51\,\mathrm{mm}^3$ and a secondary mirror with a radius of curvature of $r_2 \approx 7\,\mathrm{mm}$. The working distance is $\approx 8\,\mathrm{mm}$ and the image is formed $\approx 180\,\mathrm{mm}$ behind the objective. The magnification is ≈ 40. The mirror coatings are made out of aluminum with a protective coating. The objective is completely achromatic. The numerical aperture of the primary mirror is NA=0.5 and it collects light in a solid angle of 0.268π which means that it can theoretically collect 6.7% of the photons emitted by an ion in the center of the object plane. Taking into account that the glass beam and the secondary mirror cover about 34.7% of the light that the primary mirror would collect, about 4.4% of the light, emitted by an ion in the center of the object plane is collected and imaged.
A batch of four objectives of this kind was ordered by NIST. They were delivered in separate parts that needed to be assembled. At Sandia National Labs, the dimensions of all pieces were measured using a Zeiss coordinate measurement machine and later it was determined, which combination of pieces would fit together best. We obtained one batch of five pieces and were tasked with the assembly procedure. At PTB it was possible to make use of optical bonding techniques [131] to assemble the objective.

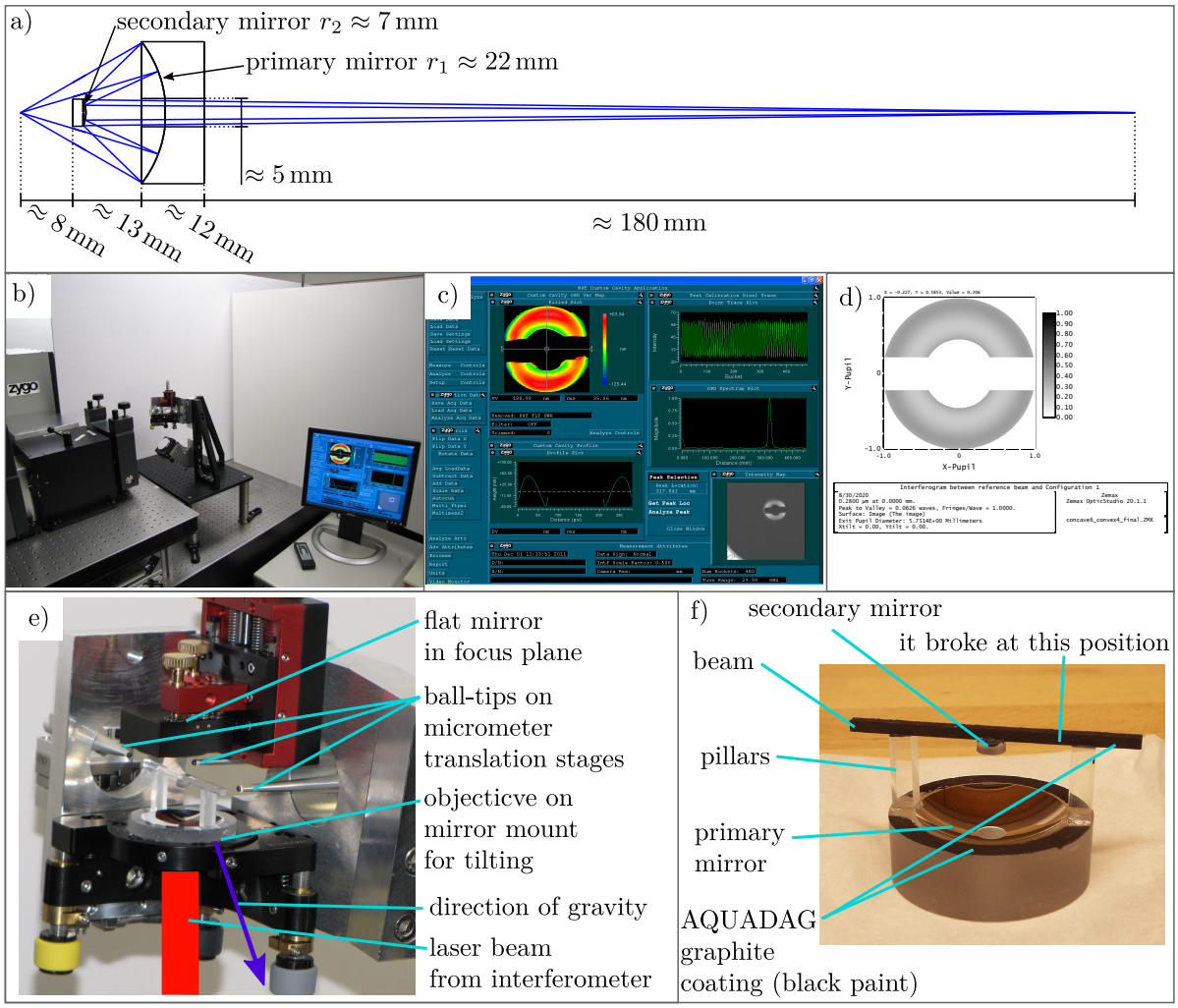

Figure 6.1: a) Optical path. The ions would be in the focus on the left side and are being imaged to the focus on the right.
b) Alignment apparatus in front of a ZYGO interferometer.
c) Screenshot of ZYGO control software while the objective was aligned. Top left and bottom right: False color and gray scale picture of interferogram.
d) Simulation of interferogram.
e) Close-up picture of alignment apparatus after bonding was finished. Unbonded, the glass beam would slide in the direction of the ball tips.
f) Picture of bonded objective, partially painted with an AQUADAG graphite-water suspension. Before a first characterization, it broke at the marked position.

The two pillars were bonded to the primary mirror. The secondary mirror was bonded to the middle of the beam. In a next step, the beam had to be bonded on the pillars in such a way that the relative position of primary and secondary mirror was as precise as possible. According to simulations, a slight relative positioning error of only 3 µm

would lead to an increase in RMS spot radius of 71%. An error of 10 µm would lead to an increase of 374%. Therefore a positioning device with at least µm accuracy and a method of observing the effects of relative mirror position change on the image quality was needed. It was developed in the context of Thomas Borchard's undergraduate work. ZEMAX OpticStudio can simulate the interferogram of a given optical layout. The simulated interferogram of the objective is shown in figure 6.1 d). At PTB a ZYGO interferometer with a probe arm of more than 5 cm diameter was available to acquire real time interferograms during the assembly. The idea was to place the objective in the probe arm of the ZYGO and move the beam relative to the pillars until an acceptable interferogram was measured and then bond it in place.
We designed an apparatus that can hold the primary mirror and is able to tilt it. It is shown in front of the ZYGO in figure 6.1 b) and a close-up is shown in figure 6.1 e). We tilted it slightly and put droplets of octane on the pillars. The octane makes the surface slippery and prevents the bonding process from starting. We placed the beam on the pillars and since it all was tilted and slippery, gravity would pull the beam to the side. Three ball-tips were mounted onto three micrometer translation stages and kept the beam from falling off the pillars. We adjusted the position of the beam relative to the pillars by moving the ball-tips until the interferogram was in good agreement with simulations. A picture of the final interferogram is shown in figure 6.1 c). We then replaced the octane with the bonding fluid. Since the ball-tips were still in position, the beam slit back into place before bonding was complete. The measured interferogram matched the simulation very well.

We painted the glass surfaces of beam and primary mirror with AQUADAG, a graphite-water suspension. This left a black graphite coating on places that do not contribute to the image formation but would introduce stray-light to the system and thereby effectively reduce contrast. We were in the process of characterizing the optical performance of the objective when we broke it by accident. The beam broke into two parts. The position of the crack is shown in figure 6.1 f). No pieces fell onto the primary mirror and it was left undamaged. The secondary mirror was also unscratched. The length of the beam was still enough tp cover the distance between the pillars. In an effort to repair the damage, we forcefully removed the two parts of the beam from the pillars and the secondary mirror from the larger beam part. We hoped to be able to bond the small mirror to the new center of the larger beam part and this new beam again onto the pillars. Unfortunately, the surface quality that was left from breaking up the bonds, was not good enough anymore. The bonding procedure failed. We resorted to a last-ditch attempt by using a UV hardening, UHV compatible glue instead of bonding fluid. After placing the glue on the pillars, we tried to apply the same alignment procedure as before but the glue was too viscous to allow for gliding of the beam on the pillars at the existing tilting angle. We placed the primary mirror with the pillars on a table and aligned the secondary mirror by hand and only guided by eye-sight and hardened the glue.

Although not at optimum performance, the newly assembled objective works and was used in during this work for imaging trapped ions.

We have characterized the objective by back-illuminating a negative USAF 1951 target (Edmund Optics NT55-622) with a sodium vapor lamp that emits at 589 nm and imaging that target with the objective onto an Andor iXon DU885 EMCCD camera. The results are shown in figure 6.2. An area of about $250 \times 250\,\mu m^2$ of the target was imaged on the $8 \times 8\,mm^2$ EMCCD chip. Since the target is larger than $250 \times 250\,\mu m^2$, we moved it around to take pictures of relevant lines. The resulting images were processed in ImageJ in the following way:

Over each element of 3 lines, we took intensity profiles perpendicular to the lines. As

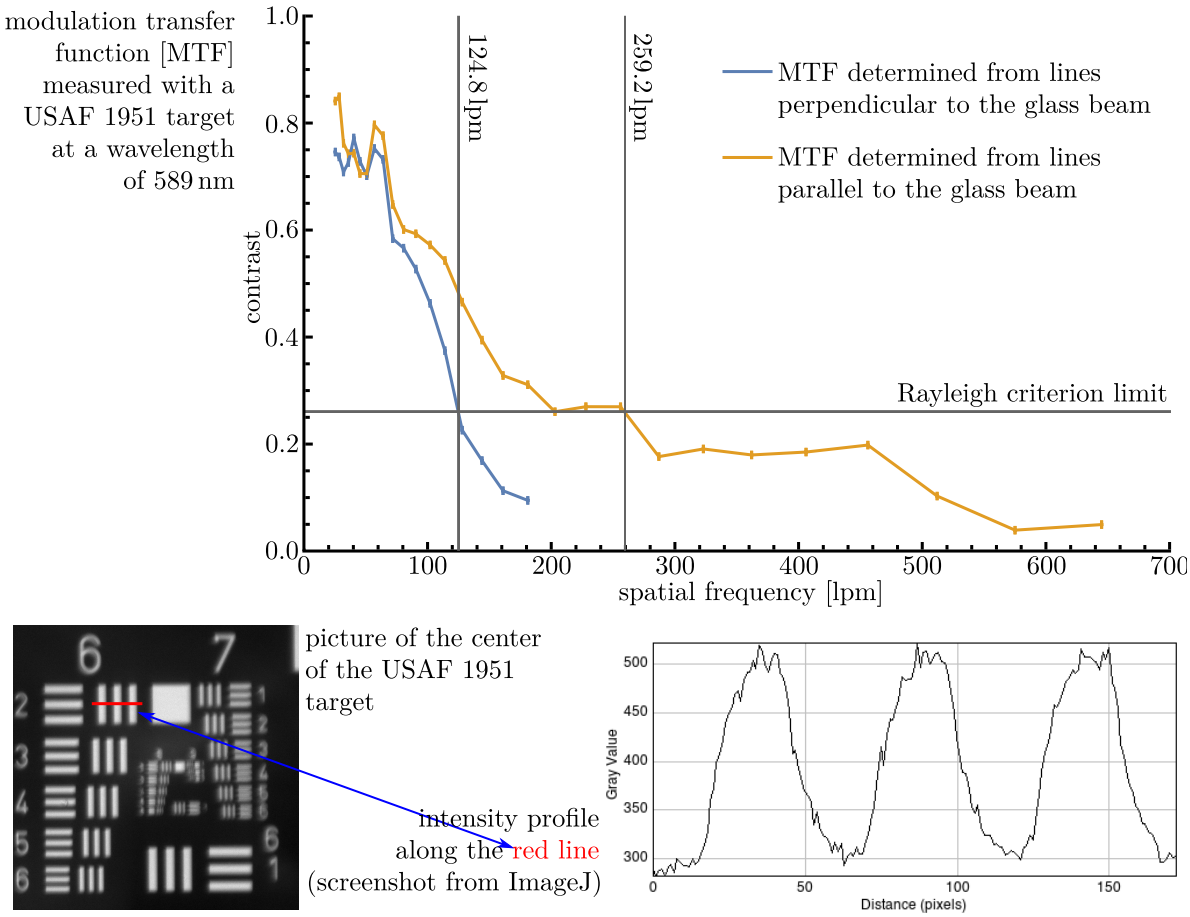

Figure 6.2: Top: Modulation transfer function of the objective at 589 nm. Bottom left: Picture of the center of a USAF 1951 target as seen by the objective. Bottom right: Intensity profile as produced by ImageJ.

an example, for vertical lines we took a horizontal intensity profile, starting at the top of the element, moved the line one pixel down and took the next intensity profile. We repeated for as often as possible until the element was scanned completely. We averaged over all profiles belonging to one element. There are three bright lines with two dark in between. We calculated contrast between the maximum intensity and the minimum of the two dark lines. Since the spatial frequency (in line pairs per mm or lpm) is known

for each element, we plotted contrast over spatial frequency to arrive at the modulation transfer function of our objective. We did this for two orthogonal directions of target-lines. The contrast between horizontal lines is worse than between vertical lines of the same size. This is due to the glass beam of the objective being parallel to the horizontal lines and Fraunhofer diffraction at the beam smears out the direction perpendicular to the beam, leading to more light between the bright horizontal lines. If we take the Rayleigh criterion for resolution as a reference, we end up with a maximum resolvable spacial frequency of 124.8 lpm in the direction perpendicular the the glass beam and 259.2 lpm in the parallel direction. Since this measurement was done at a wavelength of 589 nm but the ions emit 313 nm light and the fact that the objective is fully achromatic, we can scale the results with the wavelength and calculate the maximum resolvable spatial frequencies at 313 nm to be 234.8 lpm and 487.8 lpm. If we use the Rayleigh criterion, this means that at 313 nm two point can be distinguished, if they are at least 2.1 µm apart in the direction perpendicular to the glass beam or 1 µm apart in the parallel direction.

6.2 Relay optics

The objective is located inside the inner vacuum chamber. The light collected by the objective is focused about 180 mm behind it, which is about 10 mm below the outer vacuum chamber. Although it might have been possible to place a detector at this position, it is more advantageous to place an aperture that can cut off stray light and a relay optics system to re-image the focus onto a detector. This also leaves space to put in optical filters if the experiment requires it. As an example: In the future, one can think of implementing a second ion species for sympathetic cooling. The cooling light of that species would lead to errors in detecting the states of the sympathetically cooled species. In the focus plane, we placed an Owis SP40 slit with four blades that can be adjusted and form an arbitrary rectangular aperture with maximum size $7 \times 7\,\mathrm{mm}^2$. There were two generations of relay optics in use.

6.2.1 First version: Reflective relay optics

Figure 6.3 shows the optical layout and the mechanical design of the reflective relay optics arrangement. All components are mounted in a light-tight box. The four blades of the slit can be remote controlled by stepper motors. The light is back reflected by a flat mirror at an angle of 19.5° onto a curved mirror with a radius of curvature (roc) of 500 mm. It images the intermediate focus onto either an Andor iXon Ultra DU-888 EMCCD camera or a Hamamatsu H10682-210 photomultiplier tube (PMT). With a motorized flip mirror we can choose which of the detectors is illuminated. The optical path length from the slit to the curved mirror is 500 mm, which is the same as the length from the curved mirror to the camera. The resulting magnification factor of 1 preserves the objective's magnification of 40. A Thorlabs FW102C motorized filter wheel

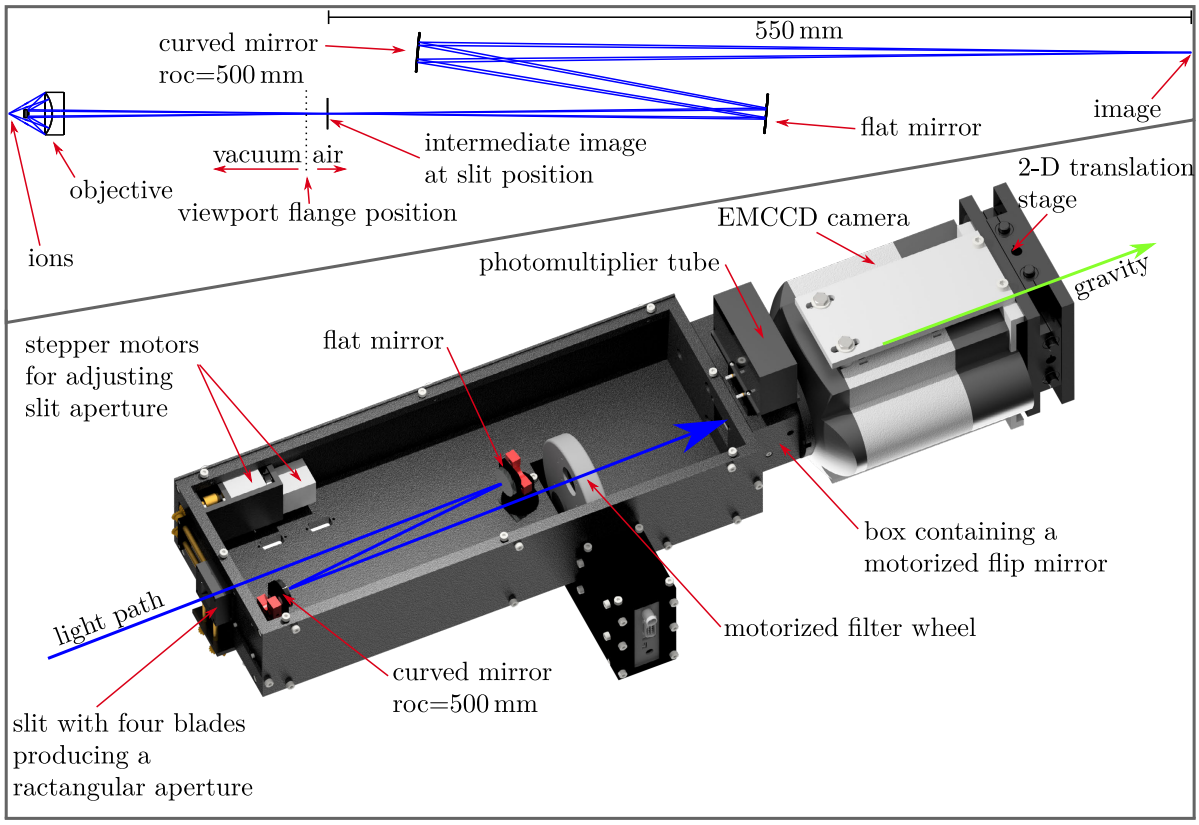

Figure 6.3: First version of the imaging system. Top: imaging path as simulated in Zemax OpticStudio. Bottom: Rendering of the relay optics and detection system.

is located in the light path. The advantage of this system is that is continues to be completely achromatic. Therefore it is suitable for simultaneous imaging of multiple ion species that emit on multiple wavelengths. There is one optical disadvantage: The curved mirror is tilted against the optical axis, which introduces an astigmatism. The resulting point spread function of an ion on the camera would be, if everything else is perfectly adjusted, elliptical instead of round. This is only a minor inconvenience since we can rotate the relay optics system so that the images of the ions smear out in a direction that is perpendicular to the direction of the trap axis along which the ions are arranged. Another disadvantage was discovered during first trapping trials. To keep the astigmatism as small as possible, we kept the angle of the mirrors with respect to the optical axis as small as possible. This leads to the flat mirror being very close to the light path, going from the curved mirror to the camera. This restricted the diameter of the flat mirror and therefore the amount of light collected. The objective has a field of view of about 400 µm. An ion directly on the optical axis would be imaged to the middle of the slit and the light would travel on to hit the center of the flat mirror and then the center of the curved mirror. The light from an ion slightly off axis would hit the flat mirror further to the side and the curved mirror even more to the side. An ion more than 50 µm off axis would not be imaged by the two mirrors, thereby reducing the

effective field of view from 400 µm to 100 µm.
A larger mirror would increase the field of view but also increase the induced astigmatism. In the early design stage, we agreed that a field of view of 100 µm would be enough and built the relay optics system accordingly.

During first trapping trials three major complications with the imaging system were discovered. 1) The adjustment range of the objective mount was too small and inaccurate. 2) During adjustment, parts the graphite coating on the objective became loose and were deposited on the trap surface. 3) The field of view was too small for convenient debugging of the first trapping trials.

First version of the objective mount

The first objective mount is shown in figure 6.4 a) and b). It is bolted to the inner wall of the inner vacuum chamber (see figure 6.4 c)). It includes an attocube ANPz101 nanopositioner with a movement range of 5 mm along the optical axis of the objective that is used for focusing. It is connected to a controller outside the vacuum vessel which itself is connected to a computer. The objective rests with the graphite covered face on 3 pins that are pressed against the objective by small beryllium-copper springs (see also figure 6.8). Except for the attocube, all positioning has to be done manually before cooldown. The rotation has to be correct such that the glass beam does not interfere with the beryllium wire mount on the Faraday cage (see figure 5.6). The lateral positioning is done by adjusting two screws that push the objective against one spring supported pin. The springs used in this mount can balance out different thermal contractions of objective and mounting structure during cooldown.
The objective had to be placed manually above the trap. The inner chamber was closed, transported 50 km by car from the PTB cleanroom to the Hannover lab, mounted to the cold-head, evacuated and cooled down. Any alignment errors would only be visible once it was cooled down. Reliable objective positioning was complicated and it had to be redone several times before the trap center was visible on the camera. By that time, multiple graphite particles were accumulated on the trap surface. Figure 6.4 d) shows pictures taken with white light and with 313 nm light. The particles are clearly visible under both lighting conditions. This trap was designed to have a trap center that was 35 µm away from the surface. The most prominent particle was large enough that is was still diffracting the 313 nm beam even if the latter was 35 µm lifted from the surface to hit the trap center. Trapping was not possible with this trap. In addition to producing a lot of stray light and hindering laser beam paths, graphite is an electrical conductor at cryogenic temperatures [132]. We were lucky that no particle was shorting any electrodes, but their presence on the electrodes effectively changes the electrode geometry in the vertical direction and might have distorted the electric field and therefore the trapping potential. The left picture in figure 6.4 d) was taken with this version of the relay optics system, while the other picture was taken with its successor. In the picture on the left, it is not clear, if the trap center is in the picture because no discriminable features were

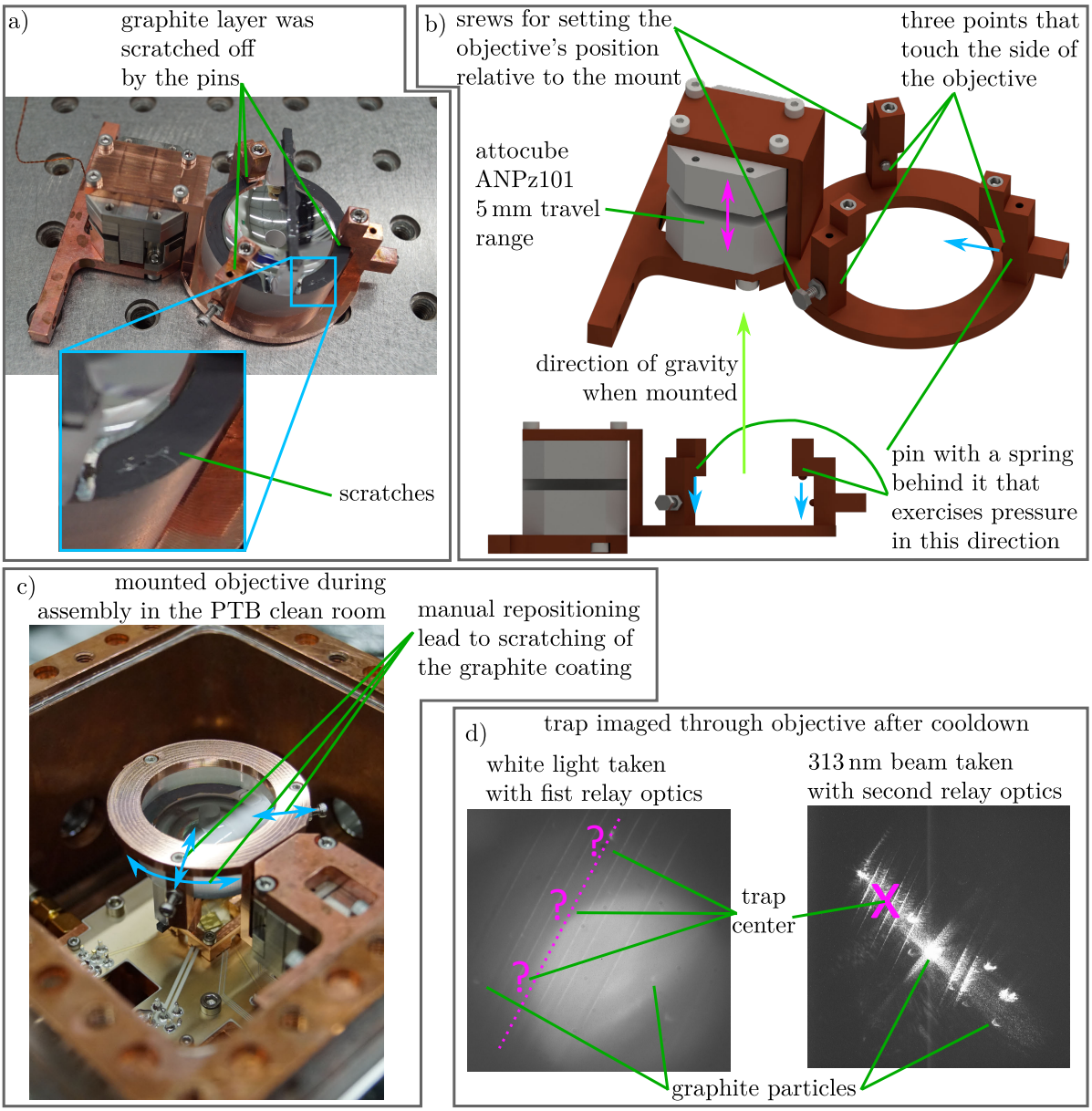

Figure 6.4: a) Picture of the first version of the objective mount with the objective present to show the scratches in the graphite coating produced by moving the objective within the mount. b) Rendering of the first generation mount. c) Picture of the objective mounted in the inner vacuum chamber. During objective alignment it was necessary to move it around, thereby producing the scratches seen in a). d) Pictures of graphite deposits on the trap surface. Left: Trap image taken with the first version of the relay optics setup with white light. The exact location of trap center could not be identified. Right: Trap image taken with se second version of the relay optics setup with 313 nm light. The trap center is marked.

visible that could indicate the location on the chip. This led to the conclusion that the field of view was so small. In the right picture, we were able to identify the trap center. It was taken after modifications were done to the relay optics. These modifications are described below.

6.2.2 Second and current version of the relay optics setup

To realize a wider field of view, we either had to replace the mirrors in the relay optics setup by larger versions, which would have entailed more astigmatism, or we had to use lenses instead. We opted for two lenses on an optical rail for two main reasons: They would fit into the existing box and they would allow for changing the magnification smoothly between of 10 and 95. A lower magnification was deemed useful for orientation on the chip and for including the trap center in the picture, even if it was slightly off center. The two pictures in figure 6.4 d) were taken with the objective in the same position but with the modified relay optics setup. Only in the right picture was the identification of the trap center location successful.
The new relay optics setup is shown in figure 6.5. We first implemented the lens-based

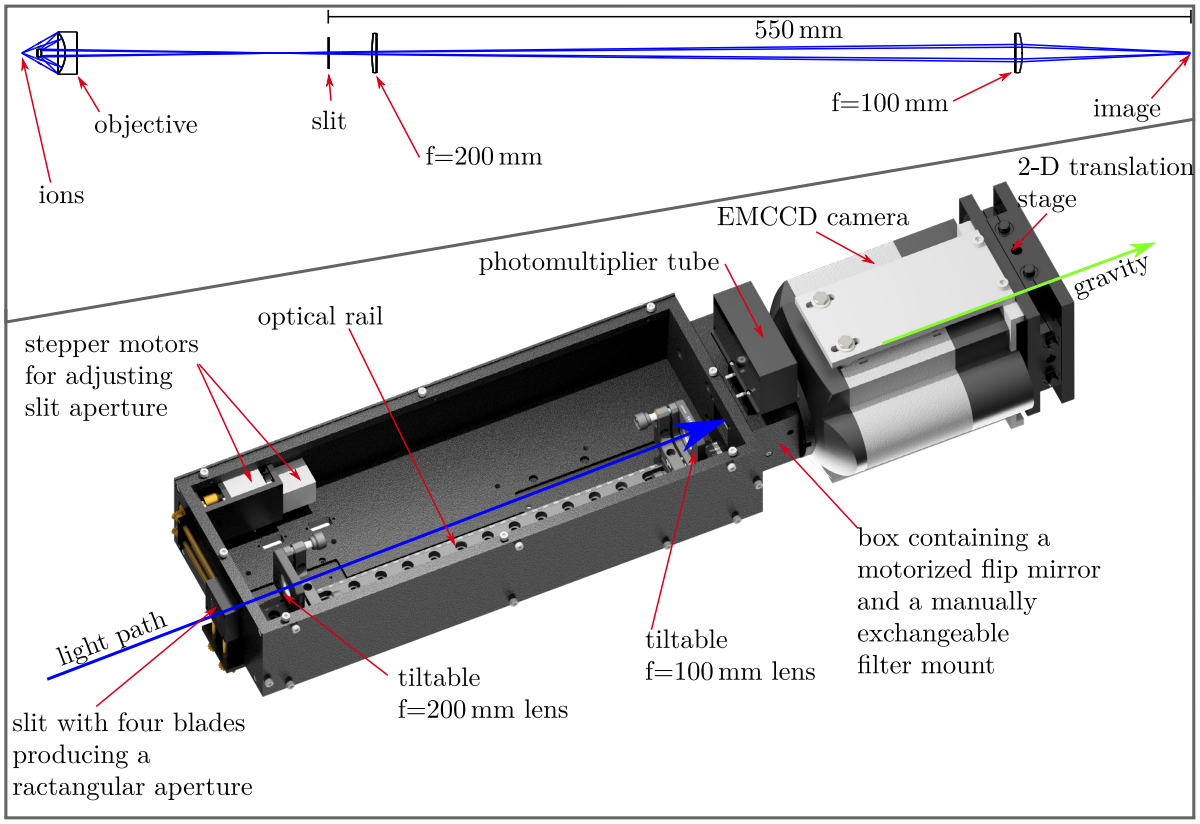

Figure 6.5: Second version of the imaging system. Top: imaging path as simulated in Zemax OpticStudio. Bottom: Rendering of the relay optics and detection system.

setup while the graphite covered trap was still under vacuum. We were finally able to see the location of the trap center and were optimistic to be able to trap. We aligned the laser beams such that we could see them touching the trap surface below the trap center. Figure 6.4 d) shows the result for the 313 nm beam. Since the objective was focused on the surface, we needed to move it away by 35 µm to have the trap center, where ions would appear, in focus. Note that this was done with the second generation trap that was designed to have an ion to surface distance of 35 µm. The third generation trap that we currently work with features a distance of 70 µm.

Nanopositioner calibration

Bureaucratic mistakes and miscommunication led to us owning an open loop nanopositioner without position readout. The attocube ANPz101 has a so called slip-stick drive: A movable platform rests on a guiding rod. A piezoelectric crystal is supplied with a saw-tooth shaped voltage pulse and expands or retracts a short distance. If the voltage flank has a substantial slope, the acceleration can generate enough force to overcome the friction between platform and guiding rod, thereby pushing or pulling a movable platform (the 'slip' part). After the pulse ends, friction dominates the process and the platform again sticks to the guiding rod. The user can choose maximum voltage and frequency of the saw-tooth pulse, thereby controlling its slope. The distance, that is covered in one step depends not only on the pulse shape but also on the weight to be moved and the direction of the movement since gravity can assist or counteract the acceleration needed to overcome friction. Additionally the operating temperature has an effect on piezo expansion [133]. There is no calibration curve available for our experimental conditions so we needed to calibrate the step size. We first tried to do step distance measurements with the interferometer that we use to observe cold-head vibrations (see section 3.3.3). In order to observe any movement at all, we needed to apply a frequency/voltage combination that let to movement by more than an interferometer fringe within a very short time that the interferometer's control circuit was not able to follow. Instead of building a new and faster interferometer, we took advantage of the fact that, because of the use of lenses, our imaging system was not completely achromatic anymore. We illuminated the trap surface with 313 nm light and focused the objective on it. We then illuminated it with 235 nm light. We had to move the objective to get a sharp image as the two wavelengths were refracted differently by the lenses. We set the controller to 50 V and 50 Hz. We had to move it by 100 steps against gravity to go from a sharp 313 nm image to a sharp 235 nm image. The way back needed only 50 steps as gravity assisted acceleration. Simulations done with Zemax OpticStudio showed that the distance between the two focal planes for the two wavelengths is about 35 µm, by coincidence the ion to surface distance. This yields a step size of 0.35 µm against gravity and 0.7 µm in the direction of gravity. Since we were not able to trap with this second generation trap, we needed to wait to confirm these values until the next generation trap was installed. The values extracted from the simulation were off by a few steps but we were close enough to observe some fluorescence as we trapped the first ion. Figure 6.6 shows the out of focus image of the first ions trapped in this system. We needed to redo the calibration as we updated our objective

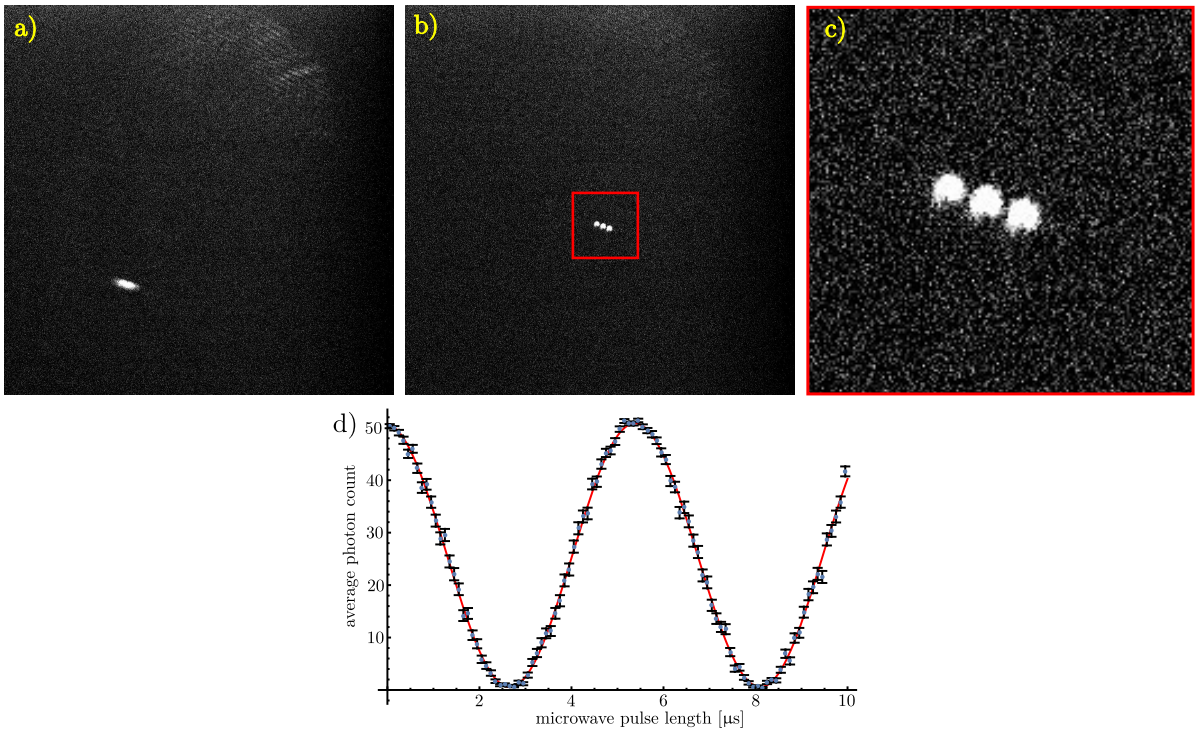

Figure 6.6: a) First picture of trapped ions. The ions are still out of focus. b) Ions in focus and centered. This is the current imaging quality. c) Close-up view of the three ions shown in b). d) Rabi flopping on the field-independent qubit transition for one ion. Data taken with the photomultiplier tube.

mount and made it lighter and the weight distribution more balanced (see section 6.2.2). The calibration we are currently using is 0.52 µm per step against gravity and 0.78 µm per step with gravity (a factor of 1.5 difference compared to the factor 2 before). The new weight is not the only contribution that changed the distance per step calibration. We have observed that it also depends on where along the 5 mm travel range the movement takes place: We have trapped ions and put them in focus. We then moved the positioner by 60 steps against gravity, leading to a defocussing of the ions. We then moved it back by 40 steps. The ions were focused again. We repeated this 10 times. The ions were still in focus. Then we moved it by 600 steps against gravity and 400 steps back. The ions were not in focus and only barely visible. Overall this was the same amount of steps but the factor of 1.5 between step sizes in different direction was not valid for a larger travel range.

Cleanroom tent

Even though we thought to have devised a way to find the trap center, we were not able to trap ions in the graphite covered trap with a surface to ion distance of 35 µm. We decided that we would need a new and clean trap and also a way to keep it clean. The

only way to keep the graphite from falling onto the trap was to reverse direction during assembly and mount the objective over-head. We assembled the inner vacuum chamber with trap inside in the PTB cleanroom but did not put the objective in. We moved the inner chamber to the Hannover lab and mounted it to the cold-head. We opened the bottom lid, mounted the objective, closed the lid again and begun evacuating. Since the lab is in no way a dust free environment like a cleanroom, we were worried, that dust particles might settle on the trap surface. Inside the lab, we built a structure of aluminum profiles with dimensions $1.3 \times 2.8 \times 2.3\,\mathrm{m}^3$. We equipped all sides with 0.5 mm thick polyvinyl chloride (PVC) sheets. On the top, we mounted a laminar flow box. Figure 6.7 shows a rendering of this home built "cleanroom tent" and a real life picture of Sebastian Halama working in it. After receiving a new, clean trap with a surface to ion

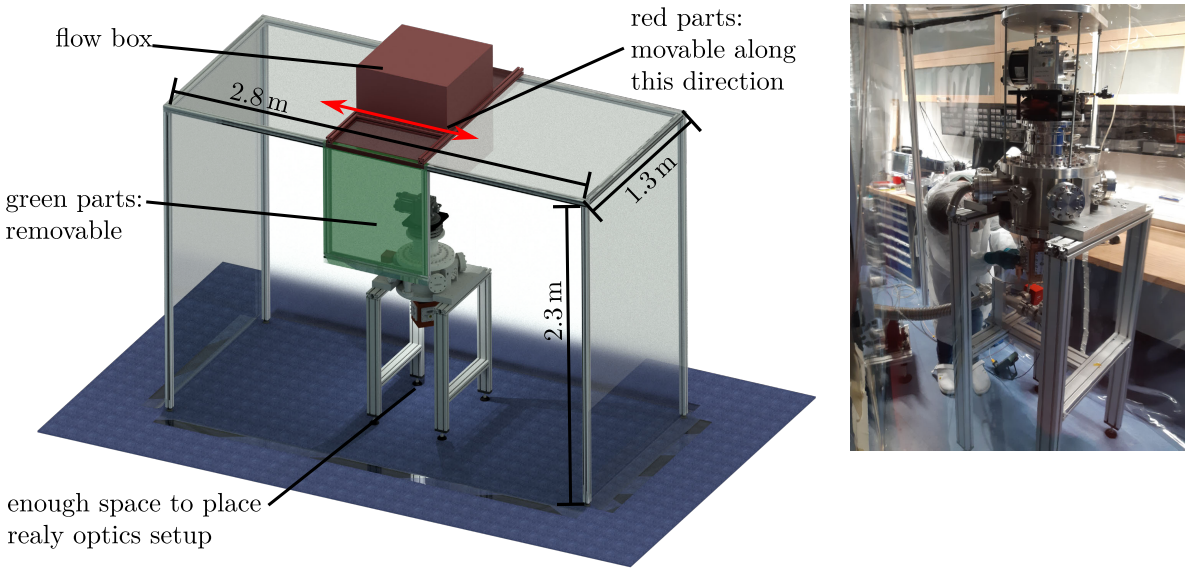

Figure 6.7: Left: Rendering of the cleanroom tent with inner vacuum chamber mounted to the cold-head inside. The red parts are part of the flow box assembly and can be moved to the side to make space for transport of the experimental setup. The green parts can be removed for the same reason.
Right: Real life picture. The inner chamber is closed and a pumping station is connected to it.

distance of 70 µm, we mounted it in the PTB cleanroom without putting the objective into the inner vacuum chamber. After transport to Hannover, we dressed in cleanroom suits and wiped all surfaces inside the tent multiple times. We then transported the vacuum hardware inside the tent, placed it directly below the flow box and cleaned it. We opened the bottom of the inner vacuum chamber and mounted the objective from below, thereby avoiding graphite particles falling onto the trap. The mounting platform was high enough that it was possible to place the relay optics and detection system below the inner vacuum chamber to check, whether we could image the trap. If not, we realigned and rechecked. Each iteration only took minutes compared to at least one

day, when we still needed to travel to a cleanroom. We were able to trap soon after we first employed the tent. We still decided that aligning the objective was messy and we designed a new objective mount which is described in the following section.

Since the clean room tent is in operation, we have not detected any additional dust from operations within the tent on our trap.

Second and current generation objective mount.

We have observed that aligning the objective, while now possible without contaminating the trap surface, still takes a lot of time to get it right.
We have designed a new objective mount that is still mounted to an attocube ANPz101 for focusing in z-direction but now also features 5 mm of x-y translation implemented through two Smaract SLC-1720-CR-UHVT-NM-TI nanopostioners. This mount also features a counter weight to reduce torque on the attocube compared to the first generation mount. To not exceed the maximum weight of 300 g, we have reduced material volume and switched from copper to titanium, which has roughly half the density. Figure 6.8 shows a rendering of the new mount and where it is mounted in the inner vacuum chamber. For it to fit into the chamber, it was necessary to mill out a pocket in the bottom lid. With this mount, we are able to move the focus over the complete trap chip surface. The

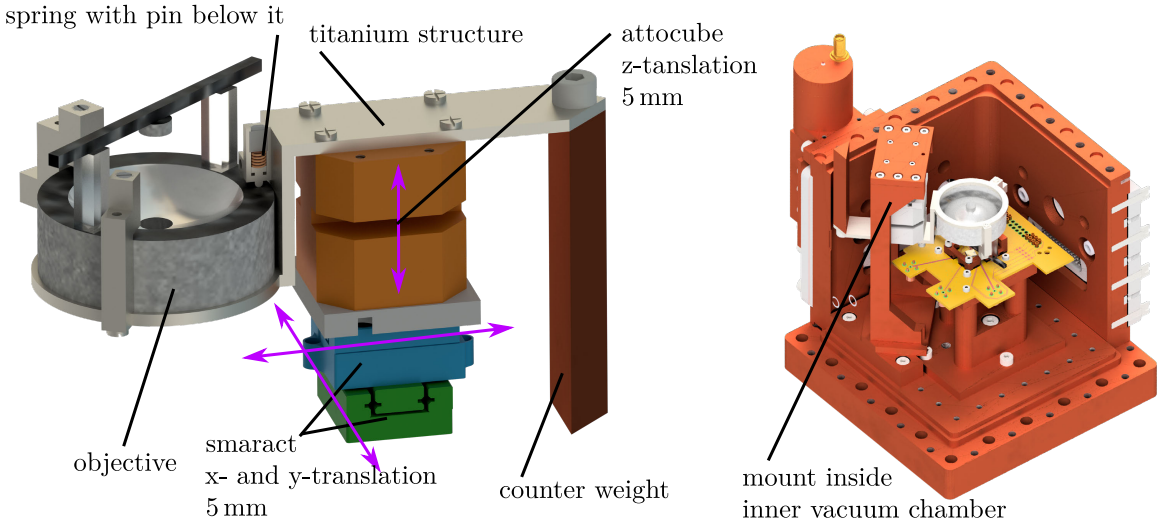

Figure 6.8: Left: Rendering of the second generation objective mount. A beryllium copper spring presses a pin against the objective. With the screw above it pressure adjustment is possible. A volume of $5 \times 5 \times 5\,\mathrm{mm}^3$ can be scanned with the 3D translation stage.
Right: Position of the mount in the inner chamber. It is mounted to the base plate that attaches the the cold head. The first generation was mounted to the wall (see figure 6.4 c)).

advantages of it become clear, when it comes to reliably align laser beams to the trap center as described in section 5.4.2. The ability to move the objective around can also play a big role when it comes to imaging larger trap structures like the one proposed in section 7.2.

6.2.3 Proposed future design of the relay optics setup

Figure 6.9 shows the beam path of a proposed new relay optics setup. It consists of

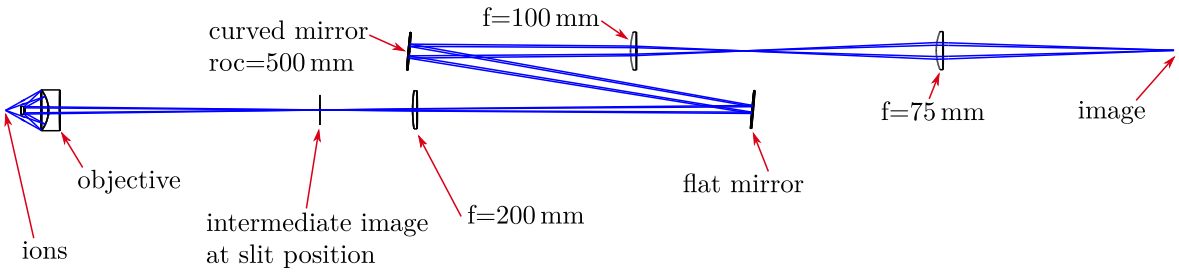

Figure 6.9: Proposed third generation relay optics setup. It combines the advantages of the first and second generation systems if all lenses are mounted on a flip-mount and the 100 and 200 mm lenses are also mounted on an optical rail.

the two mirrors from the first generation setup and combines them with three lenses. If the lenses are mounted onto flip-mounts, they can be removed to gain the narrow field of view of 100 µm, large magnification and achromaticity. If they are flipped into the beam path, a wider field of view of 400 µm is possible. The chromatic dependence can be used to calibrate the nanopositionier in future setups. If the 100 mm and the 200 mm lenses are also mounted on an optical rail, the magnification can be changed as it can be changed in the current setup. To realize this system, a new box has to be built to make room for the flipping mounts.

6.3 Detection system

The light exiting the relay optics setup passes through a box containing a motorized flip-mirror that either reflects the beam by 90° or lets it pass. If reflected it is collected by a Hamamatsu H10682-210 photomultiplier tube (PMT) directly connected to the experiment control system. If the light passes the flip mirror, it is collected by an Andor iXon Ultra DU-888 EMCCD camera. The camera is currently connected via USB to the computer. It also features a fast readout CameraLink port that is currently not in use but can potentially be of great value if it could be connected to future versions of the experiment control setup as it would offer real time feedback as a PMT does but spatially resolved.

Chapter 7

Conclusions

7.1 Summary

Over the course of this thesis, we have designed, constructed and commissioned a laboratory to operate a cryogenic surface-electrode Paul-trap with integrated microwave near-field electrodes that will allow us to drive quantum logic gates between two trapped $^9Be^+$ ions.
The trap is housed in a state of the art cryostat. The cryogenic environment at 5 K creates very low pressure vacuum conditions that are ideal for holding trapped ions undisturbed by background gas collisions. Within a confidence level of 90%, we reach a pressure of 2.5×10^{-12} mbar. The data for determining the pressure was taken during the first 5 weeks of ion trap operation. The pressure might very likely be substantially lower since we did not loose any ions due to background gas interactions since the trap became operational in late 2019.
We use a Gifford-McMahon closed cycle cooler. The intrinsic vibrations of the cold-head of this type of cooler are on the order of 100 µm. For a successful future implementation of Raman-laser systems the Raman-beams have to be phase stable to relative to each other. If the vibrations of the cold-head couple to the ion trap, the ion will move relative to the lasers and phase stability cannot be guaranteed. We have commissioned a state of the art vibration isolation system. The vibration amplitude in the horizontal direction is 51 nm with 13.5 nm RMS. In the vertical direction the amplitude is 29 nm with 7.8 nm RMS. In terms of horizontal vibrations, these results are highly competitive with other state of the art cryogenic ion trapping experiments. In terms of vertical vibrations, we are probably leading within the trapped ion community at the moment.
A cryogenic trap also suffers from lower ion heating rates and features higher conductivities of the trap electrodes compared to a room temperature equivalent.
Driving motional sidebands on trapped ions with an oscillating microwave near-field gradient via a meander electrode that is embedded in the trap-chip requires high-frequency currents to flow through that electrode. Delivering these up to several 10 W currents from a source at room temperature to the meander at 5 K requires a careful balance of resistive heat loads generated within the wiring while the currents are flowing and the static heat load due to thermal conduction. We have installed eight coaxial cables with a beryllium-copper inner conductor and a stainless steel outer conductor between the first and second cooling stage. They are thermally anchored at the first cooling stage

but electrically isolated from it. They introduce a static heat load of only 0.0034 W per cable and allow for an average microwave input power of 3.4 W at 1 GHz without heating up the system. This is about 5.8 times more power than current state of the art pulse sequences for driving two-ion gates, as they are employed at our experiment at PTB, require.
The cryostat is also equipped with 10 DC lines that support up to 1 A of current each as well as 90 DC lines for trap voltages.
We operate a very compact cryogenic radiofrequency resonator with a Q-factor of about 80 at around 100 MHz to generate the pseudopotential of the surface-electrode trap.
Stable long-term trapping of up to five ions is currently possible.
The ion trap is housed in a self sustained inner vacuum chamber made out of mostly oxygen free electrolyte copper. The copper shields it from outside magnetic field fluctuations and serves as a thermal low pass.
A fully achromatic, NA=0.5 Schwarzschild-objective with a magnification of 40 is mounted inside the inner chamber. It can be moved via a 3-axis nanopositioning stage. We can scan the complete surface of the ion trap with it. Subsequent imaging optics allow for choosing a magnification factor between 10 and 95. We can either detect the light on a photomultiplier tube or an EMCCD camera.
The laser systems for cooling and detecting the ions consists of a sum frequency generation stage of two infrared fiber lasers at 1050 nm and 1550 nm wavelength. The generated 626 nm light is frequency doubled to 313 nm, which is the cooling and detection wavelength. The red light is frequency-locked to a molecular transition in iodine. Starting with 5 W at 1550 nm and 2.5 W at 1050 nm, we reach a long term stable output of 70 mw at 313 nm. The cooling laser enters the inner vacuum chamber through a stress reducing re-entrant viewport.
We have established reliable ion loading via ablation of neutral atoms out of a beryllium target with a 1064 nm ns-pulse laser and subsequent two-photon ionization at 235 nm with a frequency quadrupled 940 nm diode laser.

7.2 Outlook

In terms of technological improvements that could be tested without having to interrupt the running system and then implemented on a short time scale, we propose five ideas:
It would be beneficial to implement an amplitude stabilized rf drive like the one in operation at our PTB experiment. This would increase the stability of the radial trap frequencies. Since these are the modes on which the microwave near-field generated by meander electrode couples, it will increase the precision of motional control.
It might also be useful to switch to a more stable method to generate the quantization field. Replacing the quite large magnetic field coils with a combination of small coils and permanent magnets, possibly temperature drift compensated by using several different magnet materials, can lead to more precise control of the ions. It has been observed at our PTB experiment that the absence of water cooled coils increases the stability

of optical setups. This might be due to vibrations resulting from the flow of water of unwanted air flow and thermal gradients due to a temperature difference between the coils and the surrounding equipment. A design is in the process of being tested during the bachelor thesis of Jannik Hertzberg.
It might also be useful to build a new relay optics setup that combines the advantages of full achromaticity at a fixed magnification for normal operations with the zoom features that a telescope offers for trap loading and debugging. A design has already been simulated; it only needs to be put together.
Migrating the over a decade old experimental control setup, which relies on an FPGA that is no longer in production, to modern hardware has to be done to make the system resilient to FPGA failure and to widen the scope of control. New control hardware based on the ARTIQ system from QUARTIQ GmbH has already been purchased and Hardik Mendpara will port the old control scripts to the new system over the course of his PhD thesis.
To reduce the amount of time during which the 235 nm laser hits the trap during loading procedures, which can potentially produce unwanted stray charges, it would be possible to switch out the mechanical shutter of that laser with a faster AOM. The most exposure time saving procedure would be to improve the trigger mechanism that triggers the 235 nm laser on the 1046 nm pulse laser.

In terms of technological improvements that can only be tested if the running system is interrupted, but could be implemented on a relatively short time scale, we propose five ideas:
Better impedance matching between the RF drive and the trap can be done by using discrete elements at cryogenic temperature instead of the currently used radiofrequency resonator. This would also have the advantage that it could potentially handle more capacitive load, something a larger future ion trap will most likely be introducing.
It might be useful to switch out the frequency doubling cavities with quasi monolithic designs. Especially a more stable and less maintenance intensive 470 nm to 235 nm cavity would improve the time it takes to load the first ion of the day.
The EMCCD camera has the potential to be connected to the new experiment control system via a real time feed through a Camera Link connection. It might be possible to achieve real time, spatially resolved single ion detection.
If the inner chamber has to be opened for some reason in the future, it might be useful to install a new Faraday cage with the gold mesh orientated at a 45° angle to the trap axis. This would lead to fewer Frauenhofer diffraction spikes along the trap axis and fewer cross-talk between ions while detecting them on the EMCCD camera. The same is true if we turn the bar that holds the secondary mirror of the Schwarzschild objective accordingly.
A new Faraday cage could also position the beryllium target one or two mm closer to the trap. This would be helpful when it comes to aligning the ablation laser. Currently it is located quite close to the edge of the viewports. Clipping on those makes aligning more difficult than it has to be.

In terms of long-term technological improvements that require a lot of remodeling, we propose three ideas:
An additional 45° viewport for observing the beryllium wire in the Faraday cage would be useful to better observe the ablation beam on the target. A 90° port would serve the same purpose. The former can only be achieved with a massive re-design of the inner chamber and producing new ports in the outer chamber. The latter can be realized by switching out the two viewports through which the cooling laser exits the two chambers. If DN40CF flanges instead of DN16CF flanges are installed, observation of the beryllium target becomes possible. This also requires the disassembly of both vacuum chambers but not a re-design of the inner chamber.
The laser setups could be rebuilt more compact and stable by making them quasi-monolithic. Having a big block of aluminum and milling out the laser path as well as spaces to place optical, opto-mechanical and diagnostic components might be beneficial for mechanical stability, ease of setup and might also be also more temperature stable. A configuration that allows for placing the sum frequency stage within a 19" rack, like that fiber lasers, might be possible. This would free up space on the optical table for future expansion of laser systems like, for example, a laser system for a second ion species.

If in the future a similar system will be set up in a different lab that has a higher ceiling, a larger vacuum chamber can be designed. At the moment, there is no way to reach the top of the radiation shield without disconnecting the low vibration interface from the outer chamber. This also leads to unmounting of all electrical feedthrough flanges on the outer chamber. This could be averted by lowering the top of the radiation shield by about 15 cm. This is currently not possible because the middle flange of the outer chamber would have to be 15 cm lower and therefore there would not be enough space for placing magnetic field coils. During disassembly, the upper part of the outer chamber to which the radiation shield is connected needs to be lifted up. A larger radiation shield in a higher chamber would need to be lifted up higher than our lab currently allows for. Overall this would lead to a tremendous amount of time being saved during the commissioning and testing phase of a new experiment.

The next phase of the experiment that was presented in this thesis will be to characterize the trap better and to implement single ion detection with the EMCCD camera as well as two qubit gates. These results will be presented in the PhD thesis of Sebastian Halama.

In the far future of this experiment or in the nearer future of a completely new one, which is based on the demonstrated technology, a multi ion quantum computer can be operated. The amount of DC electrical feedlines as well as the amount of optical access is sufficient to operate a trap similar to the QCCD concept shown in figure 7.1. There are different specialized zones in this trap. Two loading zones, one detection zone, two storage zones and an interaction zone. They are connected via transport zones and a junction.
There are two ion species operated in this trap. Beryllium ions will serve as the logic ions on which quantum logic algorithms can be run. Calcium ions serve as sympathetic

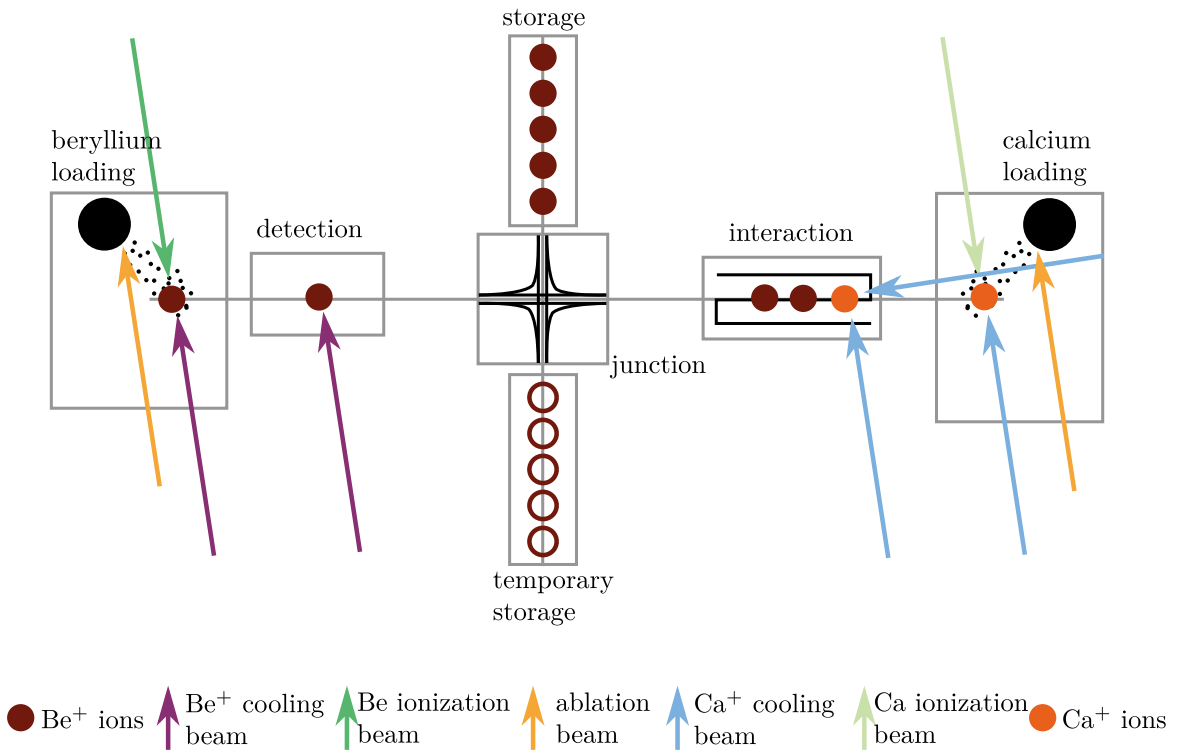

Figure 7.1: Concept of a QCCD architecture that can be implemented in our system. For description see text.

cooling ions. On the left and the right are loading zones for the respective ion species. Neutral atom targets are ablated, the emitted neutral atoms ionized and cooled down with a Doppler cooling beam. The ions are shuttled in direction of the center. The beryllium ions can be detected in a detection zone. This zone is far away from the storage section to avoid accidental detection of and subsequent loss of quantum information in the stored ions due to scattered photons. The temporary storage space is used to store ions from the main storage space in case one of the further back ions needs to be extracted. Shuttling one ion past another is not well established and needlessly complicates the already complex trap structure. Beryllium ions can be selected and transported to the interaction zone in which a calcium ion will be used to ground-state cool them and a meander structure can be used to drive microwave near field gates.
Thus the setup described in this thesis paves the way towards the realization of a scalable quantum computer based on trapped ions with a few 10 qubits. The potential for high fidelity of the integrated near-field gate approach should make operation at or beyond the fault-tolerance threshold possible.

Bibliography

[1] Richard P. Feynman: Simulating physics with computers. International Journal of Theoretical Physics **21**, 467–488 (1982). ISSN 0020-7748. 1

[2] David Deutsch: Quantum theory, the Church–Turing principle and the universal quantum computer. Proceedings of the Royal Society of London. A. Mathematical and Physical Sciences **400**, 97–117 (1985). 1

[3] P. W. Shor: Algorithms for quantum computation: Discrete logarithms and factoring. In Proc. 35th Annual Symposium on Foundations of Computer Science, Seiten 124–134. IEEE Computer Society Press, Los Alamitos (1994). 1

[4] Lov K. Grover: Quantum Mechanics Helps in Searching for a Needle in a Haystack. Physical Review Letters **79**, 325–328 (1997). 1

[5] David P. DiVincenzo: Two-bit gates are universal for quantum computation. Physical Review A **51**, 1015–1022 (1995). 1, 18

[6] Adriano Barenco, Charles H. Bennett, Richard Cleve, David P. DiVincenzo, Norman Margolus, Peter Shor, Tycho Sleator, John A. Smolin und Harald Weinfurter: Elementary gates for quantum computation. Physical Review A **52**, 3457 (1995). 1, 18

[7] T. D. Ladd, F. Jelezko, R. Laflamme, Y. Nakamura, C. Monroe und J. L. O'Brien: Quantum computers. Nature **464**, 45–53 (2010). ISSN 0028-0836. 1

[8] David P. DiVincenzo: The Physical Implementation of Quantum Computation. Fortschritte der Physik **48**, 771–783 (2000). ISSN 00158208, 15213978. 1

[9] Wolfgang Paul und Helmut Steinwedel: Ein neues Massenspektrometer ohne Magnetfeld. Zeitschrift für Naturforschung A **8**, 448–450 (1953). ISSN 1865-7109. 2, 7

[10] D. Kielpinski, C. Monroe und D. J. Wineland: Architecture for a large-scale ion-trap quantum computer. Nature **417**, 709–711 (2002). ISSN 0028-0836. 2, 3

[11] D.J. Wineland, C. Monroe, W.M. Itano, D. Leibfried, B.E. King und D.M. Meekhof: Experimental issues in coherent quantum-state manipulation of trapped atomic ions. Journal of Research of the National Institute of Standards and Technology **103**, 259 (1998). ISSN 1044677X. 2, 3, 9, 16

[12] J. I. Cirac und P. Zoller: Quantum Computations with Cold Trapped Ions. Physical Review Letters **74**, 4091 (1995). 2, 10

[13] S. Debnath, N. M. Linke, C. Figgatt, K. A. Landsman, K. Wright und C. Monroe: Demonstration of a small programmable quantum computer with atomic qubits. Nature **536**, 63–66 (2016). ISSN 1476-4687. 2

[14] Thomas Monz, Daniel Nigg, Esteban A. Martinez, Matthias F. Brandl, Philipp Schindler, Richard Rines, Shannon X. Wang, Isaac L. Chuang und Rainer Blatt: Realization of a scalable Shor algorithm. Science **351**, 1068–1070 (2016). ISSN 0036-8075, 1095-9203. 2

[15] C. Figgatt, D. Maslov, K. A. Landsman, N. M. Linke, S. Debnath und C. Monroe: Complete 3-Qubit Grover search on a programmable quantum computer. Nature Communications **8**, 1918 (2017). ISSN 2041-1723. 2

[16] Frank Arute, Kunal Arya, Ryan Babbush, Dave Bacon, Joseph C. Bardin, Rami Barends, Rupak Biswas, Sergio Boixo, Fernando G. S. L. Brandao, David A. Buell, Brian Burkett, Yu Chen, Zijun Chen, Ben Chiaro, Roberto Collins, William Courtney, Andrew Dunsworth, Edward Farhi, Brooks Foxen, Austin Fowler, Craig Gidney, Marissa Giustina, Rob Graff, Keith Guerin, Steve Habegger, Matthew P. Harrigan, Michael J. Hartmann, Alan Ho, Markus Hoffmann, Trent Huang, Travis S. Humble, Sergei V. Isakov, Evan Jeffrey, Zhang Jiang, Dvir Kafri, Kostyantyn Kechedzhi, Julian Kelly, Paul V. Klimov, Sergey Knysh, Alexander Korotkov, Fedor Kostritsa, David Landhuis, Mike Lindmark, Erik Lucero, Dmitry Lyakh, Salvatore Mandrà, Jarrod R. McClean, Matthew McEwen, Anthony Megrant, Xiao Mi, Kristel Michielsen, Masoud Mohseni, Josh Mutus, Ofer Naaman, Matthew Neeley, Charles Neill, Murphy Yuezhen Niu, Eric Ostby, Andre Petukhov, John C. Platt, Chris Quintana, Eleanor G. Rieffel, Pedram Roushan, Nicholas C. Rubin, Daniel Sank, Kevin J. Satzinger, Vadim Smelyanskiy, Kevin J. Sung, Matthew D. Trevithick, Amit Vainsencher, Benjamin Villalonga, Theodore White, Z. Jamie Yao, Ping Yeh, Adam Zalcman, Hartmut Neven und John M. Martinis: Quantum supremacy using a programmable superconducting processor. Nature **574**, 505–510 (2019). ISSN 0028-0836, 1476-4687. 2

[17] Preskill John: Reliable quantum computers. Proceedings of the Royal Society of London. Series A: Mathematical, Physical and Engineering Sciences **454**, 385–410 (1998). 2

[18] Emanuel Knill: Physics: Quantum computing. Nature **463**, 441–443 (2010). ISSN 1476-4687. 2

[19] T.P. Harty, D.T.C. Allcock, C.J. Ballance, L. Guidoni, H.A. Janacek, N.M. Linke, D.N. Stacey und D.M. Lucas: High-Fidelity Preparation, Gates, Memory, and Readout of a Trapped-Ion Quantum Bit. Physical Review Letters **113**, 220501 (2014). 2

[20] J.P. Gaebler, T.R. Tan, Y. Lin, Y. Wan, R. Bowler, A.C. Keith, S. Glancy, K. Coakley, E. Knill, D. Leibfried und D.J. Wineland: High-Fidelity Universal Gate Set for $^{9}Be^{+}$ Ion Qubits. Physical Review Letters **117**, 060505 (2016). 2

[21] C.J. Ballance, T.P. Harty, N.M. Linke, M.A. Sepiol und D.M. Lucas: High-Fidelity Quantum Logic Gates Using Trapped-Ion Hyperfine Qubits. Physical Review Letters **117**, 060504 (2016). 2, 11

[22] T.P. Harty, M.A. Sepiol, D.T.C. Allcock, C.J. Ballance, J.E. Tarlton und D.M. Lucas: High-Fidelity Trapped-Ion Quantum Logic Using Near-Field Microwaves. Physical Review Letters **117**, 140501 (2016). 2

[23] G. Zarantonello, H. Hahn, J. Morgner, M. Schulte, A. Bautista-Salvador, R.F. Werner, K. Hammerer und C. Ospelkaus: Robust and Resource-Efficient Microwave Near-Field Entangling $^{9}Be^{+}$ Gate. Physical Review Letters **123**, 260503 (2019). ISSN 0031-9007, 1079-7114. 2, 4, 7, 10, 18, 21, 67

[24] D.F.V. James: Quantum dynamics of cold trapped ions with application to quantum computation. Applied Physics B: Lasers and Optics **66**, 181–190 (1998). ISSN 0946-2171. 3, 18

[25] C. Monroe und J. Kim: Scaling the Ion Trap Quantum Processor. Science **339**, 1164–1169 (2013). ISSN 0036-8075, 1095-9203. 3

[26] J M Amini, H Uys, J H Wesenberg, S Seidelin, J Britton, J J Bollinger, D Leibfried, C Ospelkaus, A P VanDevender und D J Wineland: Toward scalable ion traps for quantum information processing. New Journal of Physics **12**, 033031 (2010). ISSN 1367-2630. 3

[27] J. Chiaverini, R.B. Blakestade, J. Britton, J.D. Jost, C. Langer, D. Leibfried und D.J. Wineland: Surface-electrode architecture for ion-trap quantum information processing. Quantum Information and Computation **5**, 419–439 (2005). 3, 9

[28] S. Seidelin, J. Chiaverini, R. Reichle, J. J. Bollinger, D. Leibfried, J. Britton, J. H. Wesenberg, R. B. Blakestad, R. J. Epstein, D. B. Hume, W. M. Itano, J. D. Jost, C. Langer, R. Ozeri, N. Shiga und D. J. Wineland: Microfabricated Surface-Electrode Ion Trap for Scalable Quantum Information Processing. Physical Review Letters **96**, 253003 (2006). 3

[29] D. L. Moehring, C. Highstrete, D. Stick, K. M. Fortier, R. Haltli, C. Tigges und M. G. Blain: Design, fabrication and experimental demonstration of junction surface ion traps. New Journal of Physics **13**, 075018 (2011). ISSN 1367-2630. 3

[30] Kenneth Wright, Jason M. Amini, Daniel L. Faircloth, Curtis Volin, S. Charles Doret, Harley Hayden, C-S Pai, David W. Landgren, Douglas Denison, Tyler Killian, Richart E. Slusher und Alexa W. Harter: Reliable transport through a microfabricated X -junction surface-electrode ion trap. New Journal of Physics **15**, 033004 (2013). ISSN 1367-2630. 3

[31] D. Kielpinski, B. E. King, C. J. Myatt, C. A. Sackett, Q. A. Turchette, W. M. Itano, C. Monroe, D. J. Wineland und W. H. Zurek: Sympathetic cooling of trapped ions for quantum logic. Physical Review A **61**, 032310 (2000). ISSN 1050-2947, 1094-1622. 3

[32] M. D. Barrett, B. DeMarco, T. Schaetz, V. Meyer, D. Leibfried, J. Britton, J. Chiaverini, W. M. Itano, B. Jelenković, J. D. Jost, C. Langer, T. Rosenband und D. J. Wineland: Sympathetic cooling of 9Be+ and 24Mg+ for quantum logic. Physical Review A **68**, 042302 (2003). 3

[33] Karan K. Mehta, Colin D. Bruzewicz, Robert McConnell, Rajeev J. Ram, Jeremy M. Sage und John Chiaverini: Integrated optical addressing of an ion qubit. Nature Nanotechnology **11**, 1066–1070 (2016). ISSN 1748-3387. 3

[34] J. True Merrill, Curtis Volin, David Landgren, Jason M. Amini, Kenneth Wright, S. Charles Doret, C-S Pai, Harley Hayden, Tyler Killian, Daniel Faircloth, Kenneth R. Brown, Alexa W. Harter und Richart E. Slusher: Demonstration of integrated microscale optics in surface-electrode ion traps. New Journal of Physics **13**, 103005 (2011). ISSN 1367-2630. 3

[35] D. H. Slichter, V. B. Verma, D. Leibfried, R. P. Mirin, S. W. Nam und D. J. Wineland: UV-sensitive superconducting nanowire single photon detectors for integration in an ion trap. Optics Express **25**, 8705–8720 (2017). ISSN 1094-4087. 3

[36] Florian Mintert und Christof Wunderlich: Ion-Trap Quantum Logic Using Long-Wavelength Radiation. Physical Review Letters **87**, 257904 (2001). 3, 10, 16

[37] C. Ospelkaus, C. E. Langer, J. M. Amini, K. R. Brown, D. Leibfried und D. J. Wineland: Trapped-Ion Quantum Logic Gates Based on Oscillating Magnetic Fields. Physical Review Letters **101**, 090502 (2008). 4, 10, 14, 15, 16

[38] Q. A. Turchette, Kielpinski, B. E. King, D. Leibfried, D. M. Meekhof, C. J. Myatt, M. A. Rowe, C. A. Sackett, C. S. Wood, W. M. Itano, C. Monroe und D. J. Wineland: Heating of trapped ions from the quantum ground state. Physical Review A **61**, 063418 (2000). 4, 20, 28

[39] Ivan A. Boldin, Alexander Kraft und Christof Wunderlich: Measuring anomalous heating in a planar ion trap with variable ion-surface separation. Physical Review Letters **120** (2018). ISSN 0031-9007, 1079-7114. ArXiv: 1708.03147. 4, 20, 28

[40] S. Sellner, M. Besirli, M. Bohman, M. J. Borchert, J. Harrington, T. Higuchi, A. Mooser, H. Nagahama, G. Schneider, C. Smorra, T. Tanaka, K. Blaum, Y. Matsuda, C. Ospelkaus, W. Quint, J. Walz, Y. Yamazaki und S. Ulmer: Improved limit on the directly measured antiproton lifetime. New Journal of Physics **19**, 083023 (2017). ISSN 1367-2630. 4, 28, 48, 49

[41] J. Chiaverini und J. M. Sage: Insensitivity of the rate of ion motional heating to trap-electrode material over a large temperature range. Physical Review A **89**, 012318 (2014). 4, 20, 28

[42] M. Carsjens, M. Kohnen, T. Dubielzig und C. Ospelkaus: Surface-electrode Paul trap with optimized near-field microwave control. Applied Physics B **114**, 243–250 (2014). ISSN 0946-2171, 1432-0649. 4, 7, 17

[43] M. Wahnschaffe, H. Hahn, G. Zarantonello, T. Dubielzig, S. Grondkowski, A. Bautista-Salvador, M. Kohnen und C. Ospelkaus: Single-ion microwave near-field quantum sensor. Applied Physics Letters **110**, 034103 (2017). ISSN 0003-6951. 4, 7, 17

[44] A. Bautista-Salvador, G. Zarantonello, H. Hahn, A. Preciado-Grijalva, J. Morgner, M. Wahnschaffe und C. Ospelkaus: Multilayer ion trap technology for scalable quantum computing and quantum simulation. New Journal of Physics **21**, 043011 (2019). ISSN 1367-2630. 4, 7

[45] H. Hahn, G. Zarantonello, M. Schulte, A. Bautista-Salvador, K. Hammerer und C. Ospelkaus: Integrated $^{9}Be^{+}$ multi-qubit gate device for the ion-trap quantum computer. npj Quantum Information **5**, 70 (2019). ISSN 2056-6387. 4, 7, 10, 21, 32

[46] H. Hahn, G. Zarantonello, A. Bautista-Salvador, M. Wahnschaffe, M. Kohnen, J. Schoebel, P. O. Schmidt und C. Ospelkaus: Multilayer ion trap with three-dimensional microwave circuitry for scalable quantum logic applications. Applied Physics B **125**, 154 (2019). ISSN 1432-0649. 4, 7

[47] Henning Hahn: Two-qubit microwave quantum logic gate with $^{9}Be^{+}$ ions in scalable surface-electrode ion traps. PhD thesis, Leibniz Universität Hannover, Hannover (2019). 4, 73

[48] Giorgio Zarantonello: Robust high fideelity microwave near-field entangling quantum logic gate. Dissertation, Leibniz Universität Hannover, Hannover (2020). 4, 7

[49] C. Ospelkaus, U. Warring, Y. Colombe, K. R. Brown, J. M. Amini, D. Leibfried und D. J. Wineland: Microwave quantum logic gates for trapped ions. Nature **476**, 181–184 (2011). ISSN 0028-0836. 4, 10, 17

[50] Martina Wahnschaffe: Engineered microwave control for trapped ions. Dissertation, Gottfried Wilhelm Leibniz Universität, Hannover (2016). 7, 18, 87, 100

[51] A.-G. Paschke, G. Zarantonello, H. Hahn, T. Lang, C. Manzoni, M. Marangoni, G. Cerullo, U. Morgner und C. Ospelkaus: Versatile Control of $^{9}Be^{+}$ Ions Using a Spectrally Tailored UV Frequency Comb. Physical Review Letters **122**, 123606 (2019). 7

[52] Samuel Earnshaw: On the nature of the molecular forces which regulate the constitution of the luminiferous ether. Trans. Camb. Phil. Soc **7**, 97–112 (1842). 7

[53] H. G. Dehmelt: Radiofrequency Spectroscopy of Stored Ions I: Storage. In D. R. Bates und Immanuel Estermann, editors, Advances in Atomic and Molecular Physics, Band 3, Seiten 53–72. Academic Press (1968). doi:10.1016/S0065-2199(08)60170-0. 7

[54] Pradip K. Ghosh: Ion Traps. International Series of Monographs on Physics. Clarendon Press, Oxford (1996). 8, 9

[55] J. H. Wesenberg: Electrostatics of surface-electrode ion traps. Physical Review A **78**, 063410 (2008). 9

[56] Mário H Oliveira und José A Miranda: Biot-Savart-like law in electrostatics. European Journal of Physics **22**, 31 (2001). 9, 10

[57] Klaus Mølmer und Anders Sørensen: Multiparticle Entanglement of Hot Trapped Ions. Physical Review Letters **82**, 1835 (1999). 10

[58] M. Johanning, A. Braun, N. Timoney, V. Elman, W. Neuhauser und Chr. Wunderlich: Individual Addressing of Trapped Ions and Coupling of Motional and Spin States Using rf Radiation. Physical Review Letters **102**, 073004 (2009). 10

[59] Sabine Wölk und Christof Wunderlich: Quantum dynamics of trapped ions in a dynamic field gradient using dressed states. New Journal of Physics **19**, 083021 (2017). ISSN 1367-2630. 10

[60] S. Olmschenk, K. C. Younge, D. L. Moehring, D. N. Matsukevich, P. Maunz und C. Monroe: Manipulation and detection of a trapped Yb+ hyperfine qubit. Physical Review A **76** (2007). ISSN 1050-2947, 1094-1622. 11

[61] V. Negnevitsky, M. Marinelli, K. K. Mehta, H.-Y. Lo, C. Flühmann und J. P. Home: Repeated multi-qubit readout and feedback with a mixed-species trapped-ion register. Nature **563**, 527–531 (2018). ISSN 1476-4687. 11

[62] D. M. Lucas, B. C. Keitch, J. P. Home, G. Imreh, M. J. McDonnell, D. N. Stacey, D. J. Szwer und A. M. Steane: A long-lived memory qubit on a low-decoherence quantum bus. arXiv:0710.4421 [quant-ph] (2007). ArXiv: 0710.4421. 11

[63] M. V. Nikolić, S. M. Radić, V. Minić und M. M. Ristić: The dependence of the work function of rare earth metals on their electron structure. Microelectronics Journal **27**, 93–96 (1996). ISSN 0026-2692. 11

[64] David R. Lide, Grace Baysinger, Lev I. Berger, Robert N. Goldberg, Henry V. Kehiaian, Kozo Kuchitsu, Gerd Rosenblatt, Dana L. Roth und Daniel Zwillinger, editors: CRC Handbook of Chemistry and Physics. CRC Press (2005). 11, 43

[65] D. J. Wineland, R. E. Drullinger und F. L. Walls: Radiation-Pressure Cooling of Bound Resonant Absorbers. Physical Review Letters **40**, 1639–1642 (1978). 11

[66] Jason Nhuyen: The linewidth and hyperfine A constant of the $^2P_{1/2}$ state of a magnesium ion confined in a linear Paul trap. PhD thesis, McMaster University, Hamilton, Ontario (2009). 12

[67] T. Andersen, K. A. Jessen und G. Sørensen: Mean-Life Measurements of Excited Electronic States in Neutral and Ionic Species of Beryllium and Boron. Physical Review **188**, 76–81 (1969). 12

[68] Teresa Meiners, Malte Niemann, Johannes Mielke, Matthias Borchert, Nicolas Pulido, Juan M. Cornejo, Stefan Ulmer und Christian Ospelkaus: Towards sympathetic cooling of single (anti-)protons. Hyperfine Interactions **239**, 26 (2018). ISSN 0304-3843, 1572-9540. 12

[69] Malte Niemann: Design and commissioning of an experiment for sympathetic cooling and coupling of ions in a cryogenic Penning trap. PhD, Leibniz Universität Hannover, Hannover (2019). 12

[70] L. Deslauriers, S. Olmschenk, D. Stick, W. K. Hensinger, J. Sterk und C. Monroe: Scaling and Suppression of Anomalous Heating in Ion Traps. Physical Review Letters **97**, 103007 (2006). 28

[71] C. Monroe, D. M. Meekhof, B. E. King, S. R. Jefferts, W. M. Itano, D. J. Wineland und P. Gould: Resolved-sideband Raman cooling of a bound atom to the 3D zero-point energy. Physical review letters **75**, 4011–4014 (1995). ISSN 1079-7114. 28

[72] M. Brownnutt, M. Kumph, P. Rabl und R. Blatt: Ion-trap measurements of electric-field noise near surfaces. Reviews of Modern Physics **87**, 1419–1482 (2015). 28

[73] G. Gabrielse, X. Fei, L. A. Orozco, R. L. Tjoelker, J. Haas, H. Kalinowsky, T. A. Trainor und W. Kells: Thousandfold improvement in the measured antiproton mass. Physical Review Letters **65**, 1317–1320 (1990). 28

[74] M. E. Poitzsch, J. C. Bergquist, W. M. Itano und D. J. Wineland: Cryogenic linear ion trap for accurate spectroscopy. Review of Scientific Instruments **67**, 129 (1996). ISSN 00346748. 29

[75] J. W Ekin: Experimental techniques for low-temperature measurements: cryostat design, material properties, and superconductor critical-current testing. Oxford University Press, New York (2015). ISBN 978-0-19-857054-7. OCLC: 976449038. 29, 31, 32, 43, 58, 59, 60, 61, 62, 63, 69, 87

[76] M. F. Brandl, M. W. van Mourik, L. Postler, A. Nolf, K. Lakhmanskiy, R. R. Paiva, S. Möller, N. Daniilidis, H. Häffner, V. Kaushal, T. Ruster, C. Warschburger, H. Kaufmann, U. G. Poschinger, F. Schmidt-Kaler, P. Schindler, T. Monz und R. Blatt: Cryogenic setup for trapped ion quantum computing. Review of Scientific Instruments **87**, 113103 (2016). ISSN 0034-6748. Publisher: American Institute of Physics. 30, 41

[77] D. De Motte, A. R. Grounds, M. Rehák, A. Rodriguez Blanco, B. Lekitsch, G. S. Giri, P. Neilinger, G. Oelsner, E. Il'ichev, M. Grajcar und W. K. Hensinger: Experimental system design for the integration of trapped-ion and superconducting qubit systems. Quantum Information Processing **15**, 5385–5414 (2016). ISSN 1573-1332. 30

[78] H. O. McMahon und W. E. Gifford: A New Low-Temperature Gas Expansion Cycle. In K. D. Timmerhaus, editor, Advances in Cryogenic Engineering, Advances in Cryogenic Engineering, Seiten 354–367. Springer US, Boston, MA (1960). ISBN 978-1-4757-0537-9. 30

[79] K. A. Gschneidner, A. O. Pecharsky und V. K. Pecharsky: Low Temperature Cryocooler Regenerator Materials. In Ronald G. Ross, editor, Cryocoolers 12, Seiten 457–465. Springer US, Boston, MA (2003). ISBN 978-0-306-47919-9. 31

[80] T. Nakagawa, T. Miyauchi, T. Shiraishi, K. Shoda, T. A. Yamamoto, Y. Fujimoto und S. Masuyama: Size and Composition Optimization of $Er_xHo_{x-1}N$ Regenerators for 4K-GM Cryocoolers. In Cryocoolers 19. Boulder, Colorado, USA (2016). 31

[81] A. T. A. M de Waele: Pulse-tube refrigerators: principle, recent developments, and prospects. Physica B: Condensed Matter **280**, 479–482 (2000). ISSN 0921-4526. 31

[82] Shannon X. Wang, Jaroslaw Labaziewicz, Yufei Ge, Ruth Shewmon und Isaac L. Chuang: Demonstration of a quantum logic gate in a cryogenic surface-electrode ion trap. Physical Review A **81**, 062332 (2010). 32

[83] P. B. Antohi, D. Schuster, G. M. Akselrod, J. Labaziewicz, Y. Ge, Z. Lin, W. S. Bakr und I. L. Chuang: Cryogenic ion trapping systems with surface-electrode traps. Review of Scientific Instruments **80**, 013103 (2009). ISSN 00346748. 32

[84] Grahame Vittorini, Kenneth Wright, Kenneth R. Brown, Alexa W. Harter und S. Charles Doret: Modular cryostat for ion trapping with surface-electrode ion traps. Review of Scientific Instruments **84**, 043112 (2013). ISSN 0034-6748, 1089-7623. 32

[85] Chao Wang und John G. Hartnett: A vibration free cryostat using pulse tube cryocooler. Cryogenics **50**, 336–341 (2010). ISSN 0011-2275. 32

[86] Leupold Florian: Bang-bang Control of a Trapped-Ion Oscillator. Dissertation, ETH Zurich (2015). 32, 44

[87] G. Pagano, P. W. Hess, H. B. Kaplan, W. L. Tan, P. Richerme, P. Becker, A. Kyprianidis, J. Zhang, E. Birckelbaw, M. R. Hernandez, Y. Wu und C. Monroe: Cryogenic trapped-ion system for large scale quantum simulation. Quantum Science and Technology **4**, 014004 (2018). ISSN 2058-9565. 32, 41

[88] P. Micke, J. Stark, S. A. King, T. Leopold, T. Pfeifer, L. Schmöger, M. Schwarz, L. J. Spieß, P. O. Schmidt und J. R. Crespo López-Urrutia: Closed-cycle, low-vibration 4 K cryostat for ion traps and other applications. Review of Scientific Instruments **90**, 065104 (2019). ISSN 0034-6748. 33, 41

[89] H. Nyquist: Certain Topics in Telegraph Transmission Theory. Transactions of the American Institute of Electrical Engineers **47**, 617–644 (1928). ISSN 2330-9431. Conference Name: Transactions of the American Institute of Electrical Engineers. 40

[90] William H. Press, Saul A. Teukolsky, William T. Vetterling und Briam P. Flannery: Numerical Recipes, The Art of Scientifc Computing. Cambridge University Press (2007). 40

[91] K. R. Brown, A. C. Wilson, Y. Colombe, C. Ospelkaus, A. M. Meier, E. Knill, D. Leibfried und D. J. Wineland: Single-qubit gate error below 10^{-4} in a trapped ion. Physical Review A **84**, 030303 (2011). 43, 44

[92] Brian C. Sawyer, Justin G. Bohnet, Joseph W. Britton und John J. Bollinger: Reversing hydride-ion formation in quantum-information experiments with Be^{+}. Physical Review A **91**, 011401 (2015). 48

[93] B. Roth, P. Blythe, H. Wenz, H. Daerr und S. Schiller: Ion-neutral chemical reactions between ultracold localized ions and neutral molecules with single-particle resolution. Physical Review A **73**, 042712 (2006). Publisher: American Physical Society. 48

[94] Karl Jousten: Handbuch Vakuumtechnik. Springer, 12 edition (2018). 58

[95] Daniel J. Rader, Wayne M. Trott, John R. Torczynski, Jamie N Castaneda und T.W. Grasser: Measurements of Thermal Accomodation Coefficients. Technical report, Sandia National Laboratories (2005). 58

[96] Guy K. White und Philip J. Meeson: Experimental techniques in low-temperature physics. Clarendon, Oxford, UK, 4 edition (2004). 58

[97] J.G. Hust und P.J. Giarratano: Thermal conductivity and electrical resistivity standard reference materials: electrolytic iron SRM's 734 and 797 from 4 to 1000 K. Technical report, National Bureau of Standars (1975). 60

[98] R. Franz und G. Wiedemann: Ueber die Wärme-Leitungsfähigkeit der Metalle. Annalen der Physik **165**, 497–531 (1853). ISSN 1521-3889. 61

[99] NIST Cryogenic Technology Resources. 63, 66

[100] Christopher E. Langer: High Fidelity Quantum Information Processing with Trapped Ions. PhD Thesis, University of Colorado, Boulder, Colorado (2006). 71

[101] Sebastian Grondkowski: Pulsgenerator für die Quanteninformationsverarbeitung mit einzelnen gespeicherten Ionen. Bachelor's Thesis, Leibniz Universität Hannover, Hannover (2012). 71

[102] R. Bowler, U. Warring, J. W. Britton, B. C. Sawyer und J. Amini: Arbitrary waveform generator for quantum information processing with trapped ions. Review of Scientific Instruments **84**, 033108–033108–6 (2013). ISSN 00346748. 71, 73

[103] Ryan Bowler: Coherent Ion Transport in a Multi-electrode Trap Array. Dissertation, University of Colorado (2015). 71

[104] Sebastian Grondkowski: Quantenkontrolle von $^{9}Be^{+}$ Hyperfein-Qubits. Masterarbeit, Leibniz Universität Hannover, Hannover (2014). 73, 77

[105] Julia-Aileen Fenske: Implementierung eines digitalen PID-Reglers mit dem Entwicklungsboard „Red Pitaya". Bachelorarbeit, Ostfalia Hochschule für angewandte Wissenschaften, Braunschweig / Wolfenbüttel (2015). 74, 99, 105

[106] S. Hannig, J. Mielke, J. A. Fenske, M. Misera, N. Beev, C. Ospelkaus und P. O. Schmidt: A highly stable monolithic enhancement cavity for second harmonic generation in the ultraviolet. Review of Scientific Instruments **89**, 013106 (2018). ISSN 0034-6748. 74, 104

[107] W.W. Macalpine und R.O. Schildknecht: Coaxial Resonators with Helical Inner Conductor. Proceedings of the IRE **47**, 2099–2105 (1959). ISSN 0096-8390. 77

[108] Fisk: Helical-Resonator Design Techniques. QST (1976). 77

[109] J. D. Siverns, L. R. Simkins, S. Weidt und W. K. Hensinger: On the application of radio frequency voltages to ion traps via helical resonators. Applied Physics B **107**, 921–934 (2012). ISSN 0946-2171, 1432-0649. 77, 80

[110] Fabian Ude: Laser und Radiofrequenzquellen für den Betrieb einer kryogenen Paulfalle. Masterarbeit, Leibniz Universität Hannover, Hannover (2018). 78, 98, 100

[111] David M Pozar: Microwave engineering. John Wiley \& Sons (2009). 80

[112] D. Gandolfi, M. Niedermayr, M. Kumph, M. Brownnutt und R. Blatt: Compact radio-frequency resonator for cryogenic ion traps. Review of Scientific Instruments **83**, 084705–084705–6 (2012). ISSN 00346748. 83

[113] Rainee N. Simons: Coplanar Waveguide Circuits, Components, and Systems. John Wiley & Sons, Inc. (2001). ISBN 978-0-471-16121-9. 86

[114] Alexander Franzen: ComponentLibrary a vector graphics library for illustrations of optics experiments. (2020). 93

[115] Hsiang-Yu Lo, Joseba Alonso, Daniel Kienzler, Benjamin C. Keitch, Ludwig E. de Clercq, Vlad Negnevitsky und Jonathan P. Home: All-solid-state continuous-wave laser systems for ionization, cooling and quantum state manipulation of beryllium ions. Applied Physics B **114**, 17–25 (2014). ISSN 1432-0649. 98

[116] Johannes Mielke: A Frequency Quadrupled Lasersystem for Photoionization of $^9Be^+$. Masterarbeit, Leibniz Universität Hannover, Hannover (2016). 98

[117] R. V. Pound: Electronic Frequency Stabilization of Microwave Oscillators. Review of Scientific Instruments **17**, 490–505 (1946). ISSN 00346748. 99

[118] R. W. P. Drever, J. L. Hall, F. V. Kowalski, J. Hough, G. M. Ford, A. J. Munley und H. Ward: Laser phase and frequency stabilization using an optical resonator. Applied Physics B **31**, 97–105 (1983). ISSN 0946-2171, 1432-0649. 99

[119] A. C. Wilson, C. Ospelkaus, A. P. VanDevender, J. A. Mlynek, K. R. Brown, D. Leibfried und D. J. Wineland: A 750-mW, continuous-wave, solid-state laser source at 313 nm for cooling and manipulating trapped $^9Be^+$ ions. Applied Physics B **105**, 741–748 (2011). ISSN 1432-0649. 102

[120] Kai Voges: Lasersysteme für Einzel-Ionen- Experimente mit $^9Be^+$. Masterarbeit, Leibniz Universität Hannover, Hannover (2014). 102

[121] H. Ball, M. W. Lee, S. D. Gensemer und M. J. Biercuk: A high-power 626 nm diode laser system for Beryllium ion trapping. arXiv:1304.1947 (2013). 102

[122] Steven A. King, Tobias Leopold, Premjith Thekkeppatt und Piet O. Schmidt: A self-injection locked DBR laser for laser cooling of beryllium ions. Applied Physics B **124**, 214 (2018). ISSN 1432-0649. 102, 103

[123] Mariia Stepanova: Laser frequency stabilization for quantum logic experiments with single trapped $^9Be^+$ ions. Bachelor's Thesis, Leibniz Universitaet Hannover (2014). 103

[124] T. W. Hänsch und B. Couillaud: Laser frequency stabilization by polarization spectroscopy of a reflecting reference cavity. Optics Communications **35**, 441–444 (1980). ISSN 0030-4018. 104

[125] H. Knöckel, B. Bodermann und E. Tiemann: High precision description of the rovibronic structure of the I2 B-X spectrum. The European Physical Journal D **28**, 199–209 (2004). ISSN 1434-6060, 1434-6079. Number: 2 Publisher: EDP Sciences. 105

[126] F. Gebert, M. H. Frosz, T. Weiss, Y. Wan, A. Ermolov, N. Y. Joly, P. O. Schmidt und P. St J. Russell: Damage-free single-mode transmission of deep-UV light in hollow-core PCF. Optics Express **22**, 15388–15396 (2014). ISSN 1094-4087. 107

[127] Piet Schmidt: Private communication. 109

[128] Johann Heinrich Lambert und E. (Ernst) Anding: Photometrie. Photometria, sive De mensura et gradibus luminis, colorum et umbrae (1760). Leipzig, W. Engelmann (1892). 112

[129] Jørgen Schou, Salvatore Amoruso und James G. Lunney: Plume Dynamics. In Claude Phipps, editor, Plume Dynamics, Springer Series in Optical Sciences. Springer US, Boston, MA (2007). ISBN 978-0-387-30453-3. 112

[130] Max J. Riedl: Optical Design Fundamentals for Infrared Systems. SPIE Press, Bellingham, WA, 2nd edition (2001). 121

[131] E. J. Elliffe, J. Bogenstahl, A. Deshpande, J. Hough, C. Killow, S. Reid, D. Robertson, S. Rowan, H. Ward und G. Cagnoli: Hydroxide-catalysis bonding for stable optical systems for space. Classical and Quantum Gravity **22**, S257–S267 (2005). ISSN 0264-9381. Publisher: IOP Publishing. 121

[132] Alan W. Smith und Ned S. Rasor: Observed Dependence of the Low-Temperature Thermal and Electrical Conductivity of Graphite on Temperature, Type, Neutron Irradiation, and Bromination. Physical Review **104**, 885–891 (1956). Publisher: American Physical Society. 127

[133] M. Locatelli, G. Lamboley, J. P. Michenaud und V. Bayot: Easy method to characterize a piezoelectric ceramic tube as a displacer. Review of Scientific Instruments **59**, 661–663 (1988). ISSN 0034-6748. Publisher: American Institute of Physics. 130

Acknowledgements

This is the part where I thank several people for their help and support and where I also acknowledge their contributions because let's be honest: strictly speaking, not every contribution was helpful. As you will notice, this is also the part that nobody proof-read.

I thank *Christian Ospelkaus* for giving me the opportunity to work on such an interesting and also potentially long-term useful project. It is not always a given that both these criteria are fulfilled in basic research. I also like to thank *Christian* to have trusted me with a lot of organizational details over the years, a privilege that is often denied to many underlings around the world. At last I would like to thank *Christian* for presenting me with the chance to fill up three labs with working science equipment and two more with basic infrastructure.

Piet Schmidt was there from the beginning and through an abundance of knowledge, ample advice and always being friendly, he kind of brought it on himself that he was asked to take on the review of this thesis. Thank you, *Piet*.

I like to thank *Christof Wunderlich* for reviewing this thesis. I hope to be working with you in the future as part the newly funded BMBF project and I also hope that this thesis contains, at least in part, some useful information for running the cryostat that we will soon commission in cooperation.

Sebastian Halama probably had the most Timko-time to endure. I am sorry. I am also very grateful that you helped me design, construct, 'run', criticize, re-design, re-contruct and run pretty much every part of this experiment. Since I cannot read your emotions I cannot claim to know, if you had as much fun as I had, but be assured: I had a lot of it. Also remember: "Wenn hier einer fuddelt, dann klatscht es!"

Martine Wahnschafffe, *Giorgio Zarantonello* and *Amado Bautista-Salvador* designed and produced all the ion traps that we used. Thank you all for your contributions and help.

I like to thank *Kai Voges*, *Johannes Mielke* and *Fabian Ude* for dumping at least one year of their student-life into this project. You guys laid the foundation for all the laser systems that I needed to re-work, but not build from scratch.

I like to acknowledge many years of support from *Anna-Great Paschke* and *Henning Hahn* on various topics.

I like to thank *Malte Niemann* for criticizing every breath that I ever took, every movement that I ever made and every idea that I ever conceived. I also like to thank *Teresa Meiners* for filling this role when Malte was not available and also for being more polite while doing so. Most of the times, you guys had a point and I appreciate it.

I came to appreciate the fact that *Malte* was almost always more annoyed by anything or anyone than I was. Noticing that he suffers more than me, made most boring, painful, cringeworthy or infuriating events more bearable. *Malte* also is the only colleague who knows the real meaning of 'sprotzen', which goes a long way with me.

I probably need to thank *Malte* for constantly throwing heavy objects in my direction, *Sebastian* for sitting in the middle without even trying to dodge and *Teresa* for regularly interrupting the throw-show with a story full of useless facts, presented with excruciating levels of detail.

I like to thank *Jojo* for trying to order me a bunch of donkeys without asking 'why', *Christian* for signing that order and *Jojo* for not going through with it.

Ralf Lehnert, immortalized as the inventor of the adapters that shall forever bear his name, was a constant source of knowledge, advice and fun. *Ralf*, thank you for putting up with me. The only thing that I regret is that we never made it to the creationist museum.

Karma has a many names. They are *Gunhild Faber*, *Elke Hünitzsch*, *Katrin Pfennig*, *Birgit Ohlendorf* and *Barbara Thiele-Bode*. When I did something very stupid, so at least once a week, a valid question to ask was 'at what distance is one of them able sense me and stop my heart from beating through sheer force of will'. Thankfully, they never did. Instead they guided me through every bureaucratic nightmare and, when none of these horrible paper-based monsters were in sight, showed off their considerable wisdom culminating in very appreciated advice.

On some days, it felt like I could not even tie my shoes without the help of *Alexander Vocino*, *Jonas Peter* and *Emil Adamzcyk*. You guys gave me invaluable help designing the mechanical components of the experiment. You also manufactured most of them, which I am thankful for. I am glad that I didn't need to spend my breaks with physicists. I also like thank you for relentlessly exploiting my cooking skills.

At last, I would like to thank my family and friends for leaving me alone during the writing-phase of this thesis, yet always being just a phone call away when I needed distraction or a pep-talk. Special thanks to *Reza* and *Dima* for pretending not to understand anything about my work in an attempt to make me feel smart and to *Olli* and *Judith* for assuring me that this is in fact not the case.

List of publications

Timko Dubielzig, Sebastian Halama, Henning Hahn, Giorgio Zarantonello, Malte Niemann, Amado Bautista-Salvador, Christian Ospelkaus:
Ultra-low vibration closed-cycle cryogenic surface-electrode ion trap apparatus.
arXiv:2008.05601 [physics, physics:quant-ph], (2020).

M. Wahnschaffe, H. Hahn, G. Zarantonello, **T. Dubielzig**, S. Grondkowski, A. Bautista-Salvador, M. Kohnen, and C. Ospelkaus:
Single-ion microwave near-field quantum sensor.
Applied Physics Letters **110**, 034103 (2017).

M. Carsjens, M. Kohnen, **T. Dubielzig**, C. Ospelkaus:
Surface-electrode Paul trap with optimized near-field microwave control.
Appl. Phys. B **114**, 243–250 (2014).

M. Niemann, A.-G. Paschke, **T. Dubielzig**, S.Ulmer, C. Ospelkaus:
CPT test with (anti)proton magnetic moments based on quantum logic cooling and read-out.
Proceedings on the 6th meeting on CPT and Lorentz Symmetry, Bloomington, Indiana World Scientific, Singapore, 41-44, (2014).

Timko Dubielzig

Research

04/2011 - 12/2020

Doctoral Studies

Leibniz Universität Hannover
Institut für Quantenoptik

PhD thesis in the group of Prof. Dr. Christian Ospelkaus

Ultra-low vibration closed-cycle cryogenic surface-electrode ion trap apparatus

University

10/2003-10/2010

Diploma in physics

Leibniz Universität Hannover
Laser Zentrum Hannover

Diploma thesis in the group of Prof. Dr. Alexander Heisterkamp

Charakterisierung eines Multiphotonenmikrokops mit Hilfe von Goldnanopartikeln und Untersuchungen zum Erstellen neuartiger Prüfkörper für die Multiphotonen-mikroskopie

School

2002

Abitur

Otto Hahn Gymnasium, Springe